



# BRNO UNIVERSITY OF TECHNOLOGY

VYSOKÉ UČENÍ TECHNICKÉ V BRNĚ

## CENTRAL EUROPEAN INSTITUTE OF TECHNOLOGY BUT

STŘEDOEVROPSKÝ TECHNOLOGICKÝ INSTITUT VUT

# DEVELOPMENT OF FOURIER TRANSFORM INFRARED SPECTROSCOPY IN HIGH MAGNETIC FIELDS

VÝVOJ INFRAČERVENÉ SPEKTROSKOPIE S FOURIEROVOU TRANSFORMACÍ V SILNÝCH  
MAGNETICKÝCH POLÍCH

## DOCTORAL THESIS

DIZERTAČNÍ PRÁCE

### AUTHOR

AUTOR PRÁCE

Ing. Jana Dubnická Midlíková

### SUPERVISOR

ŠKOLITEL

doc. Ing. Petr Neugebauer, Ph.D.

### CO-SUPERVISOR

ŠKOLITEL SPECIALISTA

doc. Mgr. Adam Dubroka, Ph.D.

BRNO 2023



## Abstract

Fourier-transform infrared (FTIR) spectroscopy in high magnetic fields, concisely FTIR magneto-spectroscopy, is a powerful spectroscopic technique used to investigate many important effects in materials, e.g., electron paramagnetic resonance, cyclotron resonance, and transitions between Landau levels. Despite their enormous potential in solid-state physics, infrared magneto-spectrometers are still relatively rare and custom-made since such systems generally require complex infrastructure. This doctoral thesis describes in detail the design and implementation of a versatile FTIR magneto-spectroscopic setup operating in the range of 50–10,000  $\text{cm}^{-1}$ , high magnetic field up to 16 T and temperatures between 2–320 K located at the Central European Institute of Technology of Brno University of Technology. This setup allows us to perform a variety of magneto-optical measurements spanning the range from THz/far-infrared (FIR) to near-infrared (NIR). It consists of a commercial FTIR spectrometer coupled to a 16 T cryogen-free superconductive magnet by the custom-designed optical coupling and transmission probes designed for experiments with multiple detectors and samples in Faraday geometry. The novelty of the setup lies in the usage of a cryogen-free superconducting magnet. We have optimized and tested the performance of the FTIR magneto-spectroscopic setup for various configurations and determined a workable setup range. The functionality of the FTIR magneto-spectroscopic setup was demonstrated by the magneto-optical measurements of the zero-field splitting in cobalt(II)-based single ion magnet in the FIR region, indirect inter-band transitions between Landau levels (LLs) in germanium in the NIR region, and inter-band transitions between LLs in graphene in the FIR region. Moreover, we measured the I-V characteristics of graphene bolometer devices.

## Keywords

Fourier-transform infrared (FTIR) magneto-spectroscopy, FTIR magneto-spectroscopic setup, cryogen-free superconducting magnet, single molecule magnets, electron paramagnetic resonance, Landau levels

## Abstrakt

Infračervená spektroskopie s Fourierovou transformací (FTIR) v silných magnetických polích, zkráceně FTIR magnetospektroskopie, je výkonná spektroskopická technika používaná ke zkoumání mnoha důležitých jevů v materiálech, např. elektronové paramagnetické rezonance, cyklotronové rezonance a přechodů mezi Landauovými hladinami. Navzdory svému obrovskému potenciálu ve fyzice pevných látek jsou infračervené magnetospektrometry stále poměrně vzácné a vyráběné na zakázku, protože takové systémy obvykle vyžadují složitou infrastrukturu. Tato disertační práce podrobně popisuje návrh a realizaci univerzálního FTIR magnetospektroskopického zařízení pracujícího v rozsahu 50–10 000  $\text{cm}^{-1}$ , silném magnetickém poli až 16 T a teplotách mezi 2–320 K umístěné na Středoevropském technologickém institutu VUT v Brně. Toto zařízení nám umožňuje provádět různá magnetooptická měření v rozsahu od THz/vzdálené infračervené oblasti (FIR) až po blízkou infračervenou oblast (NIR). Skládá se z komerčního FTIR spektrometru spojeného s 16 T bezkryogenním supravodivým magnetem pomocí na míru navržené optické spojky a přenosových sond určených pro experimenty s více detektory a vzorky ve Faradayově geometrii. Novinka tohoto uspořádání spočívá v použití supravodivého magnetu bez kryogenu. Optimalizovali jsme a otestovali výkonnost FTIR magnetospektroskopického zařízení pro různé konfigurace a určili použitelný rozsah zařízení. Funkčnost FTIR magnetospektroskopického zařízení byla prokázána magnetooptickými měřeními štěpení při nulovém poli v jednoiontovém magnetu na bázi kobaltu(II) v oblasti FIR, nepřímých mezipásmových přechodů mezi Landauovými hladinami (LLs) v germaniu v NIR oblasti a mezipásmových přechodů mezi LLs v grafenu v oblasti FIR. Kromě toho jsme změřili volt-ampérové charakteristiky grafenových bolometrických zařízení.

## Klíčová slova

infračervená magnetospektroskopie s Fourierovou transformací (FTIR), FTIR magnetospektroskopické zařízení, supravodivý magnet bez kryogenu, jednomolekulové magnety, elektronová paramagnetická rezonance, Landauovy hladiny

DUBNICKÁ MIDLÍKOVÁ, Jana. *Development of Fourier Transform InfraRed Spectroscopy in High Magnetic Fields*. Doctoral thesis. BUT CEITEC: Brno University of Technology, Central European Institute of Technology, Brno, 2023. 156 p. Supervised by doc. Ing. Petr Neugebauer, Ph.D.

## **Declaration**

I hereby declare that I have elaborated my doctoral thesis on the theme of “Development of Fourier Transform InfraRed Spectroscopy in High Magnetic Fields” independently, under the supervision of doc. Ing. Petr Neugebauer, Ph.D., co-supervisor doc. Mgr. Adam Dubroka, Ph.D., and with the use of literature and other sources of information, which are all quoted in the thesis and detailed in the References at the end of this thesis.

Ing. Jana Dubnická Midlíková



## Acknowledgement

I want to thank all those who contributed directly or indirectly to this work. First of all, I would like to thank my supervisor, doc. Ing. Petr Neugebauer, Ph.D., and co-supervisor doc. Mgr. Adam Dubroka, Ph.D. for professional guidance and consultations. I want to thank all members of our CEITEC MOTeS research group for useful discussions and comments during the development of the setup and friendly environment, namely Dr. Vinicius Santana for his tremendous willingness and help with the analysis of data, Ing. Antonín Sojka, Ph.D., Ing. Matúš Šedivý, Dr. Oleksii Laguta, for their helpful advice with mechanical design, the electronics, and the laboratory equipment, and doc. Ing. Ivan Šalitroš, Ph.D. and Ing. Jana Juráková for providing samples. Then, I would like to thank Dominik Varga (CEITEC Nano research infrastructure, Brno, Czech Republic) for the fabrication of the setup components in the mechanical workshop. I would also like to thank RNDr. Milan Orlita, Ph.D. (Grenoble High Magnetic Field Laboratory, Grenoble, France) for helpful advice during the design and optimization of the setup and fruitful discussions over the results of magneto-optical measurements and Ing. Aleš Srnka, CSc. (Institute of Scientific Instruments of the Czech Academy of Sciences, Brno, Czech Republic) for help in the organization of measurements. Special thanks belong to my beloved husband, Ladislav, and my family for their love, encouragement, and constant support.

My work and research has been financially supported by the European Research Council (ERC) through the European Union's Horizon 2020 Research and Innovation Program under Grant 714850, Ministry of Education, Youth and Sports of the Czech Republic (MEYS CR) under the INTER-EXCELLENCE Program under Grant LTAUSA19060. Moreover, I was supported by Brno Ph.D. Talent 2018 scholarship by JCMM and by Internal junior grant project within CEITEC BUT 2019. This research has been also financially supported by the MEYS CR under the project CEITEC 2020 (LQ1601) and part of the work was carried out with the support of CEITEC Nano Research Infrastructure (ID LM2015041, MEYS CR, 2016-2019), CEITEC Brno University of Technology. CzechNanoLab project LM2018110 and LM2023051, funded by MEYS CR, is gratefully acknowledged for the measurements at CEITEC Nano Research Infrastructure.

Ing. Jana Dubnická Midlíková



# Contents

<b>Introduction</b>	<b>1</b>
<b>Aims of Thesis</b>	<b>5</b>
<b>1 Theoretical Background</b>	<b>7</b>
1.1 Electromagnetic Radiation . . . . .	7
1.1.1 Maxwell's Equations . . . . .	10
1.2 Electromagnetic Spectrum . . . . .	12
1.2.1 Infrared Radiation . . . . .	13
1.3 Infrared Spectroscopy . . . . .	14
1.3.1 History of IR Spectroscopy . . . . .	15
1.3.2 Molecular Vibrations . . . . .	19
1.3.3 Lorentz Oscillator Model . . . . .	20
1.3.4 Beer-Lambert Law . . . . .	22
1.4 FTIR Spectrometer . . . . .	23
1.4.1 Michelson Interferometer . . . . .	24
1.4.2 Principle . . . . .	25
1.4.3 Advantages of FTIR Spectrometers . . . . .	30
1.4.4 Instrumentation . . . . .	32
a) Sources . . . . .	32
b) Detectors . . . . .	33
c) Beamsplitters . . . . .	36
d) Mirrors . . . . .	38
e) Winston Cone . . . . .	38
1.4.5 Spectral Analysis . . . . .	40
1.5 High Magnetic Fields . . . . .	40
1.5.1 Superconducting Magnets . . . . .	41
<b>2 FTIR Magneto-Spectroscopy</b>	<b>43</b>
2.1 Electron Paramagnetic Resonance (EPR) . . . . .	44
2.1.1 Single-Molecule Magnets (SMMs) . . . . .	46
2.2 Landau Levels (LLs) . . . . .	50
2.2.1 2D Materials . . . . .	51
2.3 State of the Art . . . . .	56

<b>3</b>	<b>Experimental Setup</b>	<b>61</b>
3.1	Beam Propagation	62
3.2	Setup Design and Components	64
3.2.1	FTIR Spectrometer	64
3.2.2	Superconductive Magnet	66
3.2.3	Optical Coupling	67
3.2.4	Transmission Probes	69
	a) Probe A - External Detection Probe	69
	b) Probe B - Internal Detection Probe	72
	c) Probe B - Chipset Probe	74
3.2.5	Movable Table	77
3.3	Technological Methods	77
3.3.1	3D Printing	77
3.3.2	Soldering	78
3.3.3	Polishing	79
3.3.4	Silver Plating	80
3.4	Testing of the Setup	80
3.4.1	Window Test	81
3.4.2	Signal Test	81
3.4.3	Leak Test	83
3.5	Performance of the Setup	84
<b>4</b>	<b>Magneto-Optical Measurements</b>	<b>87</b>
4.1	Data Analysis and Manipulation	87
4.2	Measurements at GHMFL	95
4.2.1	Pentacoordinate Cobalt(II) Single Ion Magnets (SIMs)	96
4.2.2	Mononuclear Cobalt(II) Field-Induced SMM	105
4.3	Measurements at CEITEC BUT	108
4.3.1	Zero-field Splitting in Cobalt(II)-based SIM	109
4.3.2	Indirect Interband Transitions between LLs in Germanium	115
4.3.3	Graphene	118
4.3.4	Graphene Bolometer Devices	119
	<b>Conclusion and Outlook</b>	<b>123</b>
	<b>References</b>	<b>127</b>
	<b>List of Used Abbreviations</b>	<b>151</b>
	<b>Author publications and outputs</b>	<b>155</b>

---

# Introduction

This doctoral thesis deals with Fourier-transform infrared (FTIR) spectroscopy in high magnetic fields, concisely FTIR magneto-spectroscopy, a powerful spectroscopic technique used to investigate many important effects in materials, e.g., electron paramagnetic resonance (EPR), cyclotron resonance, and transitions between Landau levels (LLs). In the thesis, we describe the design and implementation of a versatile broadband setup for FTIR magneto-spectroscopy operating in the range of  $50\text{--}10,000\text{ cm}^{-1}$ , high magnetic field up to 16 T and temperatures between 2–320 K located at the Central European Institute of Technology of Brno University of Technology (CEITEC BUT). This setup allows us to perform a variety of magneto-optical measurements spanning the range from THz/far-infrared (FIR) to near-infrared (NIR). FTIR magneto-spectroscopic setup consists of a commercial FTIR spectrometer and 16 T cryogen-free superconducting magnet coupled with custom-designed optical coupling and transmission probes for experiments performed on various samples in Faraday geometry using multiple detectors with two possibilities of their placement, outside and inside the superconducting magnet, as schematically shown in Fig. 1.

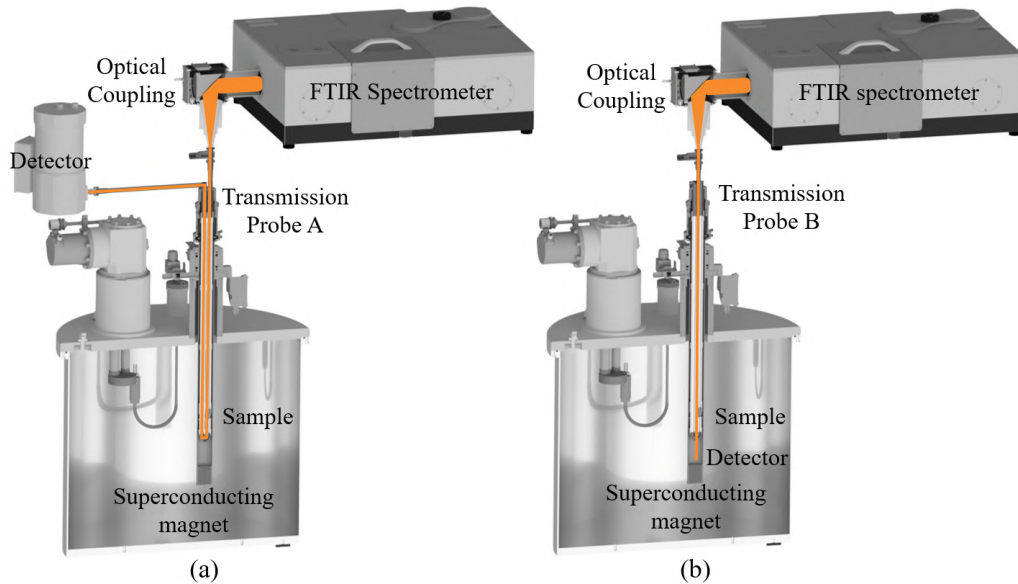


Fig. 1: The schematic of the FTIR magneto-spectroscopic setup shows the beam propagation through the setup in two configurations of the detector placement: (a) Probe A, inserted into the superconducting magnet, is designed for the detector located outside the magnet, and (b) Probe B is designed for the detector located inside the magnet.

Using various detectors, the setup spans the entire IR and partially the THz range. This aspect is particularly important because it enables the measurement of different types of samples from single molecule magnets (SMMs) in the FIR region to germanium in the NIR region, as demonstrated in the magneto-optical measurements chapter. Another novelty of the setup lies in the usage of a cryogen-free superconducting magnet.

This doctoral thesis is divided into four chapters. The first chapter, entitled “Theoretical Background,” provides a theoretical framework for understanding the key concepts and phenomena that underpin our research topic. It comprises sections about electromagnetic radiation, electromagnetic spectrum, IR spectroscopy, and FTIR spectrometer. Last but not least, the importance of high magnetic fields is explained.

Spectroscopy is one of the most fundamental and widespread experimental techniques for scientific investigation. All types of spectroscopic techniques have one thing in common; they all study the interaction of electromagnetic radiation with matter. The interactions are characterized by the energy of the radiation and its effects on materials. When the radiation energy falls within the IR region of the electromagnetic spectrum, we speak of IR spectroscopy. IR spectroscopy is considered one of the most powerful and widespread spectroscopic tools of the 20th and 21st centuries [1]. It provides detailed information about molecular vibrations. The history of IR spectroscopy can be traced back to the work of Sir William Herschel, who in 1800 discovered IR radiation beyond the red end of the visible spectrum when he investigated the heating effect of sunlight [2]. However, a major breakthrough in IR spectroscopy that led to its widespread use came in the 1970s with the introduction of Fourier-transform infrared (FTIR) spectrometers equipped with interferometers, exploiting the well-established mathematical process of Fourier transform (FT) [3]. Due to its significantly improved acquisition of IR spectra, leading to better signal-to-noise and reduced data acquisition time, the FTIR spectrometers are nowadays predominantly used spectrometers in the IR range [4]. Thus, IR spectroscopy is frequently referred to as FTIR spectroscopy.

The second chapter, entitled “FTIR magneto-spectroscopy,” introduces the core technique of the doctoral thesis and explains the physical principles and effects underpinning our research, i.e., electron paramagnetic resonance (EPR) and transitions between Landau Levels (LLs). It also describes in detail the most relevant classes of materials for our research, i.e., SMMs and 2-dimensional (2D) materials. This chapter moreover provides an overview of several state-of-the-art magneto-optical setups worldwide utilizing this method.

Why do we want to combine FTIR spectroscopy with high magnetic fields? The presence of a magnetic field is essential for studying the characteristics of materials

---

in many scientific disciplines because many physical phenomena depend explicitly on it. FTIR spectroscopy in high magnetic field or simply FTIR magneto-spectroscopy is a powerful spectroscopic technique used to investigate many important effects in materials, e.g., EPR, cyclotron resonance, and transitions between LLs [6]. In the digital world we live in today, the growing need for smaller and more energy-efficient devices has made higher density data storage one of the most significant technological quests. Therefore, research is focused on developing more compact means of data storage that can store greater amounts of data in a more energy-efficient way. Our research is aimed mainly at the investigation of SMMs, molecules displaying slow relaxation of magnetization of purely molecular origin [7, 123], thus the ability to store one bit of information at much higher densities. FTIR magneto-spectroscopy is an essential method in the characterization of SMMs due to the ability to probe molecular and electronic properties directly [9, 10]. It allows studying EPR phenomenon in SMMs with very large zero-field splitting (ZFS), mainly based on transition metal complexes [11] – [18] or lanthanides [19] – [22], in which conventional microwave EPR systems do not provide experimental access to the magnetic resonance transitions. Besides, FTIR magneto-spectroscopy also presents an ideal experimental technique that can investigate band structure and electronic properties of materials such as graphene [23] – [28]. However, despite their enormous potential in material science, IR magneto-spectrometers are still relatively rare and custom-made since such systems generally require complex infrastructure.

The third chapter, “Experimental Setup,” is dedicated to the design and implementation of the home-build FTIR magneto-spectroscopic setup at CEITEC BUT. This chapter maps the process from the design of the setup through the methods used for its assembly and testing to the summary of the setup’s performance. It consists of sections about Beam propagation, Setup Design and Components, Methods, Testing of the setup, and Performance of the setup.

The last, fourth chapter of the thesis, entitled “Magneto-Optical Measurements,” provides results of magneto-optical measurements performed on two different setups. The first section is devoted to data analysis and manipulation, describing and explaining typical analysis methodology from raw data to published results. The second section, Measurements at GHMFL, reviews the published results of the measurements performed on the IR magneto-spectroscopic setup at Grenoble High Magnetic Field Laboratory (GHMFL) of the French National Center for Scientific Research (CNRS), carried out at the time when our FTIR magneto-spectroscopic setup was not yet finished. The third section, Measurements at CEITEC, reviews results obtained from our FTIR magneto-spectroscopic setup after completing it and successfully testing the performance in several configurations. These results include the magneto-optical measurements by which the functionality of our setup was demonstrated,

i.e., the ZFS in cobalt(II)-based single ion magnet in the FIR region, indirect inter-band transitions between Landau levels (LLs) in germanium in the NIR region, and inter-band transitions between LLs in graphene in the FIR region. Moreover, the measurements of the I-V characteristics of graphene bolometer devices are shown here.

---

# Aims of Thesis

The ultimate goal of my doctoral studies and this thesis is to realize the method of FTIR spectroscopy in high magnetic fields by the development of the compact FTIR magneto-spectroscopic setup at CEITEC BUT in order to perform sensitive magneto-optical measurements on SMMs, novel 2D materials, or combination of both. It consists of several minor aims that need to be carried out to accomplish the ultimate goal. Therefore, I formulate my aims as follow:

## **1. Overall design of the FTIR magneto-spectroscopic setup**

The first aim is focused on the overall design of the compact FTIR magneto-spectroscopic setup. This comprises mainly the design of the coupling of FTIR spectrometer superconducting magnet and external detectors. The coupling consists of two main parts: optical coupling, which guides the beam out of the spectrometer to the magnet, and two types of transmission probes/waveguides, which guide the beam through the sample placed in the magnet to the detector. The first probe A is designed to measure the sample/reference signal by the detector placed outside the superconducting magnet (e.g., room temperature detectors). The second probe B is designed for the detector placed inside the superconducting magnet (i.e., sealed bolometer) and for testing measurements on graphene bolometer devices incorporated in a chipset holder. This part also includes the design of a movable table on which FTIR spectrometer and part of the setup is placed.

## **2. Assembly, testing and putting the setup into the operation**

When the design and manufacture of individual components are completed, the setup will be assembled and put into operation. This includes testing, troubleshooting the setup, and optimizing its performance to prepare it for magneto-optical measurements properly. The first step to test the setup's performance will be measuring the signal that passes through the setup and the sample/reference to the DTGS or InGaAs detector without a magnetic field. If the signal at the detector is insufficient, we will look for ways to improve it. When the signal is sufficient, we will test the performance of the setup in all possible configurations of probes, detectors, sources, and beamsplitters with no sample, just reference opening, and without a magnetic field. Then, samples with already published results will be measured to provide a comparison of the obtained results. Upon successful completion of this part, the FTIR magneto-spectroscopic setup will be functional, and magneto-optical measurements of desired samples can be carried out.

### **3. Performance of magneto-optical measurements at CEITEC BUT**

The final aim is to perform magneto-optical measurements on the home-built FTIR magneto-spectroscopic setup at CEITEC BUT. This state-of-the-art instrumentation will be useful for revealing interesting properties of SMMs with very large zero-field splitting (promising molecules for future data storage and spintronics), novel 2D materials, and testing graphene bolometric devices. After recording a sufficient number of spectra, emphasis will be placed on careful analysis of experimentally measured data (theoretical simulations and fitting) and searching for results of scientific importance, which will then be summarized and published in peer-reviewed journals.

---

# 1 Theoretical Background

In this chapter, we will provide a theoretical background and overview of the fundamental concepts relevant to the topic of the doctoral thesis, i.e., Fourier Transform Infrared (FTIR) spectroscopy in high magnetic fields. This will include an introduction to electromagnetic radiation, infrared spectroscopy, FTIR spectrometer, and high magnetic fields.

## 1.1 Electromagnetic Radiation

Electromagnetic radiation can be described as the flow of electromagnetic energy through the space or material medium. It can be considered in terms of classical (wave) or quantum (particle) theories [1].

Electromagnetic radiation is, classically speaking, a wave composed of oscillating electric and magnetic fields, hence the term "electromagnetic", acting in planes that are perpendicular to each other and to the direction of propagation [29], as shown in Fig. 1.1. The magnitudes of the electric and magnetic vectors are represented by  $E$  and  $B$ , respectively. In vacuum, the propagation velocity of electromagnetic waves is constant for all frequencies, and it is known as the speed of light, denoted as  $c$ , and has the value  $c = 2.99792458 \times 10^8 \text{ m s}^{-1}$  [30]. The phase<sup>1</sup> velocity of electromagnetic waves varies with the refractive index  $n$  of the medium and it is given by  $c/n$  [1], [29] whereas frequency is independent of the medium in which it is measured.

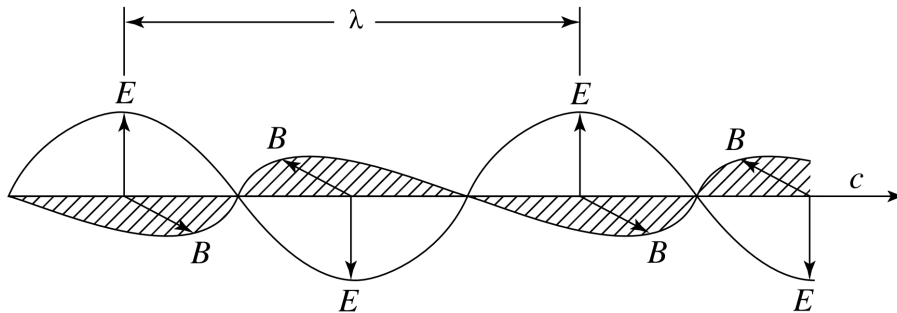


Fig. 1.1: Representation of an electromagnetic wave. Adapted from [29].

Electromagnetic radiation/wave is usually characterized by its wavelength  $\lambda$ , which is the length of one wave, and its frequency  $\nu$ , which is the number of vibrations per unit time, usually in units hertz (Hz) [31]. They are related to each other

---

<sup>1</sup>The phase velocity of a wave is the rate at which the wave propagates in any medium.

and to the speed of light  $c$  in the following way:

$$c = \lambda\nu. \quad (1.1)$$

Another unit to characterize electromagnetic waves, widely used in infrared spectroscopy, is called wavenumber,  $\tilde{\nu}$ , which represents the number of waves per unit length and is given by the following relationship:

$$\tilde{\nu} = 1/\lambda = \nu/c. \quad (1.2)$$

Wavenumber is usually expressed in units called reciprocal/inverse centimeters abbreviated as  $\text{cm}^{-1}$ , but it could be expressed in any reciprocal distance units [3]. Using frequency and wavenumber units have two main advantages over wavelength units. The first is that they remain constant regardless of the medium through which the radiation passes, whereas the wavelength decreases if the radiation passes through a medium with a refractive index  $n$  greater than that of a vacuum. The second advantage is that they are directly proportional to the energy. Therefore, a transition that requires more energy will occur at a higher wavenumber. For this reason, wavenumber units are commonly used in IR spectroscopy as opposed to wavelength units (e.g., nanometers), which are commonly used in visible and ultraviolet (UV) spectroscopy [3].

In terms of modern quantum theory, electromagnetic radiation is the flow of photons (quanta) through space. Photons are uncharged massless elementary particles that move with the speed of light in vacuum, exhibit wave-particle duality<sup>2</sup> [32] and represent a quantum of the electromagnetic field [33]. In 1900, Max Planck<sup>3</sup> postulated the quantum hypothesis that the energy of a single photon is quantized, so that all material systems can absorb or emit electromagnetic radiation only in quanta of energy  $E$ , which are proportional to the frequency of this radiation  $\nu$ , whose value is the same as that of the frequency of the electromagnetic wave of classical theory [1]. This relationship is given by Planck's equation

$$E = h\nu = hc\tilde{\nu}, \quad (1.3)$$

where  $h\nu$  is a quantum of energy, and  $h$  is a universal constant which is known as Planck's constant, which has a value  $h = 6.62606876 \times 10^{-34} \text{ J s}$  [30]. A commonly used unit of energy is the electronvolt (eV) which is defined as the kinetic energy acquired by an electron which has been accelerated by a potential difference of 1 volt (V). The electronvolt is related to the more usual unit of energy by:  $1 \text{ eV} = 1.60218 \times 10^{-19} \text{ J}$  [30].

---

<sup>2</sup>their behavior featuring properties of both waves and particles [32]

<sup>3</sup>In 1918, Max Planck was awarded the Nobel Prize in Physics for his work on quantum theory [34].

In 1913, Niels Bohr postulated that the electrons of an atom occupy specific energy states or levels (also called quantum states) that are defined by the radius of the electron's orbit around the nucleus. Atoms must absorb or emit energy equal to the energy difference between the two levels to move between different energy states, see Fig. 1.2. By moving from a higher energy state  $E_h$  to a lower energy state  $E_l$ , a photon of energy  $h\nu$  (quantum of electromagnetic radiation), is emitted of a magnitude that is precisely the energy difference  $\Delta E$  between the higher  $E_h$  and lower  $E_l$  state [3]:

$$\Delta E = E_h - E_l = h\nu. \quad (1.4)$$

Alternatively, the electron can absorb a photon  $h\nu$  and move from  $E_l$  to  $E_h$  if  $h\nu$  matches the energy difference [3].

Each element has electrons at unique energy levels corresponding to its atomic structure. When an element is exposed to radiation of all wavelengths, only the wavelengths (energy photons) corresponding to that atom's levels (energy states) can interact. The resulting pattern of energy lines, called a spectrum, coincides with the absorption or emission of photons specific to that element [3].

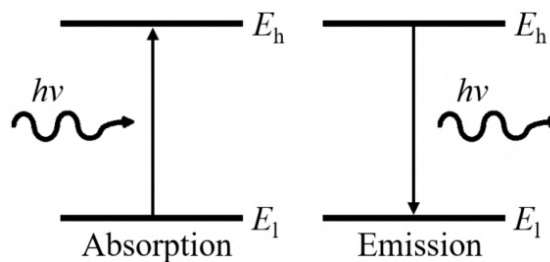


Fig. 1.2: The photon of energy  $h\nu$  whose frequency matches the energy difference between electronic levels (higher energy state  $E_h$  and lower energy state  $E_l$ ) can be absorbed or emitted as the electron transitions between the two levels. Adapted from [3].

Electromagnetic waves are produced by the acceleration of electric charges of a charged particle (e.g., an electron, which changes its velocity) [1] because any accelerating charge produces a changing electric field, which in turn creates a changing magnetic field. These changing electric and magnetic fields interact with each other and propagate through space as electromagnetic waves. In general, free charges (those not bound within an atom) emit electromagnetic radiation when accelerated. This is true for charges that change speed in a straight line in a linear accelerator, float in circles in a cyclotron, or simply oscillate back and forth in a radio antenna - if the charge moves nonuniformly, it radiates. A free charged particle can spontaneously absorb or emit a photon [35].

### 1.1.1 Maxwell's Equations

Maxwell's equations, named after the physicist and mathematician James Clerk Maxwell, are a set of fundamental equations describing the behavior of electric and magnetic fields in free space and in matter. They are essential for understanding the generation and behavior of electromagnetic waves and form the foundation of classical electromagnetism. Maxwell's equations with material equations describe the electromagnetic response of matter and the propagation of radiation in matter. One way to write these equations is in the form of macroscopic<sup>4</sup> differential equations (in SI units) [36]:

$$\nabla \cdot \mathbf{D} = \rho, \quad (1.5)$$

$$\nabla \cdot \mathbf{B} = 0, \quad (1.6)$$

$$\nabla \times \mathbf{E} = -\frac{\partial \mathbf{B}}{\partial t}, \quad (1.7)$$

$$\nabla \times \mathbf{H} = \mathbf{j} + \frac{\partial \mathbf{D}}{\partial t}, \quad (1.8)$$

where  $\mathbf{D}$  is the electric displacement,  $\rho$  is the free charge density,  $\mathbf{B}$  is the magnetic induction,  $\mathbf{E}$  is the electric field strength,  $\mathbf{H}$  is the magnetic field strength,  $\mathbf{j}$  is the current density, and  $t$  represents time. Symbols in bold represent vector quantities. Equation 1.5 is Gauss's law of electrostatics which describes the relation between electric charges and the electric field. Equation 1.6 is Gauss's law for magnetism, expressing the assumption that free magnetic monopoles do not exist. Equation 1.7 is Faraday's law of induction which describes the generation of an electric field by time-dependence of the magnetic field. Equation 1.8 is Ampère's circuital law showing that the magnetic field is generated by electric currents and changes in the electric displacement  $\mathbf{D}$  [36, 37].

The response of a dielectric (i.e., nonconducting) material to an external electric field is characterized by three macroscopic vectors:  $\mathbf{E}$ ,  $\mathbf{D}$ , and polarization  $\mathbf{P}$ , which is defined as the net dipole moment per unit volume [36]. The application of the field tends to produce many microscopic dipoles that are aligned parallel to the direction of the external field. This generates a net dipole moment, and hence polarization, in the dielectric. The microscopic dipoles will all tend to align along the field direction, and so the polarization vector  $\mathbf{P}$  will be parallel to  $\mathbf{E}$ . Assuming that the medium is isotropic and  $\mathbf{P}$  varies linearly with  $\mathbf{E}$ , we can write [36]:

$$\mathbf{P} = \epsilon_0 \chi \mathbf{E}, \quad (1.9)$$

where  $\epsilon_0$  is the electric permittivity of vacuum ( $\approx 8.854 \times 10^{-12} \text{ F}\cdot\text{m}^{-1}$ ) and  $\chi$  is the electric susceptibility of the medium.

---

<sup>4</sup>They describe the large-scale behavior of matter without having to consider atomic-scale charges and quantum phenomena like spins.

The electric displacement  $\mathbf{D}$  of the medium is related to the electric field  $\mathbf{E}$  and polarization  $\mathbf{P}$  through:

$$\mathbf{D} = \epsilon_0 \mathbf{E} + \mathbf{P} = \mu_0(1 + \chi) \mathbf{E} = \epsilon_0 \epsilon_r \mathbf{E} = \epsilon \mathbf{E}, \quad (1.10)$$

where  $\epsilon_r$ , defined as  $\epsilon_r = 1 + \chi$ , is the relative dielectric constant (permittivity), which is a very important parameter in the understanding and determining optical properties of the medium, and  $\epsilon$  is the dielectric constant of the medium.

The response of a material to external magnetic fields is treated similarly to the response of dielectrics to electric fields. The magnetization  $\mathbf{M}$  of the medium is proportional to the magnetic field strength  $\mathbf{H}$  through the magnetic susceptibility  $\chi_M$ :

$$\mathbf{M} = \chi_M \mathbf{H}. \quad (1.11)$$

The magnetic induction (flux density)  $\mathbf{B}$  is related to  $\mathbf{H}$  and  $\mathbf{M}$  through:

$$\mathbf{B} = \mu_0(\mathbf{H} + \mathbf{M}) = \mu_0(1 + \chi_M) \mathbf{H} = \mu_0 \mu_r \mathbf{H} = \mu \mathbf{H}, \quad (1.12)$$

where  $\mathbf{M}$  is the magnetization,  $\chi_M$  is the magnetic susceptibility,  $\mu_0$  is the magnetic permeability of the vacuum ( $4\pi \times 10^{-7} \text{ H}\cdot\text{m}^{-1}$ ),  $\mu_r$  is the relative magnetic permeability and  $\mu$  is the magnetic permeability of the medium [35, 36].

The last material equation, which is called Ohm's law, defines that there is a direct proportion between the current density  $\mathbf{j}$  and the electric field  $\mathbf{E}$ :

$$\mathbf{j} = \sigma_e \mathbf{E}, \quad (1.13)$$

where  $\sigma_e$  is the electrical conductivity [38].

The behavior of electromagnetic waves can be described by the differential equation which is called the wave equation, that is obtained from Maxwell's equations. Complete mathematical derivation of the electromagnetic wave equation can be found in Ref. [36]. One of the solutions of such the wave equation is a plane wave:

$$\mathbf{E} = \mathbf{E}_0 e^{i(kz - \omega t)}, \quad (1.14)$$

where  $\mathbf{E}_0$  is the amplitude of the wave,  $z$  is the direction of propagation,  $k$  is the wave vector, and  $\omega$  is the angular frequency. The magnitude of the wave vector  $k$  is given by:

$$k = \frac{2\pi}{\lambda} = \frac{\omega}{v} = \frac{n\omega}{c}, \quad (1.15)$$

where  $\lambda$  is the wavelength inside the medium.

Using the Maxwell's equations, we can relate the refractive index  $n$  of a medium to its relative dielectric constant  $\epsilon_r$ , for more details see the complex refractive index and dielectric constant section in Ref. [36]. List of optical parameters, such as  $n$  and  $\epsilon_r$ , for materials used in the millimetre and submillimetre range can be found in Ref. [39].

## 1.2 Electromagnetic Spectrum

The electromagnetic spectrum is the range of electromagnetic radiation distributed according to frequency, wavelength, or photon energy. In order of increasing frequency/energy and decreasing wavelength, it includes radio waves, microwaves (MWs), infrared (IR) radiation, visible light, ultraviolet (UV) radiation, X-rays and gamma-rays ( $\gamma$ -rays) [29]. These regions are illustrated in Fig. 1.3. There are no precise accepted boundaries between any of these adjacent regions of the electromagnetic spectrum, so the ranges usually overlap. The ranges of electromagnetic radiation in the electromagnetic spectrum are generally classified according to the kinds of chemical and physical effects they can produce on matter. At small frequencies  $\nu$  (smaller than  $10^8$  Hz), electric charges typically are the freely moving electrons in the metal components of antennas or the free electrons and ions in space that give rise to phenomena related to radio waves and MWs. In a magnetic field, exposure to radio waves only reorients nuclei, while exposure to slightly higher-energy microwaves changes the electron spin states of molecules with unpaired electrons. Microwave radiation can also change the rotational energy of molecules, which is used to heat food quickly in a microwave oven. In the infrared region of the spectrum ( $10^{12}$  to  $10^{14}$  Hz), the moving charges are primarily associated with the rotations and vibrations of molecules and the motions of atoms bonded together in materials. Electromagnetic radiation in the visible range to X-rays has frequencies that correspond to transitions between energy levels within atoms. Visible and UV radiations alter the electron energies of loosely held outer electrons of atoms and molecules, whereas X-rays can cause electron transitions between inner electron levels. Gamma rays are produced by transitions within atomic nuclei [3], [33]. The characteristics of the IR portion of electromagnetic radiation enlarged in Fig. 1.3, will be described in more detail in the following subsection.

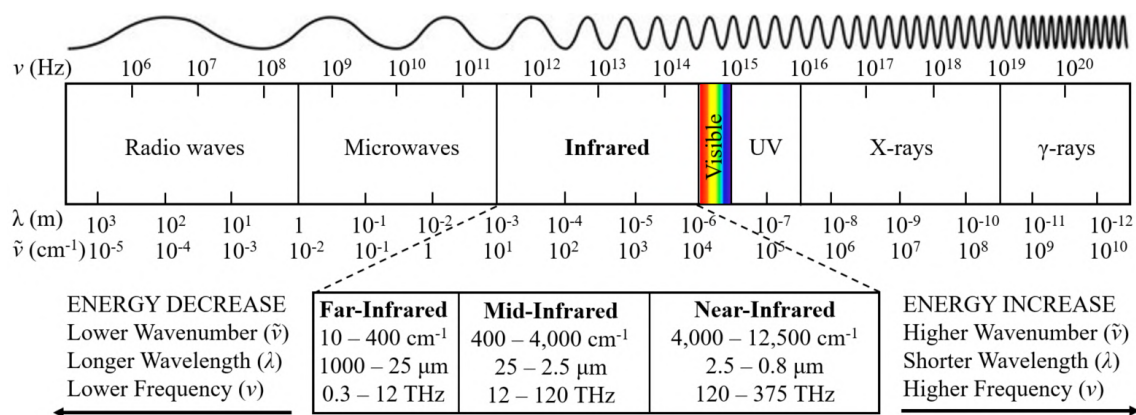


Fig. 1.3: The electromagnetic spectrum with expansion of the IR region.

### 1.2.1 Infrared Radiation

Beyond the red end of the visible range but at frequencies higher than those of MWs, there is the IR region of the electromagnetic spectrum, discovered in 1800 by Sir William Herschel [2], roughly defined in the wavenumber<sup>5</sup> range 10–12,500 cm<sup>-1</sup> (1 mm–800 nm, 1.24 meV–1.56 eV, 300 GHz–375 THz), which is rather broad in terms of energy; therefore, it is divided into three subregions: near-infrared (NIR) (4,000–12,500 cm<sup>-1</sup>), mid-infrared (MIR) (400–4,000 cm<sup>-1</sup>), and far-infrared (FIR) (10–400 cm<sup>-1</sup>) [40], as illustrated in Fig. 1.3.

Between the MWs and the IR region, there is the terahertz (THz) region partially overlapping with the FIR region filling the frequency gap<sup>6</sup>. It is usually defined as the region extending from 0.1 THz to 3 THz (3.3–100 cm<sup>-1</sup>). For the last two decades, THz spectroscopy has developed remarkably due to its intriguing applications in solid-state physics, material science, physical and analytical chemistry, biomedicine [40] – [42]. The emergence of THz spectroscopy to some extent also represented the renaissance of the FIR region [43].

Although IR radiation is invisible to the human eye, the skin perceives it as heat. It plays an important role in heat transfer and is an integral part of the greenhouse effect [33]. Every object on the Earth’s surface emits electromagnetic radiation, especially in the IR region of the spectrum. Artificial sources of IR radiation include, besides hot objects, IR light-emitting diodes (LEDs) [44], [45] employed as optoelectronic devices (such as optoisolators and in fiber-optics-based communications systems as light sources), and lasers employed for example in lidar<sup>7</sup> systems [46]. It is a technique that utilizes usually a NIR laser beam transmitted typically from an airplane, to determine the distance to an object by measuring the duration taken by the light to reflect back to the transmitter [46]. Because of its accuracy in mapping surface features, lidar is useful in creating topographical maps or 3-Dimensional (3D) maps of objects [46] – [49], see Fig. 1.4(a).

Devices used to detect IR radiation include various heat-sensitive instruments, such as thermocouple detectors, bolometers (some of which are cooled to near absolute zero to minimize their own thermal radiation), photovoltaic cells, and photoconductors composed of semiconducting materials such as silicon and lead sulfide, whose electrical conductance increases upon exposure to IR radiation [33]. Other applications of IR radiation include self-focusing cameras, security alarm systems, and night-vision devices, or TV remote controls. Overall, IR radiation

<sup>5</sup>Energy unit conversion of 1 cm<sup>-1</sup> = 10 mm<sup>-1</sup>  $\cong$  0.12 meV  $\cong$  30 GHz.

<sup>6</sup>It is also called THz gap where research was limited due to underdeveloped technologies operating in this region.

<sup>7</sup>The term “lidar” or “LIDAR” originates from the combination of “light detection and ranging” [46] or “laser imaging, detection, and ranging” [47].



Fig. 1.4: (a) A lidar map of New York City. Taken from [46]. (b) The observations of Carina Nebula taken in visible (left) and IR (right) light by the NASA/ESA Hubble Space Telescope reveal dramatically different and complementary views of an object. In the IR image, more stars are visible compare to the visible because interstellar dust scatters IR radiation less. Credit: NASA/ESA/M. Livio & Hubble 20th Anniversary Team (STScI). Taken from [50].

has a wide range of applications across various fields [51], from medical applications [52], through thermal imaging, heating, communication, meteorology and climatology [53], art conservation and analysis (IR reflectography) [54], physics and chemistry (IR spectroscopy), to space exploration (IR astronomy) [55] – [58]. IR astronomy allows researchers to observe cosmic objects through dense interstellar dust, which scatters IR radiation substantially less than visible light, see Fig. 1.4(b). However, IR radiation is partially absorbed by water vapor, carbon dioxide, and ozone in the Earth’s atmosphere (especially in the FIR region), therefore many IR astronomical observations are carried out at high altitudes by balloons, aircraft, or spacecraft [33].

In the following section, we focus solely on the application of IR radiation in IR spectroscopy.

### 1.3 Infrared Spectroscopy

IR spectroscopy is based on the vibrations of the atoms of a molecule [29]. It is a versatile experimental technique based on the vibrations of the atoms of a molecule [29] providing detailed information about molecular vibrations, which are useful for identifying molecules, studying their structure, and interactions with a surrounding

environment [1]. It is widely used in fields such as chemistry, biochemistry, and materials science and has applications in areas such as the pharmaceutical industry [59, 60], forensics [61], biomaterials [62], food industry [63, 64], paper [65, 66] and paint [67] industry, environmental analysis [68, 69], astronomy [70], etc. Therefore, it is no surprise that IR spectroscopy is considered one of the most powerful and widespread analytical spectroscopic tools of the 20th and 21st centuries [1].

The following subsection provides an overview of the most important milestones and developments in the history of IR spectroscopy, from the discovery of IR radiation to the building of the first FTIR spectrometer. After, we will firstly introduce the more general use of infrared (IR) spectroscopy related to molecular vibrations and then, Lorentz oscillator model, which is relevant to the thesis topic, will be explained. Also, Beer-Lambert law will be described here.

### 1.3.1 History of IR Spectroscopy

The history of IR spectroscopy can be traced back to the work of Sir William Herschel, a German-born British astronomer, who in 1800 discovered IR radiation as the first invisible portion of the electromagnetic spectrum that lies beyond the red end of the visible spectrum when he investigated the heating effect of sunlight dispersed by a prism on the temperature increase recorded on a thermometer. He named this radiation “Calorific Rays” [2]. The term “infrared” did not appear until late 19th century. Fig. 1.5 shows a portrait of Sir William Herschel and the experimental apparatus he used to demonstrate the existence of IR radiation.

However, the field of IR spectroscopy did not develop at that time due to difficulties in developing more sensitive temperature-measurement methods, e.i., producing suitable IR detectors [3]. Since then a variety of methods and devices have been developed to improve the experimental techniques for measuring IR spectra.

In 1822, Thomas Johann Seebeck discovered the thermoelectric effect<sup>8</sup> [72]. He made antimony/bismuth thermocouples and also an early thermopile by coupling together several such junctions. Leopoldo Nobili further developed thermopiles, which were in 1833 used by Macedonio Melloni to investigate the relative transmission of many materials. Melloni later in 1850 designed a MIR spectrometer with a slit, a rocksalt lens to provide an image of the slit, and provision for moving a slit-shaped thermopile across the spectrum generated by the fixed-position prism. This instrument remained the basic instrument for studying MIR radiation for nearly four decades, but it had limited resolution because wide slits were needed to fill the detector with radiation [73]. Samuel P. Langley decided to overcome this problem

---

<sup>8</sup>the direct conversion of temperature differences to electric voltage and vice versa via a thermocouple [71]

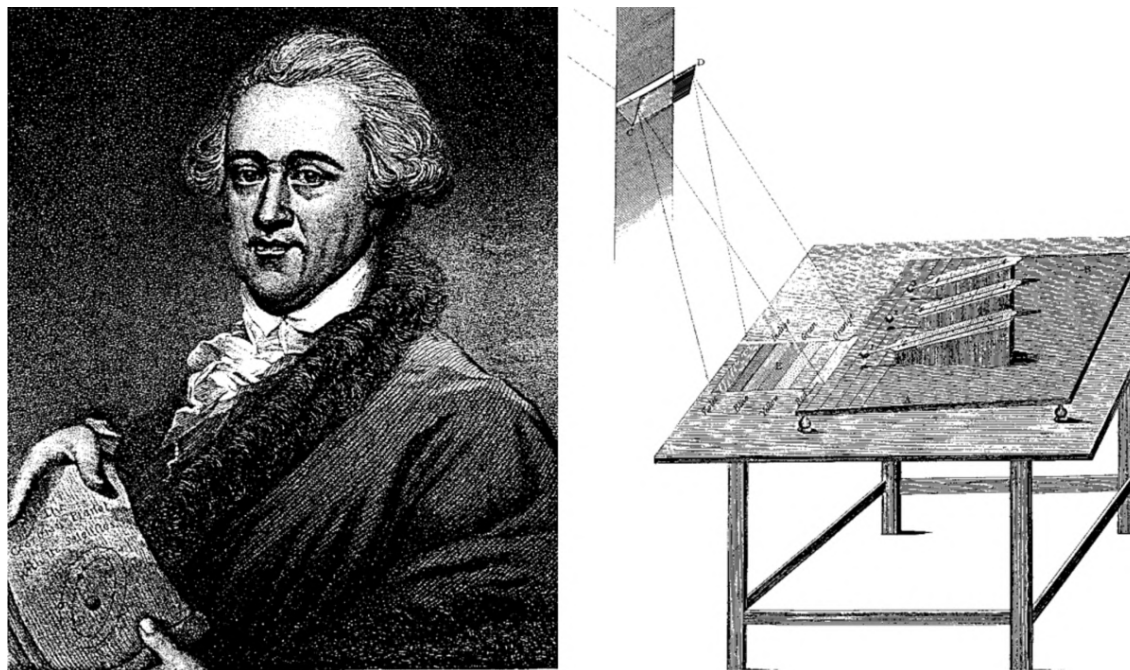


Fig. 1.5: Portrait of Sir William Herschel, the discoverer of the IR region and the apparatus he used to demonstrate the existence of IR radiation. Taken from [73].

in 1880 when he designed a small detector for use with narrow slits that also had a low heat capacity to maximize the temperature rise from the consequently reduced heat flux [74]. This detector, which he called a bolometer (a resistance thermometer), consisted of a narrow blackened platinum wire as one arm of a Wheatstone bridge whose resistance varied with the change in its temperature, a method of heat detection previously discovered by Adolf F. Svanberg in 1851. The wire was blackened to absorb radiation, and its sensitivity exceeded that of Melloni's thermopile by about three orders of magnitude [73]. In early 20th century, William W. Coblentz performed complex experiments leading to the precise measurement of IR spectra for hundreds of organic and inorganic compounds which demonstrated the use of group-characteristic IR absorptions for molecular structural analysis [75]. However, it was not until the advent of quantum theory in the first decades of the twentieth century that a general understanding of the origin of molecular spectra was achieved.

Interest in IR spectroscopy as a method for analytical chemistry grew when the first prototypes of IR spectrometers were built in the 1930s. Their commercial development, stimulated by the need for fast analytical methods in the synthetic rubber industry, quickly followed. This development also expanded the acquisition of IR spectra and motivated research into more profound theoretical studies of the features of IR spectra. Subsequent advances in electronics and electronic amplification methods during and after the Second World War provided the thermocouple detector technology that led to the development of stable double-beam spectrophotometers.

By the 1950s, IR spectroscopy had established itself as a key analytical method in academic and industrial laboratories. At that time, the instruments employed prisms as dispersive elements, but by the mid 1950s, diffraction gratings had been introduced [29]. Most IR instruments then used in the 1970s were based on prism or grating monochromators [3]. A major breakthrough in IR spectroscopy occurred with the introduction of Fourier transform infrared (FTIR) spectrometers. In 1891, Albert Michelson developed the interferometer to study the speed of light [76]. Shortly after, Lord Rayleigh discovered that the interferometer output could be converted to a spectrum by a mathematical procedure developed about seventy years earlier by the French mathematician Joseph Fourier.

However, due to the numerical complexity of the Fourier procedure, it was not until 1949 that British physicist Peter B. Fellgett calculated a spectrum from an interferogram [77]. He used Fourier transform spectroscopy to isolate the weak signals of distant stars from surrounding background noise in his doctoral thesis, discovering the multiplex advantage, which is named in his honor. There, he pointed out that interferometry provides a multiplex advantage when using broadband sources since the interferogram records superimposed signals from all the different wavelengths that reach the detector. The individual signals for each wavelength can again be recovered from the combined interferogram by mathematical analysis of the Fourier transform. He also predicted that the future development of fast computers, which could make the computational time much shorter than the time for data acquisition, would lead to the possibility of analyzing complex IR spectra with high sensitivity very conveniently [3], [73].

A few years later, Pierre Jacquinot, a French physicist, pointed out the throughput advantage of interferometers over dispersive spectrometers [78] based on the fact that the throughput of the interferometer is determined only by the diameter of the collimated beam coming from the source, whereas in the dispersive instruments, the monochromator has entrance and exit slits which restrict the amount of light that passes through it. This advantage for FTIR over dispersive instruments translated into practical improvements such as increased resolution, high-speed data collection, lower detection limits, and greater energy throughput.

However, the complex calculations required to transform the interferogram into a spectrum slowed the acceptance of FTIR spectroscopy. In 1964, the discovery of the Fast Fourier-Transform (FFT) algorithm by James Cooley and John Tukey reduced the time for the computer calculation of the transform from hours to just a few seconds. Nevertheless, it was still time-consuming to record an interferogram on paper tape or punched cards, go to a computing center, and wait for the spectrum to be calculated [3].

Another breakthrough came in 1969 when the the first commercial FTIR spectro-

meter FTS-14 of resolution  $4\text{ cm}^{-1}$  (or better) with a dedicated minicomputer was developed and sold by Digilab, illustrated in see Fig. 1.6. The design incorporated a fast-scanning mechanism for the mirror using an air bearing, a fast-response triglycine sulfate (TGS) pyroelectric thermal detector and an integrally incorporated Data General 8-kB Nova 16-bit minicomputer with a 14-bit analog to digital converter, backed up by a 500-kB disk memory for the Fourier transformation process [73].

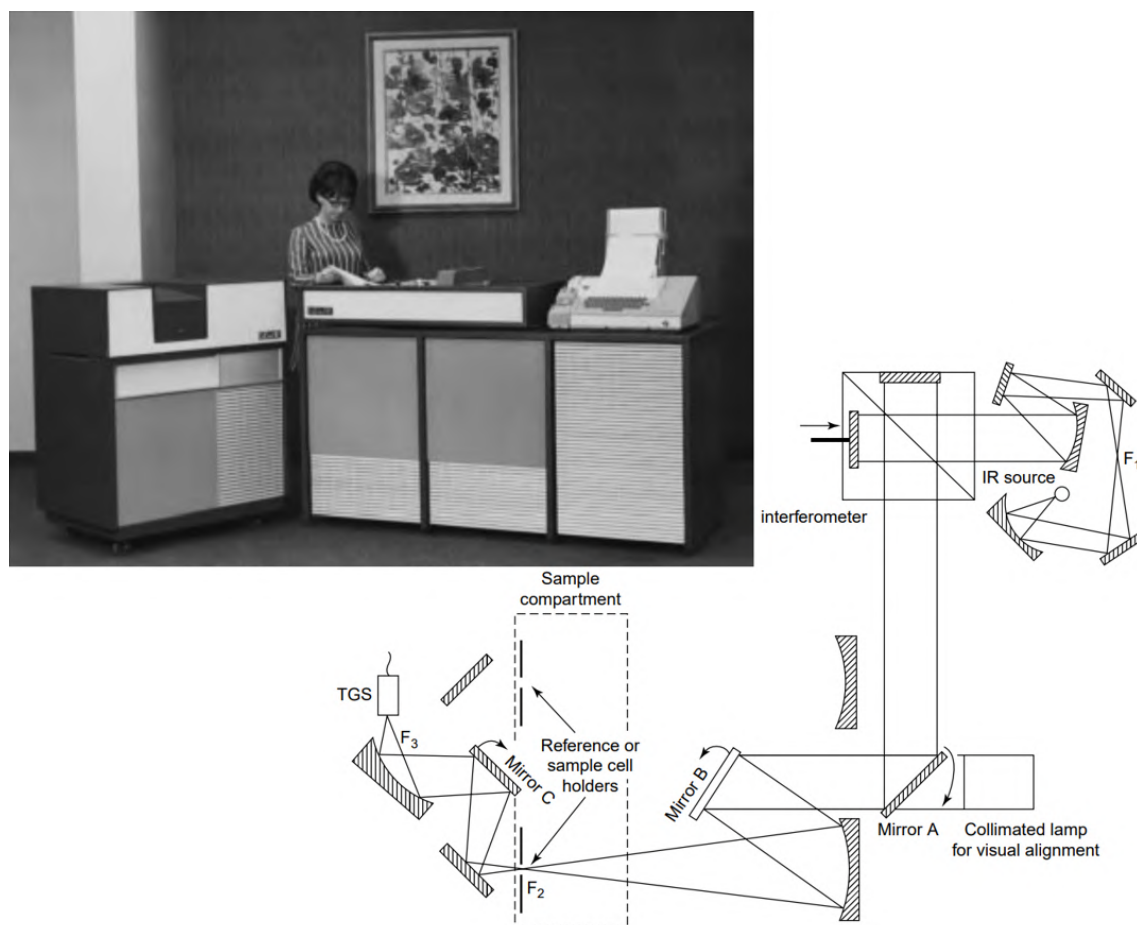


Fig. 1.6: Photography and diagram of the Digilab FTS-14 Fourier transform interferometric IR spectrometer. Adapted from [73].

For the first time, spectroscopists could see the spectrum plotted shortly after the interferogram was collected. It took less time to acquire a spectrum using the FTIR spectrometer than using the dispersive instrument. Since then, further developments in computing technology and significant price reductions have resulted in many commercial FTIR spectrometers on the market and the widespread use of FTIR spectroscopy in all branches of science and technology [3].

### 1.3.2 Molecular Vibrations

Traditional IR spectroscopy is based on the vibrations of the atoms of a molecule [29]. A typical output of the instrument used for IR spectroscopy, i.e., IR spectrometer, is the IR spectrum, typically plotted as a graph of transmittance/absorbance percentage over wavenumbers, that is obtained by passing IR radiation through a sample and measuring the intensity of the transmitted or absorbed radiation by a sample [29]. A molecule of a sample irradiated with IR radiation absorbs this radiation under the condition that the energy  $h\nu$  of the absorbed radiation is equal to the energy difference between two energy levels of vibration of a molecule (see eq. 1.4). When this condition is satisfied, a molecule absorbs IR radiation and undergoes a change in vibrational energy since the energy of IR radiation has the appropriate energy to induce translational, rotational, or vibrational motion in molecules [3]. Based on its atomic structure, each molecule produces a unique and characteristic IR spectrum that shows the frequencies at which the sample absorbs or transmits radiation creating a typical spectral pattern, sometimes called molecular fingerprint of the sample [29]. By analyzing the spectra of absorption or transmission of IR radiation by a sample, information can be obtained about the types of chemical bonds and functional groups present in the sample [3]. The specific number and position of absorption bands for each molecule is governed by its degrees of freedom, functional groups and IR selection rules.

IR spectra of molecular vibrations are the result of transitions between quantized vibrational energy states. Molecular vibrations can be the simple coupled motion of two atoms in a diatomic molecule but also the much more complex motion of each atom in a large polyfunctional molecule. Each atom has three degrees of freedom; it can move independently along each of the axes of a Cartesian coordinate system. Molecules with  $N$  atoms have  $3N$  degrees of freedom, of which three represent translational motion in mutually perpendicular directions,  $x$ ,  $y$  and  $z$  axes, and three represent rotational motion about these axes. The remaining  $3N-6$  degrees of freedom indicate the number of ways in which the atoms in the molecule can vibrate, i.e. the number of vibrational modes, which change the distances between atoms: the lengths of the chemical bonds and the angles between them [4]. According to classical mechanics, a harmonic oscillator can vibrate with any amplitude, which means it can have any amount of energy, large or small. However, quantum mechanics shows that molecules can only exist in certain energy states. In the case of harmonic potentials, these states are equidistant, while in the case of anharmonic potentials, the distances between energy levels decrease with increasing energy [79]. The energy difference for the transitions between the ground state and the first excited state of most vibrational modes corresponds to the energy of radiation in the MIR region

(400–4000  $\text{cm}^{-1}$ ).

In order for the energy from the IR photon to be transferred to the molecule via absorption, the molecular vibration must cause a change in the dipole moment of the molecule. This is a well-known selection rule for IR spectroscopy, which requires a change in dipole moment during vibration to be IR active [80]. More details about molecular vibrations can be found in Ref. [4, 79, 81].

### 1.3.3 Lorentz Oscillator Model

All types of spectroscopic techniques have one thing in common; they all study the interaction of electromagnetic radiation with matter. The interactions are characterized by the energy of the radiation and its effects on materials. Electromagnetic radiation is pure energy waves (it has no inertial mass) and thus can only interact through its electric and magnetic fields [82]. For IR spectroscopy, which utilizes frequencies from the IR portion of the electromagnetic spectrum within the frequency range  $10^{12}$ – $10^{14}$  Hz, the electric dipole transitions with the electric field are completely dominant interaction of an electron in an atom with the electromagnetic field, and the magnetic field can be ignored<sup>9</sup> [82].

The Lorentz oscillator model, named after the Dutch physicist Hendrik Antoon Lorentz, describes the optical response of bound charged particles. It is the basic starting point for understanding the general optical properties of a medium. It is a classical model for materials with characteristic resonance frequencies for optical absorption, e.g. ionic and molecular vibrations, interband transitions (semiconductors), phonons, and collective excitations [36, 83].

The classical model of the bound electrons in an atom consist of the electron held in a stable orbit with respect to the nucleus, and the spring represents the restoring force for small displacements from the equilibrium. The negatively charged electron and the positively charged nucleus form an electric dipole with a magnitude proportional to their separation. We consider the interaction between a light wave and an atom with a single resonant frequency  $\omega_0$  due to the bound electrons. We model the displacement of the atomic dipoles as damped harmonic oscillators. The force restoring the electron equilibrium position is proportional to the displacement of the electron from the equilibrium position. In addition, the electron motion is damped by a force proportional to its velocity. Simultaneously, the electron is subjected to a force from the electric field of the electromagnetic wave  $E = E_0 e^{-i\omega t}$  that induces forced oscillations of the atomic dipole. The displacement  $x$  of the electron is governed by an equation of motion of the form [36, 38]:

---

<sup>9</sup>This is, of course, the opposite situation to IR magneto-spectroscopy, where the magnetic field cannot be ignored.

$$m \frac{d^2x}{dt^2} = -m\omega_0^2 x - m\gamma \frac{dx}{dt} + qE_0 e^{-i\omega t}, \quad (1.16)$$

where  $m$  is the electron (particle) mass,  $\omega_0$  is the undamped angular frequency of the oscillator,  $\gamma$  is the damping coefficient and  $q$  is the electron (particle) charge. Because the electron is subjected to a harmonic field, we can look for the solution in a form:  $x = x_0 e^{-i\omega t}$ , where  $x_0$  is the displacement amplitude so we obtain [36,38]:

$$x = \frac{q}{m} \frac{1}{\omega_0^2 - \omega^2 - i\gamma\omega} E. \quad (1.17)$$

The displacement of the electron from their equilibrium position gives rise to a time-varying dipole moment  $p(t)$ :

$$p = qx = \frac{q^2}{m} \frac{1}{\omega_0^2 - \omega^2 - i\gamma\omega} E. \quad (1.18)$$

The contribution to the polarization by  $N$  particles per unit volume is:

$$P = Np = Nqx = \frac{Nq^2}{m} \frac{1}{\omega_0^2 - \omega^2 - i\gamma\omega} E. \quad (1.19)$$

By combining eq. 1.10 and 1.19 and substituting the plasma frequency, defined as  $\omega_{pl} = \sqrt{Nq^2/\epsilon_0 m}$ , we obtain:

$$\epsilon_r = 1 + \frac{Nq^2}{\epsilon_0 m} \frac{1}{\omega_0^2 - \omega^2 - i\gamma\omega} = 1 + \frac{\omega_{pl}^2}{\omega_0^2 - \omega^2 - i\gamma\omega}. \quad (1.20)$$

The splitting of the real and the imaginary part yields:

$$\epsilon_1(\omega) = 1 + \frac{\omega_{pl}^2(\omega_0^2 - \omega^2)}{(\omega_0^2 - \omega^2)^2 + (\gamma\omega)^2}, \quad (1.21)$$

$$\epsilon_2(\omega) = \frac{\omega_{pl}^2 \gamma \omega}{(\omega_0^2 - \omega^2)^2 + (\gamma\omega)^2}. \quad (1.22)$$

There is often more than one allowed optical absorption in real material, so their contribution is summed up over  $j$  oscillators [38]:

$$\epsilon_r(\omega) = \epsilon_\infty + \sum_j \frac{\omega_{plj}^2 \gamma \omega}{\omega_{0j}^2 - \omega^2 - i\gamma_j \omega}, \quad (1.23)$$

where  $\epsilon_\infty$  represents high-frequency limit of the dielectric function, i.e., the contribution of the optically active transitions from higher energies [38]. The eq. 1.23 presents dielectric function of independent oscillators, which is valid also for phonos. By setting  $\omega_0 = 0$ , we obtain Drude–Lorentz model for free electron systems (metals and doped semiconducotors) [36].

The dielectric function derived from the Lorentz model is shown in Fig. 1.7 on the left, calculated for an oscillator with  $\omega_0=10^{14}$  rad/s,  $\gamma=5 \times 10^{12}$  s<sup>-1</sup>,  $\epsilon_\infty=10$ . Fig. 1.7 on the right shows the real and imaginary part of the refractive index calculated from the dielectric constant using same set of parameters.

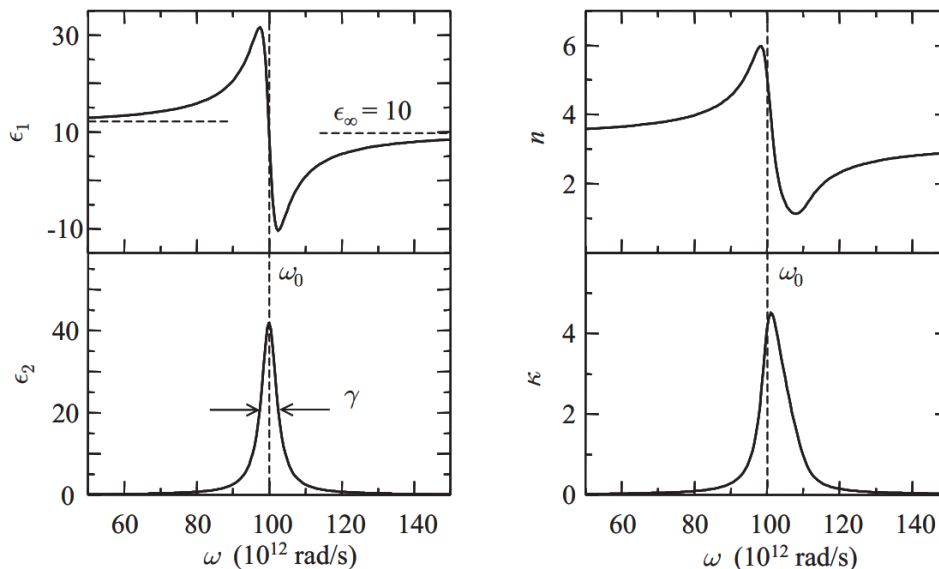


Fig. 1.7: Frequency dependence of the real and imaginary parts of the complex dielectric constant of a dipole oscillator at frequencies close to resonance is shown on left. The graphs are calculated for an oscillator with  $\omega_0=10^{14}$  rad/s,  $\gamma=5 \times 10^{12}$  s $^{-1}$ ,  $\epsilon_\infty=10$ . On the right, the real and imaginary part of the refractive index calculated from the dielectric constant is shown. Adapted from [36].

### 1.3.4 Beer-Lambert Law

The wide-ranging optical properties observed in solid-state materials can be classified into general phenomena such as reflection, propagation, and transmission. The phenomena that can occur while radiation propagates through an optical medium are refraction, absorption, luminescence, and scattering [36].

These optical phenomena can be quantified by a number of parameters that determine the properties of the medium at the macroscopic level. The reflection at the surfaces is described by the coefficient of reflection or reflectivity  $R$  and is defined as the ratio of the reflected power to the power incident on the surface. The coefficient of transmission or transmissivity  $T$  is defined as the ratio of the transmitted power to the incident power [36].

The absorption of light by an optical medium is quantified by its absorption coefficient  $\alpha$  defined as the fraction of the power absorbed in a unit length of the medium. If the beam is propagating in the  $z$  direction, and the intensity (optical power per unit area) at position  $z$  is  $I(z)$ , then the decrease of the intensity in an incremental slice of thickness  $dz$  is given by  $dI = -\alpha dz \times I(z)$ . After the integration,

we obtain Beer-Lambert or Beer's law [36]:

$$I(z) = I_0 e^{-\alpha z} \quad (1.24)$$

where  $I(0)$  is the optical intensity at  $z = 0$ . The absorption coefficient  $\alpha$  is a strong function of frequency, so that optical materials can absorb one color but not another. The propagation of light through a medium is quantified by the complex refractive index  $\tilde{n}$ . The real part of  $\tilde{n}$  determines the velocity of light in the medium, while the imaginary part determines the absorption coefficient. Beer's law shows that the intensity of light in an absorbing medium decays exponentially [36].

The absorption of an optical medium can also be quantified in terms of the absorbance  $A$  defined as [36]:

$$A = -\log_{10}(I(l)/I_0), \quad (1.25)$$

where  $l$  is the length of the absorbing medium. The ratio  $I(l)/I_0$  is also called transmittance  $T$  and it is often used in IR spectrum, plotted in units called percent transmittance ( $\%T$ ), which measures the percentage of light transmitted by a sample, calculated as  $\%T = 100 \times T$  [29].

Beer-Lambert law can be used to relate the amount of light transmitted by a sample to its properties, such as thickness or concentration [80]. The absorbance  $A$  of the solution can be written as follows [29]:

$$A = \epsilon cl, \quad (1.26)$$

where the constant  $\epsilon$  is the molar absorptivity,  $c$  is the concentration, and  $l$  is the pathlength of the sample.

## 1.4 FTIR Spectrometer

As was explained in subsection 1.3.1, a major breakthrough in IR spectroscopy that led to its widespread use came in the 1970s with the introduction of FTIR spectrometers equipped with interferometers, exploiting the well-established mathematical process of Fourier transform<sup>10</sup> (FT) [3]. Due to its significantly improved acquisition of IR spectra, leading to better SNR and reduced data acquisition time, the FTIR spectrometers are nowadays predominantly used spectrometers in the IR range [4]. Thus, IR spectroscopy is frequently referred to as FTIR spectroscopy.

The essential components of a FTIR spectrometer are schematically shown in Fig. 1.8. FTIR spectrometer consists primarily of interferometer (usually Michelson-type), source of radiation, the detector and other optical elements (beamsplitters,

<sup>10</sup>This name is in honor of the French mathematician Joseph Fourier. Fourier's theorem states that any periodic function can be expressed as a superposition of sine and cosine waves [84].

mirrors, etc.), which will be described further. Then, it includes sample compartment, amplifier, analog-to-digital converter (ADC), and of course, computer, where experiment control, data acquisition and manipulation takes place. The radiation emitted by the source goes through the interferometer, passes through the sample and is then detected. The FTIR spectroscopy is based on the principle of interference of the radiation between two beams to obtain an interferogram – analog signal at the detector originated as a function of the pathlength difference between the beams. The signal is amplified by amplifier, in which high-frequency components are filtered out. After that, the signal/interferogram is converted to digital form by an ADC and sent to the computer for FT in order to yield the conventional spectrum [29].

The principle of the operation of FTIR spectrometers and the process of spectrum acquisition is explained in detail in the next subsection.



Fig. 1.8: The essential components of the FTIR spectrometer.

### 1.4.1 Michelson Interferometer

The key component of every FTIR spectrometer is an optical device called an interferometer. The design of today's interferometers in FTIR spectrometers is based on the two-beam interferometer originally designed by Albert Abraham Michelson<sup>11</sup> in 1891 [76].

The Michelson interferometer is a device that splits the light beam propagating from the source of radiation into two beams, which travel different paths. They are then recombined into one beam, which leaves the interferometer towards a detector. The path difference between the two beams creates conditions for interference. Interference causes the change in the intensity of the beam emerging from the interferometer, which is then measured as a function of path difference by a detector. The scheme of a simple Michelson interferometer is shown in Fig. 1.9. It consists of two mutually perpendicular plane mirrors, one is fixed, and the other is movable along an axis perpendicular to its plane.

Between them, there is a beamsplitter, an optical device that splits a collimated radiation beam from the source in two parts. Ideally, one half of the incident beam is reflected to the fixed mirror, and the other one is transmitted to the movable mirror.

---

<sup>11</sup>Albert Abraham Michelson was an American physicist who is primarily known for his work on measuring the speed of light and the Michelson–Morley experiment. He was awarded a Nobel prize in Physics in 1907 for his pioneering efforts in measuring and analyzing light. It was the first Nobel prize in science awarded to an American [85].

After reflecting from these mirrors, they return to the beamsplitter, where they are split and one half of the beam goes back to the source, and the other half goes to the detector [4]. As a result of their interference, the intensity of each beam passing to the detector depends on the difference in the beam paths in the two arms of the interferometer and provides the spectral information in the FT spectrometer [4].

The movable mirror can be either moved at a constant velocity (a continuous-scan interferometer) or held at equally spaced points for fixed short periods and stepped rapidly between these points (a step-scan interferometer) [4].

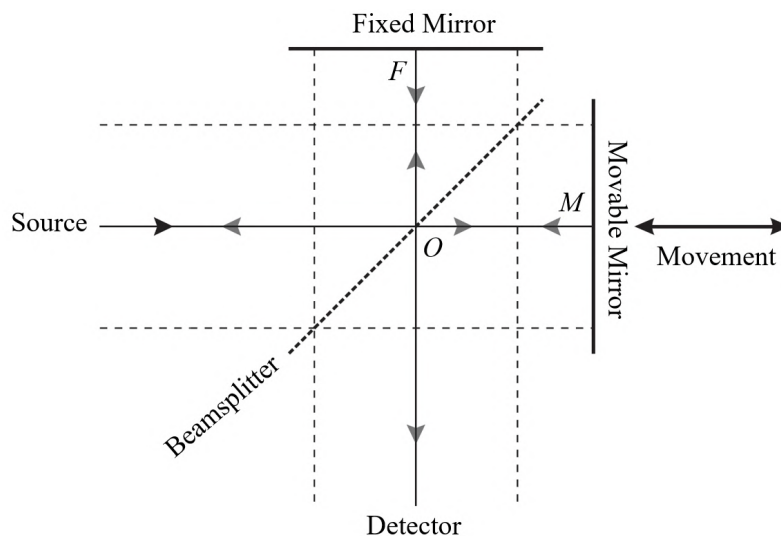


Fig. 1.9: Michelson Interferometer. Adapted from [4].

## 1.4.2 Principle

To better understand how the Michelson interferometer works, let us first consider an idealized situation where the beamsplitter is ideal<sup>12</sup>, and the IR source is monochromatic<sup>13</sup>, producing a collimated beam of only one wavelength  $\lambda$  with the wavenumber  $\tilde{\nu} = 1/\lambda$  ( $\text{cm}^{-1}$ ), and the source intensity (power) at this wavenumber denoted as  $I(\tilde{\nu})$ . The difference in distance between the beams which travel to the fixed and movable mirrors and back to the beamsplitter is  $2(OM - OF)$ , and it is called *optical path difference* (OPD) or simply *retardation*  $\delta$ . If the distances the two light beams travel in the interferometer happen to be identical, then  $\delta = 0$ , and the condition is called *zero path difference* (ZPD). In this case, the intensity of the electric field of the wave at the detector is the sum of the intensities from of beams passing through the fixed and movable mirrors. These beams are said

<sup>12</sup>reflectance and transmittance are both exactly 50%

<sup>13</sup>In reality, the IR source is polychromatic and emits light composed of many wavelengths.

to be in phase, and they *constructively* interfere. Furthermore, the condition for constructive interference is satisfied every time the retardation of the beams is an integer multiple of their wavelength, as follows:  $\delta = n\lambda$  for  $n = 0, 1, 2, \dots$ . When the retardation of the beams is one half wavelength different, the beams are out of phase and interfere *destructively*:  $\delta = (n + 1/2)\lambda$  for  $n = 0, 1, 2, \dots$ . The intensity of the beam at the detector measured as a function of retardation can be denoted as  $I'(\delta)$ . When the mirror is moved at constant velocity, the signal at the detector varies sinusoidally, and a maximum is reached each time when condition for constructive interference is satisfied. Intensity  $I'(\delta)$  is in this case equal to the intensity of the source  $I(\tilde{\nu})$ . The intensity of the beam at the detector at other values of  $\lambda$  is given by  $I'(\delta) = 0.5I(\tilde{\nu})(1 + \cos 2\pi\tilde{\nu}\delta)$ . The intensity  $I'(\delta)$  is composed of a constant direct current (DC) component equal to  $0.5I(\tilde{\nu})$  and a modulated alternating current (AC) component equal to  $0.5I(\tilde{\nu}) \cos 2\pi\tilde{\nu}\delta$ . But for spectroscopic measurements, only the AC component is important and it is referred to as the interferogram  $I(\delta)$ , see Fig. 1.10, which is for monochromatic source measured with an ideal interferometer given by the equation [4]:

$$I(\delta) = 0.5I(\tilde{\nu}) \cos 2\pi\tilde{\nu}\delta \quad (1.27)$$

In practice, the amplitude of the interferogram after detection and amplification is proportional not only to the intensity of the source but also to the beamsplitter efficiency, detector response, and amplifier characteristics. When we consider these factors, the previous equation 1.27 needs to be modified by a single wavenumber-dependent correction factor,  $H(\tilde{\nu})$ , so that the AC signal,  $S(\delta)$  (in volts), from the amplifier is:  $S(\delta) = 0.5H(\tilde{\nu})G(\tilde{\nu})I(\tilde{\nu}) \cos 2\pi\tilde{\nu}\delta$ , where  $G(\tilde{\nu})$  is the responsivity of the detector and amplifier (in  $\text{V}\cdot\text{W}^{-1}$ ); for clarity, term  $0.5H(\tilde{\nu})G(\tilde{\nu})I(\tilde{\nu})$  can be replaced by  $B(\tilde{\nu})$ , the single beam spectral intensity. The equation representing the interferogram is then:

$$S(\delta) = B(\tilde{\nu}) \cos 2\pi\tilde{\nu}\delta. \quad (1.28)$$

The parameter  $B(\tilde{\nu})$  represents the intensity of the source at a wavenumber  $\tilde{\nu}$  modified by the instrumental characteristics. The interferogram  $S(\delta)$  is mathematically the cosine FT of  $B(\tilde{\nu})$ . Hence, the spectrum is calculated from the interferogram by computing the cosine FT of  $S(\delta)$  [4]. In commercial Michelson interferometers, the movable mirror is scanned at a constant velocity  $V'$  ( $\text{cm}\cdot\text{s}^{-1}$ ). With these instruments, it is important to understand how the interferogram changes as a function of time,  $S(t)$ , rather than as a function of deceleration,  $S(\delta)$ . The retardation  $t$  seconds after the zero retardation point is given by  $\delta = 2V't$  cm. Substituting into eq. 1.28 gives us

$$S(t) = B(\tilde{\nu}) \cos 2\pi\tilde{\nu} \cdot 2V't \quad (1.29)$$

The units of the abscissa of the interferogram (retardation in centimeters or time in seconds) must always be the inverse of the units of the spectrum (wavenumber in  $\text{cm}^{-1}$  or frequency in Hz). For each cosine wave of frequency  $f$ , the amplitude of the signal after time  $t$  is given by

$$A(t) = A_0 \cos 2\pi f t \quad (1.30)$$

where  $A_0$  is the maximum amplitude of the wave. A comparison of eqs. 1.29 and 1.30 shows that the frequency  $f_{\tilde{\nu}}$  of the interferogram  $S(t)$  corresponding to the radiation of the wavenumber,  $\tilde{\nu}$  often known as the Fourier frequency, is given by the equation [4]:

$$f_{\tilde{\nu}} = 2V'\tilde{\nu} \quad (1.31)$$

In addition to the two-beam interferometers originally described by Michelson, there are many other types. Many of these interferometers do not change the difference of paths between the two beams by means of a single mirror moving at a constant velocity. With the exception of stationary interferometers used for Fourier transform spectroscopy, the optical element or combination of optical elements moves so that the difference in optical paths changes at a certain velocity, known as the optical velocity or OPD velocity,  $V$ . For a Michelson interferometer,  $V = 2V'$ . In general, the Fourier frequency for radiation with wavenumber  $\tilde{\nu}$  is given by [4]:

$$f_{\tilde{\nu}} = V\tilde{\nu} \quad \text{Hz} \quad (1.32)$$

In the particular case where the spectrum of a monochromatic radiation source is to be determined, performing the FT of the measured interferogram is a trivial operation, since the amplitude and wavelength (or wavenumber) can be measured directly from the sinusoidal interferogram. However, if the source emits either several discrete spectral lines or continuous radiation, the interferogram is more complex and a computer is required to perform the transform. If the source emits radiation with more than one wavelength, the measured interferogram is the resultant of the interferograms corresponding to each wavelength. In the case of line sources with very simple spectra, interferograms can be found that repeat at regular retardation intervals [4].

In reality, the source is a continuum and emits radiation of more than one wavelength, so the measured interferogram is the result of interferograms corresponding to each wavelength [4].

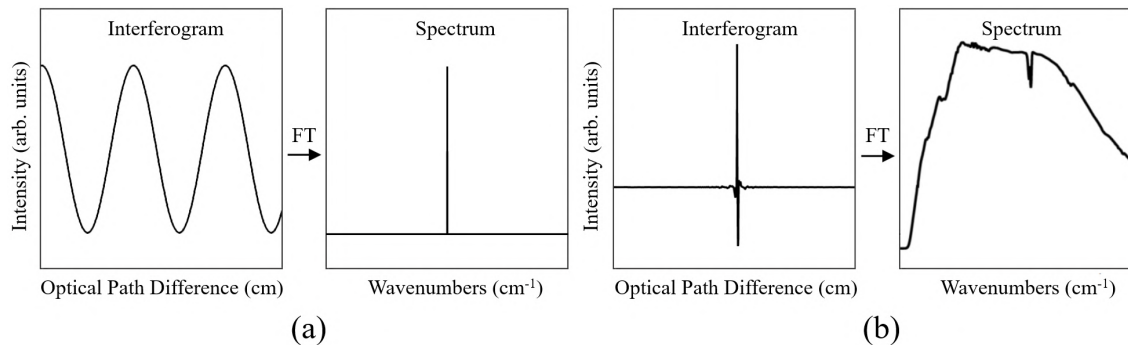


Fig. 1.10: (a) Relationship between the interferogram and spectrum of an idealized laser line. FT of a cosine wave is a line. Note that the  $x$ -axis units of the interferogram are transformed from cm to  $\text{cm}^{-1}$  when the spectrum is calculated. (b) Applying FT on typical interferogram, which is the the result of interferograms corresponding to each wavelength, retrieved from Michelson interferometer allows to calculate the corresponding spectrum.

Accordingly, this interferogram can be represented by the integral [4]:

$$S(\delta) = \int_{-\infty}^{\infty} B(\tilde{\nu}) \cos(2\pi\tilde{\nu}\delta) d\tilde{\nu}, \quad (1.33)$$

which is one-half of a cosine FT pair, where the other, called inverse FT, with  $B(\tilde{\nu})$  being the desired spectrum is then:

$$B(\tilde{\nu}) = \int_{-\infty}^{\infty} S(\delta) \cos(2\pi\tilde{\nu}\delta) d\delta, \quad (1.34)$$

It can be noted that  $S(\delta)$  is an even function, so the eq. 1.34 can be rewritten as

$$B(\tilde{\nu}) = \int_0^{\infty} S(\delta) \cos(2\pi\tilde{\nu}\delta) d\delta. \quad (1.35)$$

A detailed mathematical discussion of the FT in spectroscopy can be found in ref. [86]. Eq. 1.35 shows that theoretically one could measure the entire spectrum from 0 to  $+\infty$  (in  $\text{cm}^{-1}$ ) with infinitely high resolution. However, it also shows that to achieve this, we would have to scan the moving mirror of the interferometer over an infinitely long distance, with a  $\delta$  between 0 and  $+\infty$  cm. The result of measuring the signal at a finite delay is that the spectrum has finite resolution. If the FT were to be performed by computer, the interferogram would have to be digitized at infinitesimally small retardation intervals,  $d\tilde{\nu}$ . In practice, the signal must be digitized at finite sampling intervals. The smaller the sampling interval, the larger the spectral range that can be measured [4].

The consequence of in practice finite integration range in eq. 1.35 is also that the apparent lineshape of a spectral line, where the main band area has a series of negative and positive side lobes with diminishing amplitudes, as shown in Fig. 1.11. The process of *apodization* is the suppression of the magnitude of these oscillations/side lobes by multiplying the interferogram by a suitable function before the FT is carried out. A suitable apodization function causes the intensity of the interferogram to fall smoothly to zero at its ends [29]. For more information about these functions, see ref. [4].

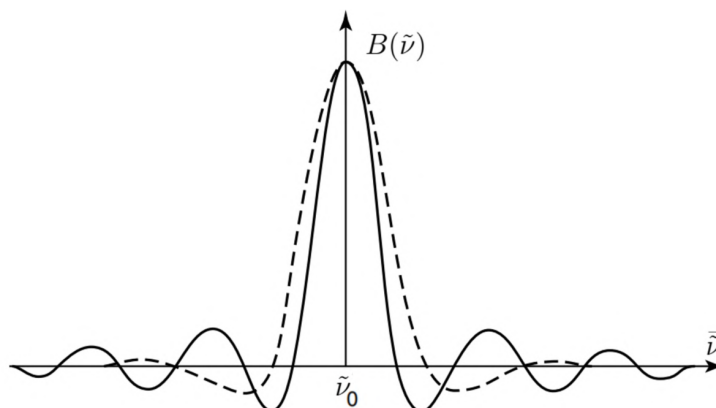


Fig. 1.11: Spectral intensity evaluated for monochromatic light with FT over a limited range in space, solid line corresponds to instrument lineshape without apodization, and dashed line with apodization, in which side lobes are smaller, but the resolution is worse. Adapted from [29].

Most modern interferometers incorporate, besides IR beam, a narrow monochromatic beam of radiation, usually from a helium–neon (HeNe) laser, which is used for the monitoring of the movable mirror position in the spectrometer interferometer, see Fig. 1.12. The laser permits the interferogram to be digitized at equal intervals of retardation [4].

In many interferometers, the scan velocity of the moving mirror can be varied. The scan speed is often reported in terms of frequency of the laser interference signal. The wavelength of the HeNe laser is 632.8 nm, so its wavenumber is  $\sim 15,800 \text{ cm}^{-1}$ . In this case, the scan “speed” is often given as 5 kHz. A physical scan speed of  $0.16 \text{ cm}\cdot\text{s}^{-1}$  ( $V = 0.32 \text{ cm}\cdot\text{s}^{-1}$ ) generates a HeNe laser frequency of 5 kHz, which is typical for a room temperature detector such as a DTGS pyroelectric detector. In contrast, the mercury cadmium telluride (MCT) detector requires a higher optical velocity, on the order of  $2.6 \text{ cm}\cdot\text{s}^{-1}$ , or the HeNe frequency of approximately 40 kHz. Using the HeNe frequency to determine the scan speed has the advantage that there is no confusion as to whether the scan rate is a physical or optical velocity [4].

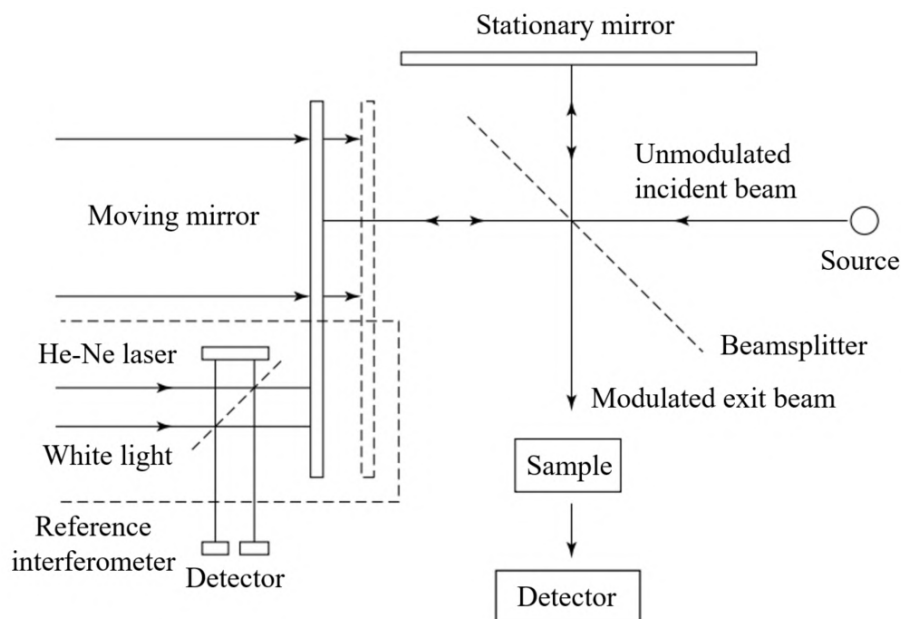


Fig. 1.12: Schematic of a Michelson interferometer, incorporating a separate reference interferometer for the laser and white channels. Adapted from [29].

### 1.4.3 Advantages of FTIR Spectrometers

To understand the powerfulness of FTIR spectrometer, it is essential to have some background information of dispersive IR spectrometer. The basic components of a dispersive IR spectrometer include a radiation source, monochromator, and detector. A monochromator is a device used to disperse or separate a broad spectrum of IR radiation into individual narrow IR frequencies. It produces a beam of light with an extremely narrow bandwidth and is the essence of a dispersive spectrometer. A monochromator consists of a splitting system, i.e., optics and a dispersive element that splits the radiation: prisms or diffraction gratings. The splitting system of the monochromator consists of two narrow slits that confine the rays at the entrance and exit of the monochromator. The slit openings can be varied with high precision by moving the slit cheeks which affects the radiation power and resolution: as the slit width increases, the power of the radiation entering the monochromator increases and the spectral resolution decreases. After diverging the entrance slit, the radiation is collimated by a parabolic mirror, named the entrance collimator, and is deflected onto a dispersive element. Depending on the optics used, the radiation then either travels back to a second parabolic mirror after reflection on the diffraction grating or passes through the prism and reflects on a plane mirror, or goes back to the same parabolic mirror and is sharply imaged on the exit slit [87].

In the past, prism monochromators were the main choice in dispersive spectrome-

ters, but later prisms were replaced by diffraction gratings which provided a better resolution that remained consistent across wide wavelength ranges and avoided problems with prism materials (e.g., hygroscopic, reflection, absorption).

The advantages of FTIR spectrometers over dispersive spectrometers are as follow:

**Fellgett's (or multiplex) advantage:** In the interferometer, all wavelengths are measured simultaneously, whereas in the monochromator, these are measured successively. With the dominant detector noise typically observed in the MIR and FIR region, FT spectrometers are better for two reasons. Firstly, they allow a longer measurement time per spectral element  $M$  resulting in a reduction of noise by a factor of  $\sqrt{M}$ . Secondly, compared to dispersive instruments, FT spectrometers require a shorter measurement time by a factor of  $1/M$  to obtain the same SNR ratio. In the NIR and visible regions, very sensitive semiconductor detectors are available so that detector noise no longer dominates here, but rather photon noise, which is proportional to the square root of the signal intensity. Thus, the Fellgett advantage is not effective in these spectral regions [4, 87].

**Jacquinot's (or throughput) advantage:** The reason for the higher light throughput of FT spectrometers compared to dispersive instruments is that the latter have monochromators with entrance and exit, which limit the amount of light that can pass through. In contrast, the interferometer throughput in FT spectrometers is only determined by the diameter of the collimated beam from the source. However, FT spectrometers need an aperture called a Jacquinot stop [4] to restrict the convergence of the collimated beam in the interferometer because convergent rays are modulated at different frequencies as the path difference is varied. This circular aperture allows more light through than a slit for a given resolution and wavelength, resulting in a higher SNR ratio [87].

**Connes (or the wavelength accuracy) advantage:** Spectra obtained using an interferometer have a higher wavenumber stability compared to dispersive spectrometers, where the scale depends on the mechanical movement of the diffraction gratings. This is because the frequency scale of FT instruments is linked to an internal reference provided by the HeNe laser, which is used for every interferogram. Additionally, scattering can be neglected as the sample position is usually located behind the modulating interferometer [87].

Moreover, FTIR spectrometry has a significant advantage in terms of speed. The mirror can move quickly over short distances, and this, combined with the improved SNR due to the Fellgett's and Jacquinot's advantages, enables spectra to be acquired in a matter of milliseconds. The precision of the IR band's position in interferometry is determined by the accuracy of the scanning mirror's position. However, by utilizing a HeNe laser as a reference, the mirror's position can be precisely determined.

### 1.4.4 Instrumentation

The main components of every FTIR spectrometer are the interferometer, sources of radiation, detectors, and other optical elements such as beamsplitters, mirrors, etc. Since the principle of operation of the Michelson interferometer was already explained above, sources and detectors will be discussed in the following paragraphs.

#### a) Sources

Vibrating atoms generate electromagnetic waves. The higher the temperature of an object, the faster the vibrations, and thus the higher spectral radiant energy [88]. Heat or thermal radiation is the primary source of infrared radiation; therefore, any object at a temperature above absolute zero emits infrared radiation [79, 88]. The warmer the object, the more infrared radiation it emits. Probably the most apparent source of IR radiation is the sun. Based on the sun, the discovery of IR radiation as a distinct region of the energy spectrum was made by the astronomer Sir William Herschel in 1800. He measured the heating effect of sunlight dispersed by a prism using a mercury glass thermometer [3].

Since IR radiation is divided into three groups, NIR, MIR, and FIR, IR sources are divided according to these three groups. The ideal continuous MIR source is based on the concept of a high-temperature blackbody. A blackbody is a hypothetical object that absorbs all incident radiation, and it is also an emitter of radiation over all wavelengths. The spectral energy density of an ideal blackbody as a function of its temperature  $T$  and the wavelength/wavenumber  $\nu$  of the emitted radiation is given by the Planck equation, one of the milestones of physics [4, 88]:

$$U(\nu, T) = \frac{2h\nu^3}{c^2} \frac{1}{e^{h\nu/kT} - 1}, \quad (1.36)$$

where  $h$  is Planck constant,  $k$  is Boltzmann constant, and  $c$  is the speed of light.

The most common MIR source used in FTIR spectrometers, is a U-shaped silicon carbide rod called Globar<sup>14</sup>. Globar is heated resistively, and its typical operational temperature is 1300 K [4]. Its emission is about 75 % of that of a blackbody [79].

Moving to the NIR region, NIR sources should be operated at higher temperatures than MIR sources. The typical NIR source is a tungsten filament light bulb, and it produces IR light close to the blackbody radiation spectrum [4].

In the FIR region, measurements are made more difficult than in MIR or NIR due to the weakness of the sources. Since the sensitivity of any measurement of a MIR or FIR spectrum is directly proportional to the spectral energy density of the source, FIR source should be as hot as possible and has an emittance of close to

---

<sup>14</sup>derived from words: “glow” and “bar” [79]

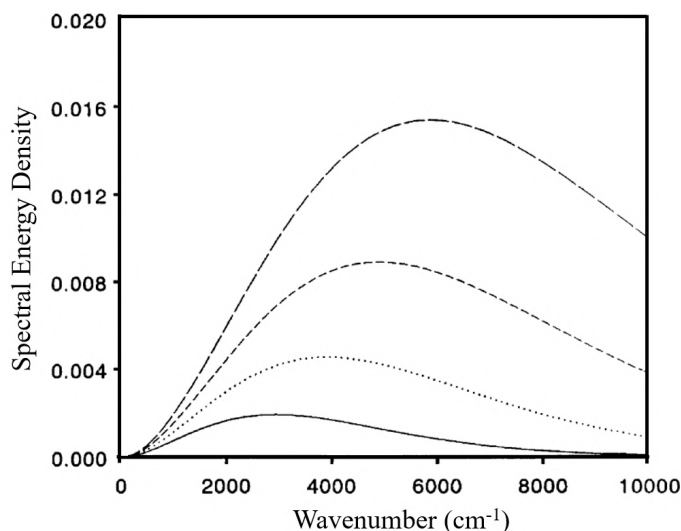


Fig. 1.13: Spectral energy density of blackbody source at 1500°C (solid line), 2000°C, 2500°C, and 3000°C (dashed line). Adapted from [4].

unity. Between 400 and 100  $\text{cm}^{-1}$ , radiant power emitted by Globar is sufficient; thus, it can be used as an FIR source in this range. However, the emissivity of a Globar becomes low below 100  $\text{cm}^{-1}$ , so in this range, it is customary to use high-pressure mercury lamp, in which emission from the plasma reinforces the emission from the hot quartz envelope of the lamp. Another option for FIR source is a synchrotron, whose radiance can be three orders of magnitude greater than those mentioned above [89]. However, it also has its limitation, which have to be taken into account, for more information see ref. [89].

## b) Detectors

A crucial component of every FTIR spectrometer is the element responsible for detecting the IR radiation - IR detector. For better classification of IR detectors and comparing their performance, it is useful to define a few quantities, such as responsivity, noise equivalent power (NEP), and specific detectivity,  $D^*$ . The responsivity is defined as the ratio of the root mean square (rms) value of the fundamental component of the electrical output signal of the detector to the rms value of the fundamental component of the input radiation power. The units of responsivity are volts per watt (V/W) [88]. The sensitivity of IR detectors is usually expressed in terms of the noise equivalent power (NEP) of the detector, which is the ratio of the rms noise voltage (in  $\text{V} \cdot \text{Hz}^{1/2}$ ), to the voltage responsivity of the detector (in V/W). It is a measure of the optical power that gives a signal equal to the noise level; the smaller the NEP, the more sensitive the detector. The NEP is proportional to the

square of the detector area,  $A_D$ , with the constant of proportionality known as the specific detectivity,  $D^*$ ; which is another commonly used measure of IR detector sensitivity. It is given by [4]:

$$D^* = \frac{A_D^{1/2}}{\text{NEP}} \quad \text{cm} \cdot \text{Hz}^{1/2} \cdot \text{W}^{-1}. \quad (1.37)$$

The higher the  $D^*$ , the higher the sensitivity of a given detector.

In general, the IR detectors can be divided into two groups: photon (also called quantum) detectors and thermal detectors. Photon detectors are based on the interaction of radiation with the electrons in a solid, causing excitation of the electrons to a higher energy state by incoming light/photons [4].

The energy of each photon is directly proportional to its wavenumber, and for a transition from one state to another to happen, the radiation's wavelength should not exceed a specific critical value  $\lambda_{max}$ . Typically, quantum detectors exhibit higher sensitivity with increasing wavelength (up to the cutoff) because the number of photons for a given amount of energy increases. As the output is controlled by the number of excited electrons, the output voltage also increases with wavelength. However, as the wavelength approaches the  $\lambda_{max}$ , the response drops sharply. This differs from thermal detectors, where the response per watt stays constant. In order to detect radiation using quantum effects, it is important to be able to excite electrons from one state to another state that has different electrical properties. This can be achieved through a method known as photoemission (phototubes and photomultipliers), which involves providing enough energy to electrons to escape from a surface and flow through a vacuum to produce an electrical current. The photoemission effect is limited to the UV, visible, and NIR (up to 1- $\mu\text{m}$ ) regions due to the requirement of high energies to release electrons from a photoemissive surface [4].

Alternatively, in the MIR and NIR regions, semiconductor detectors (such as  $p$ - $n$  junction semiconductor) are commonly used. Semiconductors possess a relatively small bandgap between the valence and conduction bands. When electrons move from the valence to the conduction band, a current can flow through the material. The photon energy in semiconductor detectors is greater than the bandgap and promotes an electron from the valence band to the conduction band. This generates a current that is used to register the detection of the photons. These detectors usually consist of two doped semiconductors. Doping is the introduction of a small amount of an element that has either more electrons ( $n$ -type or donor semiconductors) or fewer electrons ( $p$ -type or acceptor semiconductors) than the native semiconductor. The regions that have fewer electrons are referred to as "holes". When the two types of semiconductors are combined at a junction or interface, the holes and electrons move to the opposite side, creating a charge formed across the interface that prevents

further diffusion of electrons or holes. The region near the interface becomes depleted in a steady state forming a so-called  $p$ - $n$  junction. When a photon with energy greater than the bandgap is incident on the detector, electrons are produced in the conduction band and the number of holes increases in the valence band. The recombination of electrons and holes is prevented by an applied potential to the detector. Current only passes when a photon strikes the photodetector. Quantum detectors that operate in this manner include PbS, PbSe, and InSb. Other quantum detectors include II–VI combinations of semimetals, i.e., mixtures of metals from groups II and VI of the periodic table, such as MCT,  $\text{Hg}_{1-x}\text{Cd}_x\text{Te}$ ), a mixture of HgTe and CdTe. The ratio of the mixture determines the bandpass of the detector [4].

In cases where extremely high sensitivity is required, the detectors are cooled down to the temperature of LHe (4.2 K). The exceptional sensitivity of LHe-cooled detectors often necessitates the cooling of the surroundings to the temperature of liquid nitrogen ( $\text{LN}_2$ ) to minimize the noise caused by randomly emitted photons [4].

In addition to MCTs the most common  $\text{LN}_2$ -cooled quantum detectors are InSb, InAs, Ge, and InGaAs. The most popular thermoelectrically cooled detectors include MCT, InAs, InGaAs, PbSe, PbS, Ge, and Si, and some of these detectors (especially InGaAs) operate with good sensitivity at room temperature [4].

The principle of operation in the case of thermal detectors is that their temperature increases as a result of exposure to the incident IR radiation. The temperature changes are measured by any temperature-dependent mechanism, such as thermoelectric voltage, resistance, or pyroelectric voltage. They are classified according to the operating scheme: thermopile, bolometer, and pyroelectric scheme [88]. In the following text, we will focus on pyroelectric thermal detectors and bolometers because these types of detectors are currently available in our setup.

When a pyroelectric crystal undergoes a change of temperature, surface charge in a particular direction is produced. It is a result of the change in its spontaneous polarization with temperature. This effect is called “pyroelectricity” [88]. These thermal detectors employ ferroelectric materials as their heat-sensing elements, which exhibit a large spontaneous electrical polarization at temperatures below their Curie point. The change in the temperature of ferroelectric materials causes a change in the degree of polarization. The change in polarization is observed as an electrical signal when electrodes are placed on opposite faces of a material to form a capacitor. The sensing element of the pyroelectric detectors used in most FTIR spectrometers used to be triglycine sulfate (TGS). The response of a pyroelectric detector drops to zero if the temperature exceeds its Curie temperature. In this case, the element must be repolarized. Even though the electronics of most modern FTIR spectrometers incorporate automatic “repolling” of pyroelectric detectors, it was found that deuterated triglycine sulfate (DTGS) has a higher Curie temperature than TGS and

replaced it. Recently, the properties of deuterated l-alanine-doped triglycine sulfate (DLATGS) seem to be even more suitable for FTIR, so many FTIRS spectrometers are nowadays equipped with a DLATGS detector [4].

Bolometer is a very popular and widely used type of thermal detector for sensing electromagnetic radiation in a wide frequency range, including terahertz and infrared. It is a resistive element constructed from a material with a very small thermal capacity and a large temperature coefficient so that the absorbed radiation produces a large change in resistance [88]. Bolometers can be divided into several types: metal, the thermistor, semiconductor bolometer, or superconducting bolometer. Detectors of choice for many applications, including FTIR spectroscopy, are semiconductor bolometers because they are the most highly developed form of thermal detectors for low light levels, especially in the infrared and submillimeter spectral range. A significant improvement in the performance of these bolometers can be achieved by cooling as the resistance changes are much greater than at room temperature [88]. Therefore, a very popular semiconductor bolometer for FTIR spectroscopy is composite silicon bolometer cooled by liquid helium (LHe) and liquid nitrogen (LN<sub>2</sub>), which has bolometer detector element bonded to a diamond absorber. The typical composite bolometers consists of three parts: the radiation-absorbing material, the substrate determining its active area and the temperature sensor, which is mechanically and also thermally bonded to the substrate, see schematic Figure 1.14 [88].

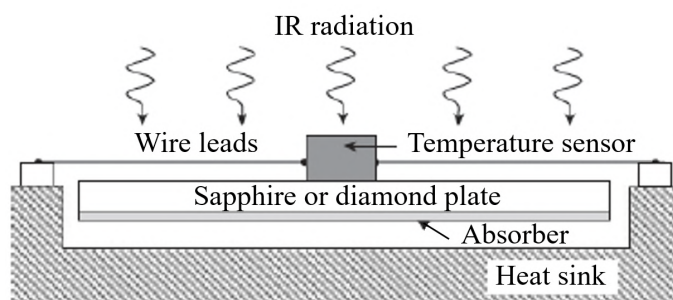


Fig. 1.14: Schematic of semiconductor composite bolometer. Adapted from [88].

### c) Beamsplitters

The role of the beamsplitter is to split the incident IR beam in two and recombine these beams into one [1]. An ideal beamsplitter is nonabsorbing, and transmits 50% of the incident light and reflects 50% of the incident light [4]. The beamsplitter material has to be chosen according to the region to be examined. To produce beamsplitters for the MIR and NIR regions, materials such as germanium or iron oxide are

coated onto an IR-transparent substrate/window such as potassium bromide (KBr) or cesium iodide (CsI) that support and protect the coated film [29]. In the MIR, the most common material used as a substrate is KBr due to their transparency over a wide spectral range from  $400\text{ cm}^{-1}$  to the NIR. However, the disadvantage of KBr is that it is hygroscopic - it absorbs water from the atmosphere. The humidity in the FTIR spectrometer must be kept low because a layer of adsorbed water can form on the surface of the KBr windows, absorbing the IR light and reducing the amount of light that reaches the detector [1]. Thin organic self-supporting films, such as polyethylene terephthalate (PET), are used in the FIR region. Many manufacturers of FTIR spectrometers use multilayer beamsplitters where as many as 15 or more different layers are deposited sequentially on the substrate to increase the spectral coverage. [4] Fig. 1.15 illustrates a scheme of a typical beamsplitter. For example, Bruker Optics deposited a thin film of Ge onto a PET substrate. The result is a multilayer dielectric germanium beamsplitter that has all the advantages of the thick beamsplitter, but it can be used for measurements at higher resolution, and, because of the very thin Ge coating, the absorption caused by phonons is minimal. The improved efficiency at long wavelength is achieved after coating a  $6\text{-}\mu\text{m}$  Mylar beamsplitter with a thin film of Ge [89].

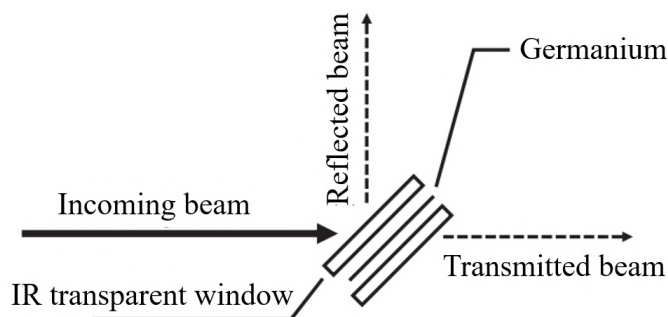


Fig. 1.15: Schematic of the beamsplitter.

Mylar<sup>®</sup>, also known as biaxially-oriented polyethylene terephthalate (BoPET), is a polyester film made from stretched PET. It exhibits high tensile strength, chemical and dimensional stability, transparency, reflectivity, gas and aroma barrier properties, and electrical insulation [90]. BoPET film was developed in the mid-1950s, originally by DuPont, Imperial Chemical Industries (ICI), and Hoechst. The term “Mylar” is a registered trademark of the DuPont Teijin Corporation [90].

#### d) Mirrors

In FTIR spectrometers, the radiation emitted by the source is collected and collimated<sup>15</sup>, passed through the interferometer, focused onto the sample, and refocused onto the detector. A parabolic (or paraboloidal) mirror or its off-axis segment is usually used to collimate the beam from the source before it is passed through the interferometer. To understand why this type of mirror is needed, it is necessary to examine the properties of the corresponding two-dimensional conical section, the parabola. As shown in Fig. 1.16, any line parallel to the axis of a parabola is reflected through its focus. Revolving the parabola about its axis produces a paraboloid. Any collimated beam of radiation parallel to the axis of a paraboloid is thus reflected through its focus. Parabolic mirrors are used in FT-IR spectrometers in two ways. A parabolic mirror can collimate any beam coming from the focus; e.g., radiation from the source is collimated by it before passing through the interferometer. Alternatively, the collimated beam can be focused by such a mirror, e.g., the collimated light from the interferometer is focused by it to the center of the sample compartment. Since the central beam of the collimated beam rarely coincides with the axis of the paraboloid, the segments of parabolic mirrors used in FTIR spectrometers are usually referred to as off-axis parabolic (or paraboloid) mirrors [4]. The focal length of a paraboloid is the distance between its focus and its vertex ( $f$  in Fig. 1.16). For an off-axis paraboloid, it is more useful to determine its effective focal length (EFL), sometimes called reflective focal length (RFL), which is the distance between the center of the segment and the focus. Besides parabolic mirrors, other optical elements found in FTIR spectrometers include plane, ellipsoidal, toroidal, and aspherical mirrors. The main purpose of plane mirrors is to ensure that the optical bench is as compact as possible. In practice, gold-coated mirrors have a reflectance of approximately 0.98. For example, an optical path with 20 mirrors, each with a reflectivity of 0.98, has a transmittance of  $0.98^{20}$ , i.e., 67%. If the mirror's reflectivity is lower, say 95%, the overall efficiency would be only 36%. Therefore, the number of plane and other mirrors should be kept to a minimum, and gold, silver, or other coatings with high reflectance should be used whenever high optical efficiency is required [4].

#### e) Winston Cone

The Winston cone<sup>16</sup>, also known as the compound parabolic concentrator, is one of the reflective non-imaging light collectors, which section comprises two parabolas with inclined axes [93]. The Winston cone's major function is to concentrate the

---

<sup>15</sup>to collimate means to make (rays of radiation) accurately parallel

<sup>16</sup>The Winston cone is named after its inventor, the physicist Roland Winston [91,92].

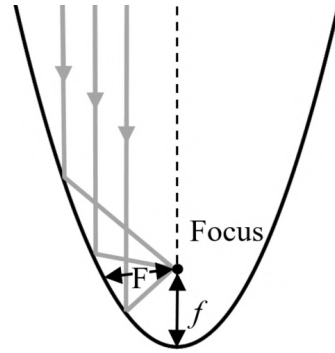


Fig. 1.16: Typical parabola, with focal length  $f$ . For the off-axis section shown on this figure, the effective focal length is  $F$ .

incident radiation into a small output aperture effectively. It is specified by input and output diameters  $d_i$  and  $d_o$ , acceptance angle  $\theta_{max}$ , and cone length  $l$ , as shown in Fig. 1.17. Any two parameters of these are sufficient to determine the geometry of the cone. Compared with an off-axis parabolic mirror, it does not need adjustment in an optical system. In comparison to the lens, the Winston cone possesses very high optical throughput and no chromatic aberration due to high reflection in the wide wavelength range. It is used to collect the incident energy of electromagnetic waves extending from microwave (MW) to visible light. It is applied for photovoltaic generation and thermal utilization to concentrate the sunlight, IR temperature sensor system, wireless communication system, and gas sensing system [93]. It is a helpful component, especially in the FIR and THz region, where the commercial products of light collectors are very scarce, employed to collect the light into a detector to improve the detector sensitivity [93].

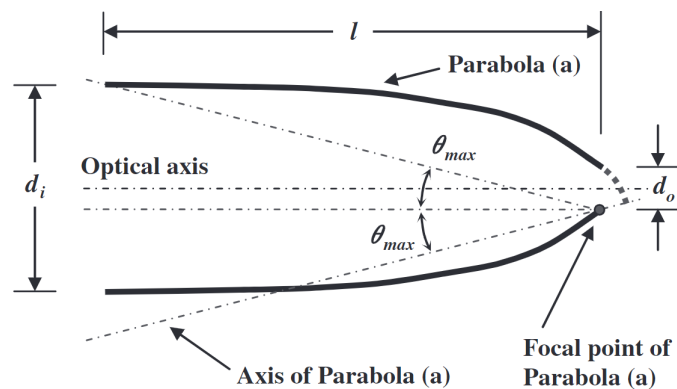


Fig. 1.17: parameters determining the specification of the Winston cone condenser. Taken from [93].

### 1.4.5 Spectral Analysis

Similarly to any signal, the quality of a IR spectrum can be described by the signal-to-noise ration (SNR). In FTIR spectroscopy, SNR can be defined as the ratio of the absorption band intensity and the intensity of the baseline. SNR is defined by the equation:

$$\text{SNR} = \text{Signal/Noise.} \quad (1.38)$$

The goal of every FTIR analysis is to maximize the spectral quality while minimizing the analysis time. To obtain an interferogram using the Michelson interferometer, the movable mirror is moved back and forth once. It is called a scan. The interferograms measured during scanning are Fourier transformed to yield a spectrum. If 8 scans are chosen, the movable mirror will move back and forth 8 times, measuring 8 separate interferograms, which are then averaged. Typically, the averaged interferogram is sent to the FTIR computer software program, which performs a FT on it in order to obtain a spectrum.

There is a link between SNR and the number of scans. SNR of a spectrum is proportional to the square root of the number scans, N [94],

$$\text{SNR} \propto N^{1/2}. \quad (1.39)$$

Another important characteristic of a spectrometer is its resolution,  $\Delta\tilde{\nu}$ . This parameter gives the smallest distance between two wavelengths (wavenumbers) that can be resolved. The lower the number (closer wavelength), the higher (better) the resolution. Since interferogram data points are collected at evenly spaced intervals, high resolution scans require more data points than low-resolution scans, thus also greater optical path differences<sup>17</sup>. Hence, the relationship between resolution and optical path difference is:

$$\Delta\tilde{\nu} \propto 1/\delta. \quad (1.40)$$

There is also relation between resolution and SNR. The scans with high resolution are proportionally noisier than low resolution ones [84].

$$\text{SNR} \propto \Delta\tilde{\nu}. \quad (1.41)$$

## 1.5 High Magnetic Fields

Many important research applications in materials science, condensed matter physics, chemistry, and biology require high magnetic fields. The presence of a magnetic

---

<sup>17</sup>This is the reason why the FTIR spectrometers with very high resolution are usually bigger than routinely used ones.

field is vital for studying the characteristics of materials in many scientific disciplines because many physical phenomena depend explicitly on it. In materials science and condensed matter physics, high magnetic fields are used to study the magnetic and electronic properties of materials. The magnetic field interacts most intensely with the electrons in the material, either by acting on electric currents generated by the quantum mechanical motion of the electrons or by coupling to the magnetic moments arising from the electrons' own/intrinsic spin. Indeed, these coupling mechanisms are the basis of most experiments using high magnetic fields to study the electronic structure of materials. However, the much weaker coupling of magnetic fields to the magnetic moments of nuclear spins is also important, which is the physical basis of nuclear magnetic resonance (NMR) techniques [5].

Magnetic fields are typically measured in units of tesla (T) or gauss (G), with 1 T equaling 10,000 G. High magnetic fields refer to magnetic fields that are much stronger than the Earth's magnetic field, which has a strength of approximately 0.5 G ( $50 \mu\text{T}$ ) at a latitude of 50 degrees [5]. The strength of high magnetic fields used in research can vary depending on the application, but they generally range from several T (e.g., a typical Magnetic Resonance Imaging (MRI) scanner features a 1.5 T magnet) to tens, or even hundreds of T in case of pulsed magnets. These fields are typically generated using specialized equipment such as superconducting magnets, resistive magnets (they operate with high losses and need a powerful water cooling system), or hybrid magnets (i.e., an outer superconducting magnet and an inner resistive magnet) which are capable of producing extremely high and stable magnetic fields [5]. They can be further divided into steady-state (or continuous) and pulsed magnets. For high-field research magnets, the primary type of coil used is the solenoid, which produces axial magnetic fields along the centerline of the bore. For more information on high magnetic fields and specific types of magnets, see ref. [95]. In the next subsection, we focus on the superconducting type of magnet that is used in our setup.

### 1.5.1 Superconducting Magnets

Achieving high magnetic fields is possible by using superconducting magnets, which were developed during the 1960s using superconducting wires [5]. A superconducting magnet is an electromagnet made from coils of superconducting wire (superconductor) which must be cooled to cryogenic temperatures using LHe during operation. In the superconducting state, the wire has no electrical resistance and therefore, can conduct much larger electric currents than ordinary wire, creating intense magnetic fields. An important characteristic of any superconductor is the maximum electric transport current density that the superconductor is able to maintain without

resistance [96].

There are two most common cryogen-cooled superconducting magnet configurations: solenoid or split-pair coils superconducting magnets, see Fig. 1.18. Unlike permanent magnets, they allow easy tuning and inverting of the magnetic field. However, the use of cryogenic fluids, such as  $\text{LN}_2$  (77 K) and LHe (4.2 K), is inevitable for their operation, which is in case of LHe quite expensive. Operating and maintaining these magnets in laboratories requires a dedicated infrastructure (helium recovery system, liquefiers) and periodic transfer of cryogenic fluids by trained personnel [97]. Nonetheless, with the development of cryogen-free superconducting magnets in recent years [97] – [99], experiments in high magnetic fields have become feasible also for facilities without LHe infrastructure. Cryogen-free superconducting magnets are becoming popular due to their relatively simple and less costly operation compared to conventional LHe-cooled superconducting magnets [97].

The cooling of the cryogen-free superconducting magnet is mostly provided by two-stage Gifford-McMahon (GM)-cycle cryocooler, which enables cooling as low as 2 K. There are two stages of cold heads for refrigeration, the first stage cools the thermal shield to prevent heat radiation from outside, and the second stage of which, connected to a SC magnet, is used to cool the magnet. The base temperature of the first stage of the cryocooler is specified to be around 33 K, while the second stage is at about 4 K [97, 98]. However, this type of cryocooler also has one disadvantage: vibrations caused by a moving displacer. A pulse tube cryocooler is another type of cryocooler that produces vibrations with smaller magnitude compared to GM cryocooled [100, 101].

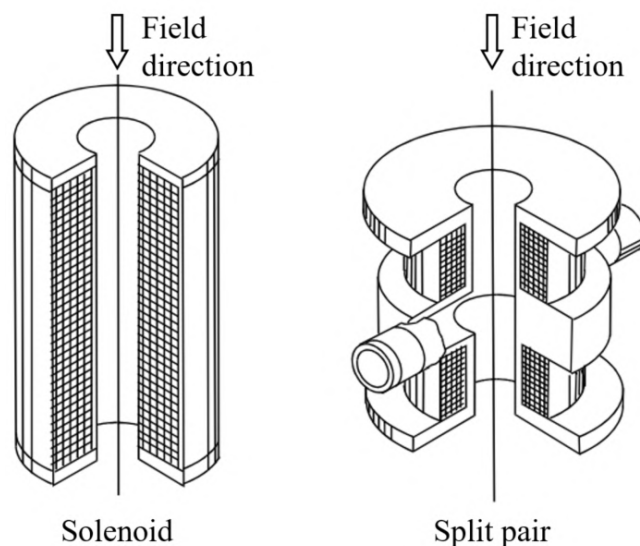


Fig. 1.18: Schematic diagram of a simple solenoid and split pair. Adapted from [102].

## 2 FTIR Magneto-Spectroscopy

This chapter focuses on the key method of this doctoral thesis, Fourier Transform Infrared Spectroscopy (FTIR) in high magnetic fields, also referred to as FTIR magneto-spectroscopy, which deals with the study of materials in magnetic fields using FTIR spectroscopy.

Spectroscopy is one of the most fundamental and widespread experimental techniques for scientific investigation. Spectroscopy performed in the IR range is particularly informative due to numerous intrinsic material responses associated with intra-band electronic transitions, collective modes, and the interaction of radiation with lattice vibrations, i.e., phonons [103]. The presence of a magnetic field is essential for studying the characteristics of materials because many physical phenomena depend explicitly on it. In general, magneto-optical experiments provide powerful tools for gaining insights into the properties of materials, and such experiments are often an ideal way to study new physical phenomena. For instance, the IR region in magnetic fields is particularly important since it covers the magnetic resonances and other important effects [5, 6] illustrated in Fig. 2.1.

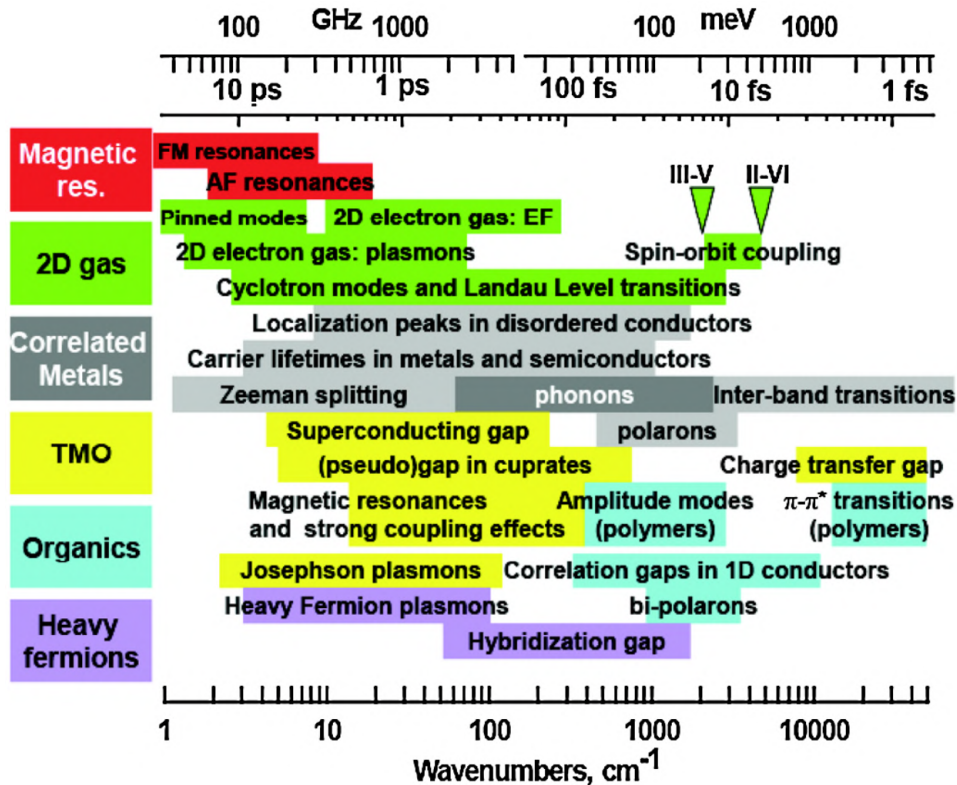


Fig. 2.1: Schematic representation of magnetic field-induced phenomena observable in the IR range. Taken from [6].

Historically, the first magneto-optical measurements in the IR range were performed in the 1950s to elucidate phenomena such as cyclotron resonance [104, 105], antiferromagnetic (AF) resonance [106], later in the 1960s, electron paramagnetic resonance (EPR) [107], then in the 1970s, transitions between Landau Levels (LLs) [108, 109], Bardeen–Cooper–Schrieffer (BCS) superconductivity [110], 2D electron gas/plasmon–phonon interaction, etc. [103]. The importance of magneto-optical measurements has not diminished over the years. FTIR magneto-spectroscopy is still a powerful spectroscopic technique (especially at low temperatures) for investigating many important physical phenomena (see Fig. 2.1) and elucidating the exotic behavior of novel materials, which are currently of great interest, such as single-molecule magnets (SMMs) [11] – [22], graphene [23] – [28], topological insulators [111] – [113], Weyl semimetals [114, 115], or superconductors [116, 117].

Our research is aimed mainly at the investigation of spin-related EPR transition-/energy splittings in transition metal compounds and other paramagnetic materials such as SMMs, molecules displaying slow relaxation of magnetization of purely molecular origin [7], thus the ability to store one bit of information at much higher densities, using FTIR magneto-spectroscopy.

In addition to SMMs, our research also focuses on investigating the band structure and electronic properties of 2D materials such as graphene [23] – [28] using FTIR magneto-spectroscopy, which probes dipole magneto-optical transitions of electrons, such as transitions between LLs.

The following sections explain the physical principles of the phenomena underpinning our research, i.e., EPR and transitions between LLs. They also describe in detail the most relevant classes of materials for our research, i.e., SMMs and 2D materials such as graphene, in which we use FTIR magneto-spectroscopy to investigate the splitting of the energy levels caused by EPR and LLs transitions. The last section presents an overview of the state-of-the-art setups, i.e., existing setups worldwide utilizing IR or FTIR magneto-spectroscopy.

## 2.1 Electron Paramagnetic Resonance (EPR)

Electron Paramagnetic Resonance (EPR), sometimes called Electron Spin Resonance (ESR), spectroscopy is a powerful technique for studying magnetic and electronic properties of materials with unpaired electrons, i.e., paramagnetic materials, such as paramagnetic complexes, radicals or defects in crystals [118]. EPR is resonant absorption of usually microwave radiation by paramagnetic molecules or ions with at least one unpaired electron spin in the presence of a static magnetic field [118]. It is based on the Zeeman effect that is the separation of the energy of spin states

in the presence of a magnetic field. In the simplest case of a free electron, where  $B$  designates the magnetic field that satisfies the resonance condition, can be expressed as

$$\Delta U = h\nu = g_e\mu_B B, \quad (2.1)$$

where  $h$  is Planck constant,  $g_e = 2.0023$  is the free-electron g-factor and  $\mu_B$  is Bohr magneton. For free unpaired electrons, it means that the splitting of the energy levels is directly proportional to the magnetic field, as shown in Fig. 2.2. Transitions between the two electronic Zeeman levels are then induced by electromagnetic radiation of the appropriate frequency  $\nu$  such that the photon energy  $h\nu$  matches the energy-level separation  $\Delta U$  [118].

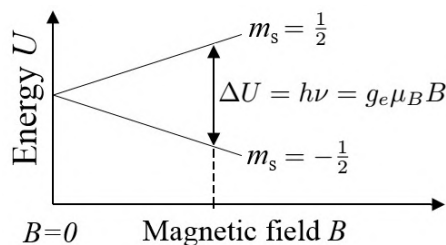


Fig. 2.2: Zeeman splitting of electron spin states. Energy diagram for a free electron in magnetic field  $B$ .

EPR spectroscopy is a fundamental spectroscopic technique for determining the physical chemical properties of paramagnetic coordination compounds and molecular magnetic materials. These compounds frequently exhibit EPR transitions over a wide range of energies, corresponding to frequencies from MHz to THz. SMMs are a special class of materials belonging to the paramagnetic coordination compounds that particularly benefit from EPR as they usually possess large zero-field splitting (ZFS). Primary sources of these energy splittings are spin-orbit and spin-spin interactions among unpaired electrons that can lead to ZFS of ground-state magnetic sublevels [119, 120]. However, conventional microwave EPR systems do not provide experimental access to the EPR transitions of SMMs with large ZFS, which are currently of interest. FTIR magneto-spectroscopy enables us to observe EPR transitions of SMMs with large ZFS, mainly based on transition metal complexes [11] – [18] or lanthanides [19] – [22], in which conventional microwave EPR systems do not provide experimental access to the magnetic resonance transitions. Moreover, it is an essential method in the characterization of SMMs due to the ability to probe molecular and electronic properties directly [9, 10].

### 2.1.1 Single-Molecule Magnets (SMMs)

In this modern digital world we live in, the growing need for smaller and more energy-efficient devices has made higher density data storage one of the most important technological quests. International Data Corporation lately published a paper [121] showing an alarming graph of exponentially growing annual size of global datasphere from 50 zettabytes in 2020 to 175 zettabytes in 2025 (3.5 times more). Therefore, research is currently focused on developing denser means of data storage that can store greater amounts of data in a more energy-efficient way. The critical research topics involve working at the level of individual atoms and molecules, representing the ultimate limit of technological miniaturization [122]. Although the investigation of SMMs is still fundamental research and all their potential applications are far from actual implementation in modern technologies, these types of systems are important and relevant for understanding the underlying physics of paramagnetic compounds at higher frequencies and magnetic fields.

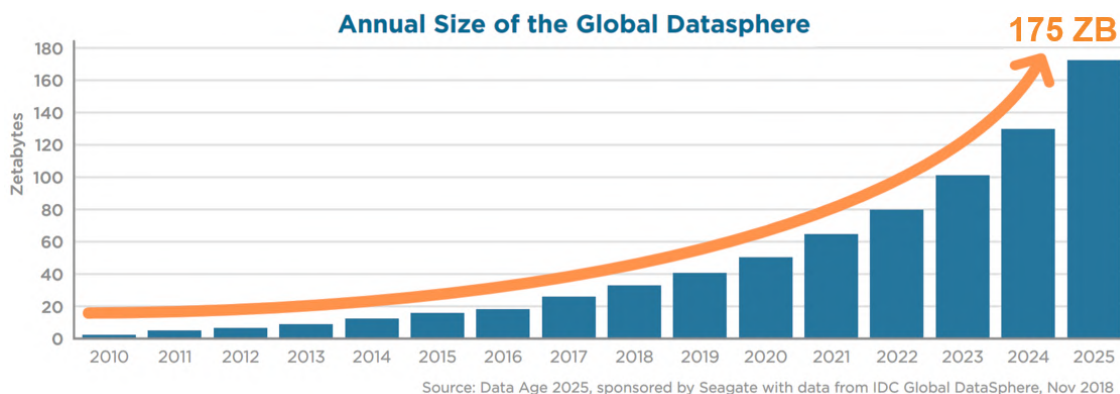


Fig. 2.3: Annual size of global datasphere. Adapted from [121].

Due to their nanometer dimensions and the ability to store one bit of information using individual spins<sup>1</sup>, molecular species built up of paramagnetic transition metals or lanthanide metal ions called SMMs give a possibility to move technology forward. Their molecular nature offers unique attributes that allow them to store information with much higher density. The first example of SMMs was Mn(III) cluster [Mn<sub>12</sub>OAc], see Figure 2.4 (a), in which slow relaxation of the magnetization was observed and published in *Nature* in 1993 [123]. Since then, they have drawn the increasing attention of the scientific community [124] – [128] due to their potential applications in high-density data storage [129], quantum computing [130], and spintronics [131, 132].

<sup>1</sup>by assigning binary 0 to one orientation of the magnetic moment, and binary 1 to its opposite orientation

The key feature of SMMs is the slow relaxation of the magnetization of purely molecular origin [7]. Commonly used characteristic quantities, which basically describes the quality of SMMs, are the blocking<sup>2</sup> temperature  $T_B$  and the effective energy barrier  $U_{eff}$  [20]. The energy barrier corresponds to the separation between the positive and negative magnetization states of a SMM. Consequently, at low temperatures, the system is trapped in one of the high-spin energy wells, see Figure 2.4 (b). The higher the barrier, the longer a material remains magnetized, therefore  $U_{eff}$  should be as large as possible [136].

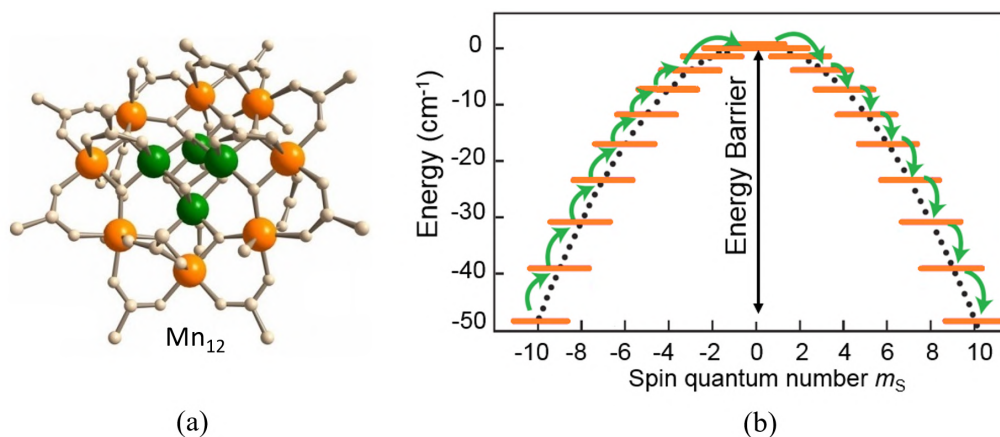


Fig. 2.4: (a) The first SMMs – molecule  $Mn_{12}$  in which slow relaxation of the magnetization at low temperature was observed in 1993. Taken from [134]. (b) Potential energy as a function of the spin quantum number. Adapted from [135].

Traditionally, the energy barrier  $U_{eff}$  of first row transition metals SMMs is estimated as  $U_{eff} = S^2|D|$  and  $U_{eff} = (S^2 - 1/4)|D|$  for integer and non-integer spin respectively [7]. In these equations,  $S$  is the total spin of the complex (spin of the ground state), and  $D$  is the magnetic anisotropy constant called the axial term of the second rank ZFS tensor [11]. ZFS is a phenomenon arising in paramagnetic systems with multiple unpaired electrons ( $S > 1/2$ ) as a result of spin-orbit coupling (SOC) and spin-spin coupling (SSC) interactions, and interaction with ligands. SOC is the interaction of the (unpaired) electron spin angular momentum with the electron orbital angular momentum, and SSC is the direct, dipolar interaction among pairs of unpaired electrons [137], and/or exchange interactions. Magnetic anisotropy is the preferential alignment of the magnetic moment along a specific direction so-called easy axis<sup>3</sup> or alternatively easy plane [7]. To improve the energy barrier,

<sup>2</sup>maximum temperature at which it is possible to observe hysteresis in the field-dependence of the magnetization [133].

<sup>3</sup>The most energetically favourable direction of spontaneous magnetization in a system [7].

scientists from the beginning focused on increasing the total spin. However, recently it was realized that with increasing  $S$ ,  $D$  actually decreases, and the energy barrier does not improve much [138, 139]. Therefore, attention turned to systems with large magnetic anisotropies  $D$  [11], especially lanthanides ( $f$ -block elements). Since 2003, when the slow relaxation of the magnetization was observed in lanthanide-based SMM by Ishikawa [140], lanthanide-based complexes are intensively investigated, and they have already yielded promising results. Slow relaxation of magnetization at the temperature above liquid nitrogen (80 K) was observed in lanthanide-based SMMs in 2018 [133]. This observation denoted a huge success in the field of molecular magnetism, since the main drawback of SMMs, which stands in the way of moving these molecules out of the lab to applications, is that they exhibit magnetic memory effects usually only in cryogenic temperatures.

An essential class of SMMs are mononuclear<sup>4</sup> complexes called Single-Ion Magnets (SIMs), that exhibit slow magnetic relaxation in the absence of the magnetic field. The single ion in SIMs can be transition metal ion, but also lanthanide-based ion. SIMs represent the most straightforward model systems based on which the physics of spin, anisotropy, and magnetic relaxation in metal complexes can be probed and understood. Hence, the study of SIMs properties and their behavior can be considered as a fundamental undertaking in the quest to fabricate functional nanoscale magnetic materials from the bottom-up [7].

Mononuclear transition-metal complexes are of current interest in molecular magnetism due to their intriguing physical properties, such as magnetic bistability<sup>5</sup> at low temperatures, or quantum tunneling of magnetization, and promising applications [17]. There has been a growing number of first-row/3  $d$ -block SIM systems reported in the literature last years. Cobalt complexes attract significant attention due to their frequently very large magnetic anisotropies [141].

In general, transition metal complexes can be separated into half-integer spin states ( $S = 1/2, 3/2$ , etc.) and integer-spin states ( $S = 1, 2$ , etc.) [142]. According to the Kramers theorem, spin levels of half-integer spin state (Kramers) ions are in the absence of an external magnetic field at least doubly degenerate. An external magnetic field removes the remaining degeneracy of the Kramers doublets. In contrast, integer spin state (non-Kramers) ions are split by ZFS to nondegenerate spin levels [143], see Fig. 2.5.

From the point of view of EPR spectroscopy (not coordination chemistry), transition metal complexes can also be divided into two classes: low-spin (LS), with  $S = 1/2$  (as  $S = 0$  is diamagnetic and useless for EPR), and high-spin (HS), with  $S > 1/2$ . The main difference between LS and HS complexes is that the phenomenon

---

<sup>4</sup>They contain only a single paramagnetic ion.

<sup>5</sup>They exhibit an energy barrier to spin reversal from  $+M_s$  to  $-M_s$  [7].

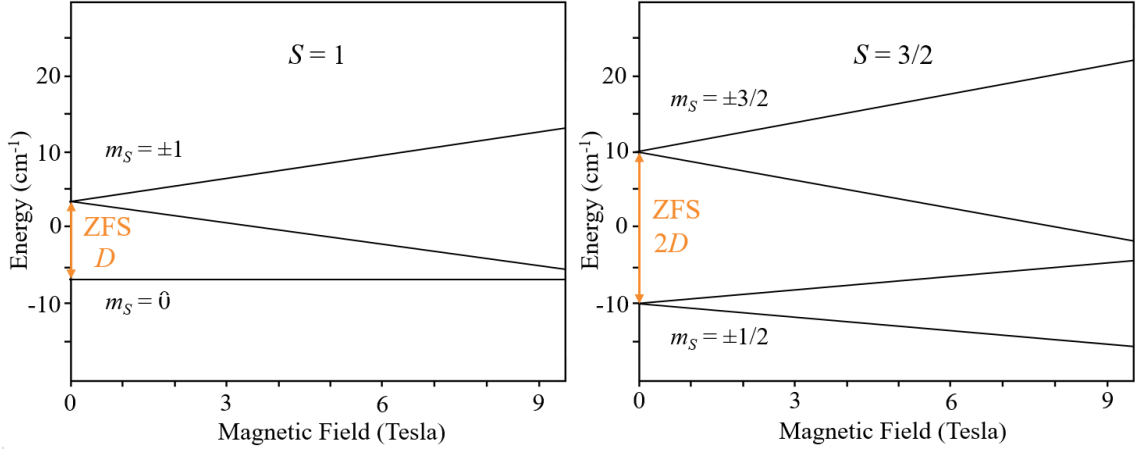


Fig. 2.5: Simulated spin sublevel energies as a function of a magnetic field with indicated ZFS ( $D$  and  $2D$ , respectively) for the two simplest HS ions :  $S = 1$  (left, representing the non-Kramers class), and  $S = 3/2$  (right, representing the Kramers class). An axial ZFS tensor was assumed in both cases, with  $D = 10 \text{ cm}^{-1}$  and  $E = 0 \text{ cm}^{-1}$ , together with isotropic  $g = 2.00$ ,  $B_0 \parallel z$ .

of ZFS only appears in HS states [142]. Since the presence of the ZFS phenomenon is essential for the determination of SMMs properties, only HS systems are relevant in this regard.

The magnetic behavior of SIMs with HS state (the interaction with nuclear spins are neglected) is governed by spin Hamiltonian in the form:

$$\hat{H} = \hat{H}_{Zee} + \hat{H}_{ZFS} = \mu_B \hat{S} g B_0 + \hat{S} D \hat{S}, \quad (2.2)$$

where  $\hat{H}_{Zee}$  denotes the electron-Zeeman interaction, and  $\hat{H}_{ZFS}$  the ZFS, with  $D$  being ZFS tensor [143]. It is convenient to define  $D$  in a local frame, where  $D$  is diagonal with  $D_x, D_y, D_z$  are the principal values of ZFS tensor, and  $z$ -axis is the main anisotropy axis, then the ZFS spin Hamiltonian can be expressed as:

$$\hat{H}_{ZFS} = D[\hat{S}_z^2 - \frac{1}{3}S(S+1)] + E(\hat{S}_x^2 - \hat{S}_y^2), \quad (2.3)$$

where  $\hat{S}$  is a spin operator, which describes the spin projection along a given axis, and  $D = 3/2D_z$  and  $E = (D_x - D_y)/2$  are the axial and rhombic ZFS parameters, respectively [143]. The role of  $D$  and  $E$  is to lift the degeneracy of the  $2S + 1$  spin microstates/sublevels associated with a given  $S$  even in the absence of an external magnetic field. For more detailed insight into the ZFS phenomenon and relationship between  $D$  and  $E$ , see ref. [137].

Accurate determination of the spin Hamiltonian parameters in transition metal complexes with large ZFS might be challenging in studying magnetic and spectroscopic properties of HS transition metal complexes [17]. Complexes with HS states

frequently exhibit EPR transitions over a wide range of energies, corresponding to frequencies from a few hundred MHz to a few THz. For precise determination of spin transition energies by EPR, frequency of the applied radiation has to match the transition energy of interest. This can be problematic to accomplish in the case of systems with very large ZFS, or systems with unknown spin transition energies. One possibility to meet this challenge is to use high-field/high-frequency EPR (HF-EPR) spectroscopy, which uses a single fixed frequency<sup>6</sup> in combination with a very broad field scans (0 – 25 T). An alternative approach is to use FTIR magneto-spectroscopy, which employs scans of the exceptionally broad frequency range (up to hundreds  $\text{cm}^{-1}$ , far beyond the range of routine EPR spectrometers) at a set of fixed magnetic fields, so the possibility to match the desired frequency is much higher. This approach can be beneficial for so-called “EPR silent” systems (usually integer-spin states), which show no EPR transitions in conventional X-band (9 – 10 GHz/ 0 – 1 T) and Q-band (33 – 35 GHz/0 – 2 T) spectrometers. Additionally, an important advantage of FTIR magneto-spectroscopy in high magnetic fields is that the ZFS can often be extracted directly from the zero-field spectrum [120].

To sum up, a substantial contribution of FTIR magneto-spectroscopy is studying EPR transitions in paramagnetic compounds, particularly multinuclear HS systems (SMMs) and mononuclear complexes (SIMs) based on transition metal ions [11] – [18], and lanthanides [19] – [22] distributed over a broad transition-energy range, which is challenging or even impossible with other, more conventional EPR techniques [9, 10].

## 2.2 Landau Levels (LLs)

The cyclotron resonance phenomenon originates from the quantization of the cyclotron orbits and energy levels of electrons subjected to intense magnetic fields, also known as Landau quantization.

If we consider a charged particle, e.g. an electron with the elementary charge  $e$  and instantaneous velocity  $v$  in an electric field  $E$  and a uniform magnetic field  $B$ , the Lorentz force  $F_L$ <sup>7</sup>, on it is given by:

$$F = e[E + (v \times B)]. \quad (2.4)$$

The magnetic force that is always perpendicular to the velocity of a charged particle, acting on the free electron with mass  $m$ , will cause circular motion. The frequency

---

<sup>6</sup>typically in the 100 – 1000 GHz range

<sup>7</sup>the combination of electric and magnetic force on a point charge due to electromagnetic fields

of this circular motion is called cyclotron frequency  $\omega_c$ . It is given by equation

$$\omega_c = \frac{eB}{m}. \quad (2.5)$$

In many semiconductors, it is possible to determine the effective masses of carriers in the conduction and valence bands near the band edges by cyclotron resonance. For these materials, mass of charged particle  $m$  in equation 2.6 is then replaced by the appropriate cyclotron effective mass  $m^*$  [144].

Under high magnetic fields, such orbits become quantized, and associated quantized energy levels are called Landau levels (LLs). The quantized energies are given by [36]:

$$E_n = (n + 1/2)\hbar\omega_c, \text{ where } n = 0, 1, 2, \dots \quad (2.6)$$

Cyclotron resonance is then the resonant absorption of light/energy with a frequency equal to the frequency difference between LLs. The LLs are degenerate, with the number of electrons per level directly proportional to the strength of the applied magnetic field. Landau quantization is directly responsible for oscillations in the electronic properties of materials as a function of the applied magnetic field, such as Shubnikov-de Haas or De Haas-van Alphen phenomenon [145, 146].

### 2.2.1 2D Materials

As was already mentioned, besides investigation of SMMs potential applicability, FTIR spectroscopy in high magnetic fields is a very convenient experimental method providing insight into the band structure and electronic properties of 2D materials, such as graphene or transition metal dichalcogenides (TMDCs). It can be used to observe cyclotron resonance, from which one can determine the effective mass of charge carriers, or LLs quantization, and, consequently, the information about mobility of charge carriers [23, 28, 145, 147]. Since its experimental discovery in 2004 [148], a single atomic layer of carbon atoms tightly packed into a honeycomb lattice called graphene, the first known two-dimensional (2D) atomic crystal, has triggered a wave of international research interest due to its remarkable mechanical, thermal, and electrical properties [149, 150]. What really makes graphene special, however, is its electrical properties. They result from the hexagonal symmetry of the graphene's crystal lattice, which has two carbon atoms in the unit cell, denoted as A and B, with an interatomic distance of 0.142 nm [151]. The lattice then consists of two intersecting triangular sublattices, each consisting of only one of the two mentioned atoms, see Fig. 2.6.

Each carbon atom has one  $s$  orbital and three  $p$  ( $p_x; p_y; p_z$ ) orbitals. Orbital  $s$  and two  $p$  orbitals, which lie in the plane of the lattice, are connected by a strong

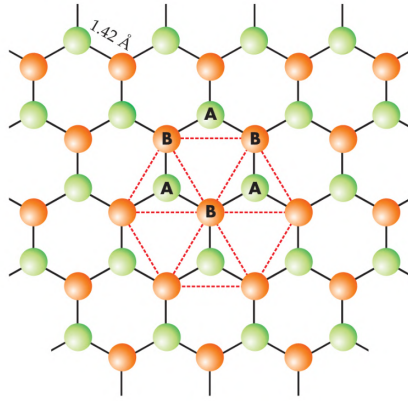


Fig. 2.6: Crystal lattice of graphene consisting of two triangular sublattices. Adapted from [151].

covalent bond with adjacent atoms and do not contribute to its conductivity. The remaining  $p$  orbital, oriented perpendicular to the plane of the lattice, hybridizes to form  $\pi$  (valence) and  $\pi^*$  (conduction) bands above and below the plane of the graphene lattice. The electrons that form these bands have the greatest influence on the electrical properties of graphene. These bands are touching at two points  $K$  and  $K'$  of the Brillouin zone, also called Dirac points, which guarantees a typical conical-shaped energy spectrum of graphene, with practically linear electronic bands/dispersion relation close to Dirac points, without a band gap, see Fig. 2.7. The Fermi level in pristine graphene lies just at the touching point of  $\pi$  and  $\pi^*$  bands, therefore graphene has a character of zero bandgap semiconductor (semimetal). Moreover, the linearity of graphene electronic bands in the vicinity of the Dirac points implies that the charge carriers in graphene behave as massless relativistic particles called Dirac fermions with constant Fermi velocity  $v_F=10^6\text{ms}^{-1}$  [151, 152].

Although graphene is the first and the most famous 2D material, the family of 2D materials is not limited to carbon crystals. To obtain other 2D crystals, the same techniques that worked for graphene can be used. For example, micromechanical or chemical exfoliation can be successfully applied to other layered materials such as BN, MoS<sub>2</sub>, and other dichalcogenides. Besides, the method of epitaxial growth can be applied to grow monolayers of BN [152].

In recent years, transition metal dichalcogenides (TMDCs), a large family of 2D layered materials, have attracted considerable attention of researchers due to their unique structural features, and interesting electrical, optical, magnetic, catalytic, energy-storage, superconductivity and thermal properties [153] – [155]. TMDCs have characteristic two-dimensional lattice structure in which the metal and chalcogen are arranged periodically in a hexagonal structure. Although TMDCs are referred to as

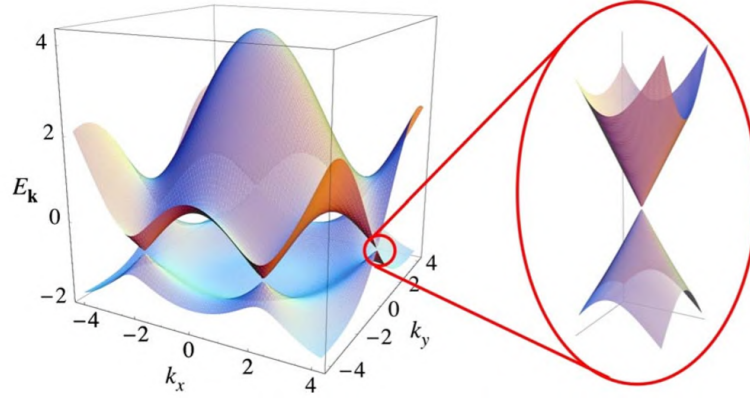


Fig. 2.7: Electronic energy bands of graphene. Taken from [150].

2D materials, their hexagonal structure is not atomically thin as in the case of graphene. It is formed according to the formula  $\text{MX}_2$ , in which one layer of M atoms is sandwiched between two layers of X atoms (X-M-X), where M is a transition metal atom (Mo, W, V, etc.) and X is a chalcogen atom (S, Se, or Te). TMDCs have shown great potential in many application fields such as electronics and optoelectronics because, unlike zero band gap graphene, many of them have a tunable thickness-dependent band gap. They are also ideal candidates for next-generation spintronic nanodevices [156, 157].

Since most of the knowledge on unique electronic properties of graphene has been deduced from conventional electric transport, optical experiments, and especially measurements under an applied magnetic field, particular attention is focused on magneto-optical investigations of these materials, such as the cyclotron resonance phenomenon [145].

In case of graphene, the application of the magnetic field  $B$  perpendicular to its plane transforms the continuous electronic spectrum into discrete and highly degenerate Landau levels with energies:

$$E_n = \text{sign}(n)v_F\sqrt{2|e|\hbar B|n|} = \text{sign}(n)E_1\sqrt{|n|}, n = 0, \pm 1, \pm 2, \dots, \quad (2.7)$$

(where  $n$  is the quantum number) characterized by a single material parameter, the Fermi velocity  $v_F$  ( $E_1 = v_F\sqrt{2\hbar eB}$ ). Landau level spectrum includes electron levels ( $n > 0$ ), hole levels ( $n < 0$ ) and zero levels ( $n = 0$ ), which is shared by both types of carriers. Furthermore, Landau levels in graphene and similar 2D Dirac materials are non-equidistant and nonlinear in magnetic field, they have unusual  $\sqrt{B}$  dependence<sup>8</sup>, see Fig. 2.8, that is a consequence of the linearity of the bands [145], and it leads to

<sup>8</sup>in contrast with the linear  $B$  dependence characteristic of non-relativistic electrons found in usual semiconductors

a number of unusual magneto-optical properties [150]. The typical example of FTIR magneto-optical spectra, low temperature FIR transmission spectra as a function of the magnetic field, of multilayer epitaxial graphene is depicted in Fig. 2.9.

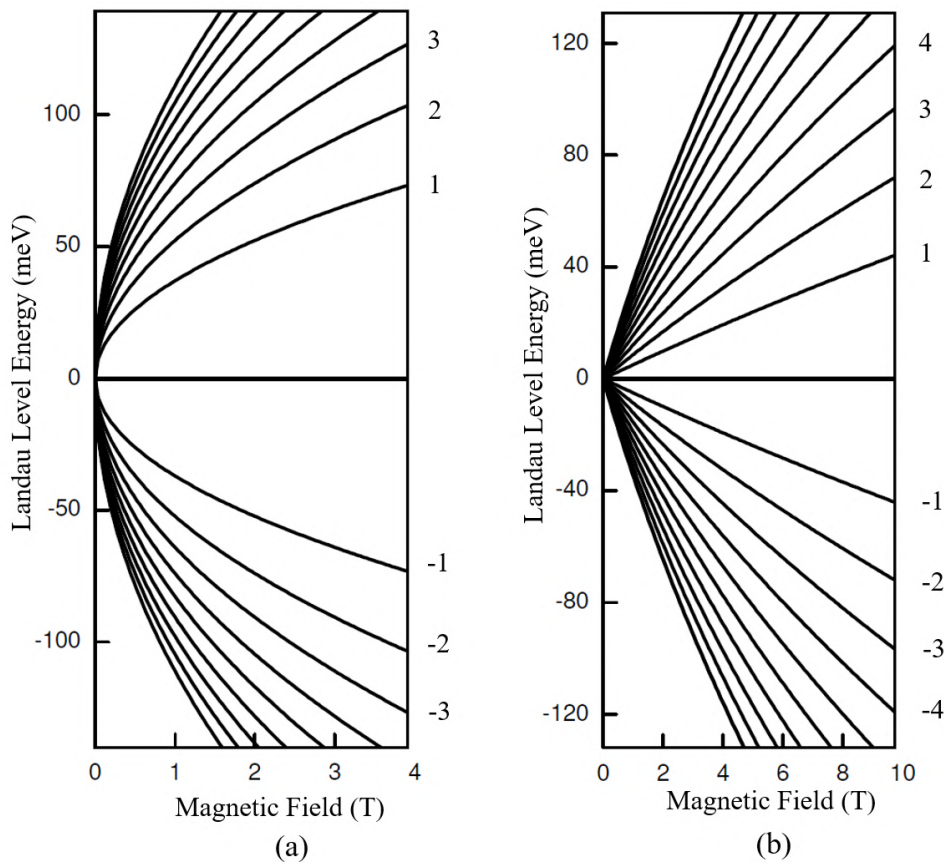


Fig. 2.8: (a) Magnetic-field dependence ( $\sqrt{B}$ ) of the Landau levels energies in graphene. (b) Magnetic-field dependence ( $B$ ) of the Landau levels energies in bilayer graphene. Adapted from [145].

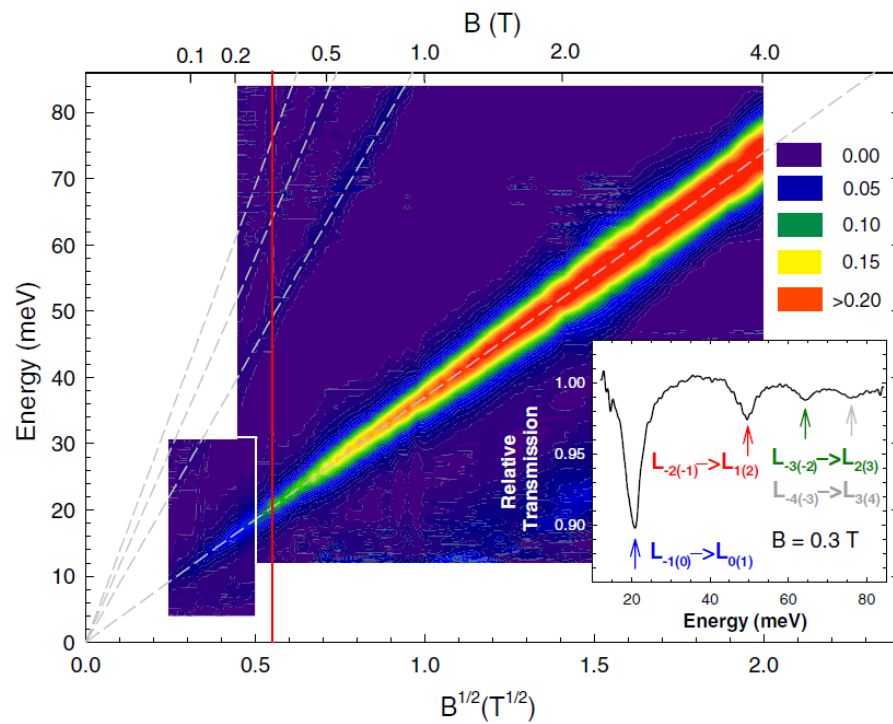


Fig. 2.9: The FIR transmission  $T$  plotted as  $-\ln T$  as a function of the magnetic field at  $T=2$  K. The inset shows the transmission spectrum at  $B=0.3$  T. Taken from [28].

## 2.3 State of the Art

A broadband instrument that covers the THz/IR spectral range coupled to a high magnetic field magnet (preferably equipped with a cryostat for temperature-dependent measurements) for magneto-optic measurements is a versatile and invaluable laboratory tool. Using such an IR magneto-spectroscopic tool/setup, we can investigate many important effects in materials, as shown in Fig. 2.1. Setups for IR magneto-spectroscopy, and the method itself, are known for more than 50 years [107, 158, 159]. Despite their enormous potential in material science, IR magneto-spectrometers are still relatively rare and custom-made since such systems generally require complex infrastructure.

Several different experimental configurations utilizing FTIR magneto-spectroscopy are available worldwide. Such systems are frequently an integral part of large research facilities for high magnetic fields, such as the Grenoble High Magnetic Field Laboratory (GHMFL) in France [13, 14] or the National High Magnetic Field Laboratory (NHMFL) in Tallahassee, Florida, USA [22]. Some research facilities utilize synchrotrons as a source of radiation to improve the power/performance in the FIR and THz regions, e.g., IR beamline U12IR at the National Synchrotron Light Source (NSLS) of Brookhaven National Laboratory [160–162], or the Helmholtz Zentrum Berlin (HZB) operating the BESSY II synchrotron [9, 163], see Fig. 2.10. However, IR magneto-spectroscopic setups can also be found at a few university laboratories/research centers [27, 103], [164] – [177].

We decided to build FTIR magneto-spectroscopic setup for our EPR laboratory at CEITEC BUT to complement our X-band spectrometer (9–10 GHz) and High-Frequency EPR spectrometer (80 GHz–1.1 THz), and to extend our laboratory capabilities for investigating EPR and other effects to the THz and IR spectral range (1.5–300 THz). Since the HF-EPR spectrometer and FTIR magneto-spectroscopic setup use the same 16 T cryogen-free superconducting magnet, the idea was to create a simple, fast, and universal setup transfer mechanism for both setups. Ing. Antonín Sojka, Ph.D. designed the magnet frame equipped with linear guide rails, servomotors, and trapezoidal screws for an automatically driven motion and a compatible movable table for the HEPR spectrometer. In the scope of this thesis, I designed another movable table for FTIR magneto-spectroscopic setup compatible with the magnet frame that secures a simple transfer of our setup and its precise alignment.

Regarding the state of the art, even though the idea of coupling of the FTIR spectrometer to a superconducting magnet is far from new, the novelty of our setup lies in the usage of a cryogen-free superconducting magnet. To the best of our knowledge and to this time, this is the first reported IR magneto-spectroscopic setup

utilizing a cryogen-free superconducting magnet. Thanks to its relatively simple design and implementation of a cryogen-free superconducting magnet, our FTIR magneto-spectroscopic setup can pave the way for other research institutions without the LHe infrastructure to perform IR magneto-optical experiments in high magnetic fields.

The following text presents several examples of scientific institutes and laboratories around the world that have magneto-optical setup which combines IR spectroscopy and high magnetic fields.

**Grenoble High Magnetic Field Laboratory (GHMFL), France** (*French National Center for Scientific Research (CNRS)*)

The Laboratoire National des Champs Magnétiques Intenses (LNCMI) (in english: National Laboratory for Intense Magnetic Fields) is a research institution of the CNRS. The LNCMI was created in 2009 by the merger of the pulsed magnetic field Laboratory of Toulouse and the Grenoble High Magnetic Field Laboratory (GHMFL). It is based at two sites: one in Grenoble, specialised in static fields, and one in Toulouse, specialised in pulsed fields. At the Grenoble site, static magnetic fields of up to 37 T are generated and long duration measurements are available thanks to the continuous cooling capacity of the neighboring river. A hybrid magnet aiming at a magnetic field of 43 T of static field in a 34 mm room temperature bore is under construction. The setup at GHMFL in the group of Dr. Milan Orlits consists of Bruker 80v FTIR spectrometer equipped with a globar and Hg-Arc lamp source, light-pipe optics, and the sample is placed inside the 16 T superconducting magnet with helium heat-exchange gas at  $T=4.2\text{K}$ , with a composite bolometer detector located inside the magnet. The sample is in the standard Faraday configuration (i.e. in transmission mode, with the magnetic field parallel to the wave vector of the probing radiation).

**THz Electron Paramagnetic Resonance / THz Spectroscopy at BESSY II, Helmholtz-Zentrum Berlin, Germany** (*Helmholtz-Zentrum Berlin für Materialien und Energie*)

The THz beamline at BESSY II employs high power broadband femto- to picosecond long THz pulses for magneto-optical THz and FIR studies. The Frequency Domain Fourier transform THz-Electron Paramagnetic Resonance (FD-FT THz-EPR) user facility at the electron-storage ring BESSY II is depicted in Fig. 2.10. The spectrometer employs intense linearly polarized broadband THz-CSR as radiation source. To reduce standing waves in the spectrometer, and at the same time conserve the polarization of the excitation beam, quasi-optical elements are inserted in the beamline. The THz beam extracted from the storage ring (depicted as

green trace) is focused on the external radiation port of a high-resolution Michelson FTIR spectrometer (Bruker IFS 125, max. resolution:  $0.0063\text{ cm}^{-1}$  or 200 MHz). Inside the FTIR spectrometer, THz radiation can be directed to a liquid-He-cooled sample cryostat ( $T = 4.5\text{--}300\text{ cm}^{-1}\text{K}$ , Bruker Optistat), which is attached to the sample compartment for zero-field FD-FT THz-EPR (blue trace) or coupled into a quasi-optical transmission line leaving the spectrometer (green trace). This line directs the radiation to an optical bench. On it, the radiation can again be switched to two different pathways through a superconducting split coil magnet. The magnet contains a variable-temperature insert (VTI) equipped with four THz-transparent z-cut quartz windows. The propagation direction of the THz radiation is defined by the vector  $k$ . Its orthogonal pathways through the magnet correspond to Faraday (green trace,  $B_0$  parallel to  $k$ ) and Voigt (red trace,  $B_0$  perpendicular to  $k$ ) configurations. In Voigt geometry, the polarization of the linearly polarized THz light can be rotated around the  $k$ -vector by a broadband rooftop-mirror polarization shifter. The magnet allows for measurements from  $T = 1.5\text{ K}$  to 300 K, at external magnetic fields variable between  $-10\text{ T}$  and  $+10\text{ T}$  ( $\pm 11\text{ T}$  with pumped He reservoir). The option to apply positive and negative magnetic fields provides additional important experimental capabilities in frequency-domain EPR. It allows for, e.g., real time monitoring of quantum tunneling of SMMs [163].

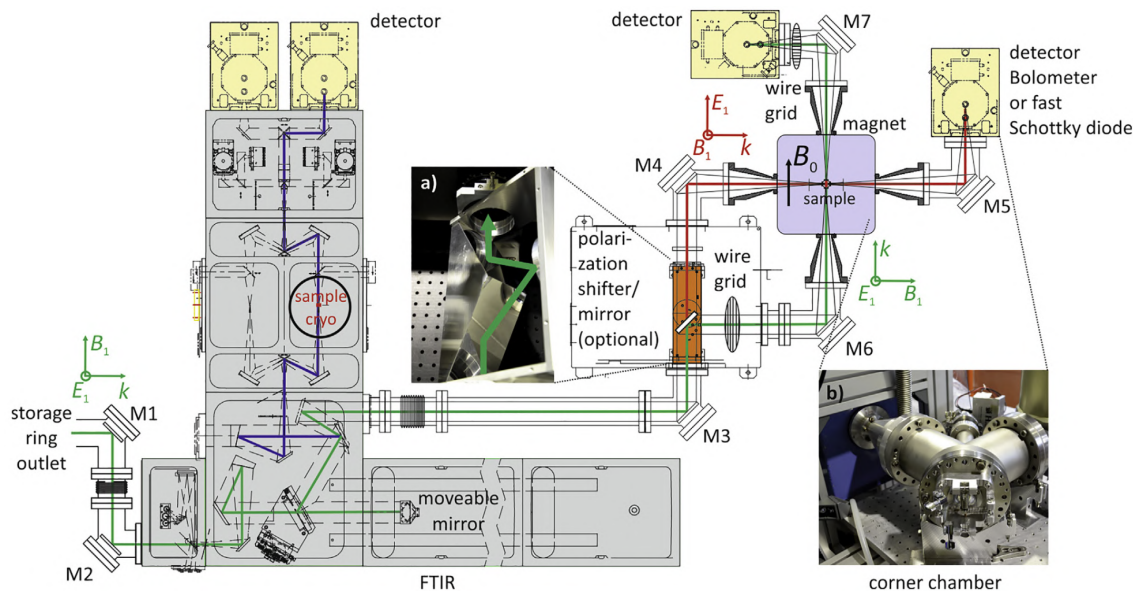


Fig. 2.10: FD-FT THz-EPR user facility at the electron-storage ring BESSY II with scheme of the optical layout of their apparatus. Adapted from [163].

**Basov Infrared Laboratory – New York, NY, USA** (*University of Columbia in City of New York – Department of Physics*)

The system, shown in Fig. 2.11, is capable of broadband frequency domain spectroscopy in the range 180 GHz to 750 THz at cryogenic temperatures. The reflection unit couples both the Martin-Puplett and the Michelson interferometer to a 9 T superconducting split coil magnet. Additionally the unit is designed to work with various detectors, including thermal bolometers and semiconducting detectors [103].

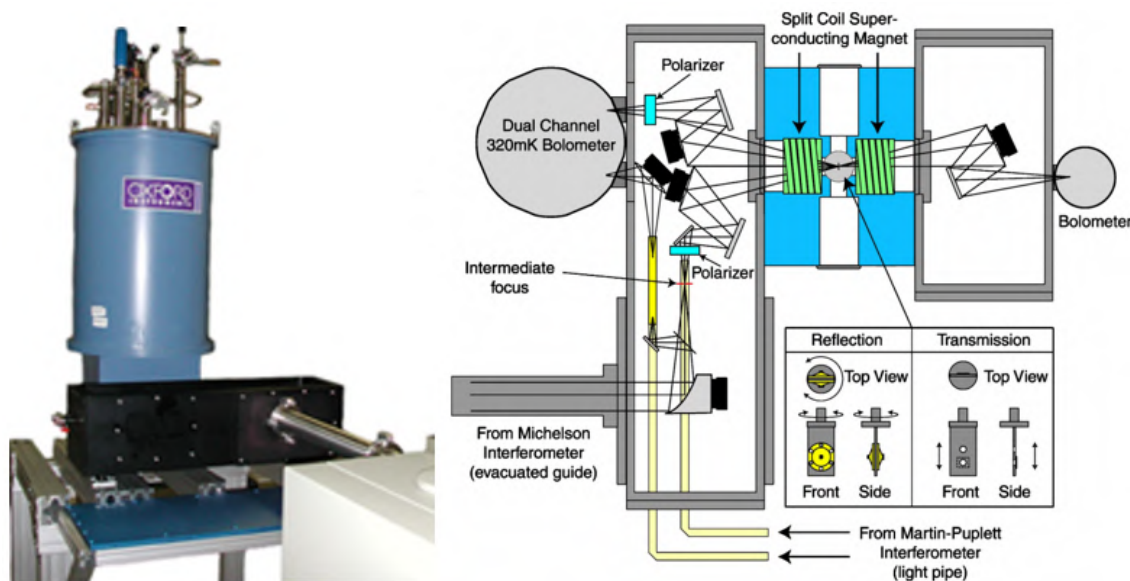


Fig. 2.11: Basov Infrared Laboratory at University of Columbia in City of New York, USA with scheme of the optical layout of their apparatus [6, 103]. Photo is from previous location at University of California, San Diego — Department of Physics.

**Institute of Physical Chemistry (IPC) – Stuttgart, Germany** (*University of Stuttgart*)

This FTIR magneto-spectroscopic setup I designed during my six-months Erasmus+ internship in 2017 at Institute of Physical Chemistry (IPC), University of Stuttgart, in the group of Prof. Joris van Slageren under the supervision of Assoc. prof. Ing. Petr Neugebauer, PhD. The description of the design, implementation and magneto-optical measurements can be found in my master's thesis [173]. Schematic figure of the FTIR magneto-spectroscopic setup at IPC, where all its components are labeled, is shown in Fig. 2.12. This set up consists of Oxford Instruments 15/17 T solenoid cryomagnet, used primarily for HFEPR configuration, FTIR Spectrometer Bruker VERTEX 70v equipped with a MIR source globar and an FIR source (external water cooled mercury Hg-Arc lamp), a detector – pumped liquid helium bolometer

(Infrared Laboratories HDL-5) – and then the components coupling the spectrometer to the magnet: movable table, optical system and transmission probe. Published results obtained from magneto-optical measurements of SMMs performed on this setup can be found in Ref. [12].

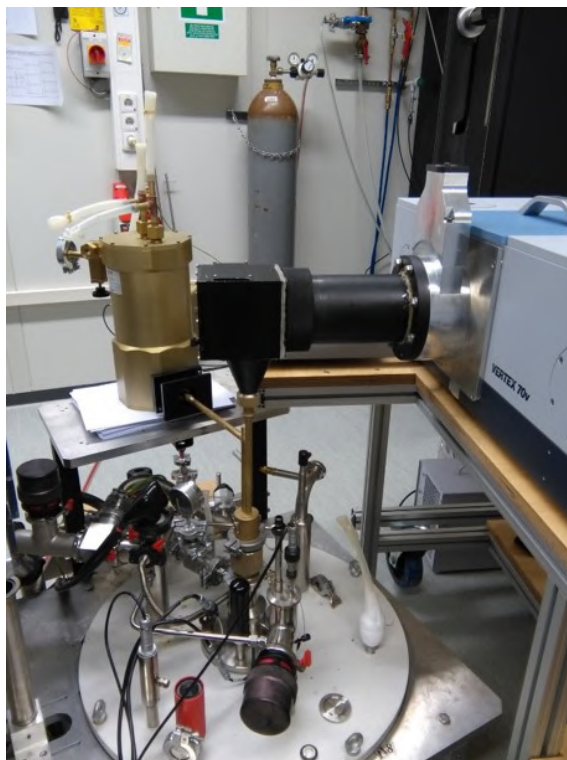


Fig. 2.12: The magneto-optical setup at Institute of Physical Chemistry (IPC), University of Stuttgart. It consists of the Oxford Instruments 15/17 Tesla solenoid superconductive magnet, the Bruker VERTEX 70v FT-IR spectrometer, the Infrared Laboratories liquid helium bolometer and the movable table, the optical system and the transmission probe.

---

## 3 Experimental Setup

As explained in the previous chapter, FTIR magneto-spectroscopy is a powerful spectroscopic technique used to investigate many important effects in materials, e.g., electron spin resonance, cyclotron resonance, and transitions between Landau levels (LLs). Despite their enormous potential in material science, infrared magneto-spectrometers are still relatively rare and custom-made since such systems generally require complex infrastructure. In this chapter, we describe the design and implementation of a versatile broadband setup for FTIR magneto-spectroscopy, spanning the range from THz/FIR to NIR,  $50 - 10,000 \text{ cm}^{-1}$  ( $200 - 1 \mu\text{m}$ ,  $6.2 - 1,240 \text{ meV}$ ,  $1.5 - 300 \text{ THz}$ ), high magnetic field up to 16 T, and cryogenic temperatures down to 2 K. Our FTIR magneto-spectroscopic setup, shown in Fig. 3.1, is based on a commercially available FTIR spectrometer Bruker Vertex 80v (Bruker Corporation, Billerica, USA) and a 16 T cryogen-free

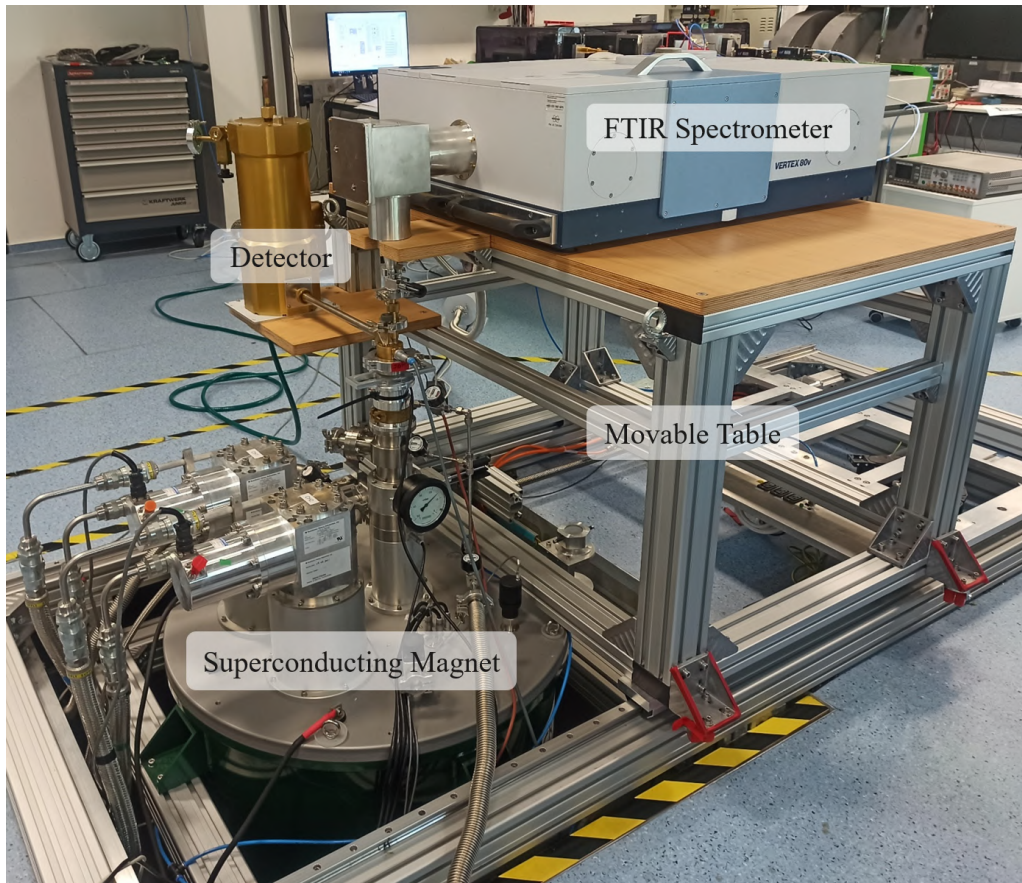


Fig. 3.1: Photograph of the FTIR magneto-spectroscopic setup at the Central European Institute of Technology of the Brno University of Technology (CEITEC BUT). The setup is in the configuration with Probe A and 1.6 K standard bolometer system.

superconducting magnet (Cryogenic Ltd., London, UK). We constructed custom-designed optics that couple the spectrometer to the superconducting magnet. It consists of optical coupling and transmission probes (A and B) designed for magneto-optical measurements with multiple detectors. Using various detectors, the setup spans the entire IR and partially the THz range. This aspect is particularly important because it enables the measurement of different types of samples from SMMs in the FIR region to germanium in the NIR region, as demonstrated in the chapter of magneto-optical measurements. Another novelty of the setup lies in the usage of a cryogen-free superconducting magnet. Additionally, the setup includes a home-built movable table on which the FTIR spectrometer, the optical coupling, and the detectors are placed.

## 3.1 Beam Propagation

The schematic of the FTIR magneto-spectroscopic setup in Fig. 3.2 shows the beam propagation through the setup in two configurations of detector placement. The beam originates in the spectrometer's source and passes through the aperture (APT = 8 mm) and beamsplitter (BMS) of the Michelson interferometer. Then, the parallel beam is guided out through an output of the spectrometer (OUT 2) to the optical coupling, in which the parallel beam from the spectrometer is reflected from the parabolic mirror at 90° and focused to its focal point located in a gate valve. When the gate valve is closed, the spectrometer and the optical coupling are evacuated to about 2 mbar pressure. The rough vacuum reaches the probe's window when the transmission probe is connected, and the gate valve is opened. After inserting the transmission probe through an airlock into a variable temperature insert (VTI) of the superconducting magnet, helium gas fills the probe. The windows in the setup, made of 35 μm thick mylar foil, keep the helium gas inside the probe and separate it from the optical coupling and surrounding environment. Two transmission probes can be attached to the optical coupling:

- a) **Probe A:** In this configuration, the detector (D) is placed outside the magnet, see Fig. 3.2(a). The beam enters the first tube and passes through the window (W). Then, it is transmitted through a sample (S) located approximately in the center of the magnetic field. At the bottom of the probe, the transmitted beam is reflected by two 90° flat mirrors (M) and propagates up through a second tube. At the end of the second tube, another 90° flat mirror (M) is located, which reflects it to a third, horizontal, tube. At the end of this tube, the beam passes through another window and goes to the detector (D).
- b) **Probe B:** In this configuration, the detector (D) is placed inside the supercon-

ducting magnet, see Fig. 3.2(b). The beam enters the tube by passing through the window (W) and propagates to a sample (S) located in the center of the magnetic field. The transmitted beam from the sample (S) goes to the detector (D) placed below the sample.

More details on probe A and probe B will be described in the following section.

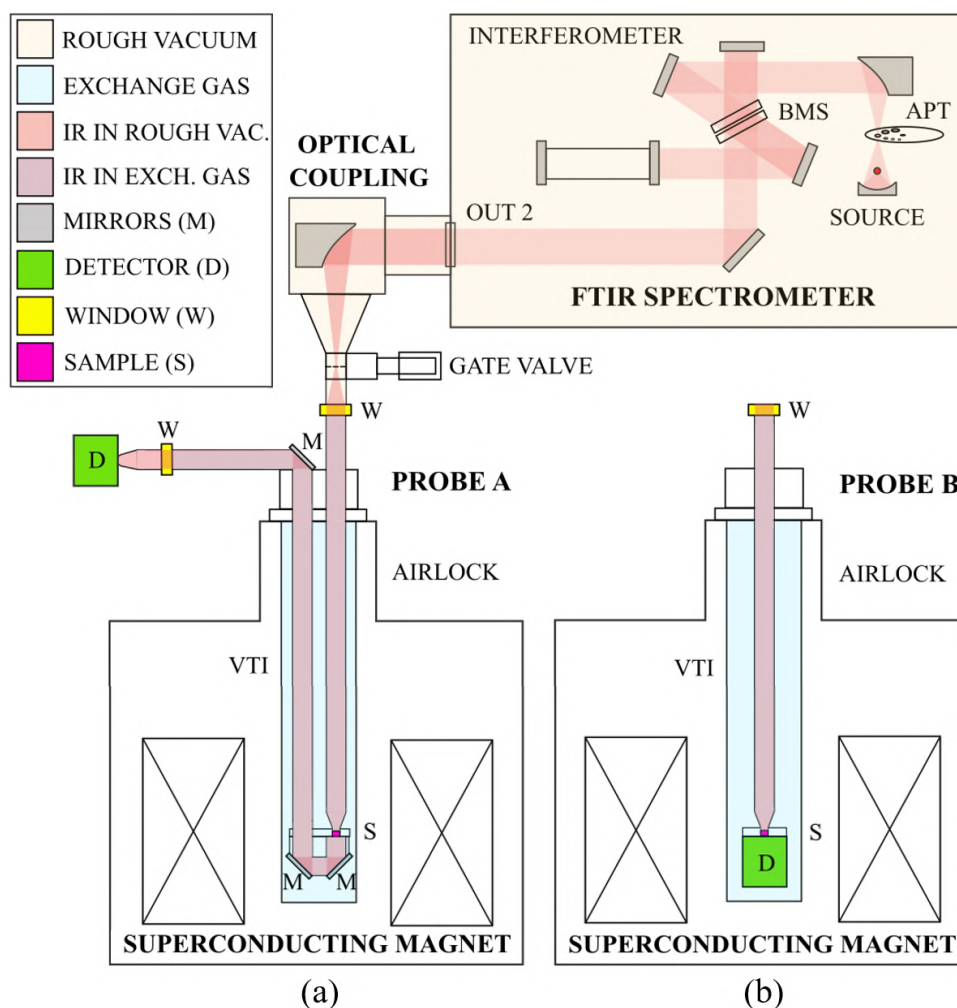


Fig. 3.2: The schematic of the FTIR magneto-spectroscopic setup shows the beam propagation through the setup in two configurations of the detector location. (a) Probe A, inserted into the superconducting magnet, is designed for the detector located outside the magnet, and (b) Probe B is designed for the detector located inside the magnet. (VTI in the figure stands for variable temperature insert, BMS stands for beamsplitter, and APT stands for aperture.)

## 3.2 Setup Design and Components

When designing the custom-designed parts of the setup, the emphasis was to ensure that all components were made from non-magnetic materials, i.e., brass, bronze, aluminum, and non-magnetic stainless steel (316L), to avoid possible complications from strong forces caused by stray fields of the magnet. Another criterion for material choice was the suitability for cryogenic temperatures. The setup's components are sealed with o-rings ensuring rough vacuum conditions.

### 3.2.1 FTIR Spectrometer

The essential component for performing FTIR magneto-spectroscopy is the FTIR spectrometer. Our experimental setup utilizes a FTIR spectrometer Bruker Vertex 80v [178] designed for spectroscopic measurements under vacuum conditions. It is supplied with an oil-free scroll vacuum pump. It has an aperture wheel which allow 12 aperture settings from 0.25 mm to 8 mm. The settings and measurements are controlled by spectroscopic software OPUS 7 [179]. Standard configuration provides apodized spectral resolution of better than  $0.2 \text{ cm}^{-1}$ . The spectrometer is currently equipped with:

- **Sources:** standard MIR source (Globar), and NIR source (tungsten halogen lamp).
- **Beamsplitters (BMS):**  $\text{CaF}_2$  for NIR range ( $1,200 - 15,000 \text{ cm}^{-1}$ ), standard KBr for MIR range ( $350 - 8,000 \text{ cm}^{-1}$ ), Mylar Multilayer for FIR range ( $30 - 680 \text{ cm}^{-1}$ ). Their efficiency as a function of spectral range is shown in Fig. 3.3.
- **Detectors:** There are standard detectors operating at room temperatures supplied together with the spectrometer: NIR InGaAs ( $4,000 - 12,800 \text{ cm}^{-1}$ ), MIR-DTGS ( $250 - 12,000 \text{ cm}^{-1}$ ), FIR-DTGS ( $10 - 700 \text{ cm}^{-1}$ ).

There is a possibility to use detectors operating at low temperatures, which were purchased additionally and can be connected to the spectrometer: a pumped LHe-cooled 1.6 K standard bolometer system [181] (Infrared Laboratories, Tuscon, USA) for the FIR range ( $5 - 670 \text{ cm}^{-1}$ ), and a 4.2 K sealed general purpose bolometer with 3 mm diamond absorber (Infrared Laboratories, Tuscon, USA) for FIR, MIR and NIR ranges ( $10 - 2,000 \text{ cm}^{-1}$ )<sup>1</sup>, which is designed to operate inside the superconducting magnet. A list of all available detectors for our setup with their specifications, such as spectral range and sensitivity, is shown in Tab. 3.1.

---

<sup>1</sup>This range of the bolometer was provided by the manufacturer, but the bolometer worked far above this range.

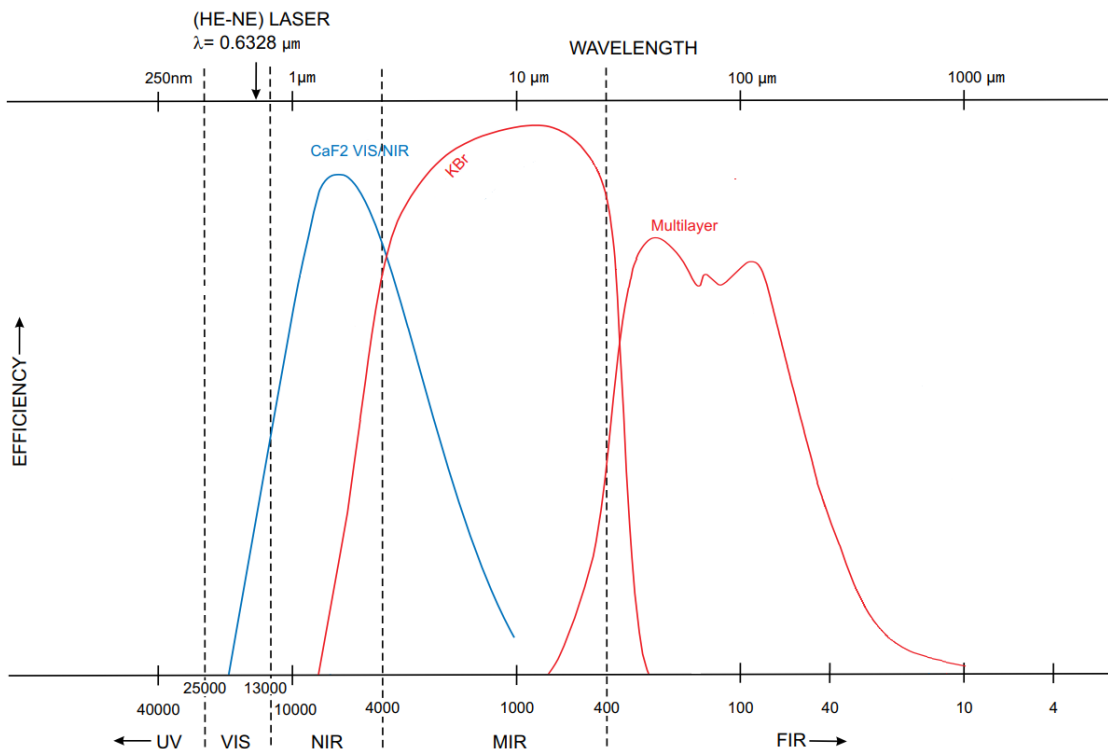


Fig. 3.3: Figure showing the efficiency of the beamsplitters available in our setup as a function of spectral range. Adapted from [180].

Detector	Spectral Range	Sensitivity
NIR-InGaAs (Room Temp.)	4,000 – 12,800 $\text{cm}^{-1}$	NEP: $< 2 \times 10^{-13} \text{ W/Hz}^{1/2}$
MIR-DTGS (Room Temp.)	250 – 12,000 $\text{cm}^{-1}$	$D^* > 4 \times 10^8 \text{ cm} \cdot \text{Hz}^{1/2} \text{ W}^{-1}$
FIR-DTGS (Room Temp.)	10 – 700 $\text{cm}^{-1}$	$D^* > 4 \times 10^8 \text{ cm} \cdot \text{Hz}^{1/2} \text{ W}^{-1}$
1.6 K Standard Bolometer (LHe)	5 – 670 $\text{cm}^{-1}$	NEP $\sim 1.87 \times 10^{-14} \text{ W/Hz}^{1/2}$
4.2 K Sealed Bolometer (LHe)	10 – 2,000 $\text{cm}^{-1}$	NEP $\sim 2.37 \times 10^{-13} \text{ W/Hz}^{1/2}$

Tab. 3.1: A table of all available detectors with their specifications such as spectral range and sensitivity.

Concerning the beam path inside the spectrometer, the schematic of the standard configuration of the FTIR spectrometer is shown in Fig. 3.4(a), and the schematic of the configuration for the FTIR magneto-spectroscopic setup, where the beam is guided out of the spectrometer through the output labeled as OUT 2 is depicted in Fig. 3.4(b). The spectrometer also has several input ports labeled as IN1/2 in Fig. 3.4, which can be used for connecting external sources such as FIR water-cooled mercury lamp that can potentially be connected to our setup in the future.

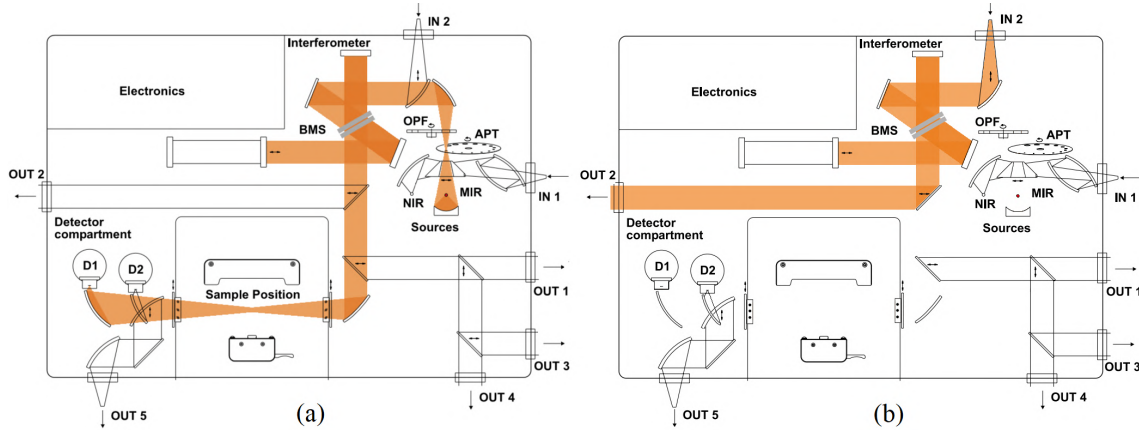


Fig. 3.4: (a) The scheme of the standard configuration of the FTIR spectrometer. (b) The schematic of the configuration for the FTIR magneto-spectroscopic setup, where the beam is guided out of the spectrometer through the OUT 2. Adapted from [182].

### 3.2.2 Superconductive Magnet

A cryogen-free superconducting magnet is a primary choice for research facilities without cryogenics infrastructure. Our setup utilizes 16 T cryogen-free superconducting solenoid magnet from Cryogenic Ltd. [183] equipped with two pulse cryocoolers and integrated variable temperature insert (VTI) with  $\varnothing 50$  mm sample space, which enables control of the temperature inside the magnet between  $T = 1.8\text{--}320$  K. The VTI incorporates a home-built airlock port for probe insertion, avoiding contamination of the closed-cycle helium environment by pumping and flushing the probe space before sliding into the operation position through the opened VTI valve [184].

The operation of the VTI system can be understood by reference to Fig. 3.5 and the description that follows. Cooling of the VTI and sample is provided by the circulation of helium in a closed circuit. The helium gas is cooled by the cryocoolers at the 40 K and 4 K stages, and then it is cooled further via expansion after the needle valve. The helium gas is stored in the “dump” vessel at room temperature. The “dry” oil-free pump drives the circulation of the helium gas (the pump must be turned on before circulation can begin). The helium gas passes out of the dump into the VTI circuit through the helium gas inlet. The gas first passes through a charcoal filter removing all impurities within the gas. Then, it flows through the first stage heat exchanger which cools the gas to 40 K. This gas then passes to the second stage of the cryo-cooler where it is cooled further to below 4.2 K and condenses in the helium pot. The liquid helium then flows through the needle valve, after which it expands and cools further to approximately 2 K. Then, it travels through

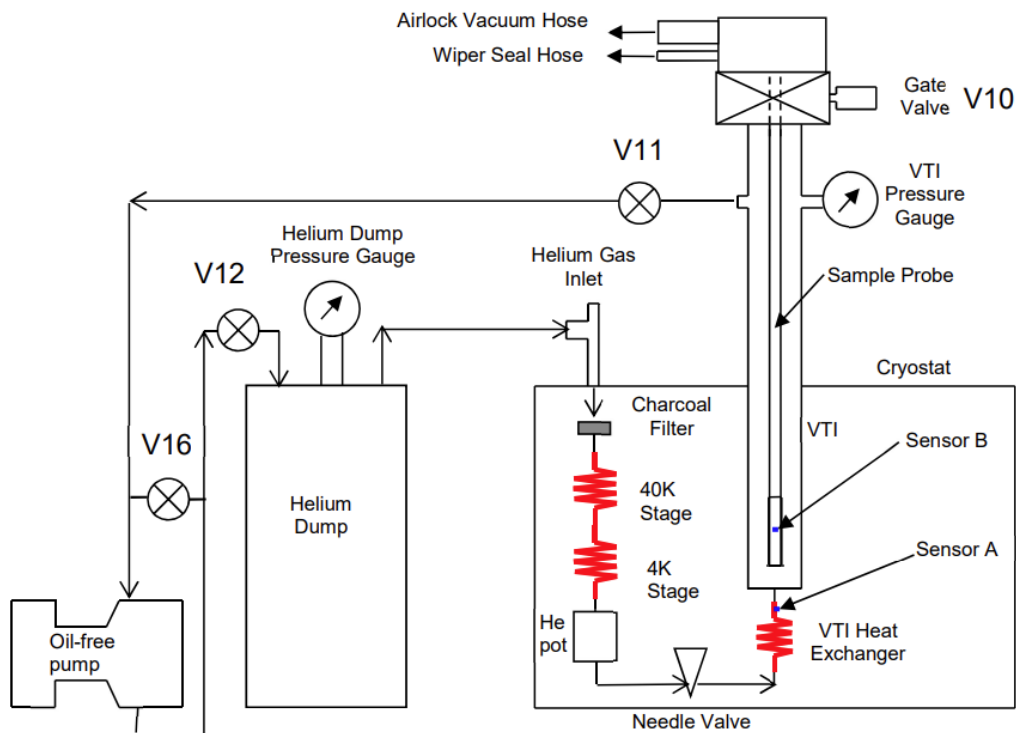


Fig. 3.5: Schematic diagram of VTI cooling circuit.

an annular tube around the sample chamber called the VTI heat exchanger. The helium gas flows up past the coil set to the top of the VTI where it exits and travels back to the pump and dump. The needle valve is set manually and needs only occasional adjustment. A dial gauge is fitted to allow the user to set and monitor the flow rate (directly related to pressure). A pressure between 5 and 15 mbar is recommended, the optimum value is specific to each system. The heat exchanger at the bottom of the VTI is fitted with a cernox<sup>TM</sup> thermometer (sensor A) and a heater controlled using the temperature controller. The heater is used to adjust the temperature of the helium gas and therefore regulate the sample temperature. We do not have calibrated magnetic field sensor in the setup yet, so the magnetic field is not calibrated. We use the conversion of the current to the magnetic field provided by Cryogenic Ltd. (magnetic field constant is 1409.1 G/A). The axial homogeneity of the magnet provided by Cryogenic Ltd. is of the order of 10 mG (0.001 mT) at 1409.1 G within the distance up to 5 mm from the center of the magnetic field.

### 3.2.3 Optical Coupling

The optical coupling (see Fig. 3.6) is designed to reflect the parallel beam from the spectrometer using a parabolic mirror and focus it to the transmission probe inserted

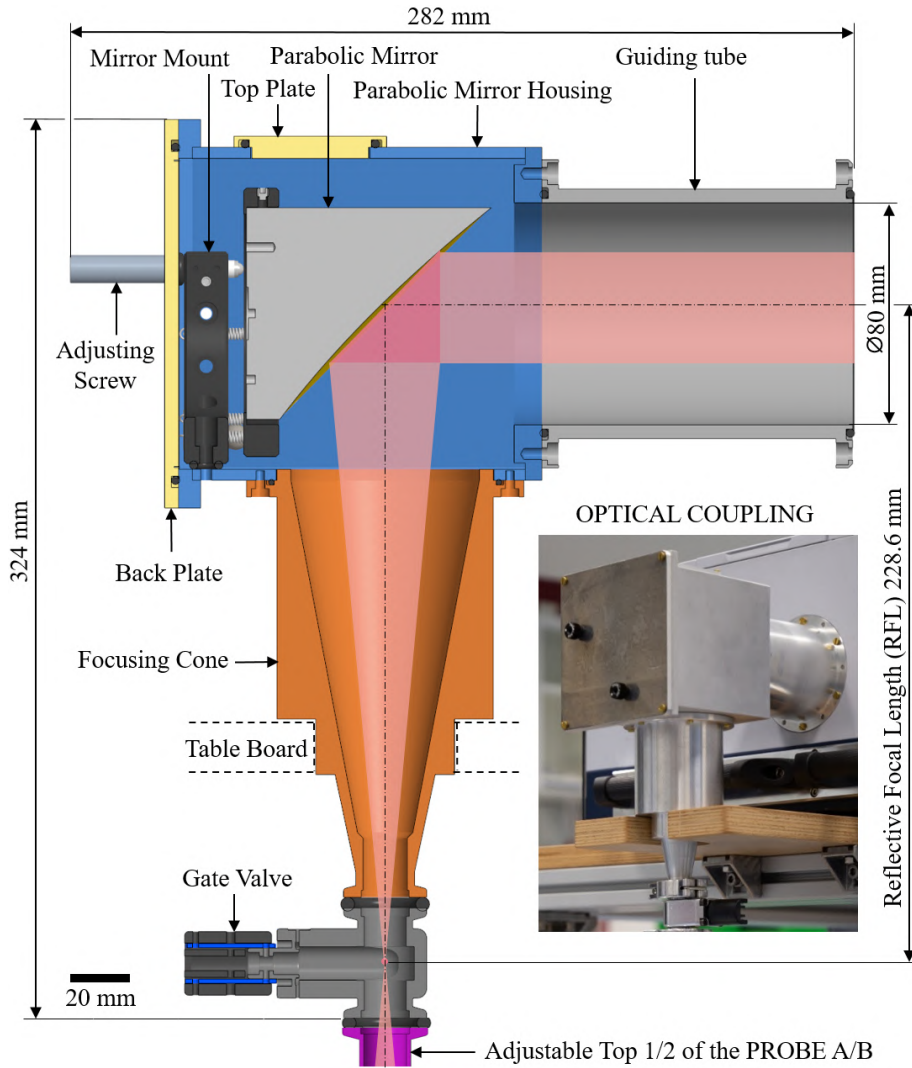


Fig. 3.6: The scheme of the optical coupling design. The optical coupling reflects the parallel beam from the spectrometer using a parabolic mirror and focuses it to Probe A or B inserted into the superconducting magnet.

into the superconducting magnet. Its main purpose is to enable proper alignment of the parabolic mirror to ensure effective coupling of the probes. The optical coupling consists of a guiding tube that is connected to the output (OUT 2) of the spectrometer displayed in Fig. 3.4, a parabolic mirror housing, a focusing cone mounted on the bottom of the housing, and a gate valve VATLOCK [185] (VAT group AG, Haag, Switzerland) with inner diameter  $\varnothing 15.1$  mm with a manual actuator. Inside the parabolic mirror housing, a precision kinematic mirror mount (Thorlabs, Newton, NJ, USA) is mounted. The mirror mount holds  $\varnothing 76.2$  mm  $90^\circ$  off-axis gold-coated parabolic mirror with RFL = 228.6 mm [186] (Thorlabs, Newton, NJ, USA). The parabolic mirror is aligned by two adjusting screws and through the opening covered by a top plate. A back plate serves to mount/dismount the parabolic mirror and the

mirror mount. The parabolic mirror reflects the beam by  $90^\circ$  and focuses it at its focus point designed to be in the middle of the gate valve. The gate valve, mounted on the end of the focusing cone, separates the optical coupling from the probe A/B connected to the coupling by an adjustable top 1 or 2. When it is opened, the space till the window at the top of the probe is pumped to a rough vacuum (2 mbar) by the spectrometer's scroll pump to reduce radiation losses caused by absorption in water vapor.

### 3.2.4 Transmission Probes

Transmission probes incorporate waveguides, in other words, or light pipes, which are tubes guiding the beam through a sample (reference) placed in the magnetic field to the detector. To reach stable cryogenic temperatures at a sample, it is necessary to reduce the heat flow from the top of the probe, which is at room temperature, to the probe tubes and a sample located inside the cryogenic helium environment. Therefore, the tubes in our setup are made of non-magnetic stainless steel (316L) due to its relatively low thermal conductivity compared with other materials traditionally used for waveguides, e.g., Nickel silver. These tubes were additionally polished inside to improve the reflectivity (to improve reflectivity even more, it is possible to coat the tubes internally with a gold layer in the future). The tubes of inner diameter 15 mm were chosen to fit two tubes side by side into the VTI with the maximal possible diameter based on the assumption that there are fewer reflections in the larger diameter tubes and thus fewer losses. Due to limited possibilities to change the dimensions of the setup, we did not use any strategies to avoid standing waves (e.g., quasi-optical systems). We rely on the fact that the influence of standing waves in the spectra is diminished by the normalization of the spectra.

#### a) Probe A - External Detection Probe

Probe A (see Fig. 3.7) is connected to the gate valve flange by an adjustable top 1 which consists of two tubes sliding in each other to adjust the suitable height (center of the magnetic field at a sample). A window mount 1 is located below, where a window (mylar foil) is sealed by two o-rings. The thickness of the window can be up to 5 mm. Probe A consists of three non-magnetic stainless steel tubes/waveguides (probe tubes 1, 2, 3) attached to a probe head, which is hermetically connected to a non-magnetic stainless steel cover tube 1. The cover tube 1 secures the smooth loading of the probe into the airlock and the VTI. The probe head has two openings on the sides designed for connectors. There is one 11-pin connector DBEE104A056-130 (Fischer Connectors, Saint-Prex, Switzerland) used for connecting the temperature sensor (T-sensor) Cernox CX 1050 HT (LakeShore Cryotronics Inc., Westerville,

USA) by Quad-Lead<sup>TM</sup> cryogenic wire 36 AWG (LakeShore Cryotronics Inc., USA). Probe tubes 1 and 2 are centered by five copper baffles that provide a lower heat transfer along the probe. The copper baffles are mounted to the brass rings attached to the probe tubes by hard soldering. On the end of probe tube 1, a polished brass sample cone focusing the beam onto a sample is attached. The sample is placed in one of two slots of a sample holder. Another opening is left empty to provide a measurement of a reference. The sample is in the Faraday configuration (i.e., in transmission mode, with the magnetic field parallel to the wave vector of the irradiation beam) and its vertical position is designed to be in the center of the magnetic field. Horizontally, the sample is 10 mm shifted from the center of the magnetic field due to the two-tube design (the field offset at this position is 0.037 mT compared to the center of the field). A sample can be a pressed powder pellet with  $\varnothing 5$  mm or a wafer sample up to 8 mm in diameter that is fixed in the sample holder by its counterpart. The temperature sensor is mounted on the side of the sample holder, close to the sample. The shape of the sample holder is designed to provide precise switching between a sample and a reference by its sliding on a holder plate. On one side, a removable pin mounted to the holder plate is slotted to the sample holder to secure one extreme position, and the second extreme position is secured by probe tube 2, shown in Probe A inset in Fig. 4. Rotation of the sample holder is enabled by a brass rod mounted to the sample holder. A rod knob above the probe head is used to rotate the rod manually. After the beam passes through the sample/reference, it is guided by a mirror mount 1 with two 90° flat mirrors covered with a polished silver layer. They reflect the transmitted beam and guide it up to probe tube 2. Then, the beam is led by the probe tube 2 to another 90° flat mirror mounted onto a mirror mount 2. The beam guided by the mirror mount 2 propagates to a horizontal probe tube 3 towards the detector. On the end of the probe tube 3, window mount 2 seals a window 2 (mylar foil or other up to 5 mm) with an o-ring. When the room temperature detectors (InGaAs, MIR-DTGS, FIR-DTGS) are used, a Winston cone (Infrared Laboratories, Tuscon, USA) that concentrates the beam to a small spot, is attached to the end of the window mount 2. In the case of the LHe-cooled standard 1.6 K bolometer system, there is no need to use this cone since one is already incorporated into the bolometer's dewar.

The main advantage of the Probe A configuration, when the detector is placed externally (outside of the magnet), is that the temperature at a sample in the VTI can be varied (useful e.g., for materials with a phase transition). Moreover, the detectors are in this configuration further from the magnet, so measurements of the reference are unnecessary since the high magnetic fields do not influence the sensitivity of detectors. On the other side, when using LHe cooled 1.6 K standard bolometer system, regular filling of the bolometer's dewar with LHe is necessary

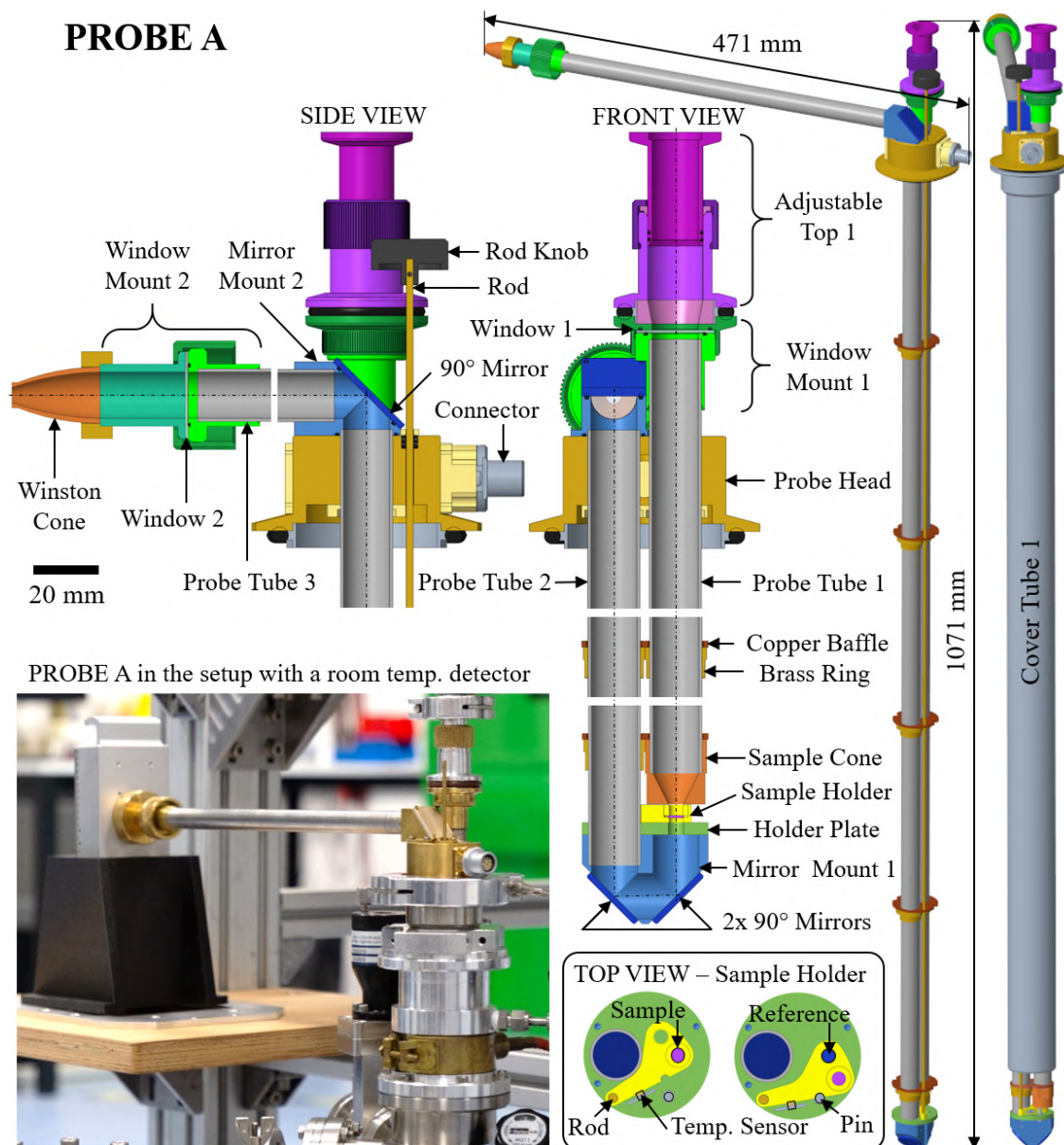


Fig. 3.7: The scheme of Probe A - External Detection Probe design with its cross-section, side views, and top view on the sample holder. This transmission probe is used as waveguides guiding the beam through a sample/reference in the magnetic field to the detector placed outside the magnet. The photograph inset displays the top parts of Probe A.

for its operation. Also, since the end of the window mount 2/winston cone is not hermetically connected to the detector, the beam is going through the air a few centimeters, which causes absorption in water vapor in FIR spectra. The absorption in water vapor can be reduced by flowing nitrogen gas into this area. Another disadvantage is that the signal at the detector is lower due to losses caused by the

relatively long optical path (approx. 2.5 meters) of the beam propagating through the probe tubes. Also, the sample is not entirely in the horizontal center of the magnetic field, as the probe consists of two probe tubes.

### **b) Probe B - Internal Detection Probe**

Probe B (see Fig. 3.8) is connected to the gate valve of the optical coupling by an adjustable top 2. Below, a window screw seals a mylar foil window with two o-rings. Probe B consists of one non-magnetic stainless steel tube/waveguide, a probe tube, attached to a probe head, which is connected to the cover tube 2 with a side port designed for inserting a piezo motor mount with a piezo step-motor LEGS Rotary LR23-50 (PiezoMotor Uppsala AB, Uppsala, Sweden). The piezo step-motor serves for automatic switching between a sample and a reference by rotation of a bronze rod mounted to a sample holder. The probe head has four openings on the sides designed for connectors. There is one 11-pin connector (DBEE104A056-130) for connecting the temperature sensor Cernox CX 1050 HT (by Quad-Lead<sup>TM</sup> cryogenic wire 36 AWG), and heater (four 25  $\Omega$  resistors in series connected by a copper wire), and one 4-pin connector SFE 102 A053-130 (Fischer Connectors, Saint-Prex, Switzerland) for connecting the sealed 4.2 K General Purpose Bolometer (Infrared Laboratories, Tuscon, USA) by Quad-Lead<sup>TM</sup> cryogenic wire 36 AWG. All wires are placed inside two wire tubes mounted along the probe tube. The temperature sensor and the heater are both mounted on the body of the sealed bolometer. The probe tube is centered by four copper baffles mounted to brass rings hard-soldered to the tube. On the bottom of the probe tube, a brass tube is mounted. Four pins with thread endings are inserted into the bottom of the brass tube and anchored in a holder plate. A Winston cone (Infrared Laboratories, Tuscon, USA) is mounted on the bottom of the brass tube. A sample holder with three slots for the samples/reference is placed under the Winston cone. The sample is again in the Faraday configuration, and its horizontal and vertical positions are designed to be in the center of the magnetic field. It can be  $\varnothing$ 5 mm pressed powder pellet or wafer sample up to 8 mm in diameter, fixed in the sample holder with its counterpart. The shape of the sample holder is designed to provide precise switching between a sample and a reference. On both sides, two pins are slotted to the sample holder to secure extreme positions. The sample holder slides on the holder plate to which the sealed bolometer is mounted. After the beam passes through the sample/reference, it is guided by a Winston cone already incorporated in the sealed bolometer to its sensitive element. At the bottom of the sealed bolometer are three pins for the bias, signal, and ground. The wires from these pins go to the 4-pin connector on the probe head. The ground wire is connected to the connector's frame, the bias wire goes to a bias box with two 9 V batteries, and

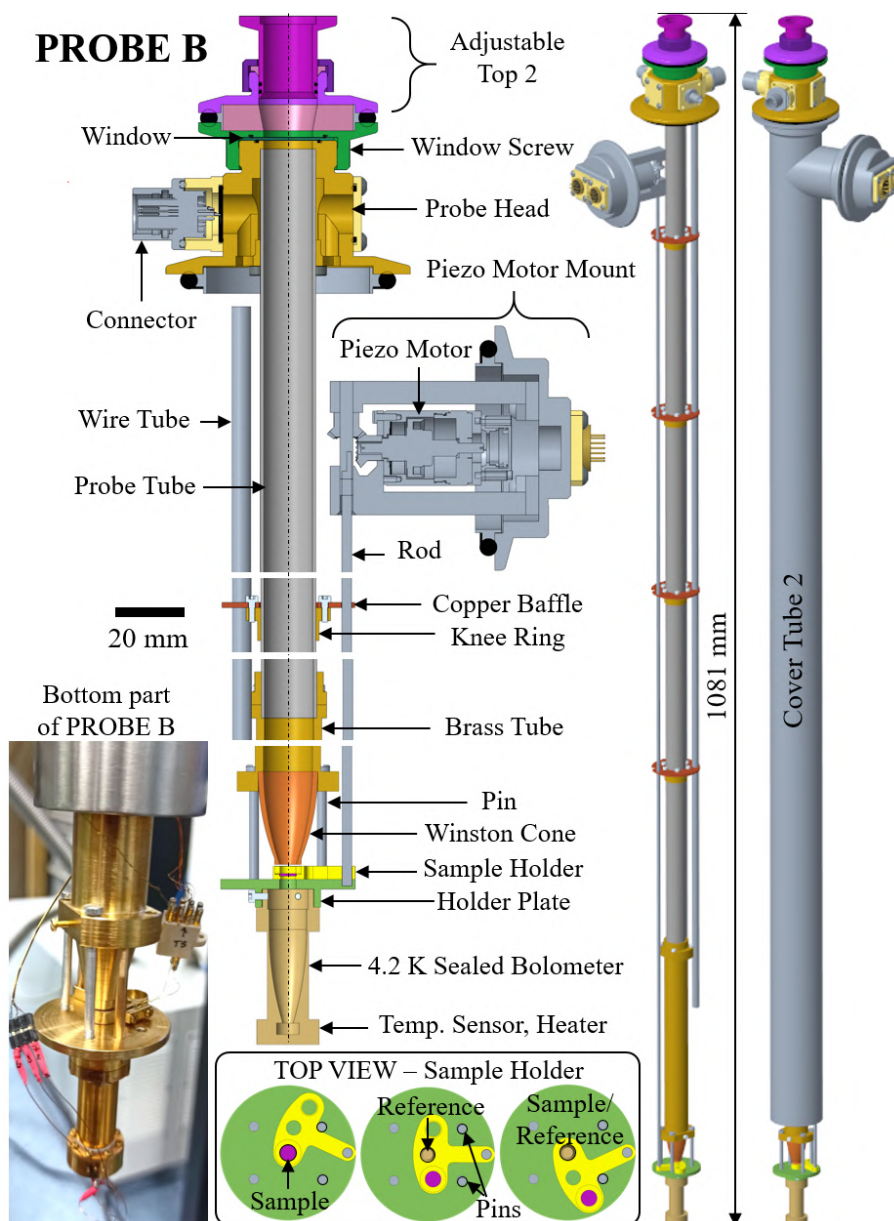


Fig. 3.8: The scheme of Probe B - Internal Detection Probe design with its cross-section, side views, and top view on the sample holder. This transmission probe is used as waveguides guiding the beam through a sample/reference in the magnetic field to the detector placed inside the superconducting magnet. The photograph inset displays the bottom parts of Probe B.

the signal wire is connected to the input of a 200 MHz High Input Impedance Voltage Amplifier HVA-200M-40-F (FEMTO<sup>®</sup> Messtechnik GmbH, Berlin, Germany). The output of the amplifier is connected to an A/D converter (Bruker Corporation, Billerica, USA) connected to the spectrometer.

A significant advantage of the Probe B configuration, when the detector is pla-

ced inside the magnet, is that we can use the LHe from the closed-cycle system used in the VTI for the operation of the sealed bolometer. Moreover, the signal at the detector is stronger due to lower losses of the beam since the optical path (approx. 1 meter) is shorter than in Probe A. Additionally, by attaching the chip sample holder [187, 188] instead of the sealed bolometer, probe B can be used for testing graphene bolometer devices [189] – [191]. However, the vibrations from the closed-cycle system might negatively influence the quality of the spectra. Another disadvantage is that since the operational temperature of the bolometer is 4.2 K, it is impossible to change the temperature on the sample and make temperature-dependent measurements. Also, the sealed bolometer is nearly in the center of the magnetic field (approx. 5 cm under the center of the magnetic field), so the reference measurements are needed due to the influence of the high magnetic field on the bolometer’s sensitivity.

### c) Probe B - Chipset Probe

Probe B - Chipset (see Fig. 3.9) is created from Probe B by attaching the chip sample holder [187] instead of the sealed bolometer and replacing a few other parts. It is connected to the gate valve of the optical coupling by an adjustable top 3. The window, window screw, probe tube, wire tubes, copper baffles, and knee rings stay the same as in Probe B. However, no piezo motor is used in this probe, and the probe head is, therefore, hermetically connected to the cover tube 1 instead of cover tube 2. This probe utilizes the same 11-pin connector for connecting the temperature sensor and heater, and an additional 16-pin connector (SFE 104 A086-130) (Fischer Connectors, Saint-Prex, Switzerland) mounted to the probe head for connecting the graphene bolometer device in the chipset by Duo-Twist<sup>TM</sup> cryogenic wire 36 AWG (LakeShore Cryotronics Inc., USA). The temperature sensor and the heater are both incorporated inside the chipset holder. Unlike Probe B, this probe has a polished focusing taper made of brass mounted on the end of the probe tube. To the focusing taper, an extension tube is connected to which a chipset holder is attached by 4 screws. The chipset holder, which contains graphene bolometric devices placed on a chip expander, was designed by Adam Lagiñ [188], [187]. A detailed view of the chipset holder with its main parts is shown in Fig. 3.10. The placement of the chip inside the chipset holder is in the Faraday configuration, and its horizontal and vertical positions are designed to be in the center of the magnetic field.

This probe will be used for testing and measurements of these graphene bolometric devices developed by Abdel El Fatimy [189]. These bolometric detectors, based on graphene quantum dot shown in Fig. 3.11, exhibit exceptionally high responsivity, combined with an extremely low electrical NEP= $2 \times 10^{-16}$  W/Hz<sup>1/2</sup> at 2.5 K),

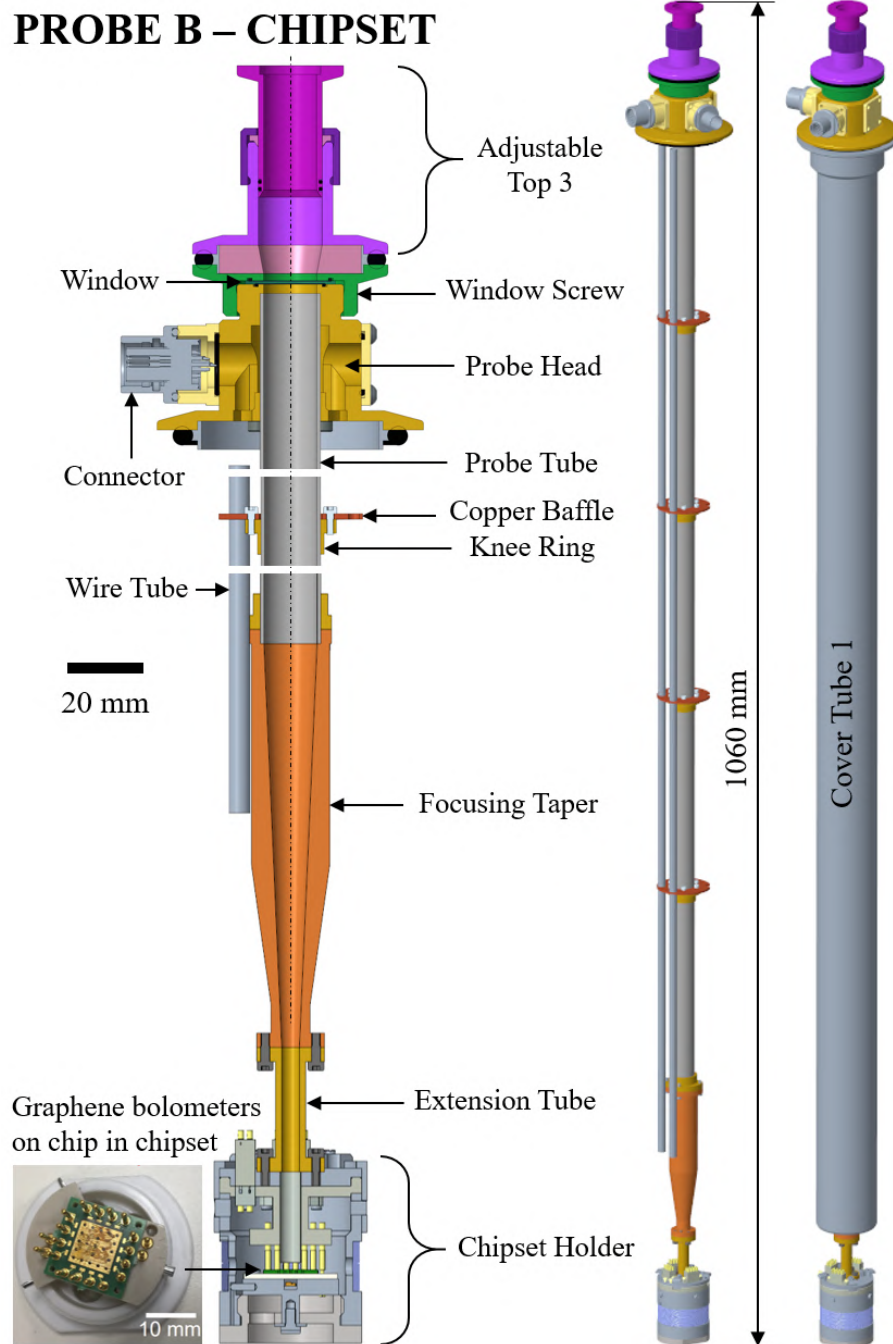


Fig. 3.9: The scheme of Probe B - Chipset Probe design with its cross-section and side views. This probe is used as a waveguide guiding the beam onto the graphene bolometric devices on the chip of the chipset holder placed inside the superconducting magnet. The photograph inset displays the graphene bolometers on the chip in the chipset.

which places them above commercial cooled bolometers [189] – [191]. The primary goals of the measurements include testing the bolometer’s response to external radiation as a function of the magnetic field, the intensity of illumination, bias voltage (inducing dc current through the device and responsible for device heating), lateral sensitivity of devices, as well as spectral functions of devices.

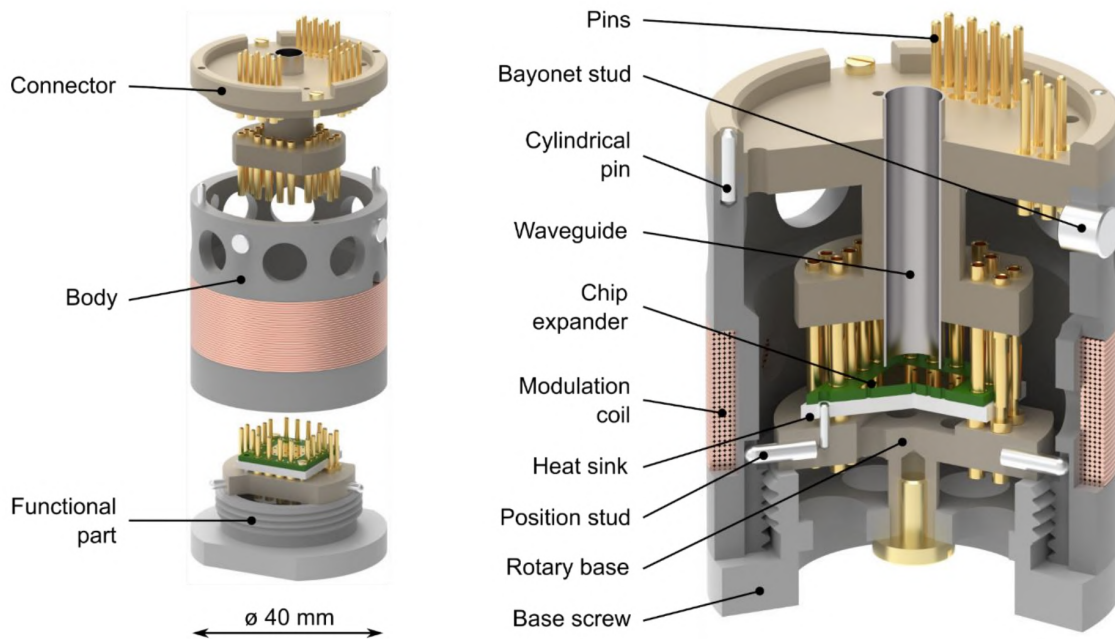


Fig. 3.10: The scheme of the chipset holder design. Taken from [188].

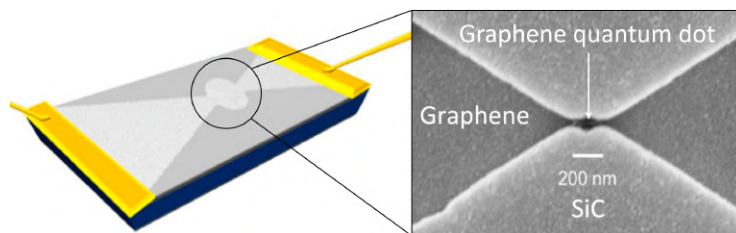


Fig. 3.11: Graphene bolometer device based on the graphene quantum dot. Adapted from [188].

### 3.2.5 Movable Table

The movable table, shown in Fig. 3.1, was designed in order to provide easy transfer of the spectrometer with its accessories to the superconducting magnet and its frame. The table is made of aluminum profiles (Bosch Rexroth AG, Lohr am Main, Germany), four  $\varnothing 50$  mm double swivel wheels with polyurethane coating (Elesa+Ganter CZ, s.r.o., Prague, Czech Republic), and three 25 mm thick multiplex wooden boards, one for the spectrometer, the second one for the support of the optical coupling, and the third one for placing the detector in Probe A configuration. The movable table secures a simple transfer of the setup and its precise alignment thanks to its compatibility with the magnet frame equipped with linear guide rails, servomotors, and trapezoidal screws for an automatically driven motion, which was initially designed by Ing. Antonín Sojka, Ph.D. for the broadband HFEPR spectrometer based on THz rapid frequency scans (THz-FRaScan-EPR) [184], [187], [192].

## 3.3 Technological Methods

Since the topic of this thesis deals with the FTIR magneto-spectroscopy method itself, all methods used in the thesis are related to the development of the FTIR magneto-spectroscopic setup. Concerning the design of the setup, 3D designs, models and drawings were created in two computer-aided design (CAD) software: Autodesk Inventor Professional 2019 and PTC CREO Parametric 6. The designed parts were manufactured by Dominik Varga at the CEITEC Nano Research Infrastructure workshop. Furthermore, several methods used for manufacturing and assembling the setup (3D printing and soldering) and optimizing its signal/performance (polishing and silver plating) are worth mentioning and describing.

### 3.3.1 3D Printing

3D printing, also referred to as additive manufacturing (AM), is a process of making three-dimensional objects from a digital file, usually, a 3D computer model created in CAD software. 3D printed object is created using additive processes by laying down successive layers (layer by layer) of material until the object is complete. One of the key advantages of 3D printing is the ability to produce very complex shapes or customized geometries (with minimal waste) that would otherwise be difficult or impossible to construct by hand, including hollow parts or parts with internal lattice structures to reduce weight. Due to the limited mechanical properties, 3D printing techniques are used mainly for producing conceptual, functional, or aesthetic prototypes rather than functional components. However, the development in the

precision, repeatability and material range of 3D printing have reached the point that some 3D printing processes are today used as an industrial-production technology. There are various 3D printing techniques, but the most common nowadays is fused deposition modeling (FDM), employing a filament of a thermoplastic material, such as polylactic acid (PLA), acrylonitrile butadiene styrene (ABS), or polyamide (PA) [193].

Some parts of the setup not exposed to cryogenic temperatures during their use, such as the room temperature detector holder and the rod knob shown in Fig. 3.12(a) and (b), respectively, were manufactured using an FDM 3D printing method due to their complex shape problematic for manufacturing in the workshop. They were printed with PLA filament using the 3D printer from TRILAB company. Firstly, we created a 3D model of the given part in CAD software and saved it as an STL (Surface Tessellation Language) file. Then, we opened the STL file in the Deltiq Kisslicer program, where the mesh data were further sliced into a file of 2D layers. Finally, we transferred the file containing 2D layers to the 3D printer and launched printing.

### 3.3.2 Soldering

Soldering is a process of joining two or more metal objects by melting and putting a filler metal (solder) into the joint, the solder having a lower melting point than the adjoining metal. Unlike welding, soldering does not involve melting the work pieces. There are two basic types of soldering, soft and hard soldering. Soft soldering utilizes solders with a lower melting point up to 450°C. They are usually based on tin-lead alloys. Because of the low temperatures in soft soldering, it does not make strong joints and is, therefore, unsuitable for mechanical load-bearing or high-temperature applications. It is commonly used in the electronics industry to form electrical connections. Hard soldering requires higher temperatures to melt the solder material, usually silver or brass alloys, with a melting temperature above 450°C. It creates a stronger mechanical bond compared to soft soldering [194].

In our setup, we used soft soldering for contacting the temperature sensor wires into the connectors. When assembling the probes, we also used hard soldering with an alloy containing silver because we needed to create a strong joint of two different metals (brass knee rings onto stainless steel probe tubes). It required a heat gun and a blowtorch, shown in Fig. 3.12(c), to achieve the temperatures at which the solder melts.

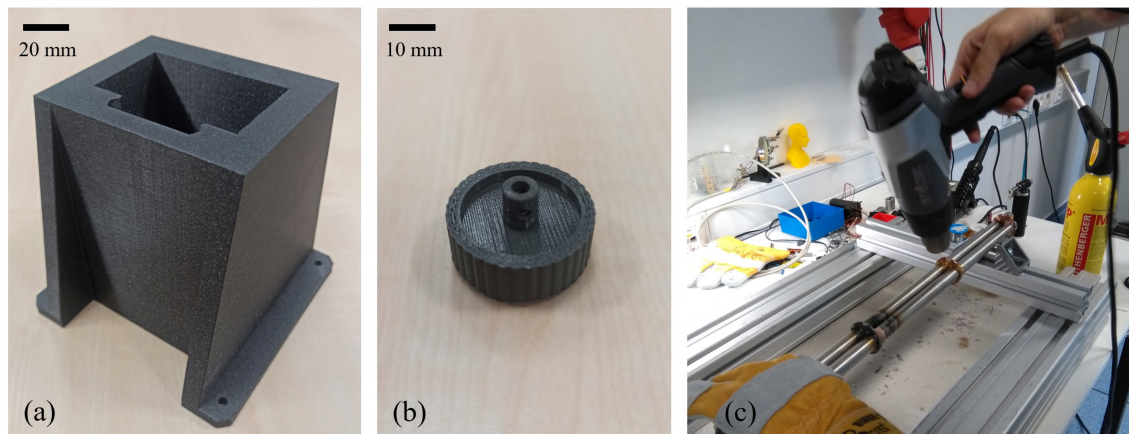


Fig. 3.12: (a) Room temperature detector holder, and (b) rod knob 3D printed by PLA filament on TRILAB 3D printer. (c) The process of hard soldering of the brass rings to the stainless steel probe tubes.

### 3.3.3 Polishing

Polishing is a process of creating a smooth and shiny surface by rubbing it or applying a chemical treatment, leaving a clean surface with a significant specular reflection. Polishing can also reduce diffuse reflection<sup>2</sup> to minimal values in materials such as metals [195].

Seamless cold-drawn non-magnetic stainless steel tubes (316L) that we used for waveguides in the setup were not reflective enough from the inside that reflected in the quality/intensity of the signal after the first tests of the beam passing through the tubes. We decided to improve the inside surface condition of the tubes by polishing them. Since no company could polish tubes of the given diameter, we polished the tubes by ourselves using mechanical polishing with different abrasive tools to remove scratches, gouges, and other damage appearing on the surface of a material. The polishing with abrasives started with coarse grain size and gradually proceeded to the finer ones to efficiently flatten the surface imperfections and obtain optimal results. For this purpose, we used different tools, from the modified kit for cleaning/polishing rifle barrels (Multi-use cleaning kit from Decathlon [196]) shown in Fig. 3.13(a), several different grain-size sandpapers, abrasive paste (Silichrom), metal polishing compounds, to polishing tools made of felt (see Fig. 3.13(b)), etc. Since this procedure proved to be successful, we also used polishing on other waveguiding parts of the setup, such as brass cones and tubes.

<sup>2</sup>Diffuse reflection is the reflection of light from a surface such that a ray incident on the surface is scattered at many angles rather than at just one angle, as in the case of specular reflection [195].

### 3.3.4 Silver Plating

Silver plating, or silver electroplating, is a chemical process of depositing a thin layer of silver onto an object made from another type of metal (such as copper, brass, nickel, etc.) employing an electric current (electrolysis<sup>3</sup>). An electrical current is passed through a specialized electrolyte solution. The electrolyte solution is created using dissolved silver ions and other select compounds. Once these ions stick to the object's surface, they form a solid layer of silver, chemically bonded to the other material [198].

To improve the intensity of the signal passing through the setup, we decided to cover the flat mirrors made of polished brass plates with a thin layer of silver by silver plating by the company Lars Chemie Brno [199], result is shown in Fig. 3.13(c). Silver was chosen due to its high reflectance (more than 95% over the 450 nm – 20  $\mu\text{m}$  [200, 201]) in the IR (also visible) spectral region, making it an excellent choice for broadband applications that span multiple spectral regions.

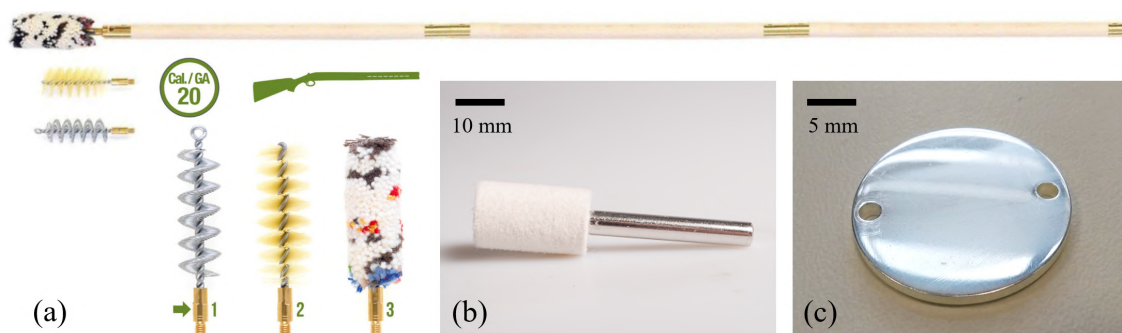


Fig. 3.13: (a) Multi-use cleaning kit for cleaning/polishing rifle barrels, and (b) polishing tool made of felt. (c) Flat brass mirrors covered with a thin layer of silver by silver plating by the company Lars Chemie Brno.

## 3.4 Testing of the Setup

Before performing the first magneto-optical measurements, it was necessary to test the setup properly. First of all, we chose suitable material for the windows used in the setup based on the transmittance tests inside the FTIR spectrometer (window test). Then the signal at the detector, after passing through the setup, was tested and subsequently optimized (signal test). Last but not least, the vacuum tightness

<sup>3</sup>Electrolysis is the passing of direct electric current (DC) through an electrolyte producing chemical reactions at the electrodes and decomposition of the materials [197].

of the probes was tested (leak test). This section will describe in detail each testing procedure.

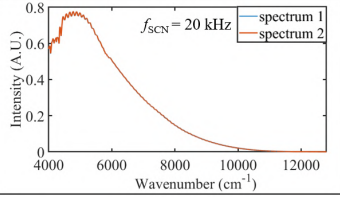
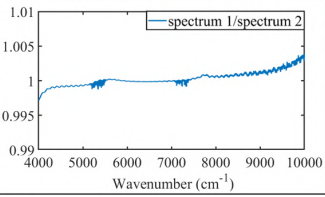
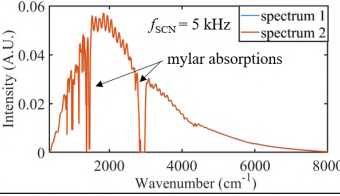
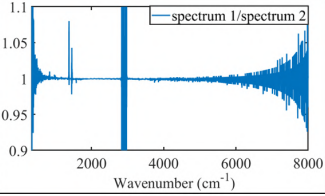
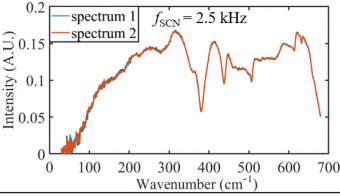
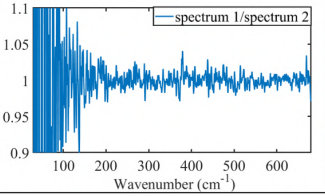
### 3.4.1 Window Test

When choosing the most suitable windows, mylar foil was selected due to its wide frequency range where it can be used [202, 203]. We tested several mylar foils with different thicknesses for their transmission inside the FTIR spectrometer. We achieved the best transmissivity results for the thinnest mylar foil ( $8\ \mu\text{m}$ ). However, we also had to take into account the resistance of the foil to tearing/ability to withstand a rough vacuum; the thinner the foil, the greater the probability of its tearing in a rough vacuum condition. Therefore, we chose the second thinnest foil ( $35\ \mu\text{m}$ ), representing the trade-off between its transmissivity and resistance in a vacuum.

The performance of the  $35\ \mu\text{m}$  thick mylar foil used in the FTIR magneto-spectroscopic setup was tested across the whole IR range in order to identify the frequency range where mylar foil can be used. We have characterized its performance inside the FTIR spectrometer Bruker Vertex 80v in three IR range configurations depending on the source, beamsplitter, and detector choice. The results from these tests are summarized in Tab. 3.2. Beamsplitters and room temperature detectors are shown with their typical operating spectral ranges. We demonstrate the performance of the mylar foil by the power spectrum, which depicts intensity versus wavenumber, and the so-called 100% line, obtained by measuring a transmission spectrum (spectrum 1) and then dividing it by a subsequent spectrum (spectrum 2). All spectra were acquired with the same scanning time (2 min), aperture (1 mm), and resolution ( $1\ \text{cm}^{-1}$ ). The interferometer scan speed  $f_{SCN}$  displayed in the power spectra was optimized for each detector based on its characteristics. From Tab. 3.2, it is clear that mylar can be used over the whole IR range from the FIR to the NIR range. However, it causes typical absorptions around  $1,500\ \text{cm}^{-1}$  and  $3,000\ \text{cm}^{-1}$  visible in MIR range power spectra and noise peaks in 100% line.

### 3.4.2 Signal Test

We tested the signal passing through the setup in Probe A configuration with room-temperature detectors without a magnetic field. Since the probe was too long and conflicted with the floor, we used the service opening in our lab to test it (see Fig. 3.14(a)). We did these measurements to determine and optimize the intensity of the signal passing through approx. 2.5 m long waveguide. Firstly, we aligned the parabolic mirror in the optical coupling with two adjusting knobs to gain the best possible signal. The alignment of the parabolic mirror is monitored visually on the

Range	Source	Beamsplitter range (cm <sup>-1</sup> )	Detector range (cm <sup>-1</sup> ) (Oper. temp.)	Power spectrum	100% line
NIR	Tungsten	CaF <sub>2</sub> 1,200 – 15,000	InGaAs 4,000 – 12,800 (Room Temp.)		
MIR	Globar	KBr 350 – 8,000	MIR-DTGS 250 – 12,000 (Room Temp.)		
FIR	Globar	Mylar Multilayer 30 – 680	FIR-DTGS 10 – 700 (Room Temp.)		

Tab. 3.2: Table of the performance of the mylar foil measured inside the FTIR spectrometer Bruker Vertex 80v (without the optical coupling and probes) in the corresponding IR range and choice of source, beamsplitter, and room temperature detector with usable spectral ranges. The power spectra (intensity vs. wavenumber) and 100% line, obtained as the division of spectrum 1 by a subsequent spectrum 2, are depicted for each IR range. Typical mylar absorptions around  $1,500\text{ cm}^{-1}$  and  $3,000\text{ cm}^{-1}$  are visible in the MIR range power spectra and noise peaks in 100% line.

computer screen using the open Opus software in the Measurement - Check Signal window, where the interferogram is displayed in real time. The aim is to obtain the highest possible signal amplitude by manually adjusting the two adjustment screws of the mirror mount. Then, we observed how the signal reacts using different settings of the optics in OPUS (aperture, scanning velocity, etc.) to obtain the setting for the strongest signal (e.g., APT = 8 mm). However, the signal was still relatively weak even after mirror alignment and finding suitable spectrometer settings. Therefore, we looked for possible reasons causing it, and the most probable explanation was that most of the signal was lost due to scattering events on the inside surface of the waveguide/probe. We decided to polish the tubes from the inside and cover the flat mirrors in the setup with a layer of silver by the processes described in the previous section. Using these methods, the signal improved approximately by a factor of three. Unfortunately, we cannot provide a precise quantitative comparison of the setup performance before and after the polishing that would allow for analyzing

the losses since we did not have all components of the setup during the assembly. Moreover, tubes of Probe B were polished before the probe assembly. We decided to compare the performance of the setup with already polished waveguides of the probes by comparing all its configurations and determining the usable range by power spectra and 100% line spectra, indicator of noise of the setup, which will be shown in the next section. After optimizing the signal, we started testing the vacuum tightness of the setup.

### 3.4.3 Leak Test

The optical coupling and both probes are in the necessary places sealed with o-rings of appropriate material, ensuring rough vacuum conditions. Since the optical coupling and probes are separate units from the vacuum point of view (when connected together separated by the probe's top window), the optical coupling is pumped by the spectrometer's pump, and the probes are in the VTI rough vacuum atmosphere, we tested their vacuum tightness separately. The vacuum tightness of the optical coupling was tested by attaching it to the spectrometer, closing the gate valve, and evacuating it by the spectrometer's scroll pump. We reached the sufficient pressure of 2 mbar, and then we proceeded to test the probes. Before inserting the probes inside the VTI of the superconducting magnet to perform magneto-optical measurements, the probes had to be tested for vacuum tightness. The leak in the probe causes air intrusion into the rough vacuum of the VTI that could freeze and block the needle valve of the VTI system. To perform the leak test, the probe (A or B) equipped with mylar foil windows was inserted into a long tube with KF50 flanges on both ends, while one flange was hermetically closed, and to another a T-part with three KF50 flanges was connected. The probe head was hermetically connected to second flange of the T-part. To third flange of the T-part we connected the turbo-molecular vacuum pump Edwards T-station 85 with the base pressure of  $1 \times 10^{-6}$  mbar, where pressure was monitored by wide range gauge connected to the station. This leak testing setup/arrangement is shown in Fig. 3.14(b). We switched the pump on and evacuated the tube for about 1 hour to reach the pressure of  $10^{-6}$  mbar. Then, the pump was switched off, and we left the leak test setup stand-by for about three days. When pressure stayed in the range of working pressure (1 mbar), the leak test was considered successful, and the probe was considered to be without leaks that could harm or block the VTI.

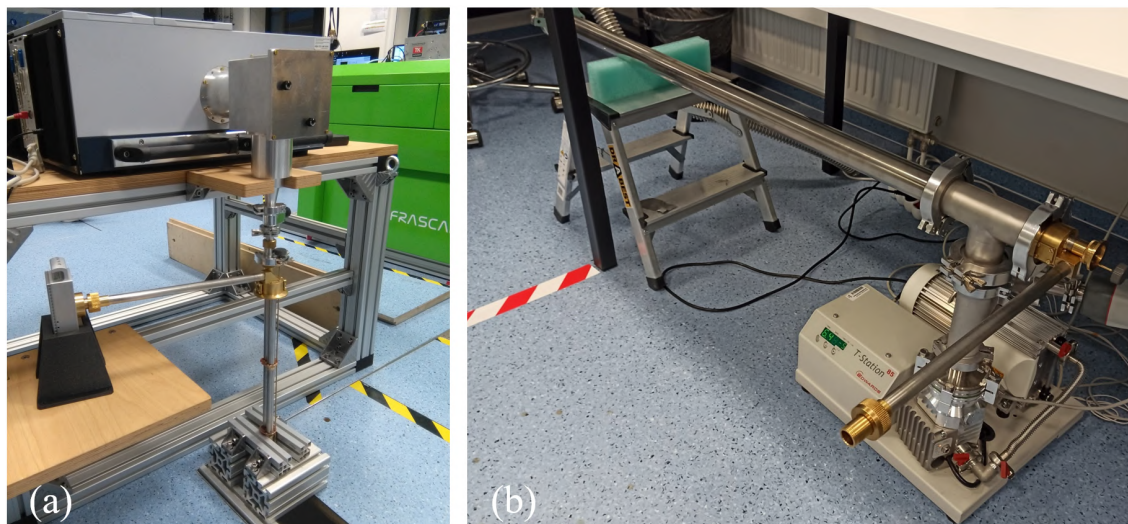


Fig. 3.14: (a) Parts of the setup 3D printed on the 3D printer TRILAB. (b) The process of hard soldering of the transmission probe.

## 3.5 Performance of the Setup

We have characterized the performance of the FTIR magneto-spectroscopic setup in several different configurations depending on the probe, source, beamsplitter, and detector choice. The results from these tests are summarized in Tab. 3.3, in which typical operating spectral ranges for beamsplitters, detectors, operating temperature ranges for detectors, and possible sample temperatures are depicted. We demonstrate the performance of the setup by the power spectrum, which depicts intensity versus wavenumber and the so-called 100% line, which is a typical indicator of the noise level of the spectroscopic system [4]. 100% line is obtained by measuring a transmission spectrum (spectrum 1) and then dividing it by a subsequent spectrum (spectrum 2). In the ideal case, the division should be a straight line at 100%. The deviation from this line represents the noise and instability of the system as a function of wavenumber (frequency) [103]. 100% line clearly displays the performance and workable setup range (fifth column of the table) for each configuration. To compare the performance between configurations in the specific IR range, 100% line spectra are plotted with the same y-axis range,  $\pm 1\%$  for the NIR configurations,  $\pm 10\%$  for the MIR and FIR configurations. These measurements were performed on an empty opening (reference) at zero magnetic field. All spectra were acquired with the same scanning time (10 min) and resolution ( $1 \text{ cm}^{-1}$ ). The interferometer scan speed  $f_{SCN}$  displayed in the power spectra was optimized for each detector based on its characteristics. As expected, the performance of the setup in configurations with room temperature FIR-DTGS and MIR-DTGS detectors is clearly worse than

Probe	Source	Beamsplitter Range (cm <sup>-1</sup> )	Detector Range (cm <sup>-1</sup> ) (Oper. temp.)	Setup range (cm <sup>-1</sup> )	Sample temp. (K)	Power Spectrum	100% Line
A	Tungsten	CaF <sub>2</sub> 1,200 – 15,000	InGaAs 4,000 – 12,800 (Room Temp.)	<b>NIR</b> 4,000 – 10,000	2 – 320		
B	Tungsten	CaF <sub>2</sub> 1,200 – 15,000	4.2 K Sealed Bolometer 10 – 2,000* (LHe-cooled)	<b>NIR</b> 2,000 – 8,000	4.2		
A	Globar	KBr 350 – 8,000	MIR-DTGS 250 – 12,000 (Room Temp.)	<b>MIR</b> 400 – 5,000	2 – 320		
B	Globar	KBr 350 – 8,000	4.2 K Sealed Bolometer 10 – 2,000* (LHe-cooled)	<b>MIR</b> 400 – 4,000	4.2		
A	Globar	Mylar Multilayer 30 – 680	FIR-DTGS 10 – 700 (Room Temp.)	<b>FIR</b> 150 – 680	2 – 320		
A	Globar	Mylar Multilayer 30 – 680	1.6 K Standard Bolometer 5 – 670 (LHe-cooled)	<b>FIR</b> 50 – 670	2 – 320		
B	Globar	Mylar Multilayer 30 – 680	4.2 K Sealed Bolometer 10 – 2,000* (LHe-cooled)	<b>FIR</b> 50 – 680	4.2		

Tab. 3.3: All possible configurations of the FTIR magneto-spectroscopic setup according to the choice of the probe, source, beamsplitter, and detector, with spectral and sample temperature ranges, and corresponding power spectrum (intensity vs. wavenumber) together with 100% line, obtained as the division of spectrum 1 by a subsequent spectrum 2. (\*This range of the bolometer was provided by the manufacturer, but the bolometer worked far above this range.)

with using LHe-cooled detectors in the FIR and MIR ranges. In all presented configurations, mylar foil (35  $\mu\text{m}$ ) windows were used in the setup, but they can be easily replaced with windows made of other materials. We have chosen mylar due to its wide frequency range where it can be used. However, mylar caused typical ab-

sorptions around  $1,500\text{ cm}^{-1}$  and  $3,000\text{ cm}^{-1}$  visible in the MIR range power spectra and noise peaks in 100% line, see Tab. 3.2. In the FIR power spectra for Probe A configuration with 1.6 K standard bolometer, we observe the absorption in water vapor because the end of the window mount 2/winston cone is not hermetically connected to the bolometer; the beam is going through the air a few centimeters. The FIR power spectrum for Probe B configuration does not exhibit absorption in water vapor since the sealed bolometer is placed inside the magnet in the helium atmosphere. Unfortunately, we cannot provide a table for the setup without the probes for a comparison that would allow for analyzing the insertion loss and standing wave patterns in the probe as a function of wavenumber. Given the use of several different detectors in the setup designed for connecting to the probes, we concluded that connecting them to the optical coupling would be difficult and inaccurate.

---

# 4 Magneto-Optical Measurements

This chapter presents magneto-optical measurements performed on two different magneto-spectroscopic setups. During the time when our FTIR magneto-spectroscopic setup built at Central European Institute of Technology Brno University of Technology (CEITEC BUT) was not yet finished, magneto-optical measurements were carried out on the magneto-spectroscopic setup at Grenoble High Magnetic Field Laboratory (GHMFL) of the French National Center for Scientific Research (CNRS) with the collaboration of RNDr. Milan Orlita, Ph.D. and Ing. Ivan Mohelský. Several SMMs/SIMs samples, prepared by Assoc. Prof. Ivan Šalitroš and Ing. Jana Juráková were measured on this setup. We analyzed the obtained data and the results, which are shown in the following section, were published in [13], [14]. When our FTIR magneto-spectroscopic setup was finished and its performance was successfully tested in all possible configurations (see the previous chapter), we decided to prove and demonstrate its functionality by magneto-optical measurements of several different samples. We began with measurements on one of the SIMs samples, measured on the setup at GHMFL, to compare the results obtained from our setup with those previously published in [13]. Then, we measured different types of samples in various configurations and ranges, e.g., *p*-type germanium in the NIR range, without previously published results, in which we observed transitions between Landau Levels (LLs). Based on the results obtained from magneto-optical measurements of these two samples, the functionality of the FTIR magneto-spectroscopic setup at CEITEC BUT was demonstrated and published in [15]. Moreover, in this chapter we show the magneto-optical measurements of graphene in the FIR region with previously published results in [23] and we also performed tests of graphene bolometers [189] – [191] in the chipset holder [187], [188] in configuration of the setup with Probe B - Chipset.

All presented figures and data in this chapter were plotted, analyzed or fitted using Matlab, besides data from measurements on graphene bolometer devices (subsection 4.3.4, which were plotted using Origin). All simulations of SMMs were calculated by means of the EasySpin Toolbox for Matlab [120].

## 4.1 Data Analysis and Manipulation

In this section, we want to demonstrate on the example of cobalt-based SIM sample **3** from ref. [13], here entitled JJ3, data analysis and manipulation from raw transmission data measured at different magnetic fields to final spectra, which are then published. Raw data obtained from the spectrometer's software Opus are plots

of intensity as a function of wavenumber for each magnetic field. When we sweep the magnetic field, we usually go from 0 T (before sweep) to 16 T and back to 0 T (after sweep), where we measure it again. We can then use only one 0 T spectrum or make an average from them, see Fig. 4.1, which we then use for zero field normalization. In Fig. 4.2, we plot the raw data measured on samples from all magnetic fields (1 T to 16 T) in one plot. In Fig. 4.3, we plot the reference raw data measured on an empty sample holder opening at magnetic fields from 1 T to 16 T. There are several different types of data normalization, which we use to remove from spectra all signals that are not related to magnetic features and contribute to the analysis of the results. We can divide the transmission spectra at magnetic fields by zero-field  $T(B)/T(0)$ , or divide subsequent transmission spectra in magnetic fields  $T(B+1)/T(B)$ , etc. One way to normalize the spectra of the sample, which we usually use, is to divide sample raw data at magnetic fields  $S(B)$  by its zero-field spectra  $S(0)$ ,  $S(B)/S(0)$ , the result is shown in Fig. 4.4. Similarly, we can normalize reference raw spectra by dividing reference spectra at magnetic field  $R(B)$  by reference spectra at zero field  $R(0)$ ,  $R(B)/R(0)$ , in Fig. 4.5. As you can see in Fig. 4.4, the baseline sometimes drifts away from its original base level (because of changes in experimental conditions during measurement, temperature influences, etc.) and the baseline correction is needed. It can be done by subtracting the horizontal line from the spectra, or it can be corrected by dividing the normalized sample by normalized reference,  $[S(B)/S(0)]/[R(B)/R(0)]$ , see Fig. 4.6. Dividing the spectra by a reference is an optional step, but we used it here mainly for baseline correction and to improve the visibility of moving signal features in the spectra. A specific range ( $50\text{-}300\text{ cm}^{-1}$ ) of normalized spectra, where we can clearly observe magnetic field-dependent features, can be enlarged as in Fig. 4.7 and plotted with magnetic field on  $y$ -axis in Fig. 4.8 for better visibility of field-dependent features. If there are several field-dependent features, we can use a function for finding local minima in the specific range ( $150\text{-}230\text{ cm}^{-1}$ ); see Fig. 4.9. Local minima of field-dependent features here are marked with magenta circles for better identification of features moving with the higher magnetic field (max. 16 T magenta line, 1 T cyan line) to higher/lower frequencies (to the right/left) caused by EPR transitions. The feature in the middle that starts occurring at  $\approx 187\text{ cm}^{-1}$  at zero magnetic field is the one we are looking for because, unlike the others, it moves to the right, which means that energy between the two energy levels is becoming bigger with a higher magnetic field. It is attributed to the EPR transition among  $m_s = \pm 3/2$  to  $m_s = \pm 1/2$  states with a higher probability of transition. For better imagination, a schematic 2D plot of spin energy levels of JJ3 vs. magnetic field in Fig. 4.10 indicates spin energy levels involved in the transitions among  $m_s = \pm 3/2$  to  $m_s = \pm 1/2$  states, where ZFS is around  $187\text{ cm}^{-1}$  and energy between the two energy levels at 5 T is  $\approx 190\text{ cm}^{-1}$ .

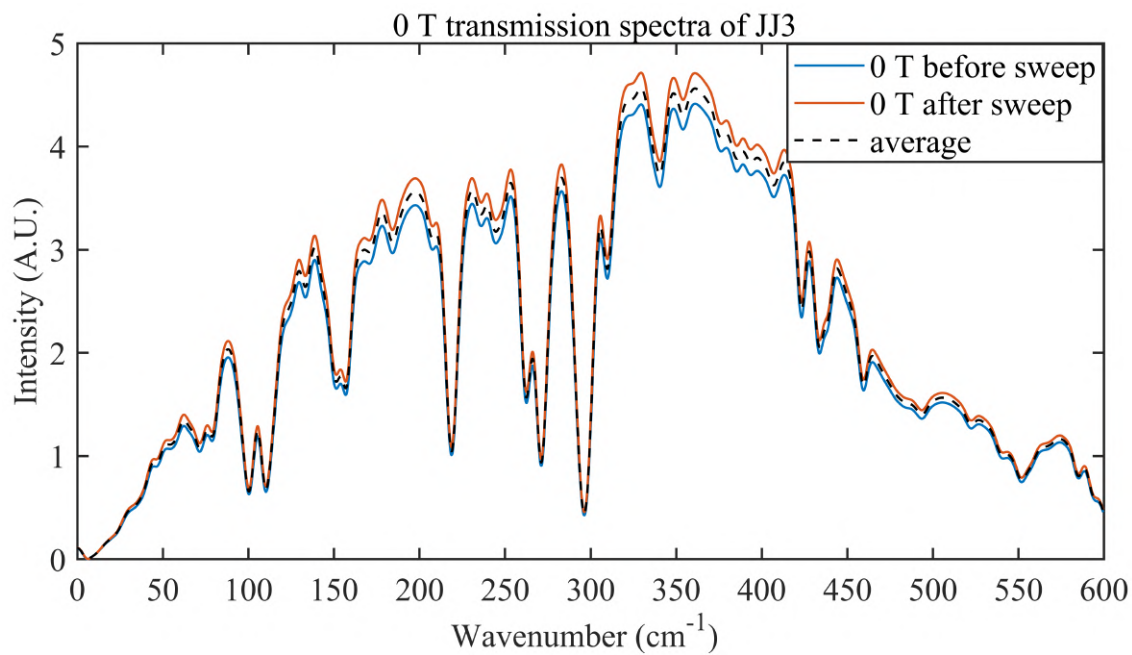


Fig. 4.1: Zero field spectra measured before (blue) and after (orange) magnetic field sweep and their average (dashed).

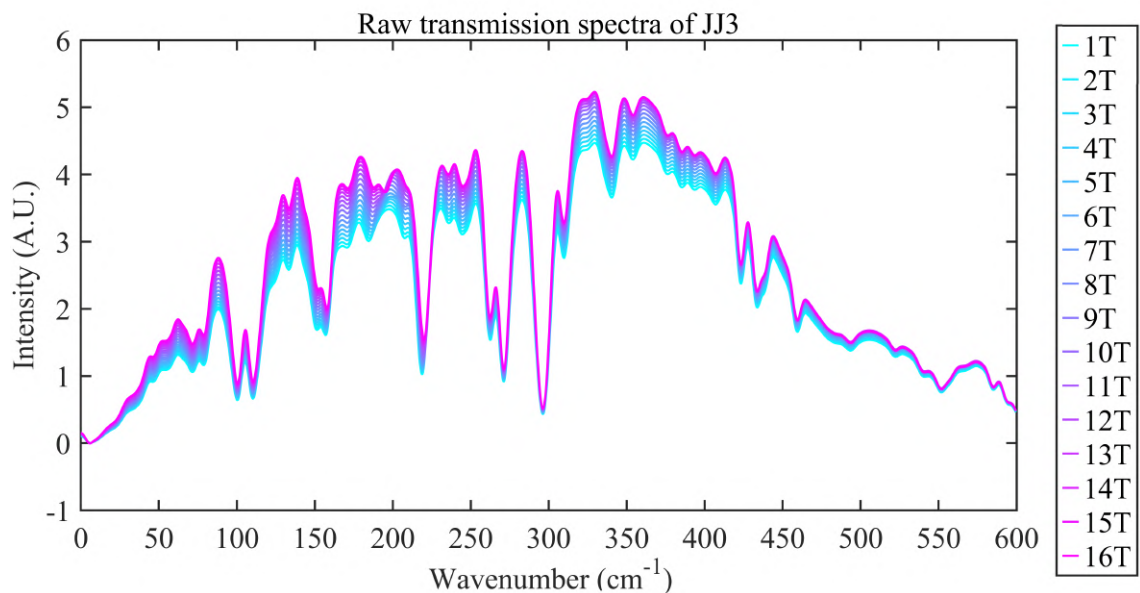


Fig. 4.2: Raw transmission spectra of sample JJ3 in magnetic fields from 1 T to 16 T.

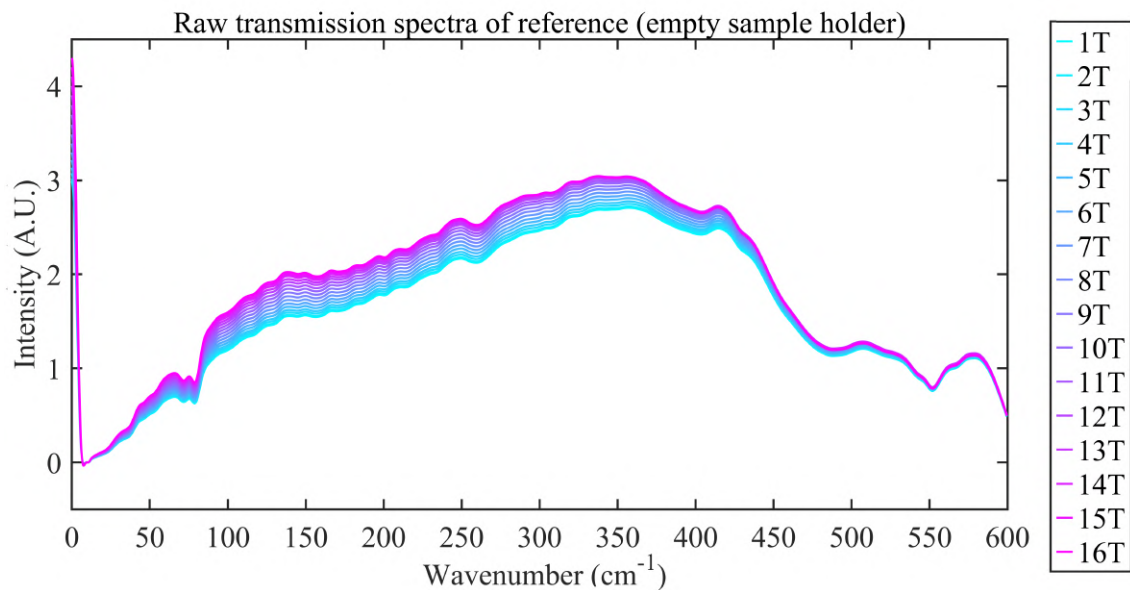


Fig. 4.3: Raw transmission spectra of reference (empty sample holder opening) in magnetic fields from 1 T to 16 T.

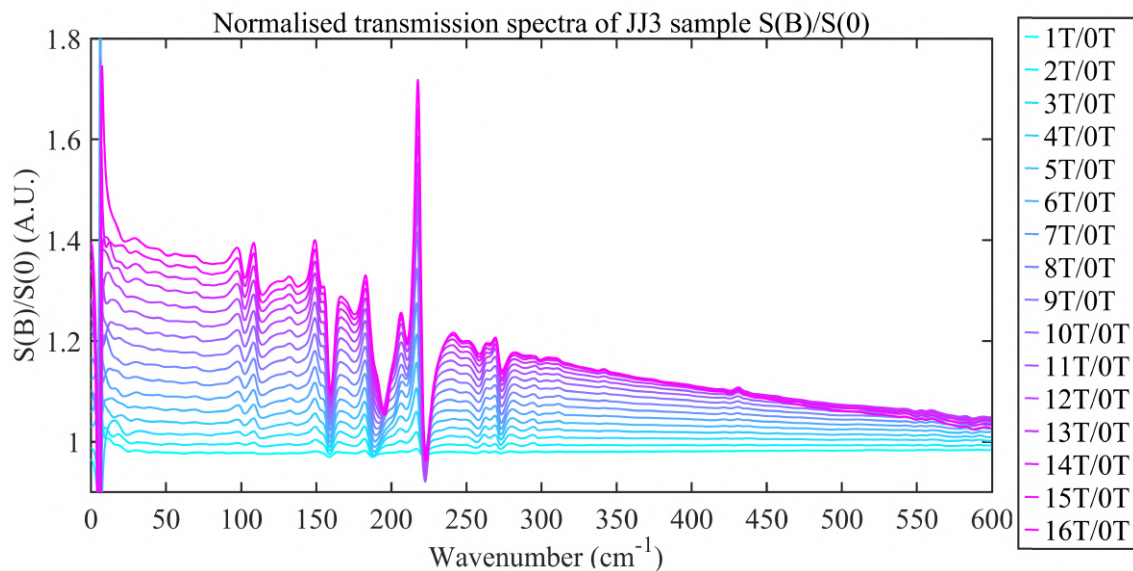


Fig. 4.4: Normalized transmission spectra  $S(B)/S(0)$  of sample JJ3 obtained by dividing sample spectra at magnetic field  $S(B)$  by sample spectra at zero field  $S(0)$ .

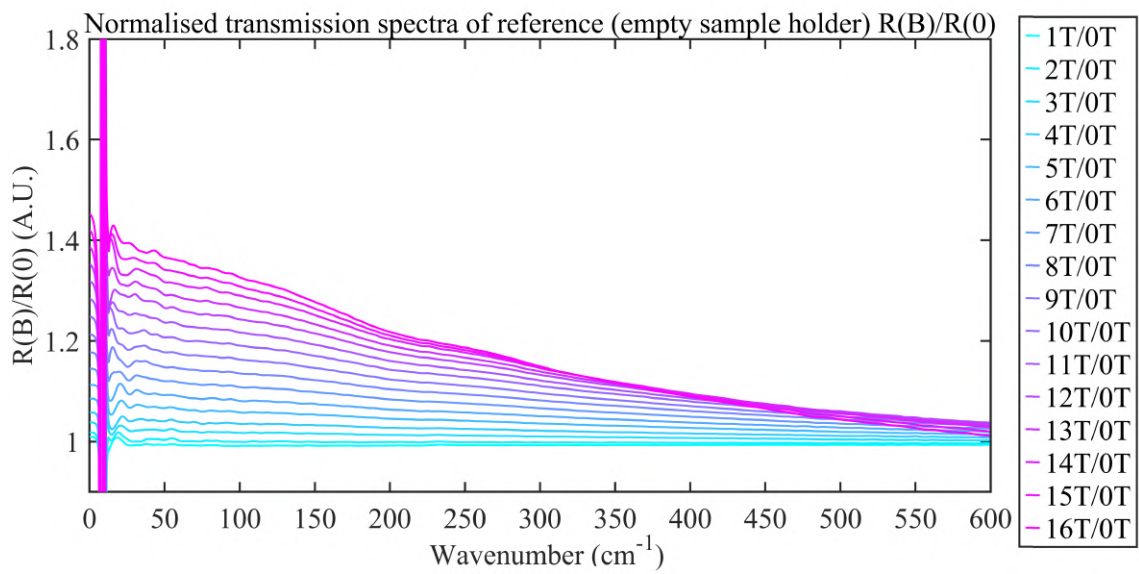


Fig. 4.5: Normalized transmission spectra  $R(B)/R(0)$  of reference obtained by dividing reference spectra at magnetic field  $R(B)$  by reference spectra at zero field  $R(0)$ .

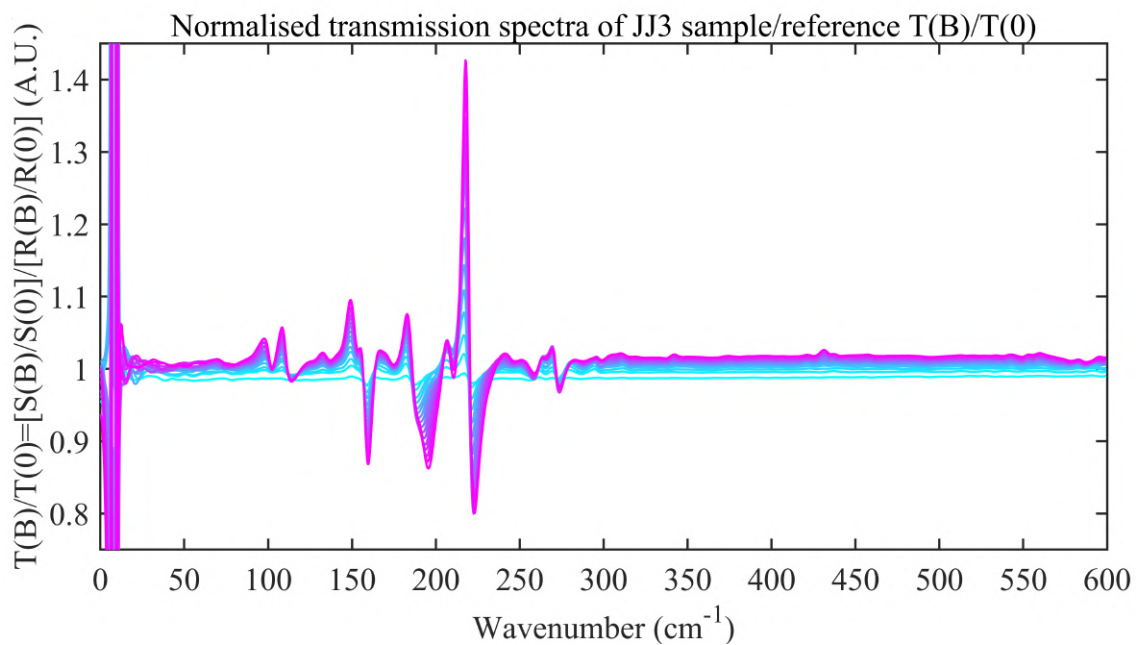


Fig. 4.6: Normalized transmission spectra  $T(B)/T(0)=[S(B)/S(0)]/[R(B)/R(0)]$  of sample JJ3 obtained by dividing normalized sample spectra  $S(B)/S(0)$  by normalized reference spectra  $R(B)/R(0)$ .

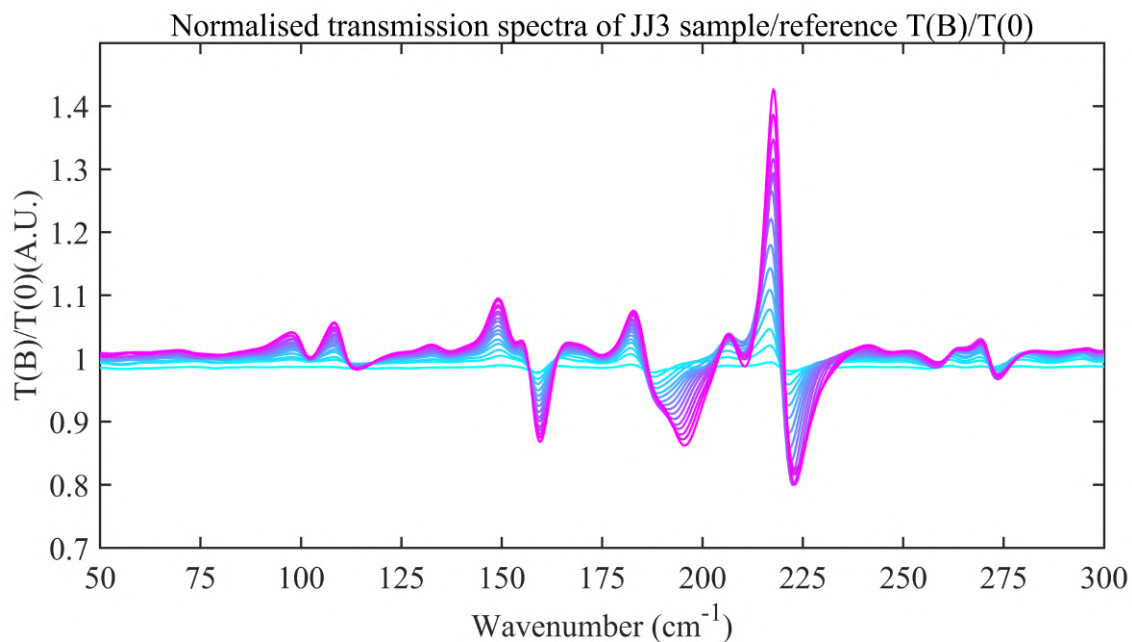


Fig. 4.7: Normalized transmission spectra  $T(B)/T(0)$  of sample JJ3 displayed in range  $50\text{-}300\text{ cm}^{-1}$ , where expected field dependent features are observed.

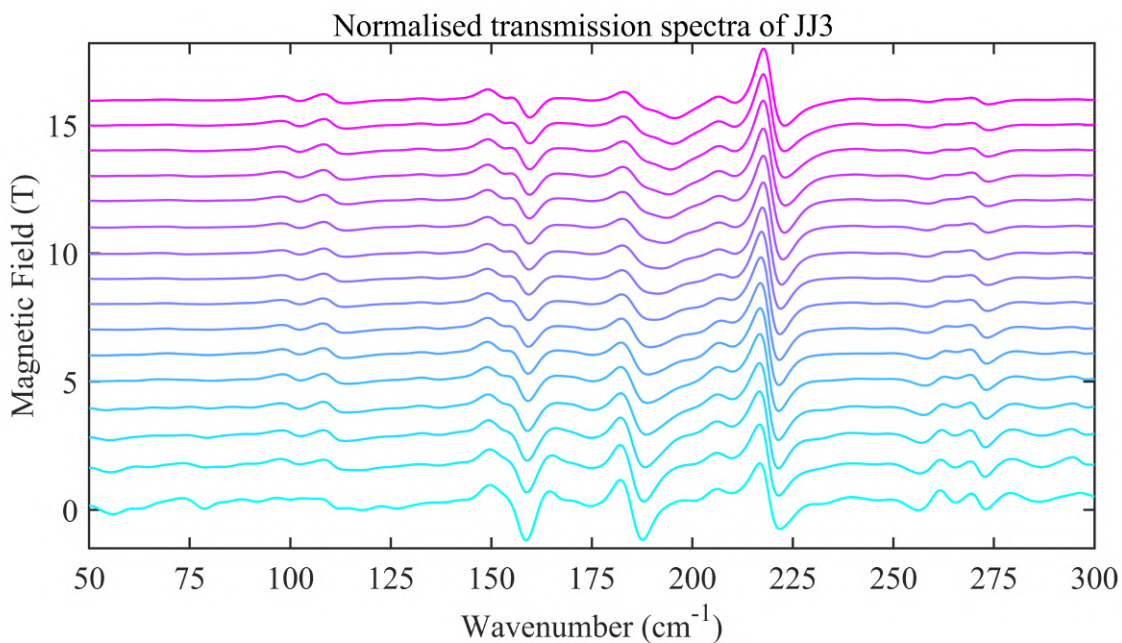


Fig. 4.8: Normalized transmission spectra  $T(B)/T(0)$  of sample JJ3 displayed in range  $50\text{-}300\text{ cm}^{-1}$  and applied magnetic field.

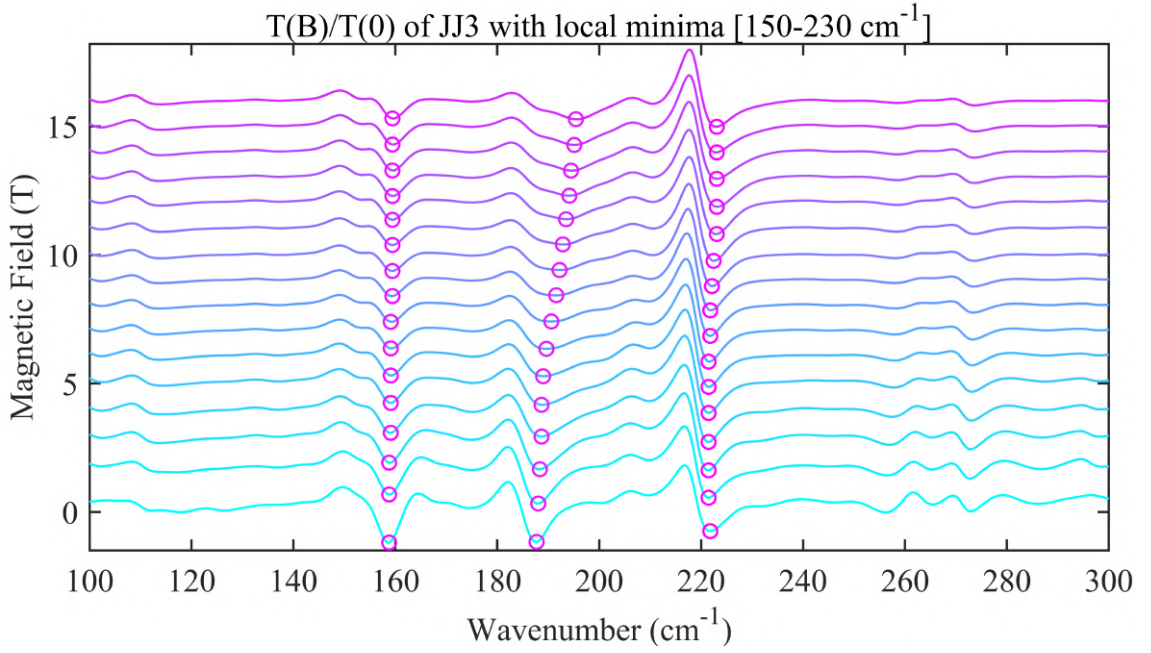


Fig. 4.9: Normalized transmission spectra  $T(B)/T(0)$  of sample JJ3 displayed in range  $100\text{-}300\text{ cm}^{-1}$  and magnetic field with local minima in the range  $150\text{-}230\text{ cm}^{-1}$  marked with magenta circles for better identification of features moving with the higher magnetic field to higher frequencies (to the right) starting around  $187\text{ cm}^{-1}$ .

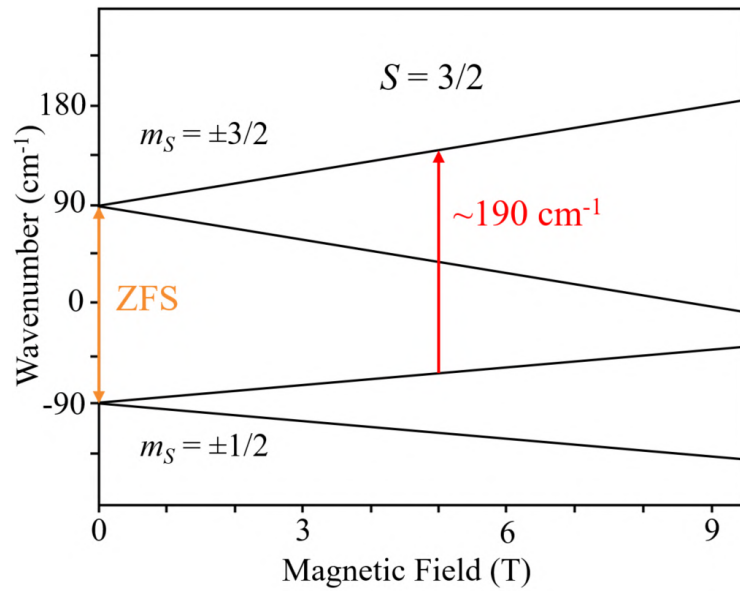


Fig. 4.10: A schematic 2D plot of spin energy levels of JJ3 vs. magnetic field with indicated spin energy levels involved in the transitions among  $m_s = \pm 3/2$  to  $m_s = \pm 1/2$  states, where ZFS is around  $187\text{ cm}^{-1}$  and transition among  $m_s = \pm 3/2$  to  $m_s = \pm 1/2$  states at  $5\text{ T}$  is  $\approx 190\text{ cm}^{-1}$ .

Normalized spectra can be visualized in the form of a color map, which can also help with the analysis of wanted features. A color map of normalized transmission spectra  $T(B)/T(0)$  of sample JJ3 with EasySpin simulation with the SH ( $S = 3/2, D = -89 \text{ cm}^{-1}, E/D = 0.162, g_{iso} = 2.1$ ) is depicted in Fig. 4.11.

As a general remark to the simulations of FIRMS spectra in this chapter, all shown simulations of FIRMS spectra were not fitted, the parameters for simulations ( $g, E$ ) were obtained from different techniques, i.e., theoretical calculations, because of broad signal features in the spectra. Our only criterion for matching simulations to spectra was the position of the ZFS. FIRMS simulations, shown as dotted lines in Fig. 4.11, show field dependent transition energies for the canonical orientations of the ZFS tensor with respect to  $B_0$ . They were calculated by means of the EasySpin Toolbox for Matlab [120] based on the SH and the parameters obtained from CASSCF-NEVPT2 calculations performed by Assoc. prof. Ján Pavlík. Red color represents the strongly allowed transitions; grey color indicates forbidden/weakly allowed transitions. These colors are based on the model of the probability of transitions implemented in EasySpin Toolbox (version 5.2.35) for Matlab [120], using which red color represents a higher probability of transition and gray low probability of transition. In the simulation, we also take into account the temperature of the measurement. Since FIRMS spectra did not provide enough resolution for the determination of the precise  $g$ -tensor, only  $g_{iso}$  was determined in simulations. It is important to mention that FIRMS in this case gave us only ZFS, not  $D$  or  $E$ . We estimated value  $D$  based on extrapolation of ZFS using `resfreqs_matrix`<sup>1</sup> function. We used  $E$  from CASSCF. However, in some cases, combination of HF-EPR or even low frequency EPR allows determining  $E/D$  and it can iteratively be used to determine  $D$  exactly from FIRMS. The value  $g_{iso}$ , which determines the slope of the moving signal feature in the spectra, was chosen to best match the signal feature in the spectra.

Definitive determination of ZFS using FTIR magneto-spectroscopy is not straightforward and can be challenging. During data analysis, we were often unsure if we had estimated the ZFS correctly because the moving signal features in the Co-based SIM spectra are quite broad. Moreover, the spectra presented are not fittings, only comparisons of simulated data with parameters obtained by different techniques. Therefore, we admit that an error may have occurred in the determination of the ZFS position. Although no evidence of the presence of different Co coordination environments (that lead to different ZFS) was reported by other techniques, these transitions could come from different Co coordination environments.

---

<sup>1</sup>EasySpin function `resfreqs_matrix` is used for calculating resonance frequencies for frequency-swept EPR. It computes frequency-domain EPR line positions, intensities and widths using matrix diagonalization.

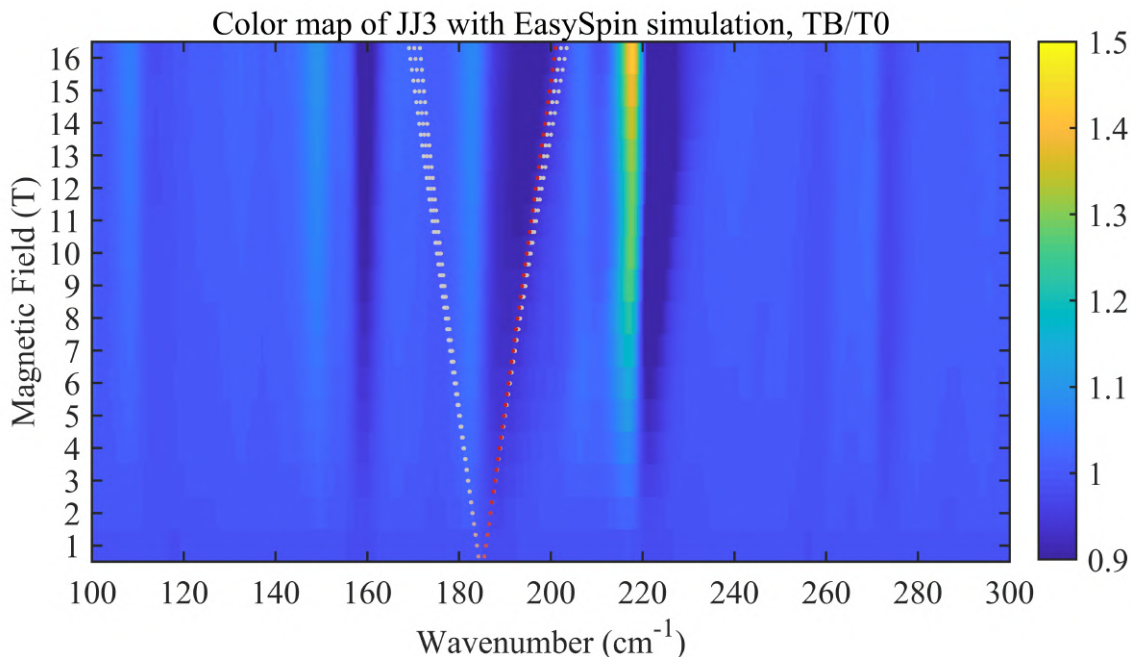


Fig. 4.11: A color map of normalized transmission spectra  $T(B)/T(0)$  of sample JJ3 with EasySpin simulation with the SH ( $S = 3/2, D = -89 \text{ cm}^{-1}, E/D = 0.162, g_{iso} = 2.1$ ) shown as dotted lines. Red color represents the strongly allowed transitions; grey color indicates forbidden/weakly allowed transitions.

## 4.2 Measurements at GHMFL

Following magneto-optical measurements were performed on the IR magneto-spectroscopic setup at GHMFL. In the publications showing these results, FTIR magneto-spectroscopy is referred to as far-infrared magneto-spectroscopy (FIRMS) [22] because EPR transitions of SMMs are occurring in the FIR range. The magneto-optical response of the studied compound has been also explored in the THz/infrared range, using the standard Faraday configuration (i.e. in transmission mode, with the magnetic field parallel to the wave vector of the probing radiation). To ensure the transparency in this spectral range, the compounds were mixed with eicosane in the indicated ratio, and subsequently pressed into pellets. To measure magneto-transmission, the radiation of a globar, or alternatively, of a mercury lamp, has been analyzed by the Vertex 80v Fourier transform spectrometer, and using light-pipe optics, delivered to the pellet placed inside a superconducting coil and kept in the helium heat-exchange gas at  $T = 4.2 \text{ K}$ . After passing through the pellet, the radiation was detected using a composite bolometer placed just below.

### 4.2.1 Pentacoordinate Cobalt(II) Single Ion Magnets (SIMs)

Following results were obtained in cooperation and published in *Inorganic Chemistry Frontiers* [13]:

Juráková, J.; **Dubnická Midlíková, J.**; Hrubý, J.; Kliukov, A.; Tadeu Santana, V.; Pavlik, J.; Moncol, J.; Čižmár, E.; Orlita, M.; Mohelský, I.; Neugebauer, P.; Gentili, D.; Cavallini, M.; Šalitroš, I. Pentacoordinate cobalt(II) single ion magnets with pendant alkyl chains: shall we go for chloride or bromide? *Inorg. Chem. Front.*, 9, 1179-1194, 2022. <https://doi.org/10.1039/D1QI01350E>.

#### Abstract

Four pentacoordinate complexes, **1-4**, of the type  $[\text{Co}(\mathbf{L1})\mathbf{X2}]$  and  $[\text{Co}(\mathbf{L2})\mathbf{X2}]$  (where  $\mathbf{L1} = 2,6\text{-bis}(1\text{-octyl-}1\text{H-benzimidazol-}2\text{-yl})\text{pyridine}$  for **1** and **2**,  $\mathbf{L2} = 2,6\text{-bis}(1\text{-dodecyl-}1\text{H-benzimidazol-}2\text{-yl})\text{-pyridine}$  for **3** and **4**;  $X = \text{Cl-}$  for **1** and **3**,  $X = \text{Br-}$  for **2** and **4**) have been synthesized, and their structures have been determined by X-ray analysis. The DC magnetic investigation confirmed the high-spin and anisotropic behavior of the metal centers of the reported compounds, and magnetic data were analyzed with respect to the spin Hamiltonian and the Griffith-Figgis Hamiltonian. CASSCF-NEVPT2 analysis enabled us to identify triaxial magnetic anisotropy for **1** and **2** and axial anisotropy for **3** and **4**, and we discuss thoroughly the relationship between geometry and orbital ordering. The  $g$ -tensor components of the ground Kramers doublet extracted from EPR spectroscopy are compatible with this prediction of magnetic anisotropy. Simulated FIRMS experimental data of **2**, **3** and **4** show very good agreement with theoretical calculations and provide precise values of zero-field splitting. The AC susceptibility measurements confirmed that the reported complexes were field-induced single-ion magnets. The slow relaxation of magnetization in **1** and **2** is mediated through two relaxation channels that are unusually close to each other. On the other hand, complexes **3** and **4** show the single-channel relaxation of magnetization, and their isostructural characteristic allowed us to study the relaxation changes caused solely by the replacement of terminal halido ligands. Finally, a wet lithographic technique has been used to evaluate both the processability of the complexes in solution and the preparation of microstructured films.

#### Far infrared magnetic spectroscopy (FIRMS)

For a definitive determination of the zero-field splitting (ZFS), FTIR magneto-spectroscopy in the FIR range, in this publication referred to as Far Infrared Magnetic Spectroscopy (FIRMS), was exploited. It enables us to observe EPR transitions of SMMs with large zero-field splitting, mainly based on transition metal complexes (SIMs), and determine ZFS directly from the spectra. For cobalt(II) complexes with

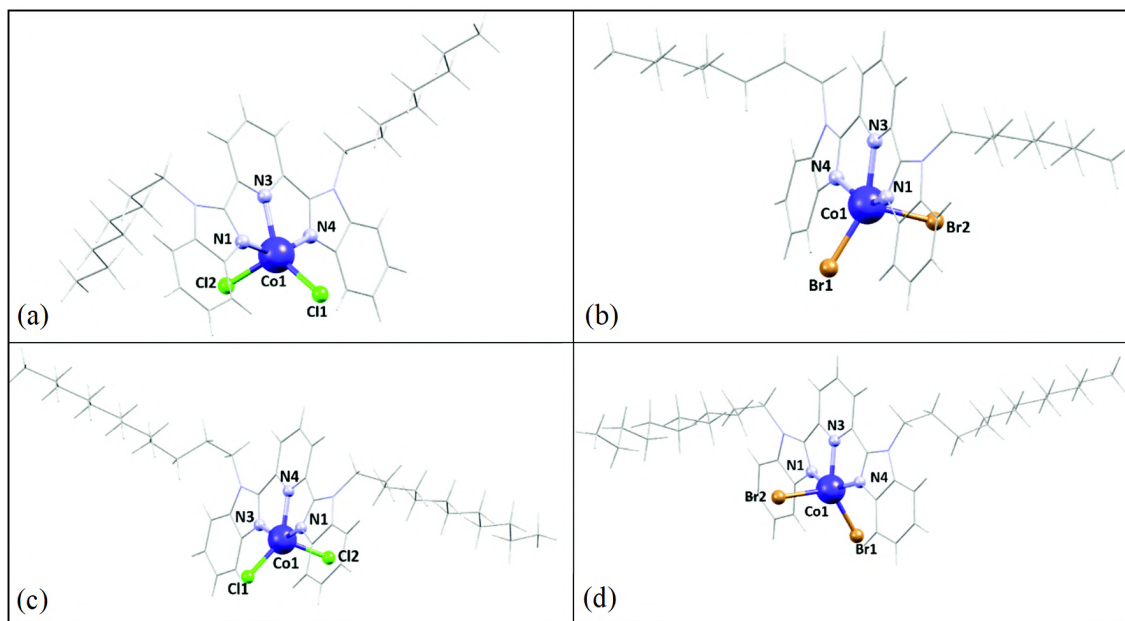


Fig. 4.12: Molecular structures of (a) **1**, (b) **2LT**, (c) **3**, (d) **4**. Adapted from [13].

$S = 3/2$ , the zero-field splitting between two Kramers doublets is equal to  $2(D^2 + 3E^2)^{1/2}$  (or  $2D$  when omitting  $E$ ). This energy gap is then directly observable in FIRMS spectra. The FIRMS spectra were recorded on pressed powder pellets of **1–4** (their molecular structures are shown in Fig. 4.12(a)–(b), respectively) diluted in eicosane and measured at  $T = 4.2$  K, and magnetic fields up to 16 T. The spectra of the sample at magnetic fields  $S(B)$  were normalized by the zero-field sample transmission spectra  $S(0)$ ,  $S(B)/S(0)$ , and their corresponding reference transmission spectra at magnetic fields  $R(0)$ ,  $R(B)/R(0)$ ,  $[S(B)/S(0)]/[R(B)/R(0)]$ . Normalized transmission spectra (Fig. 4.13, 4.15, 4.17, 4.19) were then depicted in the form of a color map for better identification of the EPR transitions (Fig. 4.14, 4.16, 4.18, 4.20). In the color maps, the tendency toward the yellow color means the absorption is suppressed by the magnetic field, whereas the dark blue color corresponds to the absorption induced by the magnetic field. All observed EPR transition were identified in the range of  $50 - 300 \text{ cm}^{-1}$ . Multiple field-dependent peaks can be found in this range, therefore the combination of theoretical calculations and magnetization experiments supported the choice of the peaks corresponding to the ZFS transition. FIRMS simulations shown in dotted lines, (Fig. 4.16, 4.18, 4.20), were calculated by means of the Easy-Spin Toolbox for Matlab [120] based on the SH and the parameters obtained from CASSCF-NEVPT2 calculations performed by Assoc. prof. Ján Pavlik. Red color represents the strongly allowed transitions; grey color indicates forbidden/weakly

allowed transitions. Since FIRMS spectra did not provide enough resolution for the determination of the precise g-tensor, only  $g_{iso}$  was determined in simulations. Changing the value of  $g_{iso}$  in the simulation by a difference of 0.1 shifts the position of the signal line at 16 T by approximately  $0.8 \text{ cm}^{-1}$ . In the normalized FIRMS transmission spectra (Fig. 4.13) and the corresponding color map (Fig. 4.14) of complex **1**, no EPR transition was observed (that could be related to a thicker sample or low/high dilution. The signal can vanish for both reasons, high dilution because there is not enough signal from the sample and low dilution because the sample is less transparent to the beam, and we have a lower signal on the detector because the beam cannot pass through. Therefore, no simulation was used in this case. A color map of normalized FIRMS transmission spectra of complex **2**<sup>2</sup> (Fig. 4.16) shows a clear field-dependence of one of the peaks, occurring at  $\approx 103 \text{ cm}^{-1}$  at zero magnetic field and attributed to the EPR transition among  $m_s = \pm 3/2$  to  $m_s = \pm 1/2$  states. Based on the simulation and assuming  $E/D = 0.251$  from the CASSCF-NEVPT2 calculations, the obtained ZFS parameter  $D$  for complex **2** is  $D = -47 \text{ cm}^{-1}$  for  $g_{iso} = 2.1$ , which is in excellent agreement with the value in Table 1 and Table 2 obtained from magnetization experiments and theoretical calculations in [13]. The same approach was applied to the complex **3**, assuming  $E/D = 0.162$ ,  $g_{iso} = 2.1$ , simulation based on CASSCF-NEVPT2 calculated parameters fits well the experimental FIRMS spectra (Fig. 4.18) and gives us  $D = -89 \text{ cm}^{-1}$ . This result is again in accordance with the  $D$  value in Table 1 and Table 2 in [13]. Similarly, in FIRMS spectra of complex **4**, based on simulation with  $E/D = 0.197$ ,  $g_{iso} = 2.7$ , parameter  $D = -89 \text{ cm}^{-1}$ , and simulation fits well the experimental FIRMS spectra (Fig. 4.20). The FIRMS result is in very good agreement with the  $D$  value from theoretical calculations and magnetization experiments in [13].

In addition, spectra were normalized by dividing a transmission spectrum measured at  $B_0$  by a spectrum measured at  $B_0 + 1 \text{ T}$  and depicted as a color map (see Fig. 4.21, 4.22, 4.23, 4.24). In the FIRMS color map of **1** in Fig. 4.21, no features are observed. However, the FIRMS color map of **2** in Fig. 4.22, revealed several weak field-dependent parallel features moving with the field to the right that appeared at zero-field around  $100 \text{ cm}^{-1}$ ,  $190 \text{ cm}^{-1}$ , and  $220 \text{ cm}^{-1}$ . For complex **3** in Fig. 4.23, these features we observed around  $160 \text{ cm}^{-1}$ ,  $190 \text{ cm}^{-1}$ , and  $220 \text{ cm}^{-1}$ . In case of complex **4** in Fig. 4.24, they occurred around  $140 \text{ cm}^{-1}$ ,  $190 \text{ cm}^{-1}$ , and  $220 \text{ cm}^{-1}$ . We do not have satisfactory explanations for these interesting features yet, but they could be related to vibronic (spin-phonon) coupling [18, 22]. Since our main interest in this work was to find ZFS parameters, appropriate interpretation of these features is out of scope of the presented thesis.

<sup>2</sup>There were two polymorphs of sample **2**, low-temperature 2LT ( $<167 \text{ K}$ ) and high-temperature 2HT ( $>167 \text{ K}$ ), but since we measured it at  $4.2 \text{ K}$ , we do consider only 2LT polymorph.

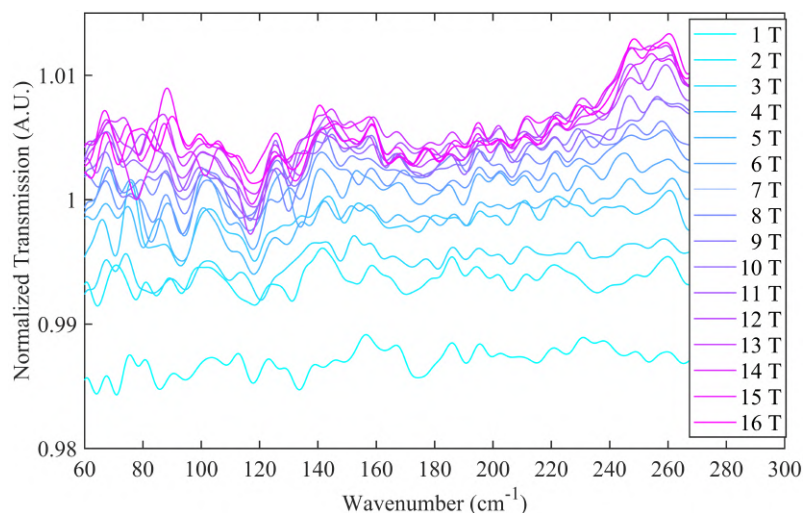


Fig. 4.13: Normalized FIRMS transmission spectra recorded on pressed powder pellet of complex **1** at  $T = 4.2\text{K}$  and magnetic field up to 16 T. Spectra were normalized by zero-field transmission spectra division and corresponding reference transmission spectra division.

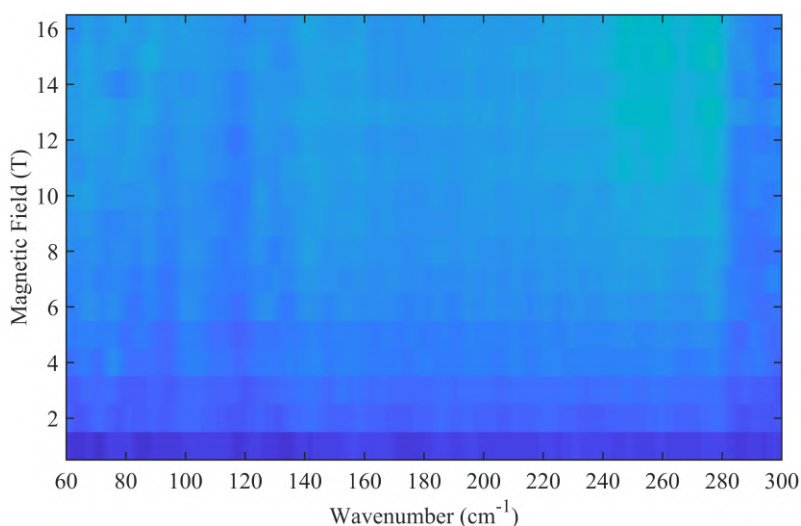


Fig. 4.14: A color map of normalized FIRMS transmission spectra recorded on pressed powder pellet of complex **1** at  $T = 4.2\text{K}$  and magnetic field up to 16 T. Spectra were normalized by zero-field transmission spectra division and corresponding reference transmission spectra division.

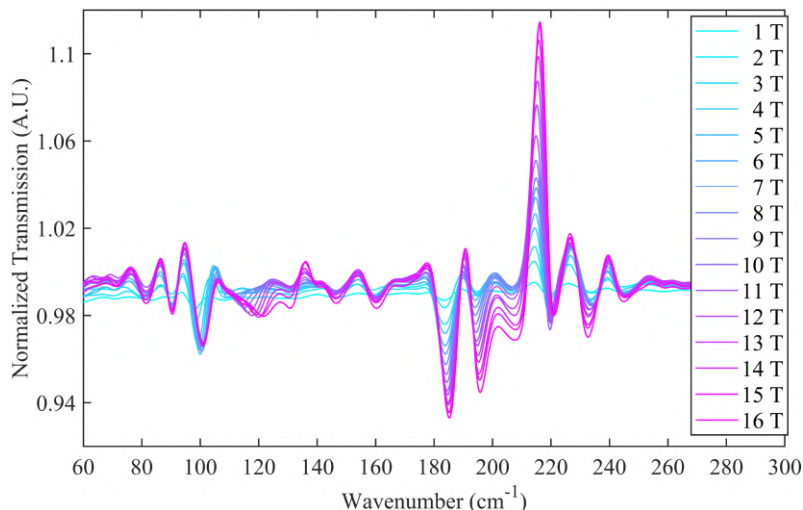


Fig. 4.15: Normalized FIRMS transmission spectra recorded on pressed powder pellet of complex **2** at  $T = 4.2$  K and magnetic field up to 16 T. Spectra were normalized by zero-field transmission spectra division and corresponding reference transmission spectra division.

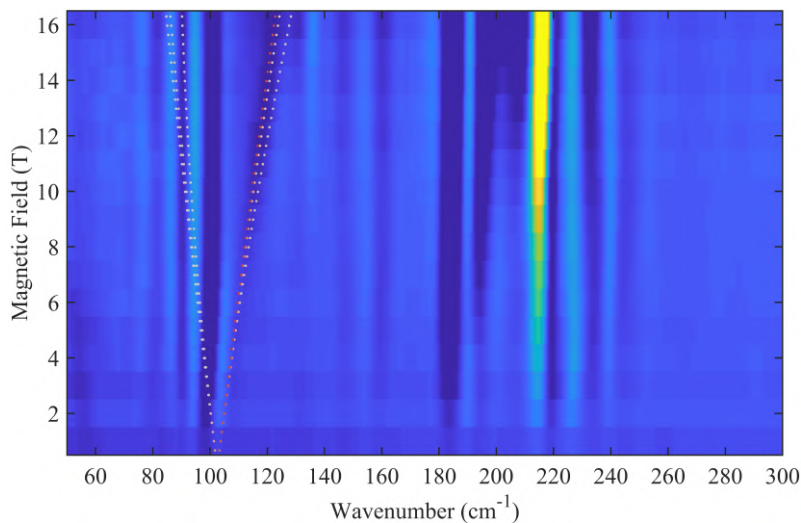


Fig. 4.16: A color map of normalized FIRMS transmission spectra recorded on pressed powder pellet of complex **2** at  $T = 4.2$  K and magnetic field up to 16 T. Simulation with the SH ( $S = 3/2, D = -47$  cm $^{-1}$ ,  $E/D = 0.251$ ,  $g_{iso} = 2.5$ ) is shown as dotted lines. Red color represents the strongly allowed transitions; grey color indicates forbidden/weakly allowed transitions. The tendency toward the yellow color means the absorption is suppressed by the magnetic field, whereas the dark blue color corresponds to the absorption induced by the magnetic field. Spectra were normalized by zero-field transmission spectra division and corresponding reference transmission spectra division.

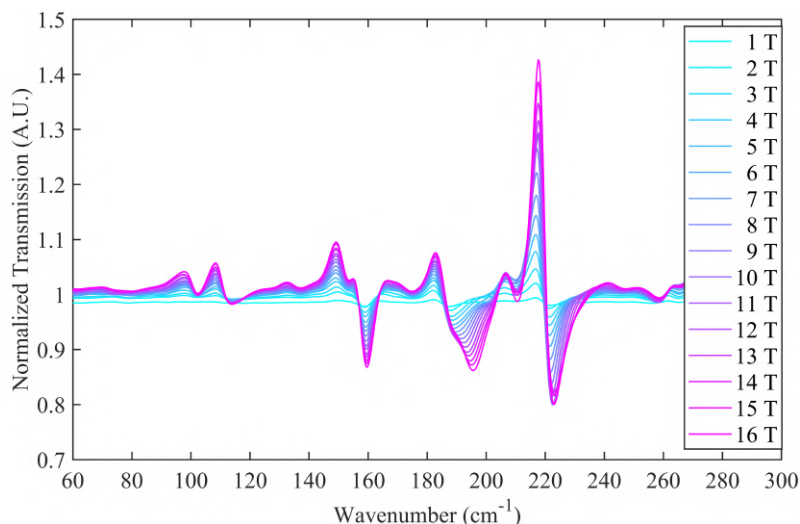


Fig. 4.17: Normalized FIRMS transmission spectra recorded on pressed powder pellet of complex **3** at  $T = 4.2$  K and magnetic field up to 16 T. Spectra were normalized by zero-field transmission spectra division and corresponding reference transmission spectra division.

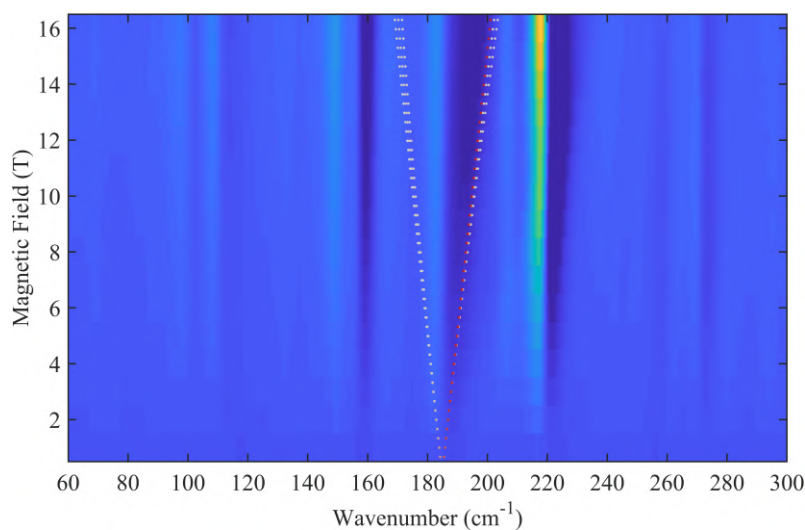


Fig. 4.18: A color map of normalized FIRMS transmission spectra recorded on pressed powder pellet of complex **3** at  $T = 4.2$  K and magnetic field up to 16 T. Simulation with the SH ( $S = 3/2, D = -89 \text{ cm}^{-1}, E/D = 0.162, g_{iso} = 2.1$ ) is shown as dotted lines. Red color represents the strongly allowed transitions; grey color indicates forbidden/weakly allowed transitions. The tendency toward the yellow color means the absorption is suppressed by the magnetic field, whereas the dark blue color corresponds to the absorption induced by the magnetic field. Spectra were normalized by zero-field transmission spectra division and corresponding reference transmission spectra division.

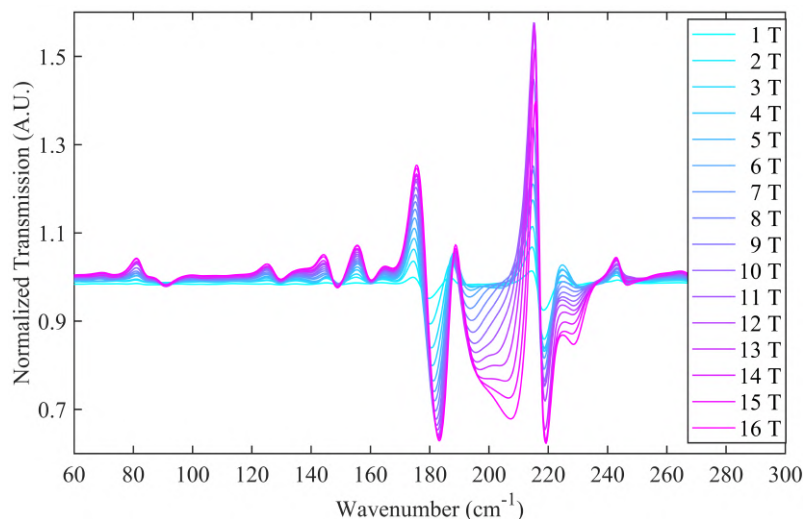


Fig. 4.19: Normalized FIRMS transmission spectra recorded on pressed powder pellet of complex **3** at  $T = 4.2$  K and magnetic field up to 16 T. Spectra were normalized by zero-field transmission spectra division and corresponding reference transmission spectra division.

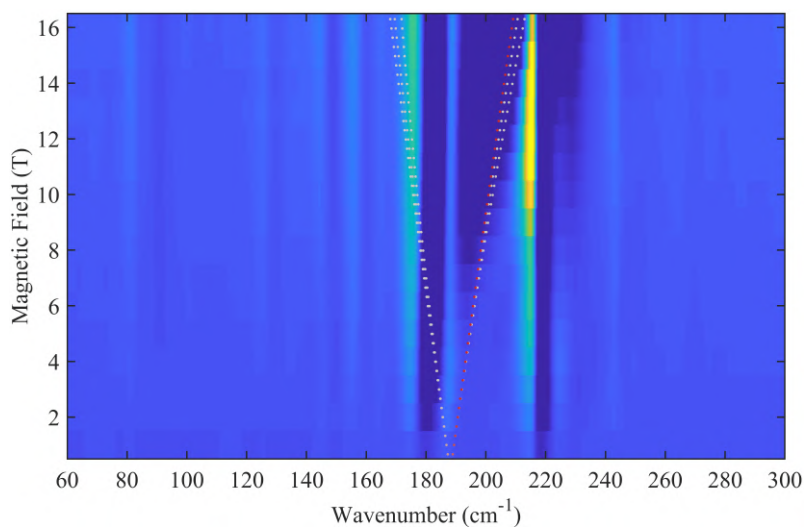


Fig. 4.20: A color map of normalized FIRMS transmission spectra recorded on pressed powder pellet of complex **4** at  $T = 4.2$  K and magnetic field up to 16 T. Simulation with the SH ( $S = 3/2, D = -89 \text{ cm}^{-1}, E/D = 0.197, g_{iso} = 2.7$ ) is shown as dotted lines. Red color represents the strongly allowed transitions; grey color indicates forbidden/weakly allowed transitions. The tendency toward the yellow color means the absorption is suppressed by the magnetic field, whereas the dark blue color corresponds to the absorption induced by the magnetic field. Spectra were normalized by zero-field transmission spectra division and corresponding reference transmission spectra division.

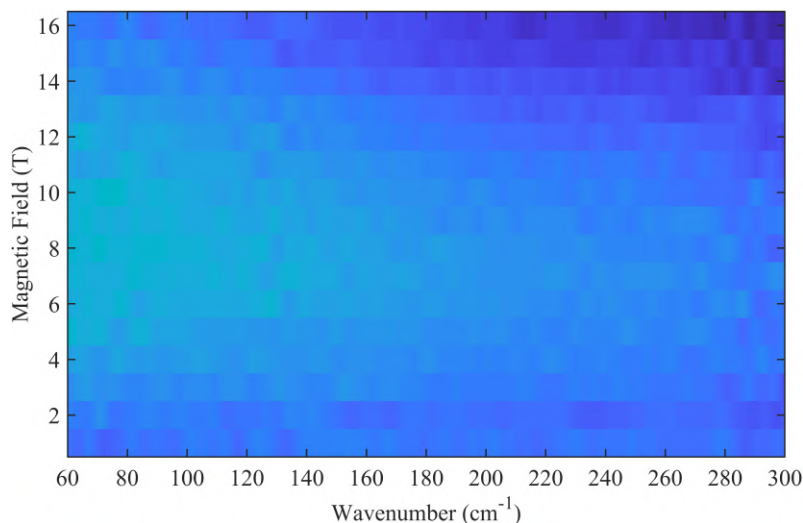


Fig. 4.21: A color map of normalized transmission spectra recorded on pressed powder pellet of complex **1** at  $T = 4.2\text{K}$  and magnetic field up to 16 T. Spectra were normalized by dividing a spectrum measured at  $B_0$  by a spectrum measured at  $B_0 + 1\text{T}$ .

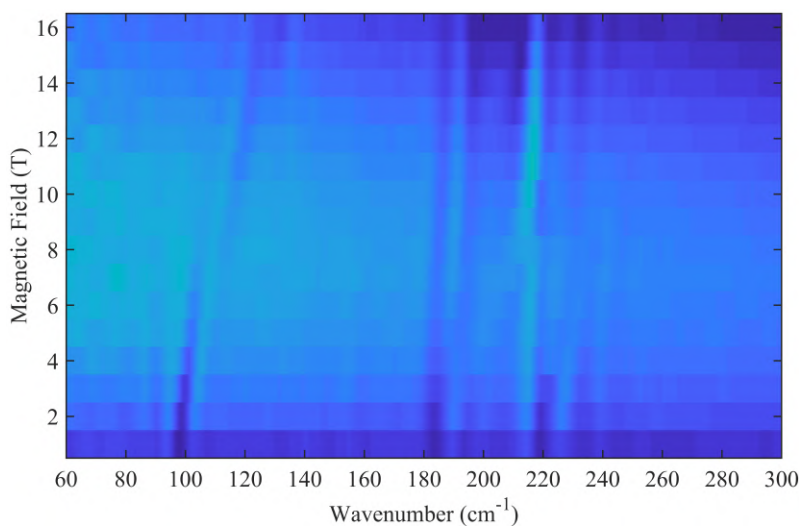


Fig. 4.22: A color map of normalized transmission spectra recorded on pressed powder pellet of complex **2** at  $T = 4.2\text{K}$  and magnetic field up to 16 T. Spectra were normalized by dividing a spectrum measured at  $B_0$  by a spectrum measured at  $B_0 + 1\text{T}$ . The appearance of the weak field-dependent parallel features moving with the field to the right at zero-field around  $100\text{cm}^{-1}$ ,  $190\text{cm}^{-1}$ , and  $220\text{cm}^{-1}$ .

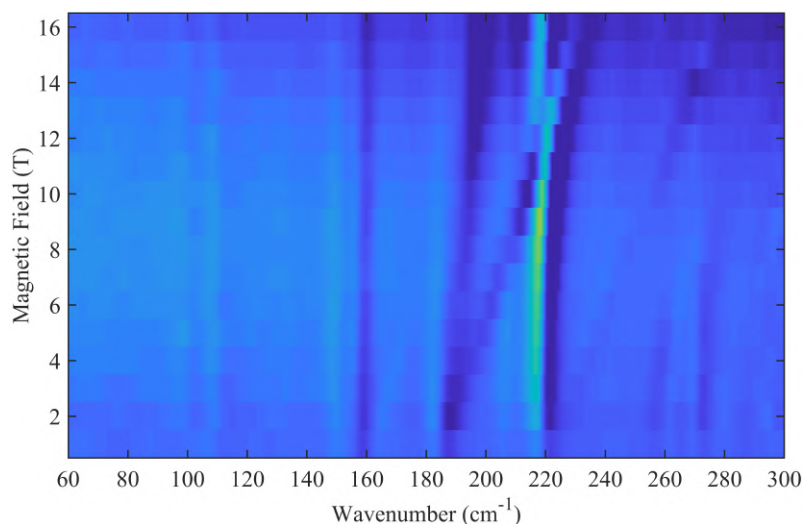


Fig. 4.23: A color map of normalized transmission spectra recorded on pressed powder pellet of complex **3** at  $T = 4.2$  K and magnetic field up to 16 T. Spectra were normalized by dividing a spectrum measured at  $B_0$  by a spectrum measured at  $B_0 + 1$  T. The appearance of the weak field-dependent parallel features moving with the field to the right at zero-field around  $160\text{ cm}^{-1}$ ,  $190\text{ cm}^{-1}$ , and  $220\text{ cm}^{-1}$ .

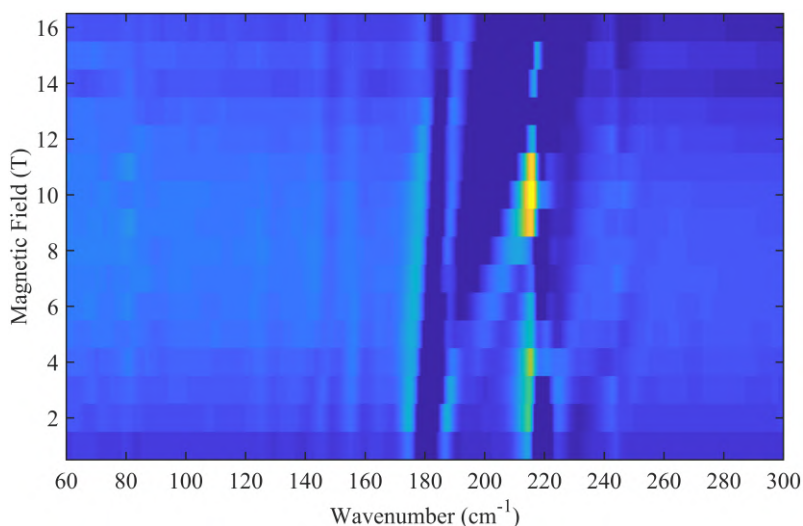


Fig. 4.24: A color map of normalized transmission spectra recorded on pressed powder pellet of complex **4** at  $T = 4.2$  K and magnetic field up to 16 T. Spectra were normalized by dividing a spectrum measured at  $B_0$  by a spectrum measured at  $B_0 + 1$  T. The appearance of the weak field-dependent parallel features moving with the field to the right at zero-field around  $140\text{ cm}^{-1}$ ,  $190\text{ cm}^{-1}$ , and  $220\text{ cm}^{-1}$ .

## 4.2.2 Mononuclear Cobalt(II) Field-Induced SMM

Following results were obtained in cooperation and published in *Crystal Growth & Design* [14]:

Malinová, N.; Juráková, J.; Brachňáková, B.; **Dubnická Midlíková, J.**; Čižmár, E.; Tadeu Santana, V.; Herchel, R.; Orlita, M.; Mohelský, I.; Moncol, J.; Neugebauer, P.; Šalitroš, I. Magnetization Slow Dynamics in Mononuclear Co(II) Field-Induced Single-Molecule Magnet. *Crystal Growth & Design*. 2023, vol. 23, no. 4, pp. 2430–2441. <https://doi.org/10.1021/acs.cgd.2c01388>.

### Abstract

The novel tridentate ligand *L* (2,6-Bis(1-(*n*-decyl)-1*H*-benzimidazol-2-yl)pyridine) was used for the synthesis of mononuclear Co(II) complex **1** of general formula [Co(*L*)Br<sub>2</sub>]. The single-crystal X-ray structural investigation confirmed the expected molecular structure and non-covalent contacts were inspected by Hirschfeld surface analysis. The electronic structure of square-pyramidal complex **1** contains an orbitally degenerate ground state which predetermines to use the Griffith-Figgis Hamiltonian for the analysis of magnetic properties. CASSCF-NEVPT2 calculations along with far-infrared magnetic spectroscopy show excellent agreement with the Griffith-Figgis Hamiltonian parameters obtained from the magnetic investigation. The high and negative value of the axial crystal field parameter  $\Delta_{ax}$  and the calculated *g*-tensor components suggest the axial magnetic anisotropy of **1**. The low-temperature EPR spectra of the studied compounds were analyzed within a simplified effective spin-1/2 model to determine effective *g*-tensor components of the ground Kramers doublet, which agree with the electronic structure predicted within the CASSCF-NEVPT2 theory. The dynamic magnetic investigation revealed field-induced single-channel slow relaxation of magnetization with maximal relaxation time  $\tau \approx 28$  ms at low temperatures. The comprehensive analysis of the field and temperature evolution of  $\tau$  indicates that all three direct, Raman, and Orbach processes are involved in slow relaxation of magnetization in **1**.

### Far Infrared Magnetic Spectroscopy (FIRMS)

The investigation of the magnetic anisotropy in that family of pentacoordinate Co(II) complexes is, however, not so straightforward. As a matter of fact, most of the studies almost exclusively use the ZFS spin Hamiltonian to analyze the static magnetic properties. The axial (*D*) and rhombic (*E*) ZFS parameters have physical meaning only if the ground state is orbitally nondegenerate and well separated from the closest excited states. Another option is the Griffith–Figgis Hamiltonian, which was originally designed for octahedral systems possessing (or approaching) an

orbitally triple-degenerate ground state. Griffith–Figgis Hamiltonian is defined by several parameters, from which we are interested in  $\Delta_{ax}$  and  $\Delta_{rh}$  that are parameters of a crystal field with axial and rhombic symmetry, respectively,  $\lambda$  is the constant of the spin–orbit interaction,  $\alpha$  is an orbital reduction factor. For more information about Griffith–Figgis Hamiltonian, see ref. [204].

To determine experimentally the separation between the ground and first excited states, FIRMS was exploited. It enables us to observe EPR transitions of SMMs with large ZFS, mainly based on transition metal complexes. In the case when the system cannot be modeled by SH, we determine the separation between the ground and first excited states directly from the spectra based on the solution of the Griffith – Figgis Hamiltonian. The FIRMS spectra were recorded for pressed powder pellets of **1**, shown in Fig. 4.25, (diluted in eicosane) at  $T = 4.2\text{ K}$ , and magnetic fields up to 16 T. The spectra of the sample at magnetic fields  $S(B)$  were normalized by the zero-field transmission spectra,  $S(0)$ , and their corresponding reference transmission spectra division  $R(B)/R(0)$ . Normalized transmission spectra, see Fig. 4.26, were then depicted in the form of a color map for better identification of the EPR transitions. In the color map, the tendency toward the yellow color means the absorption is suppressed by the magnetic field, whereas the dark blue color corresponds to the absorption induced by the magnetic field. A color map of the normalized FIRMS transmission spectra of complex **1** displayed in Fig. 4.27 shows a clear field-dependence of the peak occurring at  $\sim 186\text{ cm}_2$  at zero magnetic field and attributed to the EPR transition between the ground state and the first excited Kramers doublet.

FIRMS simulations, shown as dotted lines Fig. 4.27, were calculated by means of the EasySpin Toolbox for Matlab [120] based on the Griffith – Figgis Hamiltonian and the parameters obtained from magnetization measurement and *ab initio* calculations as an initial guess for the fitting. The red color of the simulation represents the strongly allowed transitions; the grey color indicates forbidden/weakly allowed transitions. We obtained a reasonably good fit with the following parameters:  $\Delta_{ax} = -1508\text{ cm}^{-1}$ ,  $\Delta_{rh} = -164\text{ cm}^{-1}$ ,  $\lambda = -105\text{ cm}^{-1}$ ,  $\alpha = 2.19$  (Table 1) which are highly comparable with the values obtained from the analysis of the static magnetic properties or from the CASSCF/DLPNO-NEVPT2 calculations.

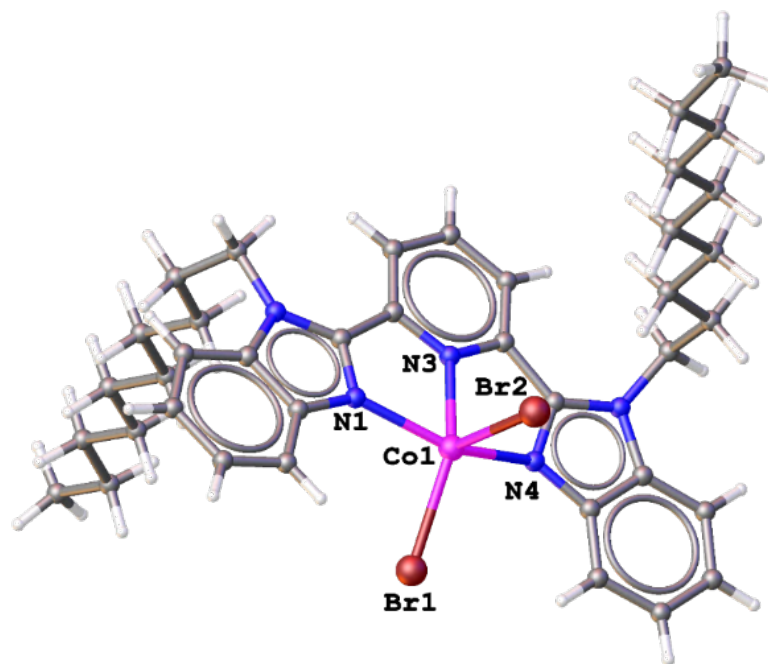


Fig. 4.25: Molecular structures of **1**. Adapted from [14].

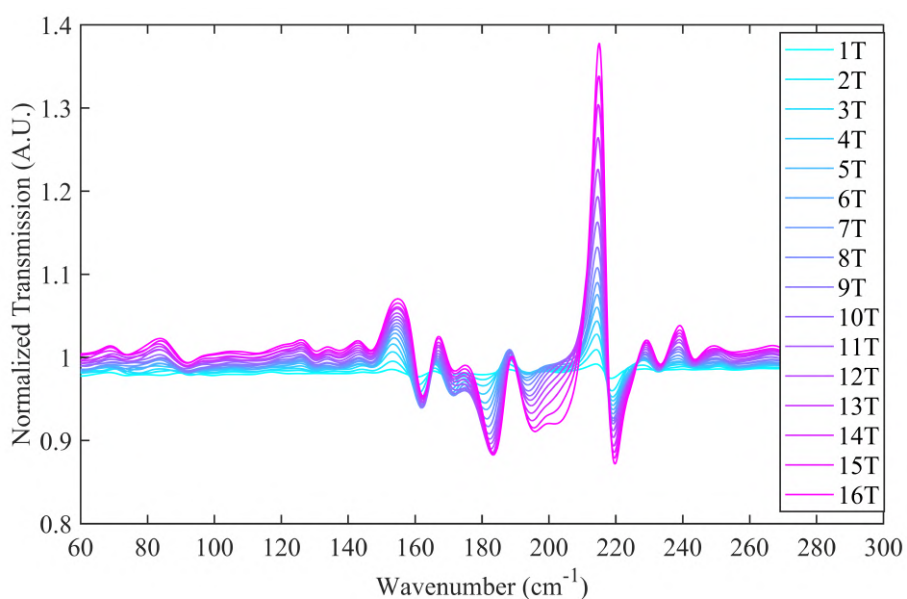


Fig. 4.26: Normalized FIRMS transmission spectra recorded on pressed powder pellet of complex **1** at  $T = 4.2\text{K}$  and magnetic field up to 16 T. Spectra were normalized by zero-field transmission spectra division and corresponding reference transmission spectra division.

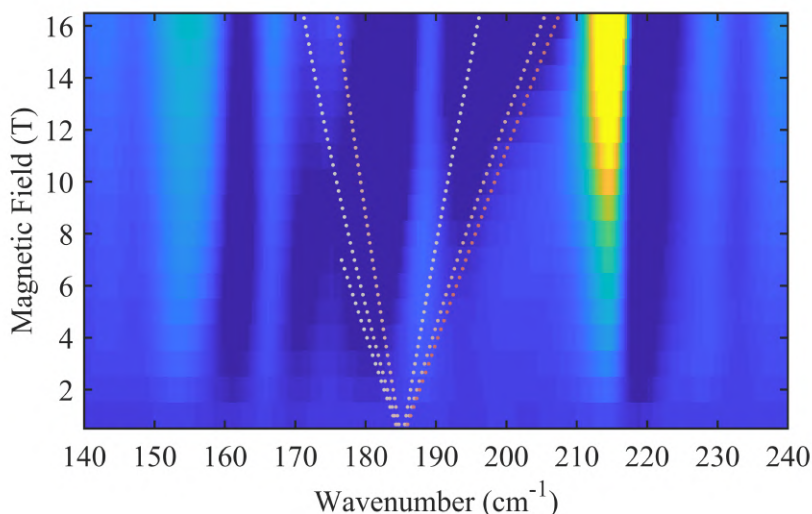


Fig. 4.27: A color map of normalized FIRMS transmission spectra recorded on pressed powder pellets of complex **1** measured at  $T = 4.2$  K and magnetic field up to 16 T. The spectra were normalized by zero-field transmission spectra and corresponding reference transmission spectra. Simulations with the Griffith – Figgis Hamiltonian ( $\Delta_{ax} = -1508 \text{ cm}^{-1}$ ,  $\Delta_{rh} = -164 \text{ cm}^{-1}$ ,  $\lambda = -105 \text{ cm}^{-1}$ ,  $\alpha = 2.19$ ) are shown as dotted lines. The red color represents the strongly allowed transitions; the grey color indicates forbidden/weakly allowed transitions. The tendency toward the yellow color means the absorption is suppressed by the magnetic field, whereas the dark blue color corresponds to the absorption induced by the magnetic field.

### 4.3 Measurements at CEITEC BUT

Following magneto-optical measurements on the FTIR magneto-spectroscopic setup located at CEITEC BUT. We demonstrate the functionality of the FTIR magneto-spectroscopic setup in various configurations on several different samples, i.e. SIM, germanium, graphene. The magneto-optical response of the studied samples has been explored in the THz/IR range, using the standard Faraday configuration. In the FIR range, we used global source and LHe-cooled bolometers for SIM sample, and room temperature DTGS detector for graphene. In the NIR range, we used Tungsten lamp and room temperature InGaAs detector to measure germanium. We also performed tests of graphene bolometers [189] – [191] in the chipset holder [187], [188] in configuration of the setup with Probe B - Chipset with global and tungsten sources. Data from magneto-optical measurements presented in this section were obtained using Labview program (created by Ing. Matúš Šedivý) that combines control of the superconducting magnet and the FTIR spectrometer.

### 4.3.1 Zero-field Splitting in Cobalt(II)-based SIM

Following results were obtained in cooperation and published in *IEEE Transactions on Instrumentation and Measurement (TIM)* [15]:

**Dubnická Midlíková, J.;** Šedivý, M.; Sojka, A.; Tadeu Santana, V.; Dubroka, A.; Neugebauer, P. A Versatile Setup for FTIR Magneto-Spectroscopy *IEEE Transactions on Instrumentation and Measurement*. 2023, vol. 72, pp. 1-11. <https://doi.org/10.1109/TIM.2023.3284943>.

#### Abstract

*Fourier-transform infrared (FTIR) magneto-spectroscopy is a powerful spectroscopic technique used to investigate many important effects in materials, e.g., electron spin resonance, cyclotron resonance, and transitions between Landau levels. Despite their enormous potential in material science, infrared magneto-spectrometers are still relatively rare and custom-made since such systems generally require complex infrastructure. This article presents a broadband setup for FTIR magneto-spectroscopy spanning the range from THz/far-infrared (FIR) to near-infrared (NIR), high magnetic field up to 16 T, and cryogenic temperatures down to 2 K. It consists of a commercial FTIR spectrometer and 16 T cryogen-free superconducting magnet coupled with custom-designed optical coupling and transmission probes for experiments with various detectors. The versatility of the FTIR magneto-spectroscopic setup is demonstrated by the magneto-optical measurements on a cobalt-based single-molecule magnet in the FIR and germanium in the NIR range.*

The functionality of the FTIR magneto-spectroscopic setup was demonstrated on two samples. The first sample was a representative of SIM with very large ZFS, which was measured in the FIR range on the magneto-optical setup at GHMFL; results of these measurements can be found in [13] for complex labeled as **3**. We chose this sample (identical 12 mg pellet) so we can compare the results obtained from our setup in the FIR range with those previously published. By the magneto-optical measurements of complex **3**, we tested the setup in the FIR region.

For cobalt(II) complexes with  $S = 3/2$ , the ZFS between two Kramers doublets is equal to  $2(D^2 + 3E^2)^{1/2}$ . This energy gap is then directly observable in FTIR magneto-optical spectra as  $2D$  (when omitting rhombicity  $E$ ).

The spectra of pressed powder pellet of pentacoordinate cobalt(II)-based complex **3** ( $[\text{Co}(\text{L}2)\text{Cl}_2]$ , where  $\text{L}2 = 2,6\text{-bis}(1\text{-dodecyl-1H-benzimidazole-2-yl})\text{-pyridine}$  (see Fig. 4.28), were recorded in Probe A configuration with 1.6 K standard bolometer in the FIR range at  $T = 2\text{ K}$ , and magnetic fields  $B$  up to 16 T. The spectra were measured with resolution  $4\text{ cm}^{-1}$ , same as in [13] (see Fig. 4.29, 4.30), and

resolution  $1 \text{ cm}^{-1}$ , see Fig. 4.31, 4.33, and 4.32. Since the peaks are very narrow, resolution  $1 \text{ cm}^{-1}$  was found to be more suitable than resolution  $4 \text{ cm}^{-1}$ . The transmission spectra of the sample at magnetic field ( $T_B$ ) were normalized by the zero-field transmission spectra of the sample ( $T_0$ ),  $T_B/T_0$ . Normalized relative transmission spectra (Fig. 4.29, 4.31) are depicted in the form of a color map in Fig. 4.32 (Fig. 4.30, 4.33) for better identification of the EPR transitions. Color maps of the normalized relative transmission spectra show a clear field-dependence of one of the peaks starting at  $\sim 186 \text{ cm}^{-1}$  at zero magnetic field attributed to the EPR transition from  $m_s = \pm 3/2$  to  $m_s = \pm 1/2$  states. In Fig. 4.32, we applied the same simulation as in [13] calculated using the EasySpin Toolbox for Matlab [120] based on the SH and the parameters  $E/D = 0.162$ ,  $D = -89 \text{ cm}^{-1}$ ,  $g_{iso} = 2.1$ . In addition, we normalized the data as  $T_B/T_{B+1}$  and applied the same simulation to confirm the peak position (see Fig. 4.33). Red color of the simulation represents the strongly allowed transitions; grey color indicates forbidden/weakly allowed transitions. The spectra obtained on our setup at CEITEC BUT shown in Fig. 4.32 are almost identical to those obtained at GHMFL (Fig. 4.30(b)). In all color maps, the tendency toward the yellow color means the absorption is suppressed by the magnetic field, whereas the dark blue color means the absorption is induced by the magnetic field.

In addition, we normalized the data by dividing a transmission spectrum of the sample  $T_B$  measured at  $B$  by a transmission spectrum  $T_{B+1}$  measured on the sample at  $B + 1 \text{ T}$ ,  $T_{B+1}/T_B$ , in order to confirm the peak position in the color map shown in Fig. 4.32 (normalized as  $T_B/T_0$ ). The  $T_{B+1}/T_B$  normalization can reveal weaker field-dependent features in the color map spectra. A color map of normalized relative transmission spectra normalized as  $T_{B+1}/T_B$  recorded on pressed powder pellet of complex **3** at 2 K, and magnetic field up to 16 T and resolution  $1 \text{ cm}^{-1}$  on the FTIR magneto-spectroscopic setup at CEITEC BUT is shown Fig. 4.33, which revealed two field-dependent lines/features moving with the field to the right that appeared at zero magnetic field around  $186 \text{ cm}^{-1}$ . The first field-dependent line with the bigger angle of inclination represents the EPR transition from  $m_s = \pm 3/2$  to  $m_s = \pm 1/2$  states, on which we applied the same simulation as previous ( $S = 3/2, D = -89 \text{ cm}^{-1}$ ,  $E/D = 0.162$ ,  $g_{iso} = 2.1$ ) shown as dotted lines. Red color of the simulation represents the strongly allowed transitions; grey color indicates forbidden/weakly allowed transitions. The red line of the simulation copies the edge of the first line well, which confirms the position of the wanted peak and the right choice of parameters in the simulation. For the second field-dependent line/feature with approx. 2.5 times smaller angle of inclination than the first line, we do not have a satisfactory explanation yet, but it could be related to vibronic (spin-phonon) coupling [22]. However, its theoretical explanation is beyond the scope of this manuscript and will be our concern in future work.

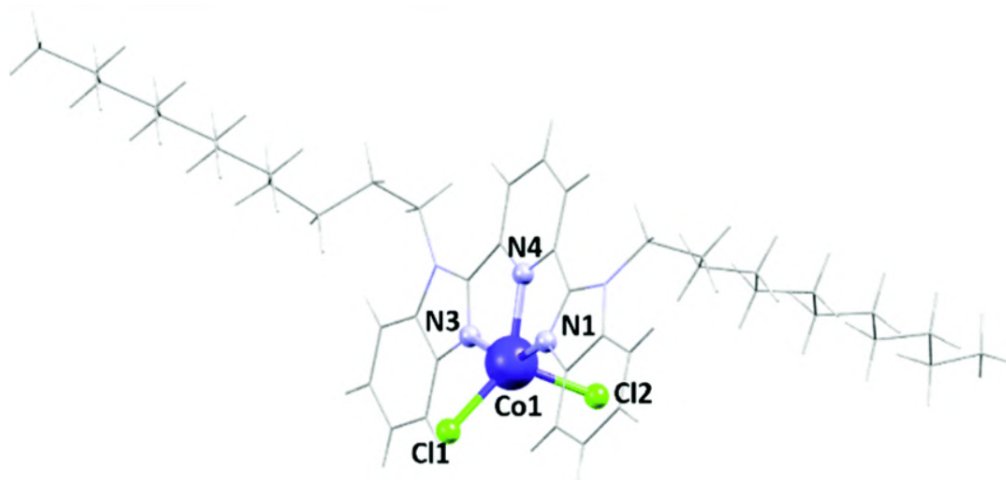


Fig. 4.28: Crystallographic structure of the pentacoordinate cobalt(II)-based complex **3**,  $[\text{Co}(\text{L}2)\text{Cl}_2]$ , where  $\text{L}2 = 2,6\text{-bis}(1\text{-dodecyl-1H-benzimidazole-2-yl})\text{-pyridine}$ . Cobalt is shown in dark blue, nitrogen in light blue, chlorine in green.

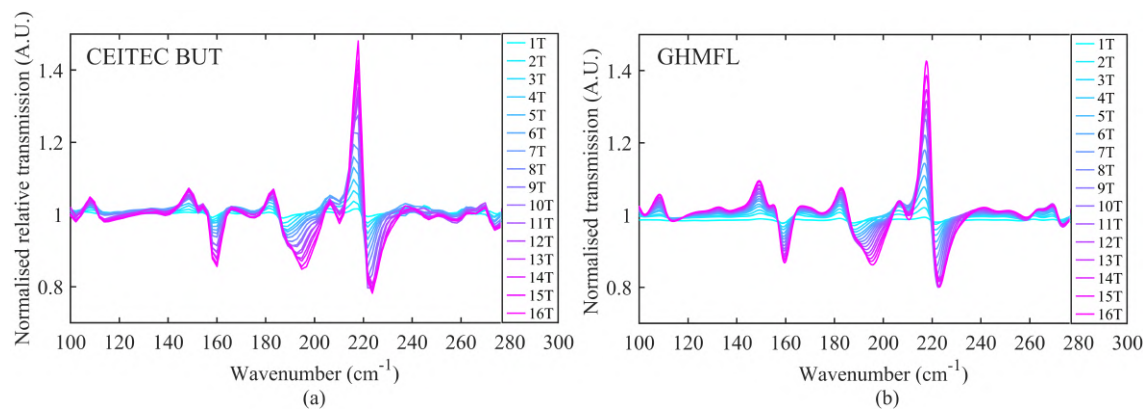


Fig. 4.29: (a) Normalized relative transmission spectra recorded on pressed powder pellet of complex **3** at  $T = 2\text{ K}$  and magnetic field up to  $16\text{ T}$  and resolution  $4\text{ cm}^{-1}$  on the FTIR magneto-spectroscopic setup at CEITEC BUT. The spectra at magnetic field ( $T_B$ ) were normalized by the zero-field transmission spectra ( $T_0$ ),  $T_B/T_0$ . (b) Normalized transmission spectra recorded on pressed powder pellet of complex **3** at  $T = 4.2\text{ K}$  and magnetic field up to  $16\text{ T}$  and resolution  $4\text{ cm}^{-1}$  at GHMFL. Spectra were normalized by zero-field transmission spectra division and corresponding reference transmission spectra division.

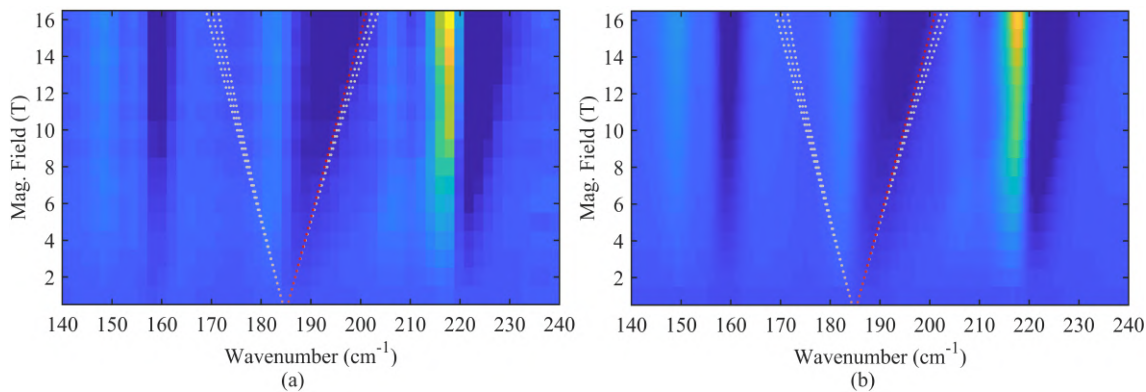


Fig. 4.30: (a) A color map of normalized relative transmission spectra recorded on pressed powder pellet of complex **3** at  $T = 2$  K and magnetic field up to 16 T and resolution  $4 \text{ cm}^{-1}$  on the FTIR magneto-spectroscopic setup at CEITEC BUT. (b) A color map of normalized transmission spectra recorded on pressed powder pellet of complex **3** at  $T = 4.2$  K and magnetic field up to 16 T and resolution  $4 \text{ cm}^{-1}$  at GHMFL. Simulations in (a) and (b) with the SH ( $S = 3/2$ ,  $D = -89 \text{ cm}^{-1}$ ,  $E/D = 0.162$ ,  $g_{iso} = 2.1$ ) are shown as dotted lines. Red color represents the strongly allowed transitions; grey color indicates forbidden/weakly allowed transitions. In the color maps, the tendency toward the yellow color means the absorption is suppressed by the magnetic field, whereas the dark blue color corresponds to the absorption induced by the magnetic field. The spectra recorded with resolution  $4 \text{ cm}^{-1}$  obtained on our setup at CEITEC BUT (a) and those obtained at GHMFL (b) are almost identical. The slight difference in the smoothness of the spectra in (b) is caused by different spectrometer settings, i.e., higher filling factor, which one of the settings of an interferogram before performing FT in the OPUS software that increases the number of data points in the spectrum that is equivalent to an interpolation resulting in smoother spectra plots, at GHMFL (in (a) filling factor = 2, in (b) filling factor = 8).

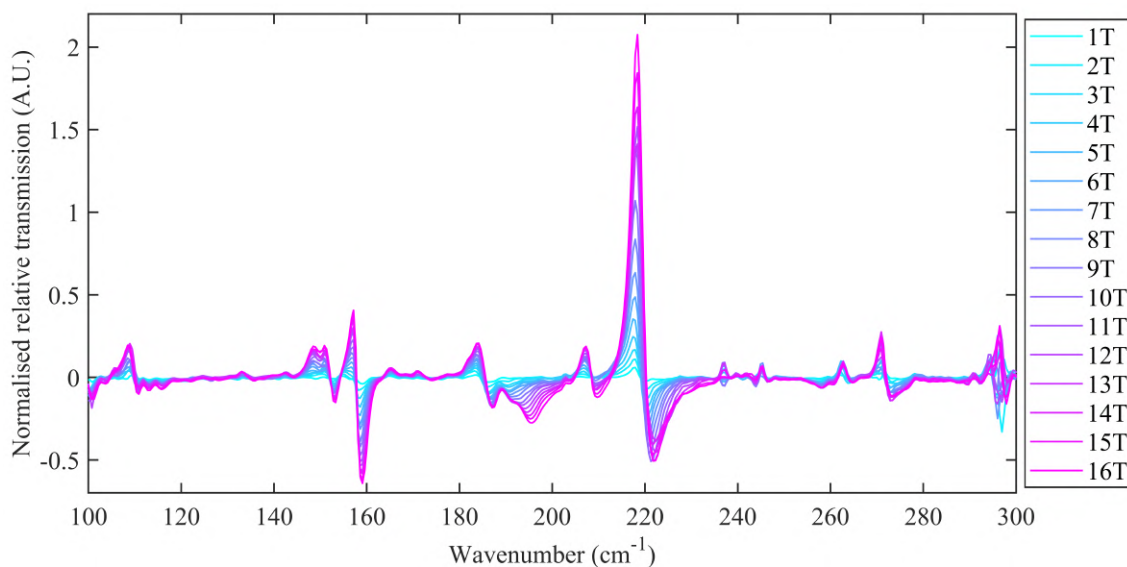


Fig. 4.31: Normalized relative transmission spectra (with baseline correction) recorded on pressed powder pellet of complex **3** at  $T = 2$  K and magnetic field up to 16 T and resolution  $1 \text{ cm}^{-1}$  on the FTIR magneto-spectroscopic setup at CEITEC BUT. The spectra at magnetic field ( $T_B$ ) were normalized by the zero-field transmission spectra ( $T_0$ ),  $T_B/T_0$ .

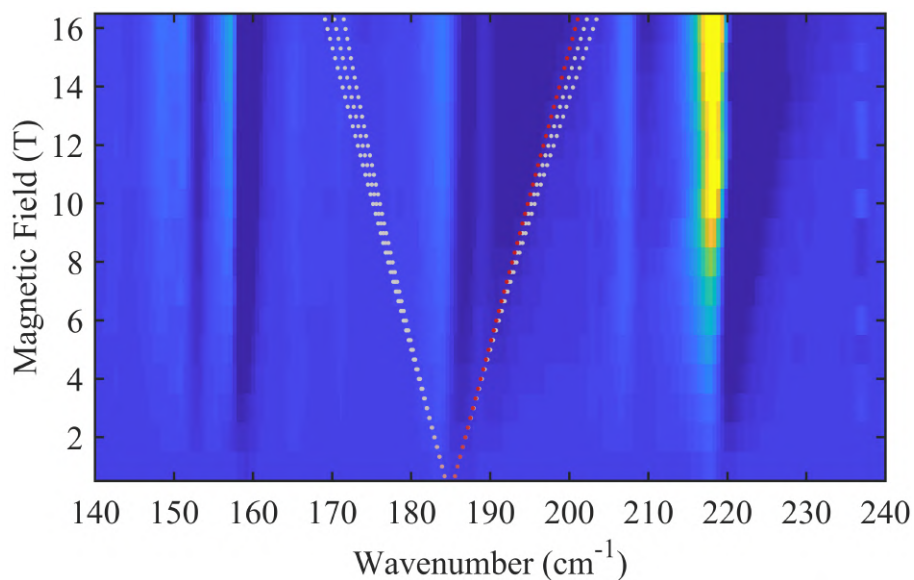


Fig. 4.32: A color map of normalized relative transmission spectra recorded on pressed powder pellet of **3** measured at  $T = 2$  K, magnetic field up to 16 T, and resolution  $1 \text{ cm}^{-1}$  obtained on our FTIR magneto-spectroscopic setup.

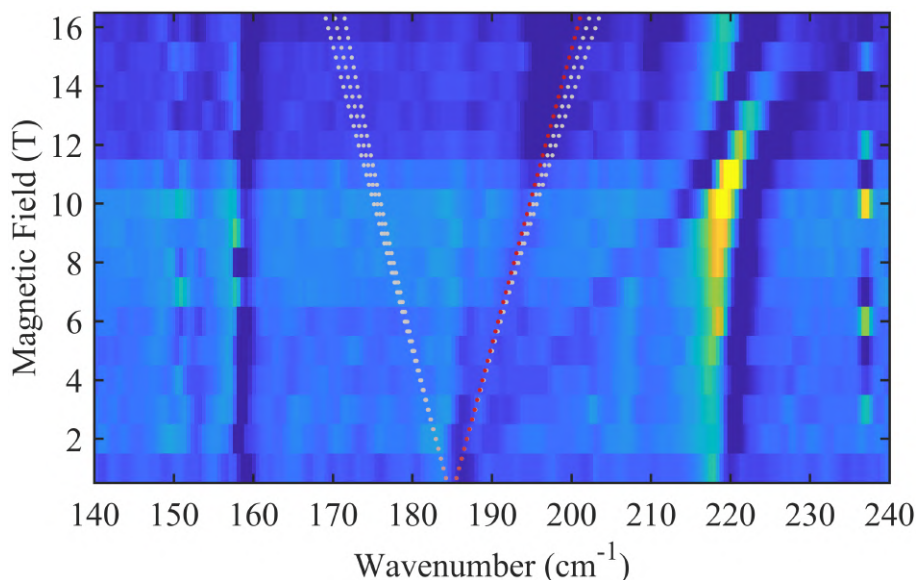


Fig. 4.33: A color map of normalized relative transmission spectra normalized as  $T_{B+1}/T_B$  recorded on pressed powder pellet of complex **3** at 2 K, magnetic field up to 16 T, and resolution  $1 \text{ cm}^{-1}$  on the FTIR magneto-spectroscopic setup at CEITEC BUT. The color map reveals two field-dependent lines/features moving with the field to the right that appeared at zero magnetic field around  $186 \text{ cm}^{-1}$ . The first line with the bigger angle of inclination is attributed to the EPR transition with applied simulation ( $S = 3/2$ ,  $D = -89 \text{ cm}^{-1}$ ,  $E/D = 0.162$ ,  $g_{iso} = 2.1$ ) shown as dotted lines. Red color represents the strongly allowed transitions; grey color indicates forbidden/weakly allowed transitions. The second line/feature has approx. 2.5 times smaller angle of inclination than the first line, and its theoretical explanation is beyond the scope of this manuscript. In the color maps, the tendency toward the yellow color means the absorption is suppressed by the magnetic field, whereas the dark blue color corresponds to the absorption induced by the magnetic field.

### 4.3.2 Indirect Interband Transitions between LLs in Germanium

Following results were obtained in cooperation and published in *IEEE TIM* [15]: **Dubnická Midlíková, J.**; Šedivý, M.; Sojka, A.; Tadeu Santana, V.; Dubroka, A.; Neugebauer, P. A Versatile Setup for FTIR Magneto-Spectroscopy *IEEE Transactions on Instrumentation and Measurement*. 2023, vol. 72, pp. 1-11. <https://doi.org/10.1109/TIM.2023.3284943>.

Since these results were published in the same publication as the results from the previous subsection entitled Zero-field Splitting in Cobalt(II)-based SIM, the abstract is given in subsection 4.3.1.

The functionality of the FTIR magneto-spectroscopic setup was demonstrated on two samples. The second sample was a well-known indirect band gap semiconductor – germanium (Ge), measured in the NIR range to observe the magneto-optical response of its absorption edge. We chose Ge due to its well-studied band structure and the amount of available literature [205], [206].

Using the FTIR magneto-spectroscopy, we can probe the band structure, e.g., Landau levels (LLs), and elucidate the electronic properties of 2D materials such as graphene [23] – [28], or semiconductors such as germanium [205], [206], [207].

The magneto-optical spectra were acquired on a very weakly p-type gallium-doped Ge ( $\rho = 11 \Omega\text{cm}$ ,  $p = 2 \times 10^{14} \text{cm}^{-3}$ ) (100) wafer at 5 K in the magnetic field  $B$  up to 16 T with Probe A and InGaAs room temperature detector in the NIR region. Fig. 4.34 shows normalized relative transmission spectra ( $T_B/T_0$ ) of Ge measured with resolution  $8 \text{cm}^{-1}$  at 64 values of applied magnetic fields  $B$  from 0.25 T to 16 T with step 0.25 T plotted with an offset for clarity. The spectra are shown in the range of absorption edge of Ge at low temperatures. The maxima correspond to individual inter-LL transitions. The minima correspond to the suppression of zero-field absorption. Normalized relative transmission spectra from Fig. 4.34 were visualized as a color map shown in Fig. 4.35(a). Fig. 4.35(b) displays a color map of the second derivative of these normalized relative transmission spectra to enhance fine structures, e.g. the splitting of LL transitions. The maxima of the signal in Fig. 4.35(b) are shown in Fig. 4.35(c).

They were analyzed using the model of transitions between LLs of parabolic bands [208]:

$$E_N = \Delta E_N + (N + \frac{1}{2})\hbar\omega_c, \quad (4.1)$$

where  $N = 0, 1, 2, \dots$  is the index of a LL,  $\Delta E_N$  is the energy value at  $B = 0$ ,  $\omega_c = eB/\mu$  is the cyclotron frequency,  $e$  is the elementary charge, and  $\mu$  is the reduced effective mass. Parabolicity of the bands leads to the linear dependence of

the energy of absorption lines to the magnetic field, which is well fulfilled in the whole measured range. The model employs three different reduced effective masses,  $\mu_1 = (0.128 \pm 0.015) m$ ,  $\mu_2 = (0.132 \pm 0.016) m$ ,  $\mu_3 = (0.138 \pm 0.014) m$  where  $m$  is the free electron mass, to account for the small splitting of LL, which becomes apparent for  $N > 3$ . The Landau level with  $N=0$  has a different value of  $\Delta E_{N=0} = 769$  meV than for  $N > 3$ ,  $\Delta E_{N>0} = 773$  meV. The latter indicates that a different phonon mediates  $N=0$  transition than  $N > 0$  transitions. Considering the value of the band gap of Ge at low temperatures of 741 meV [209], the energy of phonons amounts to 28 meV for  $N=0$  transition and 32 meV for  $N > 0$  transitions. The three values of reduced effective masses compare well with the electron effective masses obtained by Dresselhaus *et al.* for the sample with a magnetic field tilted by a few degrees from the (001) direction, see Fig. 5 in Ref. [205]. Surprisingly, the obtained effective masses compare well with the electron effective mass rather than with the reduced effective mass  $1/\mu = 1/m_{hh} + 1/m_e$ , which is expected for an indirect transition between the heavy hole band with effective hole mass  $m_{hh} = 0.29 m$  and the conduction band with effective electron mass  $m_e = 0.13 m$  for  $B$  in 001 direction. We tentatively interpret this observation as a transition between localized hole states (with a very large effective mass) to the conduction band.

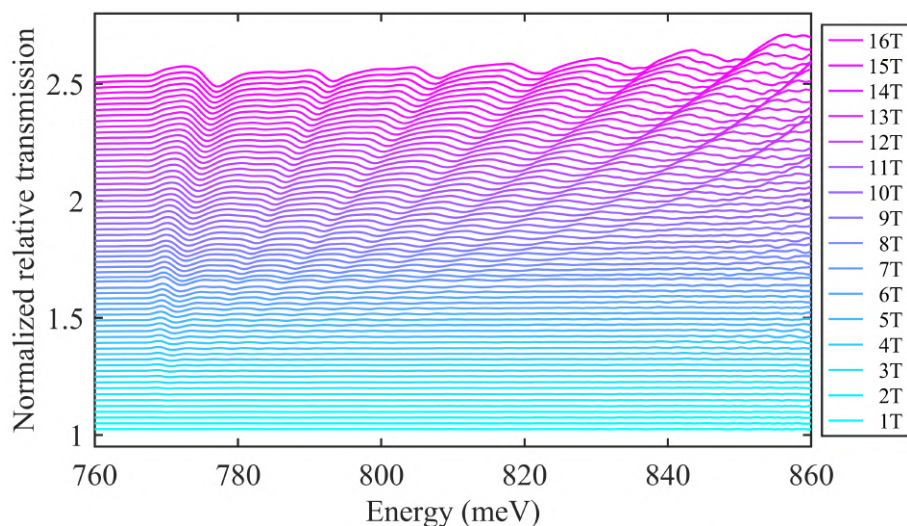


Fig. 4.34: Normalized relative transmission spectra,  $T_B/T_0$ , plotted with an offset for 64 values of applied magnetic fields from 0.25 T to 16 T with step 0.25 T. The maxima correspond to individual inter-LL transitions, and the minima emerge due to the suppression of the zero-field absorption.

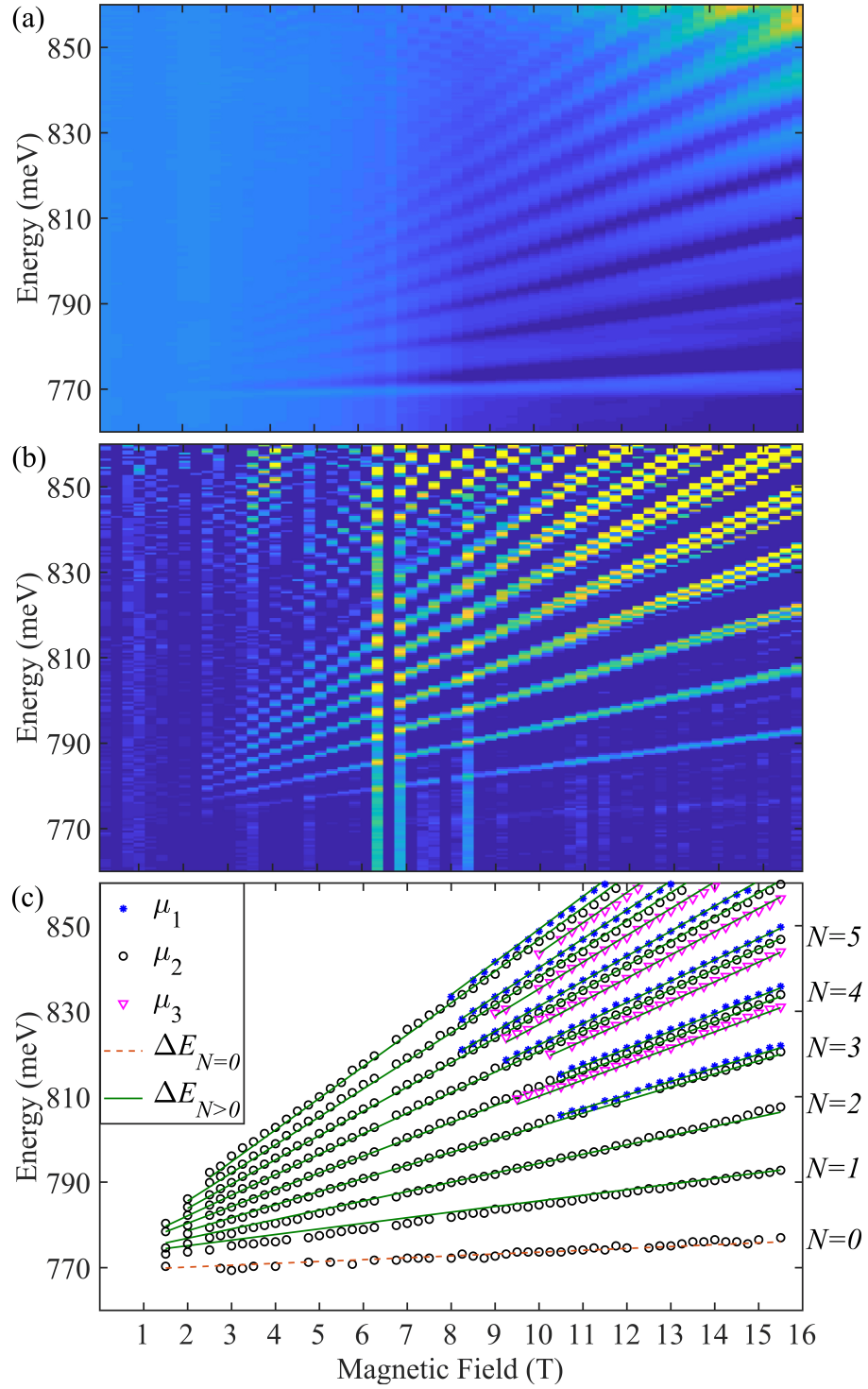


Fig. 4.35: (a) A color map of normalized relative transmission spectra from Fig. 4.34, (b) a color map of the second derivative of normalized relative transmission spectra from (a). (c) The minima of (b) fitted with a model of LL transitions as described in the text. Three markers correspond to three values of reduced effective mass. The solid and dashed lines correspond to two values of  $\Delta E_N$ .

### 4.3.3 Graphene

We decided to test the functionality of the FTIR magneto-spectroscopic setup in Probe A configuration with FIR-DTGS room temperature detector. As can be seen in Tab. 3.2, this configuration exhibited significant noise compared to the others. With these magneto-optical measurements, we want to demonstrate that even with the less sensitive room temperature detector, valuable information can be obtained when using a sufficient number of scans and sample with a strong signal.

For this measurement, we have chosen the multilayer epitaxial graphene (MEG), provided by RNDr. Jan Kunc, Ph.D., which was already measured in the FIR range on the IR magneto-optical setup at GHMFL, and the results of these measurements were published in [23]. Thus, we can compare the results obtained from our setup with those previously published.

The MEG sample was prepared by thermal decomposition from a 4H-SiC substrate and contains around 100 graphene layers, which are electrically decoupled [210, 211]. It is highly conducting in the very close vicinity of the interface with SiC, as a result of charge transfer from SiC [212, 213]. The subsequent layers are practically neutral [23, 213].

Landau levels in graphene are non-equidistant and nonlinear in magnetic field, they have unusual  $\sqrt{B}$  dependence, that is a consequence of the linearity of the bands [145]. The application of the magnetic field  $B$  perpendicular to its plane transforms the continuous electronic spectrum into discrete and highly degenerate Landau levels with energies:

$$E_N = \text{sgn}(n)\tilde{c}\sqrt{2e\hbar B|n|}, \quad (4.2)$$

The magneto-optical spectra were acquired on the MEG placed on SiC substrate at 5 K in the magnetic field  $B$  up to 4 T with step 0.25 T in Probe A configuration with FIR-DTGS room temperature detector ( $f_{SCN}=2.5$  kHz) in the FIR region and measured with 2048 scans and resolution  $6$  cm<sup>-1</sup>. A color map of normalized relative transmission spectra normalized as  $T_B/T_0$  recorded on MEG placed on SiC, shown in Fig. 4.36(a), reveals typical graphene parabolical-shaped feature. This color map is plotted with  $\sqrt{B}$ -scaled  $x$  axis in Fig. 4.36(b).  $\sqrt{B}$ -scaled blueshift can be identified as inter-LL transitions  $L_{-m} \rightarrow L_{m+1}$  with  $m=0$ , thus,  $L_{0(-1)} \rightarrow L_{1(0)}$ , which corresponds to transitions from or to the vicinity of the Fermi level [23]. The red dashed line in Fig. 4.36(b) is calculated from eq. 4.2 using Fermi velocity  $\tilde{c}=(1.02\pm 0.01)\times 10^6$  ms<sup>-1</sup> obtained from the [23]. As can be seen, the red dashed line precisely fits the dark blue feature attributed to inter-LL transitions, which means that our FTIR magneto-spectroscopic setup provided the same results as in [23].

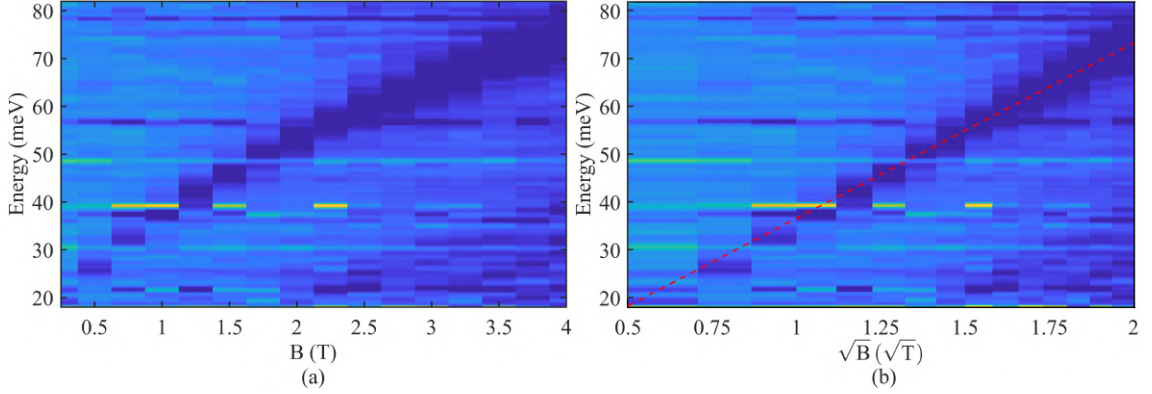


Fig. 4.36: (a) A color map of normalized relative transmission spectra of MEG on SiC, (b) a color map of normalized relative transmission spectra of MEG on SiC from (a) plotted with  $\sqrt{B}$ -scaled  $x$  axis. Dark blue linear feature in the spectra corresponds to inter-LL transitions  $L_{0(-1)} \rightarrow L_{1(0)}$ . The red dashed line was calculated from eq. 2.8 using Fermi velocity  $\tilde{c}=(1.02\pm 0.01)\times 10^6$  ms $^{-1}$  obtained from the [23].

#### 4.3.4 Graphene Bolometer Devices

Bolometers are sensitive detection devices for measuring the power of electromagnetic radiation over a wide frequency range, including the THz and IR regions. Its principle is based on heating a material with highly temperature-dependent electrical resistance caused by incident electromagnetic radiation [74]. Thanks to their high sensitivity and ability to detect a tiny amount of incident electromagnetic radiation, they are also used in current astrophysics [214], and their applicability also extends to the field of THz technology and spectroscopy [215].

Our interest in bolometric detectors was prompted by the collaborators from Georgetown University, where nanostructured graphene was used for bolometers [189–191]. Extraordinary electric, thermal and mechanical properties, high charge carrier mobility, and small heat capacity make graphene a promising material for very sensitive and responsive bolometers by using hot electrons [215]. However, pure monolayer graphene is unsuitable for functional bolometric devices due to its low temperature-dependent electrical resistance [216]. Nevertheless, this issue can be overcome by dual gate structure on bilayer graphene in such a way as to alter the graphene band gap [217], or by creating defects in graphene that cause a strong electron localization [218].

A milestone in the field of graphene-based bolometers was the research of our collaborators, who were able to advance the previous performance significantly: 100 000x increase of electrical response  $R$  and 10x lower NEP at the temperature of

2.5 K. These results were obtained by using a graphene quantum dot (GQD) [189]. Nanostructured GQDs exhibit a rapid temperature-dependent change of electrical resistance. This approach also has the advantage of a temperature range up to 77 K, at which these bolometers are still functional, making their applicability more promising compared to other approaches [217, 218]. Graphene quantum dot-based bolometers can also be used as broadband photodetectors [190, 215].

With the group of prof. Paola Barbara from Georgetown University we collaborate within Inter-Excellence USA-CZ 2019 with project LTAUSA19060 entitled “Spectroscopy of single-molecule magnets graphene bolometers”. As part of this project, we have tested the functionality of the FTIR magneto-spectroscopic setup in Probe B-chipset configuration with graphene bolometer devices placed in the chip-set holder [187, 188]. We wanted to find out the response of the graphene devices on the chip marked as 1FA4 with molecules of 1,1-diphenyl-2-picrylhydrazyl (DPPH) deposited on top [191, 215].

Firstly, we measured the resistance  $R$  vs. temperature  $T$  dependence shown in Fig. 4.37(a) of the bolometric chip 1FA4 with DPPH. As can be seen in Fig. 4.37(a), the region of interest is around 15 K as there is the most abrupt change in the resistance dependence, and hence the most sensitive region for detection of changes [215].

The next step was to check the response on the IR irradiation (NIR tungsten lamp or MIR global source) by measuring the I-V characteristics of the device at 16.7 K, which is shown in Fig. 4.37(b). However, we did not observe a clear change in the characteristic between IR source ON and OFF. Therefore, we came to the conclusion that the design of GQD devices (which were previously used in MW range and exhibit change in I-V characteristics [215]) was not suitable for IR radiation, and it needs to be redesigned for use in the IR region.

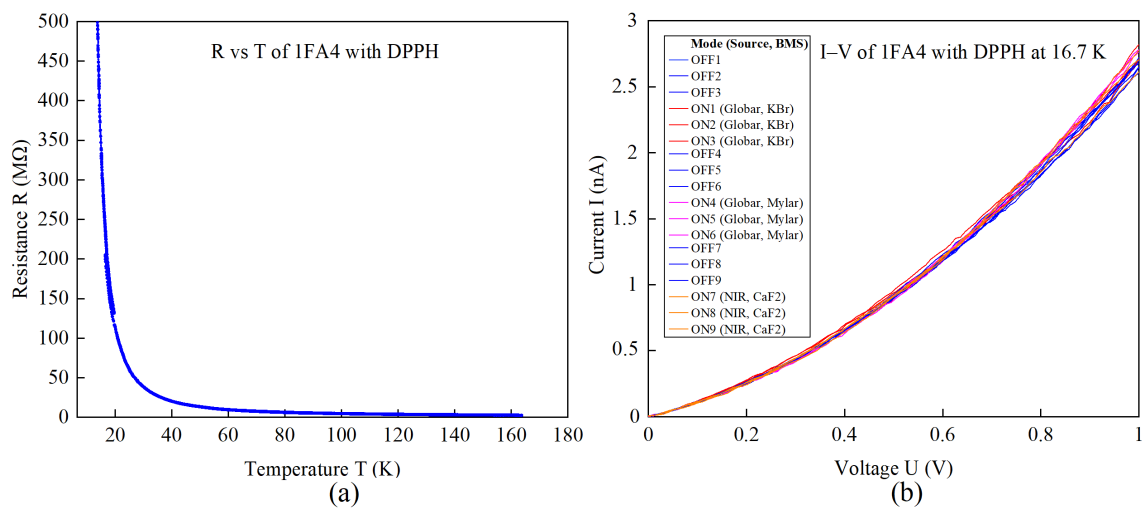


Fig. 4.37: (a) Resistance  $R$  vs. temperature  $T$  dependence of the graphene bolometric chip 1FA4 with DPPH. The region of interest is around 15 K as there is the most abrupt change in the resistance dependence, and hence the most sensitive region for detection of changes. (b) I-V characteristics of the graphene bolometric chip 1FA4 with DPPH response on the IR irradiation ON and OFF.



---

# Conclusion and Outlook

In this doctoral thesis, we have explored the use of FTIR magneto-spectroscopy as a powerful method for studying the properties of various materials, including SMMs and 2D materials. In order to fulfill the main goal of the thesis, we have developed the versatile FTIR magneto-spectroscopic setup to mediate this method at CEITEC BUT and perform sensitive magneto-optical measurements.

In the first two chapters, we provided the theoretical background with key concepts that underpin our research topic. We first introduced electromagnetic radiation and IR radiation, then we shed the light on the principles and history of IR spectroscopy, followed by a closer look at the FTIR spectrometer and its instrumentation. At the end of the first chapter, we discussed the importance of high magnetic fields. The second chapter was dedicated to the FTIR magneto-spectroscopy method itself and its applications, focusing in particular on SMMs and 2D materials. In addition, we have included here an overview of several worldwide state-of-the-art IR magneto-spectroscopic setups.

The last two chapters of the thesis present accomplishment of the three stated aims of the thesis i.e., overall design of the FTIR magneto-spectroscopic setup, and assembly, testing and putting the setup into operation in the third chapter, and performance of magneto-optical measurements in the fourth chapter.

In the third chapter, we have described in detail the design and implementation of the home-build versatile FTIR magneto-spectroscopic setup, which is based on a commercial FTIR spectrometer and the cryogen-free superconducting magnet coupled with the optical coupling and transmission probes for experiments with various detectors thanks to which the setup spans the entire IR and partially the THz range. This aspect is particularly important because it enables the measurement of different types of samples, demonstrated in the fourth chapter. A novelty of the setup lies in the usage of a cryogen-free superconducting magnet, which is a very convenient choice for facilities without LHe infrastructure. This chapter comprises also methods used for its manufacture, assembly, optimization, and testing of the setup. Within this chapter, we have tested the performance of the FTIR magneto-spectroscopic setup at zero magnetic field for various configurations to determine a usable setup range.

Last but not least, the fourth chapter of the thesis provided experimental results of magneto-optical measurements performed on two different setups. The first section is devoted to data analysis and manipulation, describing and explaining typical analysis methodology from raw data to published results. At the time when our FTIR magneto-spectroscopic setup was not yet finished, magneto-optical me-

asurements were performed on the IR magneto-spectroscopic setup at GHMFL in collaboration with the group of Dr. Milan Orlita. Thus, the second section of this chapter reviews the results of the measurements at GHMFL of two published articles about cobalt-based SMMs. The third section is devoted to measurements at CEITEC BUT performed on our FTIR magneto-spectroscopic setup in several different configurations with various types of samples. Firstly, it reviews the published results of magneto-optical measurements on cobalt(II)-based SIM in the FIR region and germanium in the NIR region. Then, it is followed by measurements of graphene in the FIR region and measurements of characteristics of graphene bolometer devices with deposited DPPH placed in the chipset holder.

To sum up, in this doctoral thesis we presented FTIR spectroscopy in high magnetic fields/FTIR magneto-spectroscopy as a powerful spectroscopic technique used to investigate many important effects in materials, e.g., EPR in SMMs with very large ZFS, mainly based on transition metal complexes or lanthanides, in which conventional microwave EPR systems do not provide experimental access to the magnetic resonance transitions, and transitions between LLs of semiconductors or 2D materials such as graphene. Furthermore, we have described in detail the versatile FTIR magneto-spectroscopic setup operating in the range 50–10,000  $\text{cm}^{-1}$ , temperatures between 2–320 K, and magnetic fields up to 16 T located at CEITEC BUT. We have designed versatile FTIR magneto-spectroscopic setup using several methods, and have tested its performance of the at zero magnetic field for various configurations to determine a workable setup range summarized in Tab. 3.2. The functionality of the setup has been demonstrated on magneto-optical measurements of cobalt(II)-based SIM in the FIR region, germanium in the NIR region, and graphene in the FIR region. The measurements of SIM have shown that the setup provides high-quality spectra and results comparable to those performed on a similar setup at GHMFL. In germanium, we observed indirect inter-band transitions between LLs and analyzed them with a model yielding three values of reduced effective masses. In graphene, we identified inter-band transitions between LLs, which correspond to transition from or to the vicinity of the Fermi level. Moreover, we tested the setup in configuration with chipset holder, in which we measured I-V characteristics of graphene bolometer devices with deposited DPPH.

In the context of prospective advancements, the flexibility of the FTIR magneto-spectroscopic setup enables further development and improvements, such as the implementation of new sample holders for different types of measurements, internal coating of waveguides with a layer of gold or silver to further enhance the transmission, etc. Our group focuses on the studies of SMMs and high-spin coordination compounds with large ZFS, including transition metals and lanthanides, exploring the physics behind their behavior still rarely reported at those energy ranges. Further-

---

more, the presented versatile setup allows performing field-induced measurements on 2D devices [189] – [191], e.g., by shifting the Fermi level in semiconductors, and electrically detected magnetic resonance (EDMR) [219, 220], which may lead to interesting discoveries. Moreover, we are interested in exploring the properties in topological materials or Weyl semimetals, which are known to exhibit exotic electronic properties under applied magnetic fields [111, 114].

Thanks to its relatively simple design and implementation of a cryogen-free superconducting magnet, the presented FTIR magneto-spectroscopic setup paves the way for other research institutions without the LHe infrastructure to perform IR magneto-optical experiments in high magnetic fields.



---

# References

- [1] CHRISTY, A. A., OZAKI, Y. and GREGORIOU, V. G. *Modern fourier transform infrared spectroscopy*. New York: Elsevier, 2001. ISBN 978-0444500441.
- [2] HERSCHEL, W. Experiments on the refrangibility of the invisible rays of the sun. (1800). *Philosophical Transactions of the Royal Society of London*. 1800, vol. 90, pp. 284–292. DOI: 10.1098/rstl.1800.0015.
- [3] DERRICK, M. R., STULIK, D. and LANDRY, J. M. *Infrared spectroscopy in conservation science*. Los Angeles: Getty Conservation Institute, 1999. ISBN 0-89236-469-6.
- [4] GRIFFITHS, P. R. and DE HASETH, J. A. *Fourier transform infrared spectrometry*. 2nd ed. Hoboken, N.J.: Wiley-Interscience, 2007. ISBN 978-0-471-19404-0.
- [5] *High magnetic field science and its application in the United States: current status and future directions*. Washington, D.C.: The National Academies Press, 2013. ISBN 978-0-309-28634-3.
- [6] BASOV, D. N., AVERITT, R. D., VAN DER MAREL, D., DRESSEL, M., and HAULE, K. Electrodynamics of correlated electron materials. *Reviews of Modern Physics* 2011, vol. 83, no. 2, pp. 471–541. DOI: 10.1103/RevModPhys.83.471.
- [7] FROST, J. M., HARRIMAN, K. L. M. and MURUGESU, M. The rise of 3-d single-ion magnets in molecular magnetism: towards materials from molecules?. *Chemical Science*. 2016, vol. 7, no. 4, pp. 2470-2491. DOI: 10.1039/C5SC03224E.
- [8] SESSOLI, R., GATTESCHI D., CANESCHI, A., NOVAK, M. A. Magnetic bistability in a metal-ion cluster. *Nature*. 1993, vol. 365, no. 6442, pp. 141-143. DOI: 10.1038/365141a0.
- [9] NEHRKORN, J., HOLLACK, K., Robert BITTL, R., SCHNEGG, A. Recent progress in synchrotron-based frequency-domain Fourier-transform THz-EPR. *Journal of Magnetic Resonance*. 2017, vol. 280, pp. 10-19. DOI: 10.1016/j.jmr.2017.04.001.
- [10] WINPENNY, R. and AROMÍ, G. *Single-molecule magnets and related phenomena*. New York: Springer, 2006. ISBN 3540332391.

- 
- [11] RECHKEMMER, Y., BREITGOFF, F. D., VAN DER MEER, M., ATANASOV, M., HAKL, M., ORLITA, M., NEUGEBAUER, P., NEESE, F., SARKAR, B., VAN SLAGEREN, J. A four-coordinate cobalt(II) single-ion magnet with coercivity and a very high energy barrier, *Nature Communications*. 2016, vol. 7, no. 10467. DOI: 10.1038/ncomms10467.
- [12] BAMBERGER, H., ALBOLD, U., DUBNICKÁ MIDLÍKOVÁ, J., SU, C.-Y., DEIBEL, N., HUNGER, D., HALLMEN, P. P., NEUGEBAUER, P., BEERHUES, J., DEMESHKO, S., MEYER, F., SARKAR, B., VAN SLAGEREN, J. Iron(II), Cobalt(II), and Nickel(II) Complexes of Bis(sulfonamido)benzenes: Redox Properties, Large Zero-Field Splittings, and Single-Ion Magnets, *Inorganic Chemistry*. 2021, vol. 60, no. 5, pp. 2953–2963. DOI: 10.1021/acs.inorgchem.0c02949.
- [13] JURÁKOVÁ, J.; DUBNICKÁ MIDLÍKOVÁ, J.; HRUBÝ, J.; KLIUIKOV, A.; SANTANA, V. T.; PAVLIK, J.; MONCOL, J.; ČIŽMÁR, E.; ORLITA, M.; MOHELSKÝ, I.; NEUGEBAUER, P.; GENTILI, D.; CAVALLINI, M.; ŠALITROŠ, I. Pentacoordinate cobalt(II) single ion magnets with pendant alkyl chains: shall we go for chloride or bromide? *Inorganic Chemistry Frontiers*. 2022, vol. 9, pp. 1179–1194, DOI: 10.1039/D1QI01350E.
- [14] MALINOVÁ, N., JURÁKOVÁ, J., BRACHŇAKOVÁ, B., DUBNICKÁ MIDLÍKOVÁ, J., ČIŽMÁR, E., SANTANA, V. T., HERCHEL, R., ORLITA, M., MOHELSKÝ, I., MONCOL, J., NEUGEBAUER, P., ŠALITROŠ, I. Magnetization Slow Dynamics in Mononuclear Co(II) Field-Induced Single-Molecule Magnet, *Crystal Growth & Design*. 2023, vol. 23, iss. 4, pp. 2430–2441. DOI: 10.1021/acs.cgd.2c01388.
- [15] DUBNICKÁ MIDLÍKOVÁ, J., ŠEDIVÝ, M., SOJKA, A., TADEU SANTANA, V., DUBROKA, A., NEUGEBAUER, P. A Versatile Setup for FTIR Magneto-Spectroscopy *IEEE Transactions on Instrumentation and Measurement*. 2023, vol. 72, pp. 1-11. DOI: 10.1109/TIM.2023.3284943.
- [16] LIU, J.-J., MENG, Y.-S., HLAVIČKA, I., ORLITA, M., JIANG, S.-D., WANG, B.-W., GAO, S. “Determination of zero-field splitting in Co<sup>2+</sup> halide complexes with magnetic and far-IR measurements. *Dalton Transactions*. 2017, vol. 46, no.23, pp. 7408-7411. DOI: 10.1039/C7DT01486D.
- [17] MISOCHKO, E. Y., AKIMOV, A. V., KORCHAGIN, D. V., NEHRKORN, J., OZEROV, M., PALII, A. V., CLEMENTE-JUAN, J. M., ALDOSHI, S. M. Purely Spectroscopic Determination of the Spin Hamiltonian Parameters in High-Spin Six-Coordinated Cobalt(II) Complexes with Large Zero-Field

- Splitting. *Inorganic Chemistry*. 2019, vol. 58, no. 24, pp. 16434-16444. DOI: 10.1021/acs.inorgchem.9b02195.
- [18] MOSELEY, D. H., STAVRETIS, S. E., THIRUNAVUKKUARASU, K., OZEROV, M., CHENG, Y., DAEMEN, L. L., LUDWIG, J., LU, Z., SMIRNOV, D., BROWN, C. M., PANDEY, A., RAMIREZ-CUESTA, A. J., LAMB, A. C., ATANASOV, M., BILL, E., NEESE, F., XUE, Z.-L. Spin-phonon couplings in transition metal complexes with slow magnetic relaxation, *Nature Communications*. 2018, vol. 9, no. 2572. DOI: 10.1038/s41467-018-04896-0.
- [19] MARX, R., MORO, F., DÖRFEL, M., UNGUR, L., WATERS, M., JIANG, S. D., ORLITA, M., TAYLOR, J., FREY, W., CHIBOTARU, L. F., VAN SLAGEREN, J. Spectroscopic determination of crystal field splittings in lanthanide double deckers. *Chemical Science*. 2014, vol. 5, no. 8. DOI: 10.1039/c4sc00751d.
- [20] HAAS, S. *Far-infrared spectroscopy of lanthanide-based molecular magnetic materials*. 2015. Dissertation. University of Stuttgart. Available from: <https://elib.uni-stuttgart.de/handle/11682/5178>.
- [21] LIDDLE, S. T. and VAN SLAGEREN, J. Improving f-element single molecule magnets. *Chemical Society Reviews*. 2015, vol. 44, no. 19, pp. 6655-6669. DOI: 10.1039/C5CS00222B.
- [22] KRAGSKOW, J. G. C., MARBEY, J., BUCH, C. D., NEHRKORN, J., OZEROV, M., PILIGKOS, S., HILL, S., CHILTON, N. F. Analysis of vibronic coupling in a 4f molecular magnet with FIRMS. *Nature Communications*. 2022, vol. 13, no. 825. DOI: 10.1038/s41467-022-28352-2.
- [23] NEUGEBAUER, P., ORLITA, M., FAUGERAS, C., BARRA, A.-L., POTEMSKI, M. How Perfect Can Graphene Be? *Physical Review Letters*. 2009, vol. 103, no. 13. DOI: 10.1103/PhysRevLett.103.136403.
- [24] SADOWSKI, M. L., MARTINEZ, G., POTEMSKI, M., BERGER, C., DE HEER, W. A. Landau Level Spectroscopy of Ultrathin Graphite Layers. *Physical Review Letters*. 2006, vol. 97, no. 26. DOI: 10.1103/physrevlett.97.266405.
- [25] JIANG, Z., HENRIKSEN, E. A., TUNG, L. C., WANG, Y.-J., SCHWARTZ, M. E., HAN, M. Y., KIM, P., STORMER, H. L. Infrared spectroscopy of Landau levels in graphene. *Physical Review Letters*. 2007, vol. 98, no. 19. DOI: 10.1103/PhysRevLett.98.197403.
- [26] NEDOLIUK, I. O., HU, S., GEIM, A. K., KUZMENKO, A. B. Colossal infrared and terahertz magneto-optical activity in a two-dimensional Dirac material.

---

*Nature Nanotechnology*. 2019, vol. 14, pp. 756–761. DOI: 10.1038/s41565-019-0489-8.

- [27] CRASSEE, I., LEVALLOIS, J., WALTER, A. L., OSTLER, M., BOSTWICK, A., ROTENBERG, E., SEYLLER, T., VAN DER MAREL, D., KUZMENKO, A. B. Giant Faraday rotation in single- and multilayer graphene. *Nature Physics*. 2011, vol. 7, pp. 48-51. DOI: 10.1038/nphys1816.
- [28] ORLITA, M., FAUGERAS, C., PLOCHOCKA, P., NEUGEBAUER, P., MARTINEZ, G., MAUDE, D. K., BARRA, A.-L., SPRINKLE, M., BERGER, C., DE HEER, W. A., POTEMSKI, M. Approaching the Dirac Point in High-Mobility Multilayer Epitaxial Graphene. *Physical Review Letters*. 2008, vol. 101, no. 26. DOI: 10.1103/PhysRevLett.101.267601.
- [29] STUART, B. *Infrared spectroscopy: fundamentals and applications*. Hoboken, NJ: J. Wiley, 2004. ISBN 0-470-85427-8.
- [30] HOLLAS, J. M. *Basic Atomic and Molecular Spectroscopy*. The Royal Society of Chemistry, 2002. ISBN 978-0-85404-667-6.
- [31] COLTHUP, N. B., DALY, L.H., WIBERLEY, S. E. *Introduction to infrared and Raman spectroscopy*. Third edition. San Diego: Academic Press, 1990. ISBN 978-0-12-182554-6.
- [32] JOOS, G. *Theoretical Physics*. London and Glasgow: Blackie and Son Limited, 1951. ISBN: 978-0216874046.
- [33] FRITZSCHE, H. and PHILLIPS, M. “electromagnetic radiation”. *Encyclopedia Britannica*, [online]. [cit. 2023-04-08], Available from: <https://www.britannica.com/science/electromagnetic-radiation>.
- [34] The Nobel Prize in Physics 1918. NobelPrize.org. [online]. [cit. 2023-04-08]. Available from: <https://www.nobelprize.org/prizes/physics/1918/summary/>.
- [35] HECHT, E. *Optics*. Addison Wesley, San Francisco, 2002. ISBN 978-0133977226.
- [36] FOX, M. *Optical properties of solids*. 2nd ed. Oxford: Oxford University Press, 2010. ISBN 9780199573370.
- [37] SEDLÁK, B. and ŠTOLL, I. *Elektrina a Magnetismus*. Academia Prada, Praha, 1993. ISBN 80-200-1004-1.

- 
- [38] FRIŠ, P. *Construction of a far-infrared ellipsometer and an experimental study of optical properties of ferromagnetic cobaltites*. Brno, 2018. 99 p. Dissertation. Masaryk University. Faculty of Science. Department of Condensed Matter Physics. Supervised by Doc. Mgr. ADAM DUBROKA, Ph.D.
- [39] LAMB, J. W. Miscellaneous data on materials for millimetre and submillimetre optics. *International Journal of Infrared and Millimeter Waves*, 1996, Vol. 17, Issue 12, pp. 1997–203). DOI:10.1007/bf02069487.
- [40] OZAKI, Y. Infrared Spectroscopy—Mid-infrared, Near-infrared, and Far-infrared/Terahertz Spectroscopy, *Analytical Sciences*, 2021, vol. 37, no. 9, pp. 1193-1212. DOI: 10.2116/analsci.20R008.
- [41] LEE, Y.-S., *Principle of Terahertz Science and Technology*. Springer, New York, 2009. ISBN: 978-0-387-09540-0.
- [42] DEXHEIMER, S. L. *Terahertz Spectroscopy: Principles and Applications*. CRC Press, Boca Raton, 2008. ISBN: 978-0849375255.
- [43] MANTSCH, H. H. and Naumann, D. Terahertz spectroscopy: The renaissance of far infrared spectroscopy. *Journal of Molecular Structure*. 2010, vol. 964, no. 1-3, pp. 1-4. DOI: 10.1016/j.molstruc.2009.12.022.
- [44] Britannica, The Editors of Encyclopaedia. “LED”. Encyclopedia Britannica, 16 Mar. 2023, <https://www.britannica.com/technology/LED>.
- [45] DAS, N. C., BRADSHAW, J., TOWNER, F., LEAVITT, R. Long-wave ( $10\mu$  m) infrared light emitting diode device performance. *Solid-State Electronics*. 2008, vol. 52, iss. 11, pp. 1821–1824. DOI: 10.1016/j.sse.2008.09.003.
- [46] GREGERSEN, E. “lidar”. Encyclopedia Britannica, [online]. [cit. 2023-04-08], Available from: <https://www.britannica.com/technology/lidar>.
- [47] TAYLOR, T. S. *Introduction to Laser Science and Engineering*. CRC Press. 2019. DOI: /10.1201/b22159.
- [48] WANG, X., PAN, H., GUO, K., YANG, X., LUO, S. The evolution of LiDAR and its application in high precision measurement. *Earth and Environmental Science*. 2020, vol. 502, iss. 1, pp. 012008, 2020. DOI: 10.1088/1755-1315/502/1/012008.
- [49] GUERRERO-RASCADO, J. L., COSTA, M. J., BORTOLI, D., SILVA, A. M., LYAMANI, H., ALADOS-ARBOLEDAS, L. Infrared lidar overlap function: an

- 
- experimental determination. *Optics Express*. 2010, vol. 18, iss. 19, pp. 20350. DOI: 10.1364/oe.18.020350.
- [50] Comparison views of ‘Mystic Mountain’: SCIENCE & EXPLORATION. THE EUROPEAN SPACE AGENCY [online]. 23/04/2010 [cit. 2023-04-25]. Available from: [https://www.esa.int/ESA\\_Multimedia/Images/2010/04/Comparison\\_views\\_of\\_Mystic\\_Mountain](https://www.esa.int/ESA_Multimedia/Images/2010/04/Comparison_views_of_Mystic_Mountain).
- [51] COLARUSSO, P., KIDDER, L. H., LEVIN, I. W., FRASER, J. C., ARENS, J. F., LEWIS, E. N. Infrared Spectroscopic Imaging: From Planetary to Cellular Systems. *Applied Spectroscopy*. 1998, vol. 52, iss. 3, pp. 106A-120A. DOI: 10.1366/0003702981943545.
- [52] TSAI, S.-R., HAMBLIN, M. R. Biological effects and medical applications of infrared radiation. *Journal of Photochemistry and Photobiology B: Biology*. 2017, vol. 170, pp. 197–207. DOI: 10.1016/j.jphotobiol.2017.04.014.
- [53] TIROL-PADRE, A., RAI, M., GATHALA, M., SHARMA, S., KUMAR, V., SHARMA, P. C., SHARMA, D. K., WASSMANN, R., LADHA, J. Assessing the performance of the photo-acoustic infrared gas monitor for measuring CO<sub>2</sub>, N<sub>2</sub>O, and CH<sub>4</sub> fluxes in two major cereal rotations. *Global Change Biology*. 2013, vol. 20, iss. 1, pp. 287–299. DOI: 10.1111/gcb.12347.
- [54] ATTAS, M., CLOUTIS, E., COLLINS, C., GOLTZ, D., MAJZELS, C., MANSFIELD, J. R., MANTSCH, H. H. Near-infrared spectroscopic imaging in art conservation: investigation of drawing constituents. *Journal of Cultural Heritage*. 2013, vol. 4, iss. 2, pp. 127–136. DOI: 10.1016/s1296-2074(03)00024-4.
- [55] GLASS, I. S. *Handbook of Infrared Astronomy*. Cambridge, England: Cambridge University Press. 1998. ISBN: 0-521-63311-7.
- [56] BECKMAN, J. E., MOORWOOD, A. F. M. Infrared astronomy. *Reports on Progress in Physics*. 1979, vol. 42, iss. 1, pp. 87–157. DOI: 10.1088/0034-4885/42/1/002.
- [57] LOW, F. J., RIEKE, G. H., GEHRZ, R. D. The Beginning of Modern Infrared Astronomy. *Annual Review of Astronomy and Astrophysics*. 2007, vol. 45, iss. 1, pp. 43–75. DOI: 10.1146/annurev.astro.44.051905.092505.
- [58] RIEKE, G., WRIGHT, G. A mid-infrared dream come true. *Nature Astronomy*. 2022, vol. 6, iss. 8, pp. 891–891, 2022. DOI: 10.1038/s41550-022-01736-6.

- [59] CLARK, D., The Analysis of Pharmaceutical Substances and Formulated Products by Vibrational Spectroscopy. In: CHALMERS, J. M. and GRIFFITHS, P. R. (Eds.) *Handbook of Vibrational Spectroscopy*, Vol. 5, Wiley, Chichester, UK, 2002, pp. 3574–3589. ISBN: 978-0471988472.
- [60] BROAD, N., GRAHAM, P., HAILEY, P., HARDY, A., HOLLAND, S., HUGHES, S., LEE, D., PREBBE, K., SALTON, N., WARREN, P. Guidelines for the Development and Validation of Near Infrared Spectroscopic Methods in the Pharmaceutical Industry. In: CHALMERS, J. M. and GRIFFITHS, P. R. (Eds.) *Handbook of Vibrational Spectroscopy*, Vol. 1, Wiley, Chichester, UK, 2002, pp. 3590–3610.
- [61] BARTICK, E. G. Applications of Vibrational Spectroscopy in Criminal Forensic Analysis. In: CHALMERS, J. M. and GRIFFITHS, P. R. (Eds.) *Handbook of Vibrational Spectroscopy*, Vol. 4, Wiley, Chichester, UK, 2002, pp. 2993–3004. ISBN: 978-0471988472.
- [62] MCCLURE, W. F. and STANFIELD, D. L. Near-infrared Spectroscopy of Biomaterials. In: CHALMERS, J. M. and GRIFFITHS, P. R. (Eds.) *Handbook of Vibrational Spectroscopy*, Vol. 1, Wiley, Chichester, UK, 2002, pp. 212–225. ISBN: 978-0471988472.
- [63] LI-CHEN, E. C. Y., ISMAIL, A. A., SEDMAN, J. AND VAN DE VOORT, F. R. Vibrational Spectroscopy of Food and Food Products. In: CHALMERS, J. M. and GRIFFITHS, P. R. (Eds.) *Handbook of Vibrational Spectroscopy*, Vol. 5, Wiley, Chichester, UK, 2002, pp. 3629–3662. ISBN: 978-0471988472.
- [64] ANDERSON, S. K., HANSEN, P. W, ANDERSON, H. V. Vibrational Spectroscopy in the Analysis of Dairy Products and Wine. In: CHALMERS, J. M. and GRIFFITHS, P. R. (Eds.) *Handbook of Vibrational Spectroscopy*, Vol. 5, Wiley, Chichester, UK, 2002, pp. 3672–2682. ISBN: 978-0471988472.
- [65] LECLERC, D. F. and TRUNG, T. P. Vibrational Spectroscopy in the Pulp and Paper Industry. In: CHALMERS, J. M. and GRIFFITHS, P. R. (Eds.) *Handbook of Vibrational Spectroscopy*, Vol. 4, Wiley, Chichester, UK, 2002, pp. 2952–2976. ISBN: 978-0471988472.
- [66] LECLERC, D. F. Fourier-Transform Infrared Spectroscopy in the Pulp and Paper Industry. In: CHALMERS, J. M. and GRIFFITHS, P. R. (Eds.) *Handbook of Vibrational Spectroscopy*, Vol. 10, Wiley, Chichester, UK, 2002, pp. 8361–8388. ISBN: 978-0471988472.

- 
- [67] CARR, C. Vibrational Spectroscopy in the Paint Industry. In: CHALMERS, J. M. and GRIFFITHS, P. R. (Eds.) *Handbook of Vibrational Spectroscopy*, Vol. 4, Wiley, Chichester, UK, 2002, pp. 2935–2951. ISBN: 978-0471988472.
- [68] VISSER, T. Infrared Spectroscopy in Environmental Analysis. In: MEYERS, R. A. (Ed.) *Encyclopedia of Analytical Chemistry*, Vol. 1, Wiley, Chichester, UK, 2000, pp. 1–21. ISBN: 978-0471988472.
- [69] GRIFFITH, D. W. T. FTIR Measurements of Atmospheric Trace Gases and their Fluxes. In: CHALMERS, J. M. and GRIFFITHS, P. R. (Eds.) *Handbook of Vibrational Spectroscopy*, Vol. 4, Wiley, Chichester, UK, 2002, pp. 2823–2841. ISBN: 978-0471988472.
- [70] GRIFFITH, D. W. T., JAMIE, I. M., KAWAGUCHI, K. Astronomical Vibrational Spectroscopy. In: CHALMERS, J. M. and GRIFFITHS, P. R. (Eds.) *Handbook of Vibrational Spectroscopy*, Vol. 4, Wiley, Chichester, UK, 2002, pp. 2803–2822. ISBN: 978-0471988472.
- [71] ONG, K. S., JIANG, L., & LAI, K. C. 4.20 Thermoelectric Energy Conversion. *Comprehensive Energy Systems*, pp. 794–815. Elsevier, 2018.
- [72] ØRSTED, H. C. (1823). New experiments by Dr. Seebeck on electromagnetic effects. *Annales de chimie et de physique*. 1823, vol. 22, pp. 199–201.
- [73] SHEPPARD, N. The Historical Development of Experimental Techniques in Vibrational Spectroscopy. In: CHALMERS, J. M. and GRIFFITHS, P. R. (Eds.) *Handbook of Vibrational Spectroscopy*, Vol. 1, Wiley, Chichester, UK, 2002. ISBN: 978-0471988472.
- [74] LANGLEY, S. P. The Bolometer and Radiant Energy. *Proceedings of the American Academy of Arts and Sciences*. 1880, vol. 16, no. 342. DOI:10.2307/25138616.
- [75] COBLENTZ, W.W., Investigations of Infrared Spectra, Parts I to V, Carnegie Institution, Publication no. 35, 65 and 97 (1905–1908). Republished by the *Coblentz Society and the Perkin-Elmer Corp.*, 1962.
- [76] MICHELSON, A. A. XXVIII. Visibility of interference-fringes in the focus of a telescope. *The London, Edinburgh, and Dublin Philosophical Magazine and Journal of Science*. 2009, vol. 31, iss. 190, pp. 256–259. DOI: 10.1080/14786449108620101. ISSN 1941-5982.

- 
- [77] FELLGETT, P. B. Theory of infra-red sensitivities and its application to investigations of stellar radiation in the near infra-red. PhD Thesis, Cambridge University Press, Cambridge (UK). 1951.
- [78] JACQUINOT, P. Caracteres communs aux nouvelles methodes de spectroscopie interferentielle, Facteur de merite. *Journal de Physique et le Radium*. 1958, vol. 19, iss. 3, pp. 223-229. DOI: 10.1051/jphysrad:01958001903022300.
- [79] SCHRADER, B. and BOUGEARD, D. *Infrared and Raman spectroscopy: methods and applications*. New York: VCH, 1995. ISBN 3-527-26446-9.
- [80] LARKIN, P. *Infrared and raman spectroscopy: principles and spectral interpretation*. Boston: Elsevier, 2011. ISBN 978-0-12-386984-5.
- [81] HASEGAWA, T. *Quantitative Infrared Spectroscopy for Understanding of a Condensed Matter* Springer Tokyo. 2017. ISBN: 978-4-431-56491-1.
- [82] STEELE, D., Infrared Spectroscopy: Theory. In: CHALMERS, J. M. and GRIFFITHS, P. R. (Eds.) *Handbook of Vibrational Spectroscopy*, Vol. 1, Wiley, Chichester, UK, 2002, pp. 44–70. ISBN: 978-0471988472.
- [83] DRESSEL, M. and GRÜNER, G. *Electrodynamics of Solids: Optical Properties of Electrons in Matter*. Cambridge. 2002. ISBN 9780521592536.
- [84] SMITH, B. C. *Fundamentals of Fourier transform infrared spectroscopy*. 2nd ed. Boca Raton, FL: CRC Press, 2011. ISBN 9781420069303.
- [85] Albert A. Michelson. Physics. *The University of Chicago Faculty: A Centennial View* [online]. [cit. 2020-08-26]. Available from: [https://www.lib.uchicago.edu/projects/centcat/fac/facch07\\_01.html](https://www.lib.uchicago.edu/projects/centcat/fac/facch07_01.html).
- [86] KAUPPINEN, J., PARTANEN, J. *Fourier transforms in spectroscopy*. Berlin: Wiley, 2001. ISBN 35-276-0029-9.
- [87] GUNZLER, H. and WEINHEIM H.-U. *IR Spectroscopy: An Introduction* Weinheim, Germany: Wiley, 2002. ISBN 3-527-28896-1.
- [88] ROGALSKI, A. *Infrared Detectors*. 2nd ed. Boca Raton, FL: CRC Press Taylor & Francis Group. 2011. ISBN 978-1-4200-7671-4.
- [89] GRIFFITHS, P. R. AND HOMES, C. C. Instrumentation for Far-infrared Spectroscopy. In: CHALMERS, J. M. and GRIFFITHS, P. R. (Eds.) *Handbook of Vibrational Spectroscopy*, Vol. 1, Wiley, Chichester, UK, 2002. ISBN: 978-0471988472.

- 
- [90] What Is Mylar? Impakcorporation.com: PACKAGING INDUSTRY EXPERTS [online]. [cit. 2023-05-13]. Available from: <https://www.impakcorporation.com/what-is-mylar>.
- [91] HINTERBERGER, H. AND WINSTON, R. Efficient light coupler for threshold Čerenkov counters, *Review of Scientific Instruments*. 1966, vol. 37, pp. 1094–1095.
- [92] WINSTON, R. Light Collection within the Framework of Geometrical Optics. *Journal of the Optical Society of America*. 1970, vol. 60, iss. 2, pp. 245. DOI: 10.1364/josa.60.000245.
- [93] AOKI, M., TRIPATHI, S. R., TAKEDA, M., HIROMOTO, N. Angle dependent condensing efficiency of Winston cone in terahertz region, *Infrared Physics & Technology*. 2013, vol. 56, pp. 8-11. DOI: 10.1016/j.infrared.2012.09.001.
- [94] KUZMANY, H. *Solid-State Spectroscopy*. Berlin, Heidelberg: Springer Berlin Heidelberg, 2009. ISBN 978-3-642-01478-9.
- [95] HERLACH, F., MIURA, N. (n.d.). *High Magnetic Fields*. World Scientific Publishing Company. 2006. DOI: 10.1142/4764.
- [96] DEW-HUGHES, D. The critical current of superconductors: an historical review. *Low Temperature Physics*. 2001, vol. 27, no. 9, pp. 713–722. DOI: 10.1063/1.1401180.
- [97] SMIRNOV, A. I., SMIRNOVA, T. I., MACARTHUR, R. L., GOOD, J. A., HALL, R. Cryogen-free superconducting magnet system for multifrequency electron paramagnetic resonance up to 12.1T. *Review of Scientific Instruments*. 2006, vol. 77, no. 035108. DOI:10.1063/1.2182571.
- [98] HIROSE, R., HAYASHI, S., SHIBUTANI, K. *Cryogen-free Superconducting Magnet*. KOBELCO TECHNOLOGY REVIEW NO. 27 NOV. 2007. Available from: [https://www.kobelco.co.jp/english/ktr/pdf/ktr\\_27/018-022.pdf](https://www.kobelco.co.jp/english/ktr/pdf/ktr_27/018-022.pdf).
- [99] AWAJI, S., WATANABE, K., OGURO, H., HANAI, S., MIYAZAKI, H., TAKAHASHI, M., IOKA, S., SUGIMOTO, M., TSUBOUCHI, H., FUJITA, S., DAIBO, M., IJIMA, Y., KUMAKURA, H. New 25 T cryogen-free superconducting magnet project at Tohoku University. *IEEE transactions on applied superconductivity*. 2013, vol. 24, no. 3, pp. 1-5. DOI: 10.1109/TASC.2013.2292367.

- 
- [100] RADEBAUGH, R. Cryocoolers: the state of the art and recent developments. *Journal of Physics: Condensed Matter*. 2009, vol. 21, no. 16. DOI: 10.1088/0953-8984/21/16/164219. ISSN 0953-8984.
- [101] WANG, C., THUMMES, G., HEIDEN, C. A two-stage pulse tube cooler operating below 4 K. *Cryogenics*. Great Britain: Elsevier Science Limited. 1997, vol. 37, no. 3, pp. 159-164.
- [102] BALSHAW, N. H. *Practical cryogenics. An introduction to laboratory cryogenics*. Oxford Instruments Superconductivity Limited, United Kingdom. 1996. ISBN 0-9527594-0-3.
- [103] PADILLA, W. J., LI, Z. Q., BURCH, K. S., LEE, Y. S., MIKOLAITIS, K. J., BASOV, D. N. Broadband multi-interferometer spectroscopy in high magnetic fields: From THz to visible. *Review of Scientific Instruments*. 2004, vol. 75, no. 11, pp. 4710-4717. DOI: 10.1063/1.1805252.
- [104] DRESSELHAUS, G., KIP, A. F., AND KITTEL, C. Observation of Cyclotron Resonance in Germanium Crystals. *Physical Review*. 1953, vol. 92, iss. 3, pp. 827–827. DOI: 10.1103/physrev.92.827.
- [105] LAX, B., ZEIGER, H. J., DEXTER, R. N., AND ROSENBLUM, E. S. Directional Properties of the Cyclotron Resonance in Germanium. *Physical Review*. 1954, vol. 93, iss. 6, pp. 1418–1420. DOI: 10.1103/physrev.93.1418.
- [106] JOHNSON, F. M., AND NETHERCOT, A. H. Antiferromagnetic Resonance in  $\text{MnF}_2$ . *Physical Review*. 1956, vol. 104, iss. 3, pp. 847–848. DOI: 10.1103/physrev.104.847.
- [107] RICHARDS, P. L., CAUGHEY, W. S., EBERSPAECHER, H., FEHER, G., AND MALLEY, M. Determination of the Zero-Field Splitting of  $\text{Fe}^{3+}$  in Several Hemin Compounds. *Journal of Chemical Physics*. 1967, vol. 47, iss. 3, pp. 1187–1188. DOI: 10.1063/1.1712038.
- [108] WANNER, M., DOEZEMA, R. E., AND STROM, U. Far-infrared surface-Landau-level spectroscopy in Bi. *Physical Review B*. 1975, vol. 12, iss. 8, pp. 2883–2892. DOI: 10.1103/physrevb.12.2883.
- [109] DOEZEMA, R. E., DATARS, W. R., SCHABER, H., AND VAN SCHYNDEL, A. Far-infrared magnetospectroscopy of the Landau-level structure in graphite. *Physical Review B*. 1979, vol. 19, iss. 8, pp. 4224–4230. DOI: 10.1103/physrevb.19.4224.

- 
- [110] TINKHAM, M. *Introduction to Superconductivity*. 2nd Edition, McGraw-Hill, New York, 1996. ISBN: 9780486134727.
- [111] MOHELSKÝ, I., DUBROKA, A., WYZULA, J., SLOBODENIUK, A., MARTINEZ, G., KRUPKO, Y., PIOT, B. A., CAHA, O., HUMLÍČEK, J., BAUER, G., SPRINGHOLZ, G., ORLITA, M. Landau level spectroscopy of Bi<sub>2</sub>Se<sub>3</sub>. *Physical Review B*. 2020, vol. 102, no. 8, pp. 1-11. DOI: 10.1103/PhysRevB.102.085201.
- [112] ORLITA, M., PIOT, B. A., MARTINEZ, G., KUMAR, N. K. S., FAUGERAS, C., POTEMSKI, M., MICHEL, C., HANKIEWICZ, E. M., BRAUNER, T., DRAŠAR, Č., SCHREYECK, S., GRAUER, S., BRUNNER, K., GOULD, C., BRÜNE, C., MOLENKAMP, L. W. Magneto-Optics of Massive Dirac Fermions in Bulk Bi<sub>2</sub>Se<sub>3</sub>, *Physical Review Letters*. 2015, vol. 114, no. 18. DOI: 10.1103/PhysRevLett.114.186401.
- [113] TIKUIŠIS, K. K., WYZULA, J., OHNOUTEK, L., CEJPEK, P., UHLÍŘOVÁ, K., HAKL, M., FAUGERAS, C., VÝBORNÝ, K., ISHIDA, A., VEIS, M., ORLITA, M. Landau level spectroscopy of the PbSnSe topological crystalline insulator, *Physical Review B*. 2021, vol. 103, no. 15. DOI: 10.1103/PhysRevB.103.155304.
- [114] POLATKAN, S., GOERBIG, M. O., WYZULA, J., KEMMLER, R., MAULANA, L. Z., PIOT, B. A., CRASSEE, I., AKRAP, A., SHEKHAR, C., FELSER, C., DRESSEL, M., PRONIN, A. V., ORLITA, M. Magneto-optics of a Weyl semimetal beyond the conical band approximation: Case study of TaP, *Physical Review Letters*. 2020, vol. 124, no. 17. DOI: 10.1103/PhysRevLett.124.176402.
- [115] HÜTT, F., KAMENSKYI, D., NEUBAUER, D., SHEKHAR, C., FELSER, C., DRESSEL, M., PRONIN, A. V. Terahertz transmission through TaAs single crystals in simultaneously applied magnetic and electric fields: Possible optical signatures of the chiral anomaly in a Weyl semimetal, *Results in Physics*, 2019, vol. 15. DOI: 10.1016/j.rinp.2019.102630.
- [116] LAFORGE, A. D., PADILLA, W. J., BURCH, K. S., LI, Z. Q., SCHAFGANS, A. A., SEGAWA, K., ANDO, Y., BASOV, D. N. Sum rules and interlayer infrared response of the high temperature YBa<sub>2</sub>Cu<sub>3</sub>O<sub>y</sub> superconductor in an external magnetic field, *Physical Review Letters*. 2008, vol. 101, no. 9. DOI: 10.1103/PhysRevLett.101.097008.

- [117] ŠINDLER, M., KADLEC, F., KADLEC, C. Onset of a superconductor-insulator transition in an ultrathin NbN film under in-plane magnetic field studied by terahertz spectroscopy. *Physical Review B*. 2022, vol. 105, no. 1. DOI: 10.1103/PhysRevB.105.014506.
- [118] WEIL, J. A. and BOLTON, J. R. *Electron paramagnetic resonance: elementary theory and practical applications*. 2nd ed. Hoboken, N.J.: Wiley-Interscience, 2007. ISBN: 978-0471-75496-1.
- [119] BOČA, R. Zero-field splitting in metal complexes. *Coordination Chemistry Reviews*. 2004, vol. 248, iss. 9–10, pp. 757–815. DOI: 10.1016/j.ccr.2004.03.001.
- [120] NEHRKORN, J., VEBER, S. L., ZHUKAS, L. A., NOVIKOV, V. V., NELYUBINA, Y. V., VOLOSHIN, Y. Z., HOLLDAK, K., STOLL, S., SCHNEGG, A. Simulating Frequency-Domain Electron Paramagnetic Resonance: Bridging the Gap between Experiment and Magnetic Parameters for High-Spin Transition-Metal Ion Complexes. *The Journal of Physical Chemistry B*. 2015, vol. 119, no.43, pp. 13816-13824. DOI: 10.1021/acs.jpcc.5b04156.
- [121] REINSEL, D. *et al.* Data Age 2025 [online]. 2018. Available from: <https://www.seagate.com/files/www-content/our-story/trends/files/idc-seagate-dataage-whitepaper.pdf>.
- [122] CHILTON, N. How to store data on magnets the size of a single atom. *The University of Manchester Magazine* [online]. 2017 [cit. 2018-03-25]. Available from: <http://www.manchester.ac.uk/discover/news/how-to-store-data-on-magnets-the-size-of-a-single-atom/>.
- [123] SESSOLI, R., GATTESCHI, D., CANESCHI, A., NOVAK, M. A. Magnetic bistability in a metal-ion cluster. *Nature*. 1993, vol. 365, no. 6442, pp. 141-143. DOI: 10.1038/365141a0.
- [124] GATTESCHI, D., CORNIA, A., MANNINI, M., SESSOLI, R. Organizing and Addressing Magnetic Molecules, *Inorganic Chemistry*. 2009, vol. 48, no. 8, pp. 3408-3419.
- [125] BENELLI, C. and GATTESCHI, D., *Introduction to Molecular Magnetism: From Transition Metals to Lanthanides*. Wiley-VCH, 2015.
- [126] VAN SLAGEREN, J. New Directions in Electron Paramagnetic Resonance Spectroscopy on Molecular Nanomagnets. *EPR Spectroscopy*. 2011, pp. 199–234. DOI: 10.1007/128\_2011\_303.

- 
- [127] VAN SLAGEREN, J., VONGTRAGOOL, S., GORSHUNOV, B., MUKHIN, A., AND DRESSEL, M. Frequency-domain magnetic-resonance spectroscopic investigations of the magnetization dynamics in  $\text{Mn}_{12}\text{Ac}$  single crystals. *Physical Review B*. 2009, vol. 79, iss. 22. DOI: 10.1103/physrevb.79.224406.
- [128] GATTESCHI, D., SESSOLI, R., AND VILLAIN, J., *Molecular Nanomagnets*. Oxford University Press, 2006.
- [129] MANNINI, M., PINEIDER, F., SAINCTAVIT, P., DANIELI, C., OTERO, E., SCIANCALEPORE, C., TALARICO, A. M., ARRIO, M.-A., CORNIA, A., GATTESCHI, D., SESSOLI, R. Magnetic memory of a single-molecule quantum magnet wired to a gold surface. *Nature Materials*. 2009, vol. 8, no. 3, pp. 194-197. DOI: 10.1038/nmat2374.
- [130] PEDERSEN, K. S., ARICIU, A.-M., MCADAMS, S., WEIHE, H., BENDIX, J., TUNA, F., PILIGKOS, S. Toward Molecular 4f Single-Ion Magnet Qubits. *Journal of the American Chemical Society*. 2016, vol. 138, no. 18, pp. 5801-5804. DOI: 10.1021/jacs.6b02702.
- [131] ROCHA, A. R., GARCÍA-SUÁREZ, V. M., BAILEY, S. W., LAMBERT, C. J., FERRER, J., SANVITO, S. Towards molecular spintronics. *Nature Materials*. 2005, vol. 4, no. 4, pp. 335-339. DOI: 10.1038/nmat1349.
- [132] WOODRUFF, D. N., WINPENNY, R. E. P. and LAYFIELD, R. A. Lanthanide Single-Molecule Magnets. *Chemical Reviews*. 2013, vol. 113, no. 7, pp. 5110-5148. DOI: 10.1021/cr400018q.
- [133] GUO, F.-S., DAY, B. M., CHEN, Y.-C., TONG, M.-L., MANSIKKAMÄKI, A., LAYFIELD, R. A. Magnetic hysteresis up to 80 kelvin in a dysprosium metallocene single-molecule magnet. *Science*. 2018, vol. 362, no. 6421, pp. 1400-1403. DOI: 10.1126/science.aav0652.
- [134] VAN SLAGEREN, J. Introduction to Molecular Magnetism [online]. Physikalisches Institut, Universität Stuttgart [cit. 2018-03-25]. Available from: <http://obelix.physik.uni-bielefeld.de/~schnack/molmag/material/123.pdf>.
- [135] LAYFIELD, R. A. and MURUGESU, M. *Lanthanides and actinides in molecular magnetism*. Weinheim: Wiley-VCH, 2015. ISBN 978-3527335268.
- [136] MISRA, S. K. *Multifrequency Electron Paramagnetic Resonance*. Weinheim, Germany: Wiley-VCH Verlag GmbH & Co., 2011. ISBN: 9783527633531.

- [137] TELSER, J. EPR Interactions - Zero-field Splittings. HARRIS, R. K. a R. D. WASYLISHEN. *EMagRes.* 2017, vol 6, pp. 207-234. Chichester, UK: John Wiley. ISBN: 9780470034590.
- [138] WALDMANN, O. A Criterion for the Anisotropy Barrier in Single-Molecule Magnets. *Inorganic Chemistry.* 2007, vol. 46, no. 24, pp. 10035-10037. DOI: 10.1021/ic701365t.
- [139] NEESE, F. and PANTAZIS, D. A. What is not required to make a single molecule magnet. *Faraday Discuss.* 2011, vol. 148, pp. 229-238. DOI: 10.1039/C005256F.
- [140] ISHIKAWA, N., SUGITA, M., ISHIKAWA, T., KOSHIHARA, S., KAIZU, Y. Lanthanide Double-Decker Complexes Functioning as Magnets at the Single-Molecular Level. *Journal of the American Chemical Society.* 2003, vol. 125, no. 29, pp. 8694-8695. DOI: 10.1021/ja029629n.
- [141] NEHRKORN, J., VEBER, S. L., ZHUKAS, L. A., NOVIKOV, V. V., NELYUBINA, Y. V., VOLOSHIN, Y. Z., HOLLDAK, K., L, S., SCHNEGG, A. Determination of Large Zero-Field Splitting in High-Spin Co(I) Clathrochelates. *Inorganic Chemistry.* 2018, vol. 57, no. 24, pp. 15330-15340. DOI: 10.1021/acs.inorgchem.8b02670.
- [142] KRZYSTEK, J., OZAROWSKI, A., TELSER, J. Multi-frequency, high-field EPR as a powerful tool to accurately determine zero-field splitting in high-spin transition metal coordination complexes. *Coordination Chemistry Reviews.* 2006, vol. 250, no. 17-18, pp. 2308-232. DOI: 10.1016/j.ccr.2006.03.016.
- [143] SCHNEGG, A. Very-high-frequency EPR. HARRIS, R. K. a R. D. WASYLISHEN. *EMagRes.* 2017, vol 6, pp. 115-132. Chichester, UK: John Wiley. ISBN 9780470034590.
- [144] KITTEL, Ch. *Introduction to solid state physics.* 2005. 8th ed. Hoboken: John Wiley. ISBN 0-471-41526-x.
- [145] ORLITA, M. and POTEMSKI, M. Dirac electronic states in graphene systems: optical spectroscopy studies. *Semiconductor Science and Technology.* 2010, vol. 5, no. 6. DOI: 10.1088/0268-1242/25/6/063001.
- [146] NEDOLIUK, I. *Infrared magneto-optical spectroscopy of boron nitride encapsulated graphene.* 2018, GENÈVE. Available from: <http://archive-ouverte.unige.ch/unige:114899>. Dissertation Thesis. UNIVERSITÉ DE GENÈVE.

- 
- [147] ORLITA, M., FAUGERAS, C., SCHNEIDER, J. M., MARTINEZ, G., MAUDE, D. K., POTEMSKI, M. Graphite from the Viewpoint of Landau Level Spectroscopy: An Effective Graphene Bilayer and Monolayer. *Physical Review Letters*. 2009, vol. 102, no. 16. DOI: 10.1103/PhysRevLett.102.166401.
- [148] NOVOSELOV, K. S., GEIM, A. K., MOROZOV, S. V., JIANG, D., ZHANG, Y., DUBONOS, S. V., GRIGORIEVA, I. V., FIRSOV, A. A. Electric Field Effect in Atomically Thin Carbon Films. *Science*. 2004, vol. 306, no. 5696, pp. 666-669. DOI: 10.1126/science.1102896.
- [149] NOVOSELOV, K. S., FAL'KO, V. I., COLOMBO, L., GELLERT, P. R., SCHWAB, M. G., KIM, K. A roadmap for graphene. *Nature*. 2012, vol. 490, no. 7419, pp. 192-200. DOI: 10.1038/nature11458.
- [150] CASTRO NETO, A. H., GUINEA, F., PERES, N. M. R., NOVOSELOV, K. S., GEIM, A. K. The electronic properties of graphene. *Reviews of Modern Physics*. 2009, vol. 81, no. 1, pp. 109-162. DOI: 10.1103/RevModPhys.81.109.
- [151] GEIM, A. K., MACDONALD, A. H. Graphene: Exploring carbon flatland. *Physics Today*. 2007, vol. 60, no. 8, pp. 35-41. DOI: 10.1063/1.2774096. Available from: <http://physicstoday.scitation.org/doi/10.1063/1.2774096>.
- [152] NOVOSELOV, K. S. Nobel Lecture: Graphene. *Reviews of Modern Physics*. 2011, vol. 83, no.3, pp. 837-849 . DOI: 10.1103/RevModPhys.83.837.
- [153] RADISAVLJEVIC, B., RADENOVIC, A., BRIVIO, J., GIACOMETTI, V., KIS, A. Single-layer MoS<sub>2</sub> transistors. *Nature Nanotechnology*. 2011, vol. 6, no. 3, pp. 147-150. DOI: 10.1038/nnano.2010.279.
- [154] YIN, Z., LI, H., LI, H., JIANG, L., SHI, Y., SUN, Y., LU, G., ZHANG, Q., CHEN, X., ZHANG, H. Single-Layer MoS<sub>2</sub> Phototransistors. *ACS Nano*. 2011, vol. 6, no. 1, pp. 74-80. DOI: 10.1021/nm2024557.
- [155] MAK, K. F., MCGILL, K. L., PARK, J., MCEUEN, P. L. The valley Hall effect in MoS<sub>2</sub> transistors. *Science*. 2014, vol. 344, no. 6191, pp. 1489-1492. DOI: 10.1126/science.1250140.
- [156] EFTEKHARI, A. Tungsten dichalcogenides (WS<sub>2</sub> , WSe<sub>2</sub> , and WTe<sub>2</sub> ): materials chemistry and applications. *Journal of Materials Chemistry A*. 2017, vol. 5, no. 35, pp. 18299-18325. DOI: 10.1039/C7TA04268J.
- [157] WANG, Q. H., KALANTAR-ZADEH, K., KIS, A., COLEMAN, J. N., STRANO, M. S. Electronics and optoelectronics of two-dimensional transition

- metal dichalcogenides. *Nature Nanotechnology*. 2012, vol. 7, no. 11, pp. 699-712. DOI: 10.1038/nnano.2012.193.
- [158] JOYCE, R. R. AND P. L. RICHARDS. Far-Infrared Spectra of  $\text{Al}_2\text{O}_3$  Doped with Ti, V, and Cr. *Physical Review*. 1969, vol. 179, no. 2, pp. 375-380.
- [159] CHAMPION, P. M., AND SIEVERS, A. J. Far infrared magnetic resonance of deoxyhemoglobin and deoxymyoglobin. *Journal of Chemical Physics*. 1980, vol. 72, iss. 3, pp. 1569-1582. DOI: 10.1063/1.439356.
- [160] MIHÁLY, L., TALBAYEV, D., KISS, L. F., ZHOU, J., FEHÉR, T., AND JÁNOSSY, A. Field-frequency mapping of the electron spin resonance in the paramagnetic and antiferromagnetic states of  $\text{LaMnO}_3$ . *Physical Review B*. 2004, vol. 69, iss. 2. DOI: 10.1103/physrevb.69.024414.
- [161] TALBAYEV, D., MIHÁLY, L., AND ZHOU, J. Antiferromagnetic Resonance in  $\text{LaMnO}_3$  at Low Temperature. *Physical Review Letters*. 2004, vol. 93, iss. 1. DOI: 10.1103/physrevlett.93.017202.
- [162] LOBO, R. P. S. M., LAVEIGNE, J. D., REITZE, D. H., TANNER, D. B., CARR, G. L. Performance of new infrared beamline U12IR at the National Synchrotron Light Source. *Review of Scientific Instruments*. 1999, vol. 70, no. 2899. DOI: 10.1063/1.1149846.
- [163] HOLLDAK, K., SCHNEGG, A. THz Electron Paramagnetic Resonance / THz Spectroscopy at BESSY II. *Journal of large-scale research facilities JL-SRF*. 2016, vol. 2. DOI: 10.17815/jlsrf-2-74. ISSN 2364-091X.
- [164] TAKEHANA, K., OSHIKIRI, M., KIDO, G., TAKAZAWA, A., SATO, M., NAGASAKA, K., HASE, M., UCHINOKURA, K. Far-infrared spectroscopy in high magnetic fields. *Physica B: Condensed Matter*. 1996, vol. 216, no. 3-4, pp. 354-357. DOI:10.1016/0921-4526(95)00516-1.
- [165] MULLER, F., HOPKINS, M. A., CORON, N., GRYNBERG, M., BRUNEL, L. C., AND MARTINEZ, G. A high magnetic field EPR spectrometer. *Review of Scientific Instruments*. 1989, vol. 60, iss. 12, pp. 3681-3684. DOI: 10.1063/1.1140474.
- [166] BROWN, D. E., DUMELOW, T., JENSEN, M. R. F., AND PARKER, T. J. A high-resolution Fourier transform spectrometer for far infrared magneto-optic spectroscopy of magnetic materials. *Infrared Physics and Technology*. 1999, vol. 40, iss. 3, pp. 219-230. DOI: 10.1016/s1350-4495(99)00013-4.

- 
- [167] KOJIMA, K. M., UCHIDA, S., FUDAMOTO, Y., TAJIMA, S. New Josephson plasma modes in underdoped  $\text{YBa}_2\text{Cu}_3\text{O}_{6.6}$  induced by a parallel magnetic field. *Physical Review Letters*. 2002, vol. 89, no. 24. DOI: 10.1103/PhysRevLett.89.247001.
- [168] KADLEC, C., KADLEC, F., GOIAN, V., GICH, M., KEMPA, M., ROLS, S., SAVINOV, M., PROKLEŠKA, J., ORLITA, M., KAMBA, S. Electromagnon in ferrimagnetic  $\epsilon - \text{Fe}_2\text{O}_3$  nanograin ceramics. *Physical Review B*. 2013, vol. 88, no. 104301. DOI: 10.1103/PhysRevB.88.104301.
- [169] WIEGERS, S. A. J., CHRISTIANEN, P. C. M., ENGELKAMP, H., DEN OUDEN, A., PERENBOOM, J. A. A. J., ZEITLER, U., MAAN, J. C. The High Field Magnet Laboratory at Radboud University Nijmegen. *Journal of Low Temperature Physics*. 2009, vol. 159, no.1-2, pp. 389-393. DOI: 10.1007/s10909-009-0076-8.
- [170] VAN MECHELEN, J. L. M., VAN DER MAREL, D., CRASSEE, I., KOLODIAZHNYI, T. Spin resonance in  $\text{EuTiO}_3$  probed by Time-Domain Gigahertz Ellipsometry. *Physical Review Letters*. 2011, vol. 106, no. 21. DOI: 10.1109/IRMMW-THz.2012.6380201.
- [171] SCHUBERT, M., KNIGHT, S., RICHTER, S., KÜHNE, P., STANISHEV, V., RUDER, A., STOKEY, M., KORLACKI, R., IRMSCHER, K., NEUGEBAUER, P., DARAKCHIEVA, V. Terahertz electron paramagnetic resonance generalized spectroscopic ellipsometry: The magnetic response of the nitrogen defect in 4H-SiC. *Applied Physics Letters*. 2022, vol. 120, no. 102101. DOI: 10.1063/5.0082353.
- [172] EARLE, K. A., TIPIKIN, D. S., FREED, J. H. Far-infrared electron-paramagnetic-resonance spectrometer utilizing a quasioptical reflection bridge. *Review of Scientific Instruments*. 1996, vol. 67, iss. 7, pp. 2502–2513. DOI: 10.1063/1.1147205.
- [173] MIDLÍKOVÁ, J. *Design of the far-infrared spectrometer coupling to a superconductive magnet and magneto-optical measurements in the far-infrared region*. Brno, 2018. Master's Thesis. Brno University of Technology. Faculty of Mechanical Engineering, Institute of Physical Engineering. Supervised by Ing. Petr Neugebauer, PhD.
- [174] NEUBAUER, D. *Optical and magneto-optical investigations on 3D Dirac and Weyl-semimetals*. 2017, Stuttgart. Available from: <https://elib.>

- [uni-stuttgart.de/handle/11682/9183](http://uni-stuttgart.de/handle/11682/9183). Dissertation Thesis. University of Stuttgart.
- [175] NEDOLIUK, I. *Infrared magneto-optical spectroscopy of boron nitride encapsulated graphene*. 2018, GENÈVE. Available from: <http://archive-ouverte.unige.ch/unige:114899>. Dissertation Thesis. UNIVERSITÉ DE GENÈVE.
- [176] KÜHNE, P., HERZINGER, C. M., SCHUBERT, M., WOOLLAM, J. A., HOFMANN, T. An integrated mid-infrared, far-infrared, and terahertz optical Hall effect instrument. *Review of Scientific Instruments*. 2014, vol. 85, no. 7. DOI: 10.1063/1.4889920.
- [177] KUHNE, P., ARMAKAVICIUS, N., STANISHEV, V., HERZINGER, C. M., SCHUBERT, M., DARAKCHIEVA, V. Advanced Terahertz Frequency-Domain Ellipsometry Instrumentation for In Situ and Ex Situ Applications. *IEEE Transactions on Terahertz Science and Technology*. 2018, vol. 8, no. 3, pp. 257-270. DOI: 10.1109/TTHZ.2018.2814347.
- [178] VERTEX 80/80v: VERTEX 80/80v FTIR spectrometers. *BRUKER* [online]. [cit. 2018-05-30]. Available from: <https://www.bruker.com/products/infrared-near-infrared-and-raman-spectroscopy/ft-ir-research-spectrometers/vertex-series/vertex-8080v/overview.html>.
- [179] OPUS Spectroscopy Software. *BRUKER* [online]. [cit. 2018-05-20]. Available from: <https://www.bruker.com/products/infrared-near-infrared-and-raman-spectroscopy/opus-spectroscopy-software.html>.
- [180] BRUKER OPTICS. Guide for Infrared Spectroscopy, 2009. [cit. 2023-08-20]. Available from: <https://www.ccmr.cornell.edu/wp-content/uploads/sites/2/2015/11/GuideforInfraredspectroscopy.pdf>.
- [181] *Infrared Laboratories*. Bolometers. Available from: <http://www.infraredlaboratories.com/Bolometers.shtml>.
- [182] *VERTEX Series: Advanced Research FTIR Spectrometers* [online]. [cit. 2018-05-15]. Available from: [https://www.bruker.com/fileadmin/user\\_upload/8-PDF-Docs/OpticalSpectroscopy/FT-IR/VERTEX/Brochures/VERTEXseries\\_Brochure\\_EN.pdf](https://www.bruker.com/fileadmin/user_upload/8-PDF-Docs/OpticalSpectroscopy/FT-IR/VERTEX/Brochures/VERTEXseries_Brochure_EN.pdf).

- 
- [183] *Cryogenic Limited*. Cryogen Free Magnet System 9-18 Tesla (CFMS). Available from: <https://www.cryogenic.co.uk/products/cryogen-free-magnet-system-9-18-tesla-cfms>
- [184] SOJKA, A. *Development of a Terahertz Magnetic Resonance Spectrometer for Electron Spin Dynamics Investigations*. Brno, 2022. Doctoral thesis. Brno University of Technology. Central European Institute of Technology. Supervised by Ing. Petr Neugebauer, PhD.
- [185] Series 012 — Mini gate valve VATLOCK. *VAT* [online]. [cit. 2018-05-20]. Available from: [http://www.vatvalve.com/en/business/valves/catalog/A/012\\_1\\_V](http://www.vatvalve.com/en/business/valves/catalog/A/012_1_V).
- [186] Protected Gold Mirrors: Features. *THORLABS* [online]. [cit. 2018-05-18]. Available from: [https://www.thorlabs.com/newgrouppage9.cfm?objectgroup\\_id=744](https://www.thorlabs.com/newgrouppage9.cfm?objectgroup_id=744).
- [187] SOJKA, A., ŠEDIVÝ, M., LAGIŇ, A., GABRIŠ, A., LÁZNIČKA, T., SANTANA, V. T., LAGUTA, O., NEUGEBAUER, P. Sample Holders for Sub-THz Electron Spin Resonance Spectroscopy, *IEEE Transactions on Instrumentation and Measurement*, vol. 71, pp. 1-12, 2022. DOI: 10.1109/TIM.2022.3164135.
- [188] LAGIŇ, A. *Design of non-resonant sample holders*. Brno, 2020. Available at: <https://www.vutbr.cz/studenti/zav-prace/detail/124733>. Bachelor thesis. Brno University of Technology, Faculty of Mechanical Engineering, Institute of Machine and Industrial Design. Supervised by Ing. Antonín Sojka.
- [189] EL FATIMY, A., *et al.* Epitaxial graphene quantum dots for high-performance terahertz bolometers. *Nature Nanotechnology*. 2016, vol. 11, no. 4, pp. 335-338. DOI: 10.1038/nnano.2015.303.
- [190] EL FATIMY, A., *et al.* Ultra-broadband photodetectors based on epitaxial graphene quantum dots. *Nanophotonics*. 2018, vol. 7, no. 4, pp. 735-740. DOI: 10.1515/nanoph-2017-0100.
- [191] MARIE, L. S., EL FATIMY, A., HRUBÝ, J., NEMEC, I., HUNT, J., MYERS-WARD, R., GASKILL, D. K., KRUSKOPF, M., YANG, Y., EL-MQUIST, R., MARX, R., VAN SLAGEREN, J., NEUGEBAUER, P., BARBARA, P. Nanostructured graphene for nanoscale electron paramagnetic resonance spectroscopy. *Journal of Physics: Materials*. 2020, vol. 3, no. 014013. DOI: 10.1088/2515-7639/ab6af8.

- [192] LAGUTA, O., SOJKA, A., MARKO, A., NEUGEBAUER, P. Rapid scan ESR: A versatile tool for the spin relaxation studies at (sub)THz frequencies. *Applied Physics Letters*. 2022, vol. 120, no. 120502. DOI: 10.1063/5.0083010.
- [193] WANG, X., JIANG, M., ZHOU, Z., GOU, J., HUI, D. 3D printing of polymer matrix composites: A review and prospective. *Composites Part B: Engineering*. 2017, vol. 110, pp. 442–458. DOI: 10.1016/j.compositesb.2016.11.034.
- [194] WHAT IS SOLDERING? A FULL GUIDE: (MEANING, DEFINITION AND TYPES). Twi-global.com: Technical knowledge [online]. [cit. 2023-05-13]. Available from: <https://www.twi-global.com/technical-knowledge/faqs/what-is-soldering>.
- [195] Polishing. En.wikipedia.org [online]. [cit. 2023-05-13]. Available from: <https://en.wikipedia.org/wiki/Polishing>.
- [196] MULTI-USE CLEANING KIT. Decathlon.co.uk [online]. [cit. 2023-05-13]. Available from: [https://www.decathlon.co.uk/p/multi-use-cleaning-kit/\\_/R-p-10934?mc=3318058](https://www.decathlon.co.uk/p/multi-use-cleaning-kit/_/R-p-10934?mc=3318058).
- [197] Electrolysis. En.wikipedia.org [online]. [cit. 2023-05-13]. Available from: <https://en.wikipedia.org/wiki/Electrolysis>.
- [198] Silver Plating. AshevilleMetalFinishing.com: The Leader in Electroplating and Anodizing [online]. [cit. 2023-05-13]. Available from: <https://www.ashevillemetalfinishing.com/2019/11/20/silver-plating/>.
- [199] LARS CHEMIE: SERVICES: SURFACE TREATMENT - SILVER PLATING. Lars.cz: Your specialist for surface treatment. [online]. [cit. 2023-05-13]. Available from: <https://www.lars.cz/en/>.
- [200] Protected Silver Mirrors: Overview. Thorlabs.com: Thorlabs Home [online]. [cit. 2023-05-13]. Available from: [https://www.thorlabs.com/newgrouppage9.cfm?objectgroup\\_id=903](https://www.thorlabs.com/newgrouppage9.cfm?objectgroup_id=903).
- [201] Metallic Mirror Coatings. EdmundOptics.com: Edmund Optics Worldwide [online]. [cit. 2023-05-13]. Available from: <https://www.edmundoptics.com/knowledge-center/application-notes/optics/metallic-mirror-coatings/>.
- [202] LABRIE, D., BOOTH, I. J., THEWALT, M. L. W., CLAYMAN, B. P. Use of polypropylene film for infrared cryogenic windows. *Applied Optics*. 1986, vol. 25, no. 2. DOI: 10.1364/AO.25.000171.

- 
- [203] LOEWENSTEIN, E. V. and ENGELSRATH, A. Polarization properties of far infra-red beamsplitters. *Le Journal de Physique Colloques*. 1967, vol. 28, no. 2, pp. 153-155. DOI: 10.1051/jphyscol:1967228.
- [204] BOČA, R. Magnetic Parameters and Magnetic Functions in Mononuclear Complexes Beyond the Spin-Hamiltonian Formalism. *Structure and Bonding*. 2006, vol. 117, pp. 1–264. DOI: 10.1007/b136907.
- [205] DRESSELHAUS, G., KIP, A. F., KITTEL, C. Cyclotron Resonance of Electrons and Holes in Silicon and Germanium Crystals. *Physical Review*. 1955, vol. 98, iss. 2, pp. 368–384. DOI: 10.1103/physrev.98.368.
- [206] YU, P. Y., and CARDONA, M., *Fundamentals of Semiconductors, Graduate Texts in Physics*, 4th ed., Springer-Verlag, Berlin Heidelberg, 2010. ISBN: 978-3-642-00710-1.
- [207] MIURA, N. Physics of semiconductors in high magnetic fields. Oxford: Oxford University Press. 2008. ISBN 978-0-19-851756-6.
- [208] KESSLER, F. R. and METZDORF, J. CHAPTER 11 - Landau Level Spectroscopy: Interband Effects and Faraday Rotation. In: LANDWEHR, G., RASHBA, E. I. *Modern Problems in Condensed Matter Sciences*, Elsevier. 1991, vol. 27, no. 1, pp. 579-675, 1991. ISBN: 978-0444885357.
- [209] VARSHNI, Y. P. Temperature dependence of the energy gap in semiconductors, *Physica*. 1967, vol. 34, no. 1, pp. 149–154. DOI: 10.1016/0031-8914(67)90062-6.
- [210] HASS, J., FENG, R., MILLÁN-OTOYA, J. E., LI, X., SPRINKLE, M., FIRST, P. N., DE HEER, W. A., CONRAD, E. H., BERGER, C. Structural properties of the multilayer graphene/4H – SiC(0001) system as determined by surface x-ray diffraction. *Physical Review B*. 2007, vol. 75, iss. 21. DOI: 10.1103/PhysRevB.75.214109.
- [211] HASS, J., VARCHON, F., MILLÁN-OTOYA, J. E., SPRINKLE, M., SHARMA, N., DE HEER, W. A., BERGER, C., FIRST, P. N., MAGAUD, L., CONRAD, E. H. Why Multilayer Graphene on 4H - SiC(0001) Behaves Like a Single Sheet of Graphene. *Physical Review B*. 2008, vol. 100, iss. 12, 2008. DOI: 10.1103/PhysRevLett.100.125504.
- [212] BERGER, C., SONG, Z., LI, X., WU, X., BROWN, N., NAUD, C., MAYOU, D., LI, T., HASS, J., MARCHENKOV, A. N., CONRAD, E. H., FIRST, P. N., DE HEER, W. A. Electronic Confinement and Coherence in Patterned

- Epitaxial Graphene. *Science*. 2006, vol. 312, iss. 5777, pp. 1191–1196. DOI: 10.1126/science.1125925.
- [213] VARCHON, F., FENG, R., HASS, J., LI, X., NGUYEN, B. N., NAUD, C., MALLET, P., VEUILLEN, J.-Y., BERGER, C., CONRAD, E. H., MAGAUD, L. Electronic Structure of Epitaxial Graphene Layers on SiC: Effect of the Substrate. *Physical Review Letters*. 2007, vol. 99, iss. 12. DOI: 10.1103/PhysRevLett.99.126805.
- [214] RICHARDS, P. L., MCCREIGHT, C. R. Infrared Detectors for Astrophysics. *Physics Today*. 2005, vol. 58, pp. 41–47. DOI: 10.1063/1.1897522.
- [215] HRUBÝ, J. *Preparation and Characterization of Graphene Based Hybrid Materials*. Brno, 2017. 91 p. Master-s thesis. Brno University of Technology. Faculty of Mechanical Engineering. Supervised by Ing. Petr NEUGEBAUER, Ph.D.
- [216] TAN, Y. W., ZHANG, Y., STORMER, H. L., KIM, P. Temperature dependent electron transport in graphene. *European Physical Journal: Special Topics*. 2007, vol. 148, pp. 15–18. DOI: 10.1140/epjst/e2007-00221-9.
- [217] YAN, J., KIM, M. H., ELLE, J. A., SUSHKOV, A. B., JENKINS, G. S., MILCHBERG, H. M., FUHRER, M. S., DREW, H. D. Dual-gated bilayer graphene hot-electron bolometer. *Nature Nanotechnology*. 2012, vol. 7, pp. 472–478. DOI: 10.1038/nnano.2012.88.
- [218] HAN, Q., GAO, T., ZHANG, R., CHEN, Y., CHEN, J., LIU, G., ZHANG, Y., LIU, Z., WU, X., YU, D. Highly sensitive hot electron bolometer based on disordered graphene. *Scientific Reports*. 2013, vol. 3, no. 3533. DOI: 10.1038/srep03533.
- [219] SOLODOVNYK, A., LAGUTA O., PROKHOROV, SEGANTINI M., NAYDENOV B., NEUGEBAUER P., GREULICH-WEBER S., KALABUKHOVA E. AND SAVCHENKO D. Spin dynamics of the exchange-coupled nitrogen donors in heavily doped n-type 15R SiC monocrystals: multi-frequency EPR and EDMR study. *Physical Review B*. 2023, vol. 107, no. 155202. DOI:10.1103/PhysRevB.107.155202.
- [220] SOLODOVNYK, A., SAVCHENKO D., LAGUTA O., and NEUGEBAUER P. Implementation of Broadband Electrically Detected Magnetic Resonance in a sub-THz FraScan Spectrometer *IEEE Transactions on Instrumentation and Measurement*. 2023, vol. 72, pp. 1-8. DOI: 10.1109/TIM.2023.3284951.



---

# List of Used Abbreviations

2D	2-Dimensional
3D	3-Dimensional
ABS	Acrylonitrile Butadiene Styrene
AC	Alternating Current
ADC	Analog-to-Digital Converter
AM	Additive Manufacturing
APT	Aperture
BMS	Beamsplitter
BoPET	biaxially-oriented polyethylene terephthalate
BUT	Brno University of Technology
CAD	Computer-Aided Design
CEITEC	Central European Institute of Technology
CNRS	French National Center for Scientific Research
CW-EPR	Continuous Wave Electron Paramagnetic Resonance
DC	Direct Current
DLATGS	Deuterated L-alanine-doped Triglycine Sulfate
DPPH	1,1-diphenyl-2-picrylhydrazyl
DTGS	Deuterium Triglycine Sulfate
EPR	Electron Paramagnetic Resonance
ERC	European Research Council
ESR	Electron Spin Resonance
FD-FT	Frequency Domain Fourier Transform
FDM	Fused Deposition Modeling

FFT	Fast Fourier Transformation
FIR	Far-Infrared
FIRMS	Far Infrared Magnetic Spectroscopy
FT	Fourier Transform
FTIR	Fourier Transform Infrared
GHMFL	Grenoble High Magnetic Field Laboratory
GM	Gifford-McMahon
GQD	Graphene Quantum Dot
HeNe	Helium-Neon
HF-EPR	High-field/high-frequency EPR
HF-EPR	High Frequency/Field Electron Paramagnetic Resonance
HS	High-Spin
HZB	Helmholtz Zentrum Berlin
IF	Impact Factor
IPC	Institute of Physical Chemistry
IR	Infrared
LEDs	Light-Emitting Diodes
LHe	Liquid Helium
LIDAR	Light Detection and Ranging or Laser Imaging, Detection, and Ranging
LL	Landau Level
LLs	Landau Levels
LN <sub>2</sub>	Liquid Nitrogen
LS	Low-Spin
MCT	Mercury Cadmium Telluride
MEG	Multilayer Epitaxial Graphene

---

MEYS CR Ministry of Education Youth and Sports of the Czech Republic

MIR Mid-Infrared

MRI Magnetic Resonance Imaging

MW Microwave

MWs Microwaves

NEP Noise Equivalent Power

NHMFL National High Magnetic Field Laboratory

NIR Near-Infrared

NMR Nuclear Magnetic Resonance

NSLS National Synchrotron Light Source

OPD Optical Path Difference

PA Polyamide

PET Polyethylene terephthalate

PLA Polylactic Acid

RFL Reflective Focal Length

SH Spin Hamiltonian

SIM Single-Ion Magnet

SIMs Single-Ion Magnets

SMM Single-Molecule Magnet

SMMs Single-Molecule Magnets

SNR Signal-to-Noise Ratio

SOC Spin-Orbit Coupling

SSC Spin-Spin Coupling

STL Surface Tessellation Language

TIM Transactions on Instrumentation and Measurement

TGS Triglycine Sulfate

THz-EPR Terahertz Electron Paramagnetic Resonance

THz-FRaScan Terahertz Rapid Frequency Scans

TMDCs Transition Metal Dichalcogenides

UV Ultraviolet

VTI Variable Temperature Insert

ZFS Zero-Field Splitting

ZPD Zero Path Difference

---

# Author publications and outputs

**Publications (09/2023)** <https://orcid.org/0000-0003-1381-7469>

- **Dubnická Midlíková, J.**; Šedivý, M.; Sojka, A.; Tadeu Santana, V.; Dubroka, A.; Neugebauer, P. A Versatile Setup for FTIR Magneto-Spectroscopy *IEEE Transactions on Instrumentation and Measurement*, vol. 72, pp. 1-11, 2023. DOI: 10.1109/TIM.2023.3284943. (Impact Factor (IF)=5.33, Q1, 0 cit.)
- Malinová, N.; Juráková, J.; Brachňáková, B.; **Dubnická Midlíková, J.**; Čižmár, E.; Tadeu Santana, V.; Herchel, R.; Orlita, M.; Mohelský, I.; Moncol, J.; Neugebauer, P.; Šalitroš, I. Magnetization Slow Dynamics in Mononuclear Co(II) Field-Induced Single-Molecule Magnet. *Crystal Growth & Design*, 23, 4, 2430–2441, 2023. DOI: 10.1021/acs.cgd.2c01388. (IF=4.01, Q1, 0 cit.)
- Juráková, J.; **Dubnická Midlíková, J.**; Hrubý, J.; Kliukov, A.; Tadeu Santana, V.; Pavlik, J.; Moncol, J.; Čižmár, E.; Orlita, M.; Mohelský, I.; Neugebauer, P.; Gentili, D.; Cavallini, M.; Šalitroš, I. Pentacoordinate cobalt(II) single ion magnets with pendant alkyl chains: shall we go for chloride or bromide? *Inorg. Chem. Front.* 9, 1179-1194, 2022. DOI: 10.1039/D1QI01350E. (IF=7.78, Q1, 10 cit.)
- Bamberger, H.; Albold, U.; **Dubnická Midlíková, J.**; Su, C.-Y.; Deibel, N.; Hunger, D.; Hallmen, P. P.; Neugebauer, P.; Beerhues, J.; Demeshko, S.; Meyer, F.; Sarkar, B.; van Slageren, J. Iron(II), Cobalt(II), and Nickel(II) Complexes of Bis(sulfonamido)benzenes: Redox Properties, Large Zero-Field Splittings, and Single-Ion Magnets. *Inorg. Chem.* 60, 2953–2963, 2021. DOI: 10.1021/acs.inorgchem.0c02949. (IF=5.44, Q1, 12 cit.)

## Internships

- 10/2021 – One-month research stay at the **Department of Physics, Georgetown University** in Washington DC, USA, group of Prof. Paola Barbara. Topic: *Transport measurements on graphene bolometer devices.*
- 04/2019 – One-month research stay at **Grenoble High Magnetic Field Laboratory (GHMFL)** in France, sponsored by CEITEC mobility contribution 2018. French National Center for Scientific Research (CNRS), group of Dr. Milan Orlita. Topic: *FTIR measurements with graphene bolometer devices.*
- 04/2018 – Short-Term Scientific Mission in Molecular Spintronics (MOLSPIN) in Germany sponsored by COST Action scholarship. **Institute of Physical Chemistry at University of Stuttgart**, group of prof. Joris van Slageren, Topic: *Coupling of the far-infrared spectrometer to a superconductive magnet and magneto-optical measurements in far-infrared region.*

- 04/2017 – Research stay at **Grenoble High Magnetic Field Laboratory (GHMFL)** in France, sponsored by University of Stuttgart. French National Center for Scientific Research (CNRS), group of Dr. Milan Orlita. Topic: *Infrared magneto-spectroscopy of mononuclear Co-complexes*.
- 02-07/2017 – Erasmus+ scholarship project in Germany, **Institute of Physical Chemistry at University of Stuttgart**, group of prof. J. van Slageren. Topic: *Coupling of the FIR spectrometer to a 17 T superconducting magnet*.

## Conferences

- 09/2022 – Alpine Conference on Magnetic Resonance in Solids 2022, Chamonix-Mont-Blanc, France – **Oral contribution** (round table presentation)
- 06/2021 – 17th International Conference on Molecule Based Magnets (ICMM2021), Manchester, United Kingdom (online) – **Poster contribution, award**
- 09/2019 – 11th European Federation of EPR groups (EFEPR) Conference Bratislava 2019, Slovakia – **Poster contribution**
- 07/2018 – International Conference on Nanoscience+Technology 2018 (ICN+T 2018) Brno, Czech Republic – **Poster contribution**

## Summer Schools, Workshops, Retreats

- 09/2021 – CEITEC PhD Retreat 2021, Brno, Czech Republic (online) – **Oral contribution** (flash talk)
- 11/2019 – 8th School of the European Federation of EPR groups on Advanced EPR (EFEPR School 2019) Brno, Czech Republic – **Poster contribution**
- 06/2019 – CEITEC PhD Joint Retreat in Hotel Luna, Czech Republic – **Oral contribution** (flash talk)
- 06/2019 – Plasmon Enhanced Terahertz Electron Paramagnetic Resonance (PETER) Project - International Workshop, Hirschegg, Austria
- 06/2019 – 2nd MOTeS Retreat 2019, Masłowski, Poland – **Oral contribution**
- 11/2018 – 3rd CEITEC NANO User meeting, Brno – **Poster contribution**
- 10/2018 – Plasmon Enhanced Terahertz Electron Paramagnetic Resonance (PETER) Summer School in Brno, Czech Republic – **Oral contribution**
- 09/2018 – V. International School for Young Scientists. Magnetic Resonance and Magnetic Phenomena in Chemical and Biological Physics, St. Petersburg, Russia – **Poster and Oral contribution** (flash talk)
- 06/2019 – 1st MOTeS Retreat 2018 in Vyhne, Slovakia – **Oral contribution**

## Projects

- 12/2019 – **Inter-Excellence USA-CZ 2019** (LTAUSA19060) – member of the international solving team.

- 
- 03/2019 – **Internal junior grant project** within the CEITEC BUT 2019 – principal investigator.
  - 01/2019 – **Brno PhD Talent 2018** project – principal investigator.

## Awards

- 06/2021 – **Outstanding Poster Presentation Prize** at ICMM2021 conference in Manchester (UK) awarded by RSC Inorganic Chemistry Frontiers.
- 12/2018 – **Brno PhD Talent 2018** Scholarship – awarded by JCMM Brno.
- 10/2018 – **Edwards Award 2018** – 4th place for my master’s thesis.

## Products/Functional Specimens

- Movable Table for FTIR Magneto-Spectroscopic Setup
- FTIR Magneto-Spectroscopic Optical Coupling
- FTIR Magneto-Spectroscopic Transmission Probe for External Detectors
- FTIR Magneto-Spectroscopic Transmission Probe for Internal Detectors
- FTIR Magneto-Spectroscopic Transmission Probe with Chipset Holder

## Teaching

- 09-12/2020 (winter semester) – **Principles of Measurement (1ZM)** in Engineering at Faculty of Mechanical Engineering, Brno University of Technology.
- 09-12/2019 (winter semester) – **Principles of Measurement (1ZM)** in Engineering at Faculty of Mechanical Engineering, Brno University of Technology.
- 02-05/2019 (summer semester) – **Physics (BF)** at Faculty of Mechanical Engineering, Brno University of Technology.
- 09-12/2018 (winter semester) – **Principles of Measurement (1ZM)** in Engineering at Faculty of Mechanical Engineering, Brno University of Technology.

## Voluntary Activities

- 11/2019 – **8th School of the European Federation of EPR groups on Advanced EPR 2019** in Brno, Czech Republic, co-organizer.
- 09/2019 – **Researcher’s Night 2019** at CEITEC BUT, performing experiments for public.
- 09/2018 – **Researcher’s Night 2018** at CEITEC BUT, performing experiments for public.
- 07/2018 – **International Conference on Nanoscience+Technology 2018 (ICN+T 2018)** Brno, Czech Republic, navigator of the conference participants.